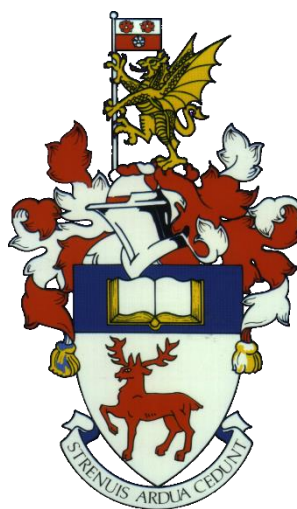


UNIVERSITY OF SOUTHAMPTON

FACULTY OF ENGINEERING AND PHYSICAL SCIENCES

School of Chemistry



DESIGN OF HETEROGENEOUS CATALYSTS FOR THE UTILISATION OF CARBON DIOXIDE AND TANDEM REACTIONS

by

William Robert Webb

Thesis for the degree of Doctor of Philosophy

September 2018

UNIVERSITY OF SOUTHAMPTON

ABSTRACT

FACULTY OF ENGINEERING AND PHYSICAL SCIENCES

CHEMISTRY

Thesis for the degree of Doctor of Philosophy

**DESIGN OF HETEROGENEOUS CATALYSTS FOR THE UTILISATION OF CARBON DIOXIDE
AND TANDEM REACTIONS**

William Robert Webb

The adoption of green technologies and principles by the chemical industry, and chemistry as a whole, is urgently required to help mitigate and ultimately reverse the alarming trends in global greenhouse gas emissions. Green processes such as carbon dioxide utilisation enable the incorporation of a waste material in the production of valuable synthetic chemicals. The catalysed reaction of CO₂ with epoxides is a particularly attractive example as the cyclic carbonate product has wide-ranging commercial applications. Recyclable, heterogeneous catalysts are at the forefront of research efforts to produce cyclic carbonates in a sustainable manner.

Through the development of an imidazole based organocatalyst covalently bound *via* pendant silanols to mesoporous silica, the efficacy and principles of heterogenised imidazoliums as catalysts for cyclic carbonates production was established. A facile anchoring strategy allowed for manipulation of the active site, which, with detailed physico-chemical and spectroscopic characterisation, established the catalytic mechanism, allowed for progressive optimisation and improved catalytic application.

The robustness of the anchoring method and the excellent activity of the functionalised imidazole catalysts led to their incorporation into supports of greater complexity. By employing analogous immobilisation methods, an imidazolium species was anchored to hierarchically porous aluminophosphates and silicoaluminophosphates where careful tuning of the framework properties improved the reaction selectivity towards the cyclic carbonate product.

Further heterogenisation of functionalised imidazoles onto the coordinatively unsaturated sites within the metal organic framework (MOF), MIL-101(Cr), resulted in a hybrid MOF with

exceptional activity for the reaction of CO₂ and epoxides, under halide-free and solvent-free conditions. Comprehensive characterisation, in combination with molecular modelling simulations, allowed for structure-property relationships to be established, enabling optimisation to afford high cyclic carbonate yields whilst employing short reaction times, relatively benign conditions and low catalyst loadings.

To further illustrate the scope of hybrid MOFs for sustainable applications the robust MOF, UiO-66(Zr), was exploited in a tandem catalytic reaction. Colloidal deposition of gold nanoparticles onto UiO-66-NH₂ framework enabled successive alcohol oxidation-Knoevenagel condensation reactions to be achieved at good yields, for a range of substrates. Furthermore the extension of the capabilities of the aforementioned MIL-101(Cr) framework to a different, epoxidation-CO₂ utilisation cascade reaction demonstrated the vast scope of applications achievable with hybrid MOFs for green and sustainable catalytic processes.

Table of Contents

ABSTRACT i

| | |
|--|----------------------|
| Table of Contents | iii |
| Table of Tables | vii |
| Table of Figures | <b.xi< b=""></b.xi<> |
| Table of Equations | xxv |
| Academic Thesis: Declaration of Authorship..... | xxvii |
| Acknowledgements | xxix |
| Definitions and Abbreviations..... | xxx |
| Chapter 1 Introduction..... | 1 |
| 1.1 Catalysts and catalysis..... | 1 |
| 1.1.1 Fundamentals and principles of catalysis | 1 |
| 1.1.2 Quantification of Activity | 5 |
| 1.1.3 Classes of catalyst..... | 7 |
| 1.1.4 Creation of heterogeneous catalysts | 8 |
| 1.1.5 Green Chemistry and Sustainability | 15 |
| 1.2 Carbon dioxide as a feedstock | 17 |
| 1.2.1 Fundamentals of reactions with CO ₂ | 17 |
| 1.2.2 CO ₂ utilisation..... | 17 |
| 1.3 Tandem reactions..... | 24 |
| 1.3.1 Gold Nanoparticles..... | 25 |
| 1.4 Aims and objectives..... | 32 |
| Chapter 2 Experimental Techniques | 33 |
| 2.1 Synthetic techniques | 33 |
| 2.1.1 Mesoporous silica and hierarchically porous AlPO and SAPO based organocatalysts | 33 |
| 2.1.2 Imidazole functionalisation of MIL-101(Cr) | 36 |
| 2.1.3 MNPs UiO-66-NH ₂ for tandem reactions..... | 39 |
| 2.1.4 MIL-101(Cr) for the epoxidation of styrene | 41 |

| | | |
|------------------|---|-----------|
| 2.2 | Characterisation Techniques | 43 |
| 2.2.1 | X-Ray Diffraction (XRD) | 44 |
| 2.2.2 | Surface analysis <i>via</i> gas adsorption | 47 |
| 2.2.3 | Thermogravimetric Analysis (TGA) | 50 |
| 2.2.4 | Thermogravimetric mass spectroscopy (TG-MS) | 51 |
| 2.2.5 | Nuclear Magnetic Resonance (NMR) Spectroscopy | 52 |
| 2.2.6 | Solid state NMR | 55 |
| 2.2.7 | Ultraviolet – Visible Spectroscopy (UV-vis) | 56 |
| 2.2.8 | Fourier Transform – Infrared Spectroscopy (FT-IR) | 58 |
| 2.2.9 | X-ray Photoelectron Spectroscopy (XPS) | 60 |
| 2.2.10 | Gas Chromatography (GC) | 63 |
| 2.2.11 | Gas Chromatography-Mass Spectrometry (GC-MS) | 65 |
| 2.2.12 | Electron Microscopy | 66 |
| 2.2.13 | Inductively Coupled Plasma – Optical Emission Spectroscopy (ICP-OES) | 69 |
| 2.2.14 | Elemental Analysis | 69 |
| 2.2.15 | Electron Paramagnetic Resonance (EPR) Spectroscopy | 70 |
| Chapter 3 | Harnessing silanols for heterogeneous, organocatalytic CO₂ utilisation..... | 73 |
| 3.1 | Heterogeneous organocatalysts for CO ₂ utilisation | 74 |
| 3.1.1 | Heterogeneous phosphonium catalysts | 74 |
| 3.1.2 | Heterogeneous ammonium catalysts | 76 |
| 3.1.3 | Heterogeneous imidazolium catalysts | 78 |
| 3.2 | Aims and objectives | 83 |
| 3.3 | Mesoporous silica based imidazolium organocatalysts | 84 |
| 3.3.1 | Characterisation of silica anchored imidazolium | 84 |
| 3.3.2 | Coupling of carbon dioxide and epoxides | 87 |
| 3.4 | Hierarchically porous supports | 107 |
| 3.5 | Immobilised N-heterocyclic carbenes | 117 |
| 3.5.1 | Characterisation | 117 |
| 3.5.2 | Catalytic testing | 122 |
| 3.6 | Future work and conclusions | 125 |

| | |
|---|------------|
| 3.6.1 Silica based imidazolium organocatalysts..... | 125 |
| 3.6.2 HP AlPO-5 based imidazolium organocatalysts | 125 |
| 3.6.3 Heterogeneous NHCs | 126 |
| Appendix A | 127 |
| A.1 ²⁹ Si CP and DE solid state NMR | 128 |
| A.2 Pore size distributions | 128 |
| A.3 TGA curves of pore diameter catalysts | 129 |
| A.4 NMR confirmation of anion exchange | 130 |
| Chapter 4 Imidazole functionalised MIL-101(Cr) for enhanced CO₂ utilisation | 133 |
| 4.1 Introduction to MIL-101(Cr) | 134 |
| 4.1.1 Structure and properties..... | 134 |
| 4.1.2 CO ₂ adsorption and catalysis..... | 136 |
| 4.1.3 Coordinatively unsaturated sites (CUS) | 137 |
| 4.2 Aims and objectives..... | 138 |
| 4.3 Results and discussion..... | 139 |
| 4.3.1 Characterisation | 139 |
| 4.3.2 Catalytic testing..... | 158 |
| 4.4 Conclusions and future work | 172 |
| 4.4.1 Conclusions..... | 172 |
| 4.4.2 Future work..... | 173 |
| Appendix B | 175 |
| B.1 FESEM image of MIL-101(Cr) collapse | 175 |
| B.2 NIR of MIL-101(Cr) and MIL-101-Me..... | 175 |
| B.3 FT-IR of 1-methyl imidazole | 176 |
| B.4 Full CO ₂ isotherms | 176 |
| Chapter 5 Metal Organic Frameworks for use in tandem catalytic reactions | 177 |
| 5.1 Metal Organic Frameworks for tandem reactions..... | 178 |
| 5.1.1 Tandem reactions with MOFs | 178 |
| 5.1.2 UiO-66 family structure and properties..... | 180 |

| | | |
|--------------------------------|--|------------|
| 5.2 | Aims and objectives | 185 |
| 5.3 | Tandem oxidation-Knoevenagel condensation | 187 |
| 5.3.1 | Characterisation..... | 187 |
| 5.3.2 | Tandem oxidation-KV reaction | 200 |
| 5.3.3 | Oxidation optimisation | 204 |
| 5.4 | Tandem epoxidation-CO ₂ utilisation | 221 |
| 5.4.1 | MIL-101(Cr) | 221 |
| 5.5 | Conclusions and Future Work..... | 227 |
| 5.5.1 | Oxidation-Knoevenagel..... | 227 |
| 5.5.2 | Alkene epoxidation-CO ₂ utilisation | 229 |
| Appendix C | | 231 |
| C.1 | GC-MS identification of condensation products | 231 |
| C.2 | Au NPs size distribution images | 231 |
| Chapter 6 Summary | | 233 |
| 6.1 | Harnessing silanols for heterogeneous, organocatalytic CO ₂ utilisation | 233 |
| 6.1.1 | Ongoing and Future Work | 234 |
| 6.2 | Imidazole functionalised MIL-101(Cr) for enhanced CO ₂ utilisation | 235 |
| 6.2.1 | Ongoing and Future Work | 235 |
| 6.3 | Metal Organic Frameworks for use in tandem catalytic reactions | 237 |
| 6.3.1 | Ongoing and Future Work | 238 |
| References | | 239 |

Table of Tables

| | |
|---|----|
| Table 1: Comparison of the merits and disadvantages of heterogeneous and homogeneous catalyst systems. | 7 |
| Table 2: The twelve principles of green chemistry. | 15 |
| Table 3: Summary of MOFs used for styrene oxide (SO) or propylene oxide (PO) and CO ₂ reactions. ^a MOF name unknown, the two Co MOFs have different structures. | 23 |
| Table 4: Summary of different MOF materials, the tandem processes catalysed and the active sites employed. | 25 |
| Table 5: Summary of the most common routes to synthesis of gold nanoparticle in solution ^[170] | 28 |
| Table 6: Summary of Au/MOFs used for the oxidation of benzyl alcohol. ^a Undertaken in alcohol therefore ester product. ^b Benzaldehyde. | 30 |
| Table 7: Mono functionalised imidazole structures, abbreviation used and ¹ H NMR tabulation. | 34 |
| Table 8: Summary of peak positions and tabulations for diPrIm(I). | 35 |
| Table 9: Partial charges for atoms on MIL-101(Cr) and MIL-101-Me. | 38 |
| Table 10: Potential parameters and atomic charges of CO ₂ and N ₂ | 39 |
| Table 11: Summary of the techniques used and information obtained during material evaluation. | 44 |
| Table 12: ²⁹ Si chemical environments and characteristic chemical shifts, chemical shifts are approximate for reference and based upon those from Chapter 3 and those reported by Baccile <i>et al</i> ^[221] | 56 |
| Table 13: Summary of UV-vis peak positions for MIL-101(Cr), UiO-66-NH ₂ and Au NPs. | 57 |
| Table 14: Nomenclature used to describe different stretching modes. | 59 |
| Table 15: Summary of key IR vibrations and peak positions. | 59 |
| Table 16: Analyte and internal standard masses and corresponding molar quantities then converted to ratio. C and IS in this instances relate to cinnamyl alcohol and internal standard respectively. | 64 |

| | |
|---|-----|
| Table 17: Peak area responses for triplicate measurement of each calibration solution and calculated peak ration of analyte to standard. C and IS in this instances relate to cinnamyl alcohol and internal standard respectively. | 64 |
| Table 18: Overview of supported phosphonium catalysts. ^a n-butyl chain. Propylene oxide substrate for all entries. ^c Flow conditions. ^d Poly(4-vinylbenzyl-tributylphosphorous-co-ethylene dimethacrylate). ^e Poly(ethylene glycol). Conv = conversion, Sel = selectivity. | 75 |
| Table 19: Summary of immobilised quaternary ammonium organocatalysts. ^a AGE = allyl glycidol ether. ^b Precipitated and dried. ^c Yield (%). | 77 |
| Table 20: Polymer supported imidazolium moieties for cyclic carbonate production. PO = propylene oxide, AGE = Allyl glycidol ether, CS = Cytosan, DVB = divinylbenzene, PS = polystyrene. | 79 |
| Table 21: Summary of silica immobilised imidazolium organocatalysts for cyclic carbonate production. ^a Polymer covalently linked to silica (PIL = Poly ionic liquid). ^b 0.05 wt. % not mol %. ^c Not covalently bonded, deposited by physical interaction. SO = styrene oxide. | 80 |
| Table 22: Summary of R group functionality along with naming convention used, with respect to Figure 46. | 84 |
| Table 23: Loading of diPrIm(I) on various silica supports, determined by CHN analysis using the nitrogen value for calculation | 89 |
| Table 24: Comparison of elemental analysis and TGA weight loss percentages for the range of pore diameter catalysts and Cabosil, diPrIm imidazolium for all. TGA mass loss curves normalised to 100 °C. | 89 |
| Table 25: Surface area and pore volume measurements on SiO ₂ and diPrIm(I) functionalised SiO ₂ . Values in brackets in the unmodified silica row are quoted from manufacturers specifications. | 94 |
| Table 26: Elemental CHN % before and after use for the 30 Å diPrIm(I)/SiO ₂ . Loading calculated based off the nitrogen content of the material. | 104 |
| Table 27: Summary of styrene oxide to styrene carbonate by HP SAPO-5 and silica based material with similar pore distribution. Analysed by ¹ H NMR, mesitylene used ITSD. | 113 |

| | |
|---|-----|
| Table 28: CHN % values for the diPrIm(I)/HP AlPO-5, with loading calculated from the nitrogen percentage..... | 115 |
| Table 29: Summary of styrene oxide to styrene carbonate by HP AlPO-5 and silica based materials. TON based upon organic component. Analysed by ^1H NMR, mesitylene used ITSD. | 115 |
| Table 30: ICP-OES results from Medac Ltd. showing the presence of potassium following the carboxylate synthesis stage. | 119 |
| Table 31: Summary of MIL-101(Cr) based catalysts for CO_2 and epoxide coupling. ^a Solvent free. ^b phosphotungstic acid | 136 |
| Table 32: BET surface area values for MIL-101(Cr) variants showing the effect of HNO_3 addition and washing cycles. ^a Synthesised from entry 1..... | 142 |
| Table 33: Elemental analysis for MIL-101(Cr) and MIL-101-Me samples. Loading (mmol g^{-1}) based upon nitrogen percentage. ^a Nitrogen content below detection limits so assumed to be zero..... | 144 |
| Table 34: Carbon, hydrogen, nitrogen, chromium and fluorine percentages as determined by ICP-OES for MIL-101(Cr) and MIL-101-Me. | 146 |
| Table 35: Carbon, hydrogen and nitrogen percentage values for MIL-101-Me samples with different loading based off N %. | 166 |
| Table 36: Recycle tests on MIL-101-Me, conditions, 5 g of butylene oxide (69 mmol), 20 bar CO_2 at RT, 200 mg of MIL-101-Me (1.88 mmol g^{-1} imidazole loading), 45 min. | 168 |
| Table 37: Summary of MOF based catalyst for tandem oxidation Knoevenagel condensation reactions. ^a Conversion of benzyl alcohol..... | 179 |
| Table 38: Surface area and pore volume values for the UiO-66 and UiO-66- NH_2 analogues... | 189 |
| Table 39: Summary of weight loss percentages for the four synthesised materials with comparison to the theoretical amounts..... | 191 |
| Table 40: Maximum and minimum NP sizes measured for Au NPs and Au/UiO-66 from TEM. | 196 |
| Table 41: Weight % loadings of gold on the two UiO-66 variants. | 199 |
| Table 42: Summary of oxidation and Knoevenagel investigations and overall tandem reactions. Reaction conditions: Cinnamyl alcohol (0.1 g), Au/UiO-66- NH_2 (40 mg; 0.87 wt. | |

%) TBHP (1.2 eq), *t*-BuOH (7 mL), 10 hours, 70 °C. ^a40 mg of UiO-66-NH₂ used.

^bMalononitrile added at 10 hours (0.1 g). Monitored by GC with chlorobenzene as ITSD (0.2 g). 200

Table 43: Summary of maximum, minimum and average diameter of Pd and Pt NPs measured on Pd/UiO-66 and Pt/UiO-66 respectively. 208

Table 44: Loading values of Pt and Pd on the UiO-66 framework..... 209

Table 45: Summary of maximum, minimum and average diameter of Au NPs measured for Au/UiO-66 and Au/UiO-66 (following one use for benzyl alcohol oxidation).211

Table 46: Summary of maximum, minimum and average diameter of Pt and Pd NPs measured by TEM following a single use for benzyl alcohol oxidation. 212

Table 47: Comparison between MNP loading before and after catalysis. ^aResult from catalyst collected during the studies of benzyl alcohol oxidation, Table 48. 213

Table 48: Conversion, selectivity and yield values for the oxidation of a range of alcohol to their respective aldehydes followed by Knoevenagel condensation with malononitrile. Reaction conditions: 40 mg Au/UiO-66-NH₂, 80 °C, 0.75 mmol alcohol, 1.2 eq TBHP (aq), 7 mL *t*-BuOH, 0.75 mmol malononitrile, see table for reaction times. ^aPublished values. ^bReaction was stopped as hexanoic acid only was produced. 214

Table 49: Size distribution summary for Au NPs on UiO-66-NH₂. Sample size were 44 and 43 for hexane and methanol respectively. 220

Table 50: Reaction conditions, conversion and selectivity values for styrene epoxidation in acetonitrile by Au NPS onMIL-101(Cr) variants, first entry analysed by ¹H NMR. ^aReflux conditions were stated. 226

Table of Figures

| | |
|--|----|
| Figure 1: Energy level diagram of a reaction displaying both catalysed and un-catalysed pathways, for the conversion of A and B to the product, C..... | 2 |
| Figure 2: Generic catalytic cycle where A and B are the starting materials and C the product. The main processes in the cycle are labelled. | 3 |
| Figure 3: Depictions of the A) Eley-Rideal mechanism and B) Langmuir-Hinshelwood mechanism. | 4 |
| Figure 4: Depiction of conversion of A to B, C and D using a catalyst, with B the desired product for the reaction. | 5 |
| Figure 5: L-proline catalysed aldol reaction. ^[11] | 9 |
| Figure 6: A) covalent attachment <i>via</i> a tether and B) electrostatic interaction. | 9 |
| Figure 7: Diagrammatic representation of an organocatalytic moiety supported within the pore of a mesoporous silica, with silanol sites highlighted. Produced from reference to and adaption of Figure 16 from Thomas <i>et al</i> , <i>Angew. Chemie - Int. Ed.</i> 2005 , <i>44</i> , 6456–6482 ^[8] | 10 |
| Figure 8: Methoxy displacement in trimethoxysilane tether resulting in covalent immobilisation. | 11 |
| Figure 9: Representation of MCM-41 supported L-proline for an aldol reaction ^[26] | 12 |
| Figure 10: Diagrammatic representation of MOF synthesis, where green sphere indicates metal and blue line is the linker (bidentate)..... | 13 |
| Figure 11: Representation of modulated synthesis of a MOF. | 14 |
| Figure 12: A) production of cyclic carbonate from a diol and phosgene B) 100 % atom efficient reaction of CO ₂ and epoxides to form cyclic carbonate and C) production of polycarbonates (ethylene carbonate shown for all cases)..... | 19 |
| Figure 13: Known mechanism for cyclic carbonate production catalysed by TBAB..... | 19 |
| Figure 14: A) rearrangement of epoxide to aldehyde and B) diol formation from ring opening with water..... | 20 |

| | |
|--|----|
| Figure 15: Depiction of silanol functionalisation resulting in covalent anchoring of ionic pair organic moiety to silica. Commonly X = Cl, Br, I and Y = N (either quaternary or part of an imidazolium ring) or P..... | 21 |
| Figure 16: A) 'Traditional reaction route' of A to C <i>via</i> B using two catalysts, in two steps with isolation of B in-between. B) Tandem reaction route where A reacts to C catalysed by a catalyst with two active sites, without isolation of B. | 24 |
| Figure 17: Energy level diagram for bulk, nanoparticle and atomic gold species tending towards discrete energy levels..... | 26 |
| Figure 18: Representation of the increase in surface atoms as percentage of the total number of atoms within a nanoparticle as size decreases. | 27 |
| Figure 19: Visual representation of NP-MOF locations and nomenclature used..... | 29 |
| Figure 20: Route to Oxidation-Knoevenagel tandem reaction employing a MOF based system, active sites in green..... | 31 |
| Figure 21: Diagrammatic representation of constructive diffraction of X-Rays..... | 45 |
| Figure 22: Representation of a unit cell (fcc) with (111) plane shown..... | 46 |
| Figure 23: Refinement of HP AlPO-5 using AlPO-5 literature reference (blue) to refine experimental pattern (red). | 46 |
| Figure 24: Representation of the characteristic shape of Type II and Type IVa isotherms, produced with reference to Thommes <i>et al</i> ^[212] | 48 |
| Figure 25: Langmuir and BET gas adsorption theories, whereby the Langmuir model shows solely monolayer formation and the BET model shows the formation of multiple layers prior to monolayer occurrence. | 48 |
| Figure 26: Diagrammatic representation of a TGA curve with labels affixed | 51 |
| Figure 27: Diagrammatic representation of a nucleus with spin $I > 0$ in a magnetic field, $B > 0$. Orientations are shown with different energies ($2I+1$ (labelled m_I) orientations are possible). | 52 |
| Figure 28: ^1H NMR spectra of the reaction of styrene oxide to styrene carbonate, with mesitylene added following the reaction. | 53 |
| Figure 29: Depiction of magic angle spinning NMR..... | 55 |

| | |
|---|----|
| Figure 30: Schematic representation of a d-d transition in d^3 Cr(III)..... | 57 |
| Figure 31: Hooke's Law whereby a diatomic molecule is seen to be two masses, m_1 and m_2 connected by a spring with a force constant of k | 58 |
| Figure 32: Representation of photoelectron emission from the 1s level..... | 61 |
| Figure 33: Exemplar XPS spectra displaying Cr2p, O1s, N1s and C1s peaks as labelled..... | 62 |
| Figure 34: Schematic of Gas Chromatography system | 63 |
| Figure 35: Example calibration curve based off the data displayed in Table 16 and Table 17, where | 64 |
| Figure 36: Schematic representation of scanning electron microscopy..... | 67 |
| Figure 37: Electron beam transmission through a sample with depiction of different electron scattering occurrence. | 68 |
| Figure 38: Spin state energies as a function of the magnetic field B_0 , β is the Bohr magneton and g_e is the spectroscopic g -factor..... | 70 |
| Figure 39: Schematic representation of g tensor and the EPR absorption and 1 st derivatives which result from this. Spherical system (red), whereby $g_x = g_y = g_z$ and axial system (green) whereby, $g_x = g_y < g_z$ | 71 |
| Figure 40: Depiction of silanol functionalisation resulting in covalent anchoring of ionic pair organic moiety to silica. Commonly $X = Cl, Br, I$ and $Y = N$ (can be part of an imidazolium ring) or P | 74 |
| Figure 41: Possible acceleration mechanism on the synergistic hybrid catalyst, proposed by Takahashi <i>et al</i> ^[238] | 76 |
| Figure 42: Depiction of three common routes to ammonium based organocatalysts for CO_2 coupling to epoxides. Note: this methodology is applicable to imidazole and imidazolium creation. | 76 |
| Figure 43: Imidazolium salt produced upon immobilisation to a silica support..... | 78 |
| Figure 44: N-heterocyclic carbene formation following deprotonation of an imidazolium..... | 82 |
| Figure 45: Carboxylate formation following introduction of a CO_2 atmosphere to the carbene | 82 |
| Figure 46: Imidazole with R group depicting where functionality differs. | 84 |

| | |
|---|----|
| Figure 47: ^1H NMR spectra of diPrIm (inset) with peak labels and associated integrals. 400 MHz, CDCl_3 , TMS reference | 85 |
| Figure 48: ^1H NMR spectra of diPr-imidazolium, diPrIm(I), formed from reaction with (3-iodopropyl)trimethoxysilane (structure inset). 400 MHz, CDCl_3 , TMS reference | 86 |
| Figure 49: Diagrammatic representation of covalent anchoring of imidazolium species to silica, <i>via</i> pendant silanols. | 86 |
| Figure 50: Conversion of butylene oxide to butylene carbonate (shown) over time by 1-methylimidazolium on silica (Melm(I)/ SiO_2). Reaction conditions: 115 °C, t = as per x axis, 20 bar CO_2 , 5 g butylene oxide, 0.1 % catalyst, solvent free. Analysed by ^1H NMR, mesitylene as ITSD. Inset: plot of $\ln[\text{butylene oxide}]$ versus time. | 87 |
| Figure 51: TGA curves for diPrIm(I) anchored onto different pore diameter silica supports. The curve was normalised to 100 °C in all cases. Conditions: range 30-900 °C, ramp rate 10 °C/min, Air flow: 50 mL/min. | 90 |
| Figure 52: ^{13}C solid state CP NMR (black, diPrIm(I)/ $\text{SiO}_2(150 \text{ \AA})$) and solution (green, diPrIm(I) oil) NMR spectrum (left) and ^{29}Si solid state CP NMR for diPrIm(I)/ $\text{SiO}_2(150 \text{ \AA})$. Note: the region of 75 – 80 ppm has been omitted from the ^{13}C spectrum to remove the large CDCl_3 present in the solution spectrum in order to adjust the scale to aid comparison. | 91 |
| Figure 53: N_2 adsorption and desorption isotherm for A) 30 Å B) 60 Å C) 150 Å and D) 250 Å mesoporous, in all cases blank silica (black), diPrIm/ SiO_2 (green), adsorption isotherm (solid) and desorption isotherm (dotted). | 92 |
| Figure 54: N_2 adsorption and desorption curves for blank mesoporous $\text{SiO}_2(150 \text{ \AA})$ (black), diPrIm(I)/ $\text{SiO}_2(150 \text{ \AA})$ (green), adsorption isotherm (solid) and desorption isotherm (dotted). | 93 |
| Figure 55: Average turnover frequency numbers for styrene oxide to styrene carbonate conversion over a range of pore diameter silica supports. Reaction conditions: 115 °C, 2 hours, 20 bar CO_2 , 5 g styrene oxide, 0.1 % diPrIm(I)/ SiO_2 (No support is diPrIm(I) at 0.1 %). Analysed by ^1H NMR, mesitylene as ITSD. Standard deviation shown based upon two measurements. | 95 |

| | |
|--|-----|
| Figure 56: Average Conversion (green) and selectivity (black) values for the coupling of CO ₂ with various epoxides. Reaction conditions: 115 °C, 6 hours, 20 bar CO ₂ , 5 g epoxide, 0.1 % diPrIm(I)/SiO ₂ (150 Å) . Analysed by ¹ H NMR, mesitylene as ITSD. Standard deviation shown based upon two measurements. | 96 |
| Figure 57: Depiction of electron donating effect and electron withdrawing effect of linear alkane and phenyl epoxide R groups respectively. | 97 |
| Figure 58: Comparison of epoxide side chain length and TOF. Trendline applied to data with correlation shown. Reaction conditions: 115 °C, 6 hours, 20 bar CO ₂ , 5 g epoxide, 0.1 % diPrIm(I)/SiO ₂ (150 Å) . Analysed by ¹ H NMR, mesitylene as ITSD. Standard deviation shown based upon two measurements. | 97 |
| Figure 59: TOF values for styrene carbonate formation by differently functionalised silica anchored imidazolium catalysts, inset: catalyst structure with R group location. Reaction conditions: 115 °C, 6 hours, 20 bar CO ₂ , 5 g styrene oxide, 0.1 % RIm(I)/SiO ₂ (150 Å) . Analysed by ¹ H NMR, mesitylene as ITSD. | 98 |
| Figure 60: Conversion (black) and turnover frequency (TOF, green) for diPrIm(I)/SiO ₂ (150 Å) for a range of loadings. Reaction conditions: 115 °C, 6 hours, 20 bar CO ₂ , 5 g styrene oxide, 0.1 g catalyst. Analysed by ¹ H NMR, mesitylene as ITSD. | 100 |
| Figure 61: Conversion values of CO ₂ and butylene oxide to butylene carbonate with diPrIm/SiO ₂ (150 Å) and different anions. Reaction conditions: 115 °C, 6 hours, 20 bar CO ₂ , 72 mmol butylene oxide, 0.1 mol % loading catalyst. Analysed by ¹ H NMR, mesitylene as ITSD. | 101 |
| Figure 62: Mechanism of cyclic carbonate formation, catalysed by diPrIm(I)/SiO ₂ | 102 |
| Figure 63: Recycle study on 30 and 250 Å diPrIm(I)/SiO ₂ . 1 st trial reaction conditions: 115 °C, 2 hours, 20 bar CO ₂ , 5 g styrene oxide, 0.1 mol % diPrIm(I)/SiO ₂ . Analysed by ¹ H NMR with mesitylene as ITSD. For collection and washing details, see experimental section. Light and dark green indicate each batch was tested twice. | 103 |
| Figure 64: ¹³ C solid state NMR for as synthesised diPrIm(I)/SiO ₂ 30 Å (green) and diPrIm(I)/SiO ₂ 30 Å post catalysis/recovered (black) and ²⁹ Si solid state NMR for as synthesised. diPrIm(I)/SiO ₂ 30 Å (green) and diPrIm(I)/SiO ₂ 30 Å post catalysis/recovered (black). In all cases the spectra are CP not DE in order to resolve all peaks clearly. | 104 |

| | |
|--|-----|
| Figure 65: N ₂ adsorption and desorption isotherms for SiO ₂ (black), diPrIm(I)/SiO ₂ (green) and diPrIm(I)/SiO ₂ recovered (blue). Silica was 150 Å for all. Inset: BET surface areas for the three materials. | 105 |
| Figure 66: TGA curves for as synthesised diPrIm(I)/SiO ₂ (150 Å, green) and diPrIm(I)/SiO ₂ following a single use and washing with DCM (150 Å, black). Conditions: range 30-900 °C, ramp rate 10 °C/min, Air flow: 50 mL/min..... | 106 |
| Figure 67: Diagrammatic representation of imidazolium grafting to HP SAPO-5, anchoring location depicted as within the mesopore, and isomorphous Si doping within the framework. R = 2,6-diisopropylphenyl..... | 108 |
| Figure 68: Powder XRD of diPrIm(I)/HP-SAPO-5 (green) and HP-SAPO-5 (black) to show retention of structural integrity. Patterns stacked to aid comparison. | 109 |
| Figure 69: FT-IR spectra of diPrIm(I)/HP-SAPO-5 with regions 3800-2400 cm ⁻¹ and 1350-1800 cm ⁻¹ shown to aid peak identification. Obtained as a KBr disc at RT, sample degassed beforehand..... | 110 |
| Figure 70: Solution ¹³ C spectrum for diPrIm(I)-trimethoxysilane oil (black) and solid state ¹³ C of diPrIm(I)/HP SAPO-5 (green), left. ²⁹ Si solid state NMR of diPrIm(I)/HP SAPO-5 (green) and as synthesised HP SAPO-5 (black), right. Note: the region of 75 – 80 ppm has been omitted from the ¹³ C spectrum to remove the large CDCl ₃ solvent peak to aid comparability. ²⁹ Si NMR was obtained by CP..... | 111 |
| Figure 71: N ₂ isotherm for HP SAPO-5 (black) and diPrIm(I)/HP SAPO-5 (green), inset: pore distributions for HP SAPO-5 (black) and diPrIm(I)/HP SAPO-5 (green). Adsorption isotherm (solid line) and desorption isotherm (dotted line). | 112 |
| Figure 72: Proposed capping method to reduce the number of silanols present in the framework mesopores after imidazolium grafting..... | 114 |
| Figure 73: Diagrammatic representation of imidazolium grafting to HP AlPO-5, anchoring location depicted as within the mesopore. R = 2,6-diisopropylphenyl. | 114 |
| Figure 74: Representation of isomorphous substitution of P with Si, leading to Brønsted acid site creation in the SAPO (right) as opposed to the AlPO (left). | 115 |
| Figure 75: Imidazolium deprotonation to form the respective carbene followed by carboxylate formation upon introduction of a CO ₂ atmosphere..... | 117 |

| | |
|---|-----|
| Figure 76: A) FT-IR of MesIm/SiO ₂ (black) and MesCO ₂ /SiO ₂ (green) prepared as KBr discs. B) FT-IR of MesCO ₂ /SiO ₂ (green) and MesCO ₂ /SiO ₂ following soxhlet washing (black dots) prepared as KBr discs. Data normalised for comparison..... | 118 |
| Figure 77: C1s and K2p regions of A) MesIm(I)/SiO ₂ and B) MesCO ₂ /SiO ₂ . Raw data (black) with fittings labelled in associated colour. | 119 |
| Figure 78: Thermogravimetric measurement of MesIm/SiO ₂ (black) and MesCO ₂ Im/SiO ₂ (green), 1st derivative also shown MesIm/SiO ₂ (black dots) and MesCO ₂ Im/SiO ₂ (green dots)..... | 120 |
| Figure 79: Thermogravimetric MesIm/SiO ₂ (black) and MesCO ₂ Im/SiO ₂ (green) and mass spectrum data for m/z of 44 for MesIm/SiO ₂ (black dots) and MesCO ₂ Im/SiO ₂ (green dots). | 121 |
| Figure 80: Mass spectrum snapshot for MesCO ₂ /SiO ₂ when T = 120 °C (approximate ion current peak maximum for m/z = 44) | 122 |
| Figure 81: Conversion values of butylene oxide by Me, iPr and tBu materials, imidazolium (black) and carboxylate (green) for all cases. Reaction conditions: 115 °C, 6 hours, 20 bar CO ₂ at RT, 72 mmol butylene oxide, 0.1 % mol loading catalyst. Analysed by ¹ H NMR, mesitylene as ITSD. | 123 |
| Figure 82: Proposed mechanism for the carboxylate catalyst. R ₂ equal to structure shown in Table 22. | 124 |
| Figure 83: Proposed tandem reaction to produce cyclic carbonates from olefins..... | 126 |
| Figure 84: Single Cr ₃ O trimer (left) and three Cr ₃ O trimers depicting interconnectivity by terephthalate linkers (right). Only O-C-O depicted of outward facing terephthalate linkers. Oxygen (red), chromium shown as octahedral environment (green) fluorine/hydroxyl (pink), carbon (black) and oxygen of water (blue). | 134 |
| Figure 85: Hexagonal and pentagonal windows, with dimensions shown (top). Cage structures formed as part of MTN zeotype structure (bottom). Oxygen (red), chromium as octahedral environments (green) and carbon (black). | 135 |
| Figure 86: Representation of Cr ₃ O trimer water removal to create coordinatively unsaturated sites (CUS). Oxygen (red), chromium (green) fluorine/hydroxyl (pink), carbon (black) and oxygen of water (blue). | 137 |

| | |
|---|-----|
| Figure 87: Diagrammatic representation of dehydration of MIL-101(Cr) followed by post synthetic modification by functionalisation of the created CUS with an imidazole..... | 138 |
| Figure 88: Insertion of carbon dioxide into an epoxide forming a cyclic carbonate | 138 |
| Figure 89: FESEM images of A) MIL-101(Cr) hydrothermally synthesised with no additive (after ethanol and NH_4F treatment) B) MIL-101-Me by PSM on sample synthesised with no additive C) MIL-101(Cr) with HNO_3 additive (after ethanol and NH_4F treatment) and D) MIL-101-Me by PSM on batch synthesised with HNO_3 additive. Samples gold coated for 20s prior to imaging..... | 140 |
| Figure 90: Powder XRD patterns of MIL-101(Cr) simulated (blue), MIL-101(Cr) with HNO_3 (green) and MIL-101-Me (black). Y values offset for comparison. | 141 |
| Figure 91: N_2 adsorption and desorption isotherms of MIL-101(Cr) as synthesised (blue) and MIL-101(Cr) following ethanol and NH_4F washing (green)..... | 142 |
| Figure 92: N_2 adsorption isotherms for MIL-101(Cr) (green), MIL-101-Me (black), MIL-101(Cr) simulated (light green) and MIL-101-Me (grey) | 143 |
| Figure 93: TGA profiles for MIL-101(Cr) (green) and MIL-101-Me (black), taken in air at $10^\circ\text{C}/\text{min}$ ramp rate..... | 145 |
| Figure 94: XPS spectra for A) Survey scan of MIL-101(Cr) (green) and MIL-101-Me (black) with regions highlighted, B) $\text{Cr}2\text{p}$ region of MIL-101(Cr), C) $\text{C}1\text{s}$ region of MIL-101(Cr), D) $\text{N}1\text{s}$ region of MIL-101(Cr) (green) and MIL-101-Me (black). For B-D raw data is shown as data points. | 147 |
| Figure 95: X-band continuous wave (CW) detected EPR spectra of MIL-101(Cr) (green) and MIL-101-Me (black) recorded at ambient temperature and pressure..... | 148 |
| Figure 96: A) DR UV-Vis, visible range spectra of MIL-101(Cr) (green) and MIL-101-Me (black). B) DR UV-Vis spectra of MIL-101(Cr) (green) and MIL-101-Me (black). For both: in air (dotted curves) and after outgassing the samples at 150°C for 1h (solid lines). | 149 |
| Figure 97: A) FT-IR spectra of MIL-101(Cr) and MIL-101-Me upon outgassing at 150°C for 1h. B) Full FT-IR spectra of MIL-101(Cr) and MIL-101-Me, recorded in KBr after outgassing the samples at room temperature for 2 hours. For both: MIL-101(Cr) (green) and MIL-101-Me (black). | 150 |

- Figure 98: FT-IR difference spectra of decreasing CD₃CN coverages (from vapour pressure to vacuum) of MIL-101(Cr) (green curve) and MIL-101-Me (black curve). Samples were outgassed at 150 °C prior to dosing. The band at 2261 cm⁻¹ corresponds to physisorbed CD₃CN.152
- Figure 99: DR UV-Vis spectra of CO₂ adsorption (100 mbar, dotted lines) at room temperature on MIL-101(Cr) (green) and MIL-101-Me (black). Solid lines refer to non-dosed samples under vacuum, dashed lines to the samples upon outgassing CO₂ (at RT).153
- Figure 100: a) side on view of electrostatic potential maps around the Cr₃O trimer in MIL-101(Cr) (left) and MIL-101-Me (right) b) top-down electrostatic potential maps around the Cr₃O trimer in MIL-101(Cr) (left) and MIL-101-Me (right). Above: structure shown in a) without electrostatic potential maps, for reference.154
- Figure 101: Adsorption isotherms of CO₂ in MIL-101(Cr) and MIL-101-Me at 298 K. MIL-101-Me experimental (black circle), MIL-101(Cr) experimental (dark green square), MIL-101-Me simulated (grey triangle) and MIL-101(Cr) simulated (light green triangle). Desorption not shown to aid clarity, see Appendix B4 for full isotherm.155
- Figure 102: Simulated favorable CO₂ adsorption sites in one cross-sectional pentagonal cluster of MIL-101-Me. Chromium octahedra (blue), nitrogen (yellow), fluorine (green) and carbon (black), hydrogen atoms are hidden. For illustrative purposes - framework oxygen are red, carbon dioxide oxygen are pink. Numbers 1, 2 and 3 relate to distinct binding sites with distances of 2.17, 2.43 and 3.19 Å respectively.156
- Figure 103: Radial distribution functions of A) CO₂ around the unsaturated Cr of MIL-101(Cr) (green) and MIL-101-Me (black), B) CO₂ around F atom of MIL-101(Cr) (green) and MIL-101-Me (black) and C) CO₂ around imidazole group in MIL-101-Me N2 (black) and C4-Im (blue). CO₂ pressure is 1000 mbar for all. D) Cr₃O cluster of MIL-101-Me depicting atom labelling – note: labelling is the same for MIL-101(Cr) minus those for the imidazole.157
- Figure 104: Conversion values for butylene oxide to butylene carbonate for MIL-101-R, whereby R relates to the functionality on the non-grafting nitrogen. Reaction conditions: butylene oxide (55 mmol), catalyst MIL-101-R (0.075 mol %), solvent free, 115

| | |
|---|-----|
| °C, 1.5 hours, 20 bar CO ₂ (at RT). Analysed by ¹ H NMR using mesitylene as an internal standard. | 158 |
| Figure 105: Conversion of butylene oxide to butylene carbonate over time. Reaction conditions: 5 g epoxide, 5 hours, 115 °C, time: see axis, 20 mg MIL-101-Me (1.88 mmol/g loading), 20 bar CO ₂ (at RT). Analysed by ¹ H NMR using mesitylene as an internal standard. Note: each time point is a separate reaction. | 159 |
| Figure 106: Conversion values of butylene oxide for the reaction with CO ₂ to butylene carbonate (shown). Reaction conditions: butylene oxide (55 mmol), catalyst MIL-101-Me (0.96 mmol/g, 0.075 % mol), solvent free, 115 °C, 1.5 hours, 20 bar CO ₂ (at RT). Analysed by ¹ H NMR using mesitylene as an internal standard. Melm denotes 1-methylimidazole. *Blank (no catalyst) reaction time 24 hours. **Free imidazole reaction time 6 hours. | 160 |
| Figure 107: UV-Vis spectra of MIL-101(Cr) (green) and physical mixture of MIL-101(Cr) + Melm (blue). The physical mixture spectra is post-catalysis, the MIL-101(Cr) is as synthesised. | 161 |
| Figure 108: Favourable adsorption site for epoxide and CO ₂ in a Cr ₃ O cluster trimer of MIL-101-Me; a “cave” formed by two grafted 1-methyl imidazole groups and F atom is shown. Note: butylene oxide side chain (-CH ₂ CH ₃) was removed in order to ease the computational strain. | 162 |
| Figure 109: A) Radial distribution functions for epoxide and F atom in MIL-101(Cr) and MIL-101-Me and B) RDF for epoxide and CO ₂ cluster formation in MIL-101(Cr) and MIL-101-Me. For both MIL-101(Cr) (green) and MIL-101-Me (black). | 163 |
| Figure 110: A) Favourable adsorption site for epoxide and CO ₂ in a (Cr ₃ O) ₃ cluster of MIL-101-Me, as determined by DFT modelling. B) Epoxide and CO ₂ cluster with molecular orbitals shown. | 164 |
| Figure 111: A) Distances between CO ₂ and epoxide in the alternative cluster of CO ₂ and epoxide in MIL-101-Me. B) Molecular orbital depiction showing π- π interaction. | 165 |
| Figure 112: Adsorption isotherms of CO ₂ by MIL-101(Cr) and varied MIL-101-Me analogues at 298 K. MIL-101(Cr) (green, square), MIL-101-Me with 1.19 mmol/g loading (black circle) and MIL-101-Me with 1.89 mmol/g loading (dark grey triangle) and MIL-101-Me with 2.13 mmol/g loading (light grey triangle). | 166 |

| | |
|--|-----|
| Figure 113: Average values for the conversion of butylene oxide to butylene carbonate with differing values of imidazole loading. Reaction conditions: butylene oxide (69 mmol), catalyst MIL-101-Me (0.06 % mol), solvent free, 115 °C, 1.5 hours, 20 bar CO ₂ (at RT). Analysed by ¹ H NMR using acetonitrile as an internal standard. Note: 'zero' loading denotes the blank framework MIL-101(Cr). Errors shown from two repeat measurements. | 167 |
| Figure 114: UV-Vis spectra of MIL-101(Cr) (green), MIL-101-Me pre-catalysis (black) and MIL-101-Me post-catalysis (blue), following the reactions undertaken in Table 36. ... | 169 |
| Figure 115: Nitrogen adsorption and desorption curves of MIL-101-Me (black) and MIL-101-Me after a single use in butylene oxide to butylene carbonate reaction (blue), reaction undertaken at 1 bar CO ₂ | 170 |
| Figure 116: FESEM image of MIL-101-Me following a single reaction with butylene oxide and CO ₂ , Sample was gold sputtered for 20 seconds prior to imaging. | 170 |
| Figure 117: Powder XRD of MIL-101(Cr) (green), MIL-101-Me as synthesised (black) and MIL-101-Me for three cycles of use (blue). | 171 |
| Figure 118: Example of tandem reaction on a MOF where A to B is catalysed by the linker, 1, and B to C is catalysed by the metal centre, 2..... | 178 |
| Figure 119: Tandem oxidation-Knoevenagel condensation reaction..... | 179 |
| Figure 120: A) Two Secondary building units (SBUs) of UiO-66 detailing the Zr ₆ cluster, linked <i>via</i> a terephthalate. B) Zr square antiprismatic coordination sphere: 1) μ_3 bridging oxygen, 2) bidentate terephthalate linkers and 3) μ_3 bridging hydroxyls. For all: Zr – blue (spheres and polyhedra); C – black spheres; O – red spheres and H – pink spheres..... | 180 |
| Figure 121: A and B) two representations of crystal structure of UiO-66 with pore window highlighted in yellow (A) and pores shown (B). C) Octahedral pore and D) Tetrahedral pore. For all: Zr – blue (polyhedra); C – black spheres; O – red spheres and H – have been hidden | 181 |
| Figure 122: Structures of terephthalic acid (left) and 2-aminoterephthalic acid (right). | 182 |
| Figure 123: Diagrammatic representation of a tandem oxidation-Knoevenagel condensation reaction ^[373] | 185 |

| | |
|---|-----|
| Figure 124: Proposed tandem reaction to convert an alkene to a cyclic carbonate with CO ₂ utilisation <i>via</i> and epoxide. | 186 |
| Figure 125: SEM images of UiO-66 (left) and UiO-66-NH ₂ (right). Samples sputter coated with gold for 20s prior to imaging. | 187 |
| Figure 126: Nitrogen adsorption isotherms of UiO-66 (red) and Au/UiO-66 (blue). For both: adsorption curve (solid) and desorption curve (dotted). | 188 |
| Figure 127: Nitrogen adsorption isotherms for UiO-66-NH ₂ (purple) and Au/UiO-66-NH ₂ (green). For both: adsorption curve (solid) and desorption curve (dotted). | 189 |
| Figure 128: TGA curves of A) UiO-66 and Au/UiO-66, B) 1 st derivative of UiO-66 and Au/UiO-66, C) UiO-66-NH ₂ and Au/UiO-66-NH ₂ and D) 1 st derivative of UiO-66-NH ₂ and Au/UiO-66-NH ₂ . In all cases UiO-66 (red), Au/UiO-66 (blue), UiO-66-NH ₂ (purple) and Au/UiO-66-NH ₂ (green). TGs taken in air at 10 °C/min ramp rate. | 190 |
| Figure 129: A) Powder X-ray diffraction of UiO-66 (red) and Au/UiO-66 (blue) and B) UiO-66-NH ₂ (purple), Au/UiO-66-NH ₂ (green). Values beyond that of 10 theta have been scaled 10 times as the two peaks below that have high intensity relatively, with UiO-66-simulated (black) for both. | 192 |
| Figure 130: FT-IR of A) UiO-66-NH ₂ (purple) and Au/UiO-66-NH ₂ (green), B) 4-aminoterephthalic acid (black). The left region of both peaks has been expanded in order to highlight the N-H peaks. | 193 |
| Figure 131: UV-vis of Au/UiO-66 (blue), Au/UiO-66-NH ₂ (green) and Au NPs in methanol (inset, black, peak labelled for visualisation aid). | 194 |
| Figure 132: A) TEM of Au NPs (as synthesised in methanol) and B) Au/UiO-66. Each histogram plot based on statistical analysis of Au NPs (red) and Au/UiO-66 (blue) from 4 and 3 three images respectively. | 195 |
| Figure 133: XPS survey scan for UiO-66 (red), Au/UiO-66 (blue) and Au/UiO-66-NH ₂ (green) with regions of interest highlighted. | 197 |
| Figure 134: High resolution scans of the framework regions of UiO-66-NH ₂ | 198 |
| Figure 135: Au4f region showing sputtered gold (black), Au/UiO-66-NH ₂ (green) and Au/UiO-66 (blue). Fitted curves in grey for samples. | 199 |

| | |
|--|-----|
| Figure 136: Tandem reaction of cinnamyl alcohol to cinnamylidene malononitrile <i>via</i> cinnamaldehyde using Au/UiO-66-NH ₂ . Reaction conditions: 40 mg Au/UiO-66-NH ₂ , 70 °C, TBHP, 0.75 mmol cinnamyl alcohol, 1.2 equiv. TBHP(aq), 7 mL <i>t</i> -BuOH, 0.75 mmol malononitrile. Dotted line at 10 hours indicates the addition of the malononitrile ^[373] | 201 |
| Figure 137: FT-IR of A) Au/UiO-66-NH ₂ before catalysis (green) and after catalysis (blue). B) 2000-1000 cm ⁻¹ region. | 202 |
| Figure 138: A) Knoevenagel condensation reaction between benzaldehyde and malononitrile and B) Imine formation by reaction of benzaldehyde with the amine functionalities of the MOF. R = UiO-66-NH ₂ extended framework. | 203 |
| Figure 139: XRD patterns of UiO-66 (red), Pd/UiO-66 (orange) and Pt/UiO-66 (turquoise). Values beyond that of 10 theta have been scaled 10 times as the two peaks below that have high intensity relatively..... | 205 |
| Figure 140: Nitrogen isotherms of Pd/UiO-66 (orange) and Pt/UiO-66 (turquoise), with BET surface area values, inset. For both: adsorption curve (solid) and desorption curve (dotted)..... | 206 |
| Figure 141: XPS regions for A) Pd on Pd/UiO-66, with Pd peaks offset, above, for visualisation, and B) Pt on Pt/UiO-66. | 207 |
| Figure 142: TEM image of Pt/UiO-66 with histogram detailing Pt NP size distribution. Measurements undertaken on three images of Pt/UiO-66. | 207 |
| Figure 143: TEM image of Pd/UiO-66 with histogram detailing Pd NP size distribution. Measurements undertaken on three images of Pd/UiO-66..... | 208 |
| Figure 144: Benzyl alcohol oxidation conversion (left) and selectivity towards benzaldehyde and benzoic acid (right). Reaction conditions: 20 mg MNPs/UiO-66, 80 °C, 0.75 mmol benzyl alcohol, 1.2 eq TBHP (aq), 7 mL <i>t</i> -BuOH, 24 hours..... | 209 |
| Figure 145: TEM image (left) of Au/UiO-66 following use for the oxidation of benzyl alcohol, histogram (right) of Au NP size. Measurement undertaken on two images of Au/UiO-66 (used)..... | 211 |
| Figure 146: TEM images of Pd and Pt NPs on UiO-66 after use in the oxidation of benzyl alcohol with size distribution histogram shown (right). Measurements undertaken on two images for both Pd and Pt/UiO-66 (used). | 212 |

| | |
|---|-----|
| Figure 147: Tandem cascade of alcohol to aldehyde followed by Knoevenagel condensation. | 214 |
| Figure 148: A) Au/UiO-66 and crystal with partial coverage (inset) and B) Au/UiO-66-NH ₂ detailing non-uniform deposition across crystals within the same sample. | 216 |
| Figure 149: TEM images of Au/UiO-66-NH ₂ using acetic acid as the modulator. | 217 |
| Figure 150: TEM images of samples prepared through attempted encapsulation of Au NPs with A) NPs highlighted appearing centred to the MOF particle and B) Au NP not encapsulated. | 218 |
| Figure 151: TEM images of Au NPs on UiO-66-NH ₂ synthesised in methanol and hexane. | 219 |
| Figure 152: Proposed tandem reaction to convert styrene to styrene carbonate <i>via</i> the epoxide using an oxidant and CO ₂ . | 221 |
| Figure 153: Conversion of styrene and selectivity towards styrene oxide by MIL-101(Cr) (green) and no catalyst (blue). For both: conversion (solid) and selectivity (dashes). Reaction conditions: Acetonitrile (5 mL), 70 °C, 4.8 mmol styrene, 1.2 eq TBHP (5.5 M/decane) and 20 mg MIL-101(Cr) (green only). Analysed by GC, chlorobenzene (0.1 g) as ITSD. | 222 |
| Figure 154: Conversion of styrene and selectivity towards styrene oxide by MIL-101(Cr) (green), MIL-101(Cr) synthesised with 50 mol % benzoic acid (light blue) and MIL-101(Cr) synthesised with 100 mol % benzoic acid (purple). For all: conversion (solid) and selectivity (dashes). Reaction conditions: Acetonitrile (5 mL), 70 °C, 4.8 mmol styrene, 1.2 eq. TBHP (5.5 M/decane) and 20 mg catalyst (as above). Analysed by GC, chlorobenzene (0.1 g) as ITSD. Benzoic acid mol % are with respect to the linker. | 223 |
| Figure 155: TEM images of Au@MIL-101(Cr) formed from a double solvent approach of water/hexane followed by reduction with NaBH ₄ . | 224 |
| Figure 156: XPS spectra for Au@MIL-101(Cr) of A) C1s region, B) survey scan of Au@MIL-101(Cr) with Cr 2p, O 1s, C 1s and Au 4f regions highlighted, C) Cr2p region and D) Au4f region, with sputtered Au reference added. Note: black (dotted) is baseline for all. | 225 |
| Figure 157: SEM images of UiO-66-NH ₂ synthesised with acetic acid (600:1, linker) with A) Triethylamine (TEA) addition (8 mM) and B) no TEA. Measurements of size undertaken on the images shown. | 229 |

Table of Equations

| | |
|---|----|
| Equation 1: Gibbs Free Energy equation, whereby H denotes enthalpy, T the temperature, S entropy and G corresponds to the Gibbs free energy..... | 1 |
| Equation 2: Rate equation for a simple reaction, where k is the rate constant and the rate is first order with respect to A and B, thus second order overall. | 4 |
| Equation 3: Arrhenius equation where k is the rate constant, A the pre-exponential factor, E_a the activation energy, T the temperature and R the ideal gas constant. | 4 |
| Equation 4: Conversion, defined as the loss of starting material during a reaction. | 5 |
| Equation 5: Selectivity, defined as the percent of the desired product relative to all products of the reaction. | 5 |
| Equation 6: Yield, whereby the conversion value is adjusted for the mass balance that was calculated at the end of the reaction. | 5 |
| Equation 7: Mass balance equation for determining the different in starting and final total mols. | 6 |
| Equation 8: Turnover number, detailed as the total number of catalytic cycles completed per active site. Note: conversion is not in percent in this instance..... | 6 |
| Equation 9: Turnover frequency, defined as the TON per unit time, thus has units of time^{-1} | 6 |
| Equation 10: Bragg's Law. | 45 |
| Equation 11: BET equation whereby p is pressure, p_0 is standard pressure, n_m is the volume of gas required to form a monolayer, V is volume of gas adsorbed at pressure P and finally C is the BET constant..... | 49 |
| Equation 12: Equation for monolayer determination whereby the gradient $(G) = C - 1nmC$ and the intercept (I) is equal to $1nmC$ | 49 |
| Equation 13: Determination of surface area whereby N_{Av} is Avogadro's constant, and σ is the cross sectional area of the sorbent..... | 49 |
| Equation 14: Modified Kelvin equation where γ is the surface tension of the adsorbent, V is the molar volume, r_p is the pore radius and t_c the thickness of the adsorbed multilayer film ^[212] | 50 |

- Equation 15: Means to determine moles of A within an NMR solvent, given the moles of the ITSD, the integrals ITSD and A and the number of protons (nH) for each. 54
- Equation 16: Determination of binding energy (BE) of the ejected photoelectron where $h\nu$ is the incident photon energy (h = Planks constant, ν = frequency), KE is the kinetic energy of the ejected photoelectron and ϕ is the work function of the spectrometer..... 60
- Equation 17: Relationship between peak areas of and moles of components adjusted by the R_f value. A and IS stand for analyte (to be determined) and internal standard respectively. 65
- Equation 18: Rearranged equation to find the concentration of an analyte from the peak area response recorded with R_f value applied. A and IS stand for analyte (to be determined) and internal standard respectively. 65
- Equation 19: The de Broglie equation where h is Planck's constant, and p is the relativistic momentum of the electron and λ is the wavelength..... 66

Academic Thesis: Declaration of Authorship

I, William Robert Webb declare that this thesis and the work presented in it are my own and has been generated by me as the result of my own original research.

Design of heterogeneous catalysts for the utilisation of carbon dioxide and tandem reactions

I confirm that:

1. This work was done wholly or mainly while in candidature for a research degree at this University;
2. Where any part of this thesis has previously been submitted for a degree or any other qualification at this University or any other institution, this has been clearly stated;
3. Where I have consulted the published work of others, this is always clearly attributed;
4. Where I have quoted from the work of others, the source is always given. With the exception of such quotations, this thesis is entirely my own work;
5. I have acknowledged all main sources of help;
6. Where the thesis is based on work done by myself jointly with others, I have made clear exactly what was done by others and what I have contributed myself;
7. Parts of this work have been published as:
 - a) Hinde, C. S.; Webb, W. R.; Chew, B. K. J.; Tan, H. R.; Zhang, W.-H.; Hor, T. S. A.; Raja, R. *Chem. Commun.* **2016**, 52, 6557–6560.
8. Parts of this work have been presented at the following conferences:
 - a) British Zeolite Association (BZA) Conference 2015, Chester, UK (*oral*)
 - b) The Science behind CO₂ Capture and Conversion 2015, Matanzas, Cuba (*oral*)
 - c) International Conference on Carbon Dioxide Utilisation XIV 2016, Sheffield, UK (*oral*)
 - d) 6th IMRE Scientific Research Forum 2017, Singapore (*poster*)
 - e) International Conference on Materials for Advanced Technologies 2017, Singapore (*poster*)
 - f) American Chemical Society (ACS) National Meeting 2018, Boston, USA (*oral*)
9. Other contributions to work that has been published:
 - a) D. Ansovini, C. J. J. Lee, C. S. Chua, J. Ong, H. R. Tan, W. R. Webb, R. Raja and Y.-F. Lim, *J. Mater. Chem. A*, 2016, **4**, 9744–9749.
 - b) A. Buchard *et al*, *Faraday Discuss.*, 2015, **183**, 463–487.
 - c) M. North *et al*, *Faraday Discuss.*, 2015, **183**, 261–290.

d) E. Remiezowicz *et al*, *Faraday Discuss.*, 2015, **183**, 463-487.

Signed: William Robert Webb

Date: 21/09/2018

Acknowledgements

I would like to take a moment and acknowledge the people who have helped during the four years of my PhD both inside and out of work, without whom I would not be here now. I have been incredibly lucky to have conducted my PhD research across two countries, starting in Southampton and finishing in Singapore. I have hugely enjoyed my time in both places and count myself lucky to have been able to split my research in this manner; in particular to experience a new country and culture whilst in Singapore.

First and foremost, I must thank my supervisor, Professor Robert Raja. From the outset of my PhD and throughout the four years of my research the knowledge and guidance Robert has given me has been invaluable to my development as a chemist. I am thankful for all the effort Robert has always put into discussing my work, my ideas, carefully editing my writing and presentations for conferences which his support allowed me to attend, and from which I have learnt so much. The support, effort and advice – not just limited to my PhD studies and especially during my time in Singapore – that Robert has provided has extended beyond that of a traditional supervisor and is very much appreciated.

I would like to thank Dr Pier Sazio for his help throughout the first year of my PhD which was vital for me coming to understand a new project, field and equipment. Thank you also to Dr Jinghua Teng and Dr Zhongxing Zhang for their supervision, advice and assistance during my time in Singapore.

My time in Southampton would not have been the same without the rest of the Raja Group and a close group of friends. From the Raja group I'd like to make a special mention of the help of Chris Hinde who became somewhat of a mentor to me in the short time he was around following his return from Singapore; and to Steph Newland for putting up with all my questions, queries and issues over the first year of my PhD and showing me the ropes at conferences! Lastly, Matt, thank you for your guidance, advice, patience and assistance with my work, all of which has been invaluable. Dan and Jack thank you for your help during my stay in Singapore and Pavan and Allison for your efforts as project students. To Steph, Luke, Cameron and India it has been a pleasure to share work, lunches, dinners, laughs, trips to the gym and beyond, and a house and flat (Cameron and India) with you.

I have been incredibly lucky during my time in Singapore to have coincided with a wonderful group of friends – Marie, Steve, Ben, Tom, Pepe, Matt and Sam, thank you. Most notably, I have been fortunate enough to spend my studentship at A*STAR with two brilliant scientists,

colleagues and friends in Elizabeth Ellis and Alexandra Ho who have shaped my time in IMRE – it wouldn't have been the same without them.

A special thanks to Zoe, who for the last two years has been an ever present source of encouragement, positivity and companionship; the experiences we have shared exploring Singapore and beyond have been incredible and I look forward to our future adventures together.

Finally, and in true acknowledgements style, I could not have reached where I am now without my family and most importantly my parents, Carol and Peter Webb. Their love and support throughout the ups and downs of my PhD has been constant, as ever, I owe them so much.

Definitions and Abbreviations

Where used throughout this work all attempts have been made to define an abbreviation in the first instance of use to aid the reader. Some of the more important examples are listed below.

Abbreviation Definition

| | |
|----------|--|
| AA | Acetic acid |
| BE | Binding energy |
| BET | Brunauer Emmett Teller |
| CHNS | Carbon, Hydrogen, Nitrogen and Sulphur |
| CUS | Coordinatively Unsaturated Site |
| DFT | Density Functional Theory |
| DI | De-ionised |
| DMF | N,N-Dimethylformamide |
| EA | Elemental Analysis |
| EPR | Electron Paramagnetic Resonance |
| FCC | Face Centred Cubic |
| FID | Flame Ionisation Detector |
| FT | Fourier Transform |
| FWHM | Full Width Half Maximum |
| GC | Gas Chromatography |
| GCMC | Grand Canonical Monte Carlo |
| GC-MS | Gas Chromatography – Mass Spectrometry |
| HP | Hierarchically Porous |
| ICP –OES | Inductively-Coupled Plasma – Optical Emission Spectroscopy |
| Im | Imidazole |
| IR | Infrared |
| ITSD | Internal Standard |

| | |
|-------|--|
| KE | Kinetic Energy |
| KI | Potassium Iodide |
| LSPR | Localised Surface Plasmon Resonance |
| LUMO | Lowest Unoccupied Molecular Orbital |
| MOF | Metal-Organic Framework |
| MPa | Mega Pascal |
| MS | Mass Spectroscopy |
| NHC | N-Heterocyclic Carbene |
| NIR | Near Infrared |
| NMR | Nuclear Magnetic Resonance |
| PEEK | Polyether ether ketone |
| PO | Propylene Oxide |
| PVA | Polyvinyl Alcohol |
| PVP | Poly-Vinylpyrrolidone |
| PXRD | Powder X-Ray Diffraction |
| RBF | Round Bottomed Flask |
| Rf | Response Factor |
| RPM | Revolutions per minute |
| RT | Room Temperature |
| SEM | Scanning Electron Microscopy |
| SO | Styrene Oxide |
| SPR | Surface Plasmon Resonance |
| ssNMR | solid-state Nuclear Magnetic Resonance |
| TBAB | <i>tert</i> -Butylene Ammonium Bromide |
| TBHP | Tertiary Butyl Hydrogen Peroxide |
| TEA | Triethylamine |

| | |
|--------|--------------------------------------|
| TEM | Transmission Electron Microscopy |
| TGA | Thermogravimetric Analysis |
| TG-MS | Thermogravimetric- Mass Spectroscopy |
| THF | Tetrahydrofuran |
| TMS | Tetramethylsilane |
| TOF | Turnover Frequency |
| TON | Turnover Number |
| UV-vis | Ultra-Violet Visible |
| WRT | With Respect To |
| XPS | X-Ray Photoelectron Spectroscopy |
| XRD | X-Ray Diffraction |

Chapter 1 Introduction

1.1 Catalysts and catalysis

1.1.1 Fundamentals and principles of catalysis

The chemical industry is hugely reliant on catalysts and catalysis. The manufacture of fuels, fine chemicals, pharmaceuticals and plastics are all processes which operate with a catalyst at their core. The terms *catalyst* and *catalysis* were coined by Jöns Jacob Berzelius in 1836 upon consideration of the work undertaken by Sir Humphry Davy and others who first reported platinum acting as an oxidation catalyst^[1]. A catalyst is defined by Shriver and Atkins^[2] as *a substance which increases the rate of a reaction without itself being consumed*. Catalysts therefore make reactions more efficient, faster and in many cases greener than the un-catalysed pathway. To this end Shriver and Atkins also note that these materials will *play a steadily increasing role in achieving a cleaner environment, through destruction of pollutants and development of cleaner industrial processes*. In the modern chemical industry the value of catalysts is vast, a point proven by Thomas and Thomas' statistic that *90 % of all chemical manufacturing processes worldwide employ catalysts*^[1]. Great emphasis is therefore placed on the research and development of catalysts capable of driving new reactions or existing reactions in a more efficient manner.

In a given reaction, both kinetics and thermodynamics determine the rate at which the reaction will proceed, if at all. Reaction progression is determined by the Gibbs Free Energy (ΔG) calculated by Equation 1.

$$\Delta G = \Delta H - T\Delta S$$

Equation 1: Gibbs Free Energy equation, whereby H denotes enthalpy, T the temperature, S entropy and G corresponds to the Gibbs free energy.

At a given temperature, if the total Gibbs free energy of the products is lower than that of the reagents, then the Gibbs energy change is negative, so the reaction will occur. For a reaction to be thermodynamically favoured it must have a negative Gibbs free energy change. During the course of a reaction, an energy barrier, the activation energy (E_a), must be overcome. How fast the reaction progresses, its kinetics, is inherently linked to the E_a ^[3]. Alteration of the activation energy of a given reaction induces a change in the rate of the reaction, but, as the position of the

equilibrium cannot be shifted, the rate of both the forward and reverse reactions are modified proportionally.

A catalyst functions by providing a lower energy pathway through which the reaction can occur. The catalyst achieves this by lowering the E_a for the reaction, which then will proceed through one or more transition states that have lower energies than the non-catalysed route, see Figure 1. The Gibbs energy of the two pathways (catalysed and un-catalysed) is still the same overall but the energy barrier is not. The catalysed route is therefore more energy efficient, due to the lower energy barrier needed to be overcome, and so the reaction can be run under less forcing conditions – i.e. at lower temperatures.

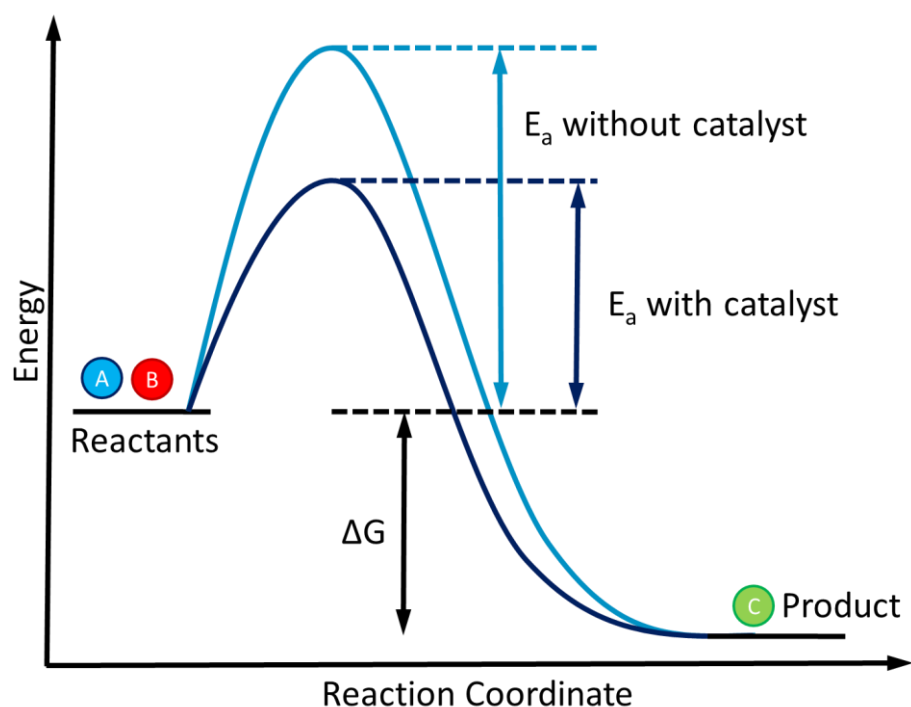


Figure 1: Energy level diagram of a reaction displaying both catalysed and un-catalysed pathways, for the conversion of A and B to the product, C.

Reduction of the activation energy, as achieved by a catalyst, is possible through a variety of means, as detailed by Masel^[4,5]. The rate at which the reaction progresses can be increased by:

- *Reaction initiation,*
- *Intermediate stabilisation,*
- *Holding reactants in close proximity,*
- *Weakening of bonds through stretching,*
- *Donating and accepting electrons,*
- *Holding reactants in the correct configuration,*
- *Efficient energy transfer.*

Additionally, catalysts can be employed to block side reactions so improving the selectivity of the reaction towards the desired product^[4]. As a catalytic reaction progresses, the reactants bind to the catalyst and intermediates are formed and stabilised by the catalyst. The energies of the intermediates dictate the energy of the various transition states, the highest of which will govern the E_a of the reaction. The products are formed on the catalyst and subsequently dissociate from it causing the regeneration and enabling further reactions to occur. In so doing, a catalytic cycle ensues, a basic schematic of which is shown in Figure 2. The reaction within the catalytic material occurs at a location known as the active site. Whilst predominantly associated with enzymes and their specific catalytic site, it can be used for all catalysts to describe the location where the substrate reacts and is converted to a product.

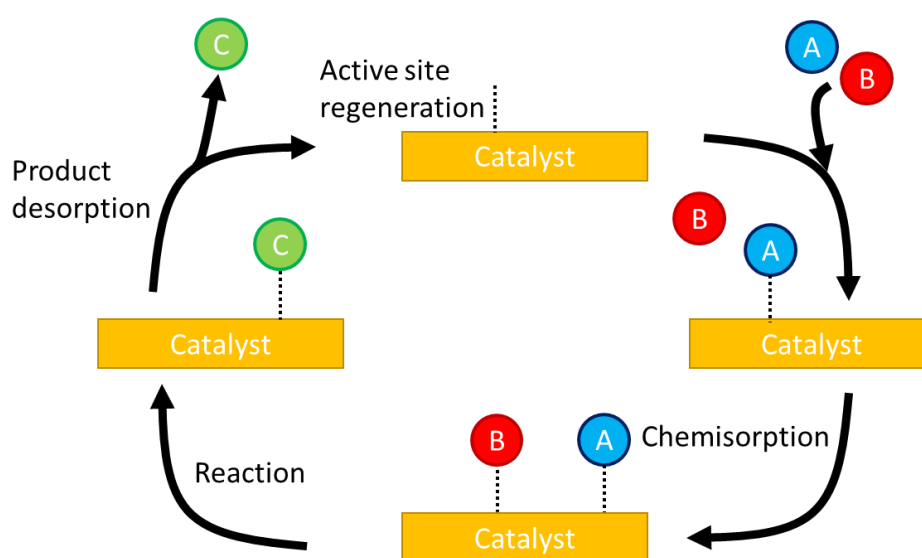


Figure 2: Generic catalytic cycle where A and B are the starting materials and C the product. The main processes in the cycle are labelled.

The course of the conversion of A and B to C, as depicted in Figure 2, is very simplistic in describing the intermediate species that form and react on a bulk surface. In reality, a catalytic cycle can go through multiple different mechanisms but most can be placed into one of three categories:

- *Langmuir-Hinshelwood mechanism where all reactants are adsorbed and react,*
- *Eley-Rideal mechanism where a molecule collides with an adsorbed species and reacts,*
- *A precursor mechanism during which one reactant is weakly bound and one is strongly bound during reaction progression^[4].*

The first two of these processes are depicted in Figure 3, detailing how the progression of a catalytic reaction upon a surface relies on the adsorption of one or more of the intermediates onto the surface which will activate them for subsequent reaction.

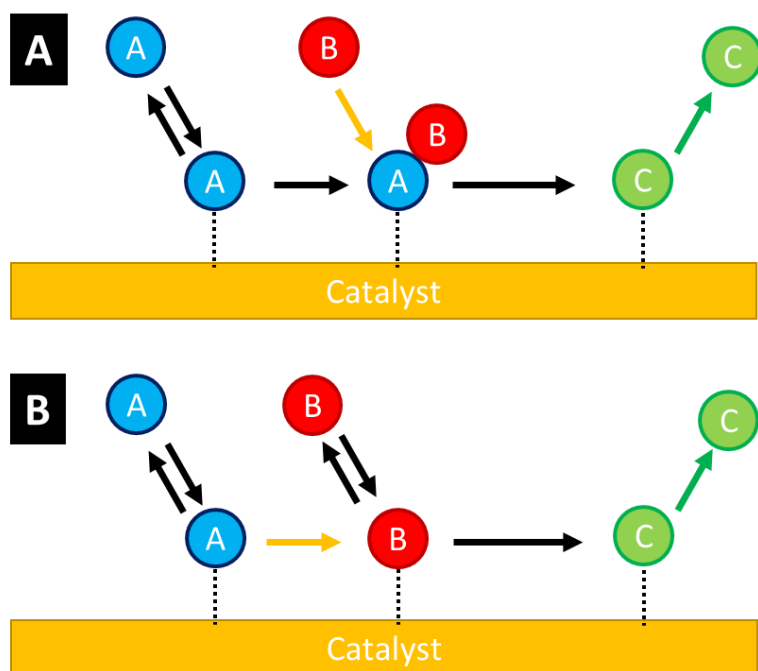


Figure 3: Depictions of the A) Eley-Rideal mechanism and B) Langmuir-Hinshelwood mechanism.

Mass transport is key upon consideration of the rate of the reaction. Catalyst type will alter the rate of a reaction, which is quantifiable. For a simple case, as above, the rate of reaction is dependent on the concentration of the two reagents, Equation 2.

$$Rate = k[A][B]$$

Equation 2: Rate equation for a simple reaction, where k is the rate constant and the rate is first order with respect to A and B, thus second order overall.

The Arrhenius equation, Equation 3, allows the rate of a reaction to be linked, *via* the rate constant, to the temperature at which the reaction is occurring. This enables the determination of the activation energy of a reaction pathway, at the reaction temperature. Quantification of the activation energy for a reaction allows catalyst efficiency to be evaluated and compared between catalysts^[3].

$$k = Ae^{-\frac{E_a}{RT}}$$

Equation 3: Arrhenius equation where k is the rate constant, A the pre-exponential factor, E_a the activation energy, T the temperature and R the ideal gas constant.

The logarithmic form of the Arrhenius equation, above, gives a linear relationship from which the activation energy can be calculated.

1.1.2 Quantification of Activity

Quantification of catalytic ability between different types of catalysts, section 1.1.3, or catalysts of the same type with a specific variation, is vital to discovery, design and improvement of catalytic materials. Literature will most often report the results of a catalytic reaction in terms of conversion and selectivity.

$$\text{Conversion (\%)} = \frac{SM \text{ initial (mol)} - SM \text{ final (mol)}}{SM \text{ initial (mol)}} \times 100$$

Equation 4: Conversion, defined as the loss of starting material during a reaction.

$$\text{Selectivity (\%)} = \frac{\text{desired product (mol)}}{\sum \text{all products (mol)}} \times 100$$

Equation 5: Selectivity, defined as the percent of the desired product relative to all products of the reaction.

These two terms, as defined in the above two equations, state the amount of substrate which has reacted after a certain period of time (conversion) and the extent to which the catalyst is capable of favouring a specific product over another (selectivity). The selectivity of reactions is important as it is possible for a catalyst to achieve complete conversion of the starting material yet produce none of the desired product. For example in the below, Figure 4, it is conceivable that the catalyst could facilitate the completed conversion of A yet produce only C and D (side-products). The quoting of both conversion and selectivity together when detailing the progression of a reaction is therefore important.

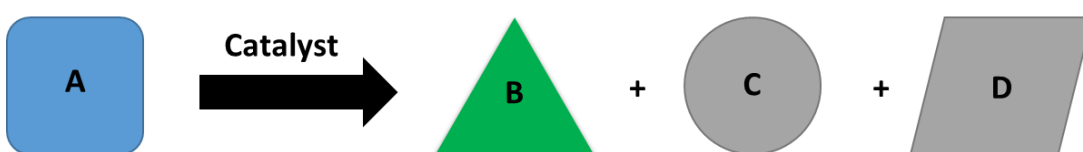


Figure 4: Depiction of conversion of A to B, C and D using a catalyst, with B the desired product for the reaction.

It is often then that the conversion and the selectivity are combined into one metric, yield, which as per Equation 6, is a function of the two with respect to the product being discussed.

$$\text{Yield (mol \%)} = 100 \times \frac{\text{desired product (mol)}}{\text{initial substrate (mol)}} = \text{Conversion} \times \frac{\text{Selectivity}}{100}$$

Equation 6: Yield, whereby the conversion value is adjusted for the mass balance that was calculated at the end of the reaction.

Another consideration is the mass balance of the reaction. The above conversion and selectivity equations assume that the total number of moles within the system is a constant throughout, such that the conversion of A to B, C and D occurs with the sum of the mols of B, C and D being equal to that of A (if conversion is 100 %). In reality this is not always the case as some products may not be detected by the analysis technique being employed or there could be decomposition products which are lost during the course of the reaction (small or gaseous molecules).

Differences between the amounts placed into the system, upon initial weighing, and those calculated during the analysis must therefore be determined, this is the mass balance (MB). Mass balance is calculated by determining the difference between the molar amount weighed into the system at the beginning of the reaction and those that are measured during the reaction mixture analysis.

$$\text{Mass balance (\%)} = \frac{\Sigma \text{ mols measured}}{\Sigma \text{ mols initial}} \times 100$$

Equation 7: Mass balance equation for determining the different in starting and final total mols.

The conversion, selectivity and yield equations do not take into account the amount of catalyst employed in the reaction and in so doing, do not factor in its activity. For this to occur it is more prudent to present turnover number (TON) and turnover frequency (TOF) values alongside conversion and selectivity data to enable analysis of the catalytic efficiency.

$$\text{Turnover number (TON)} = \frac{SM \text{ (mol)}}{\text{catalyst (mol)}} \times \text{conversion}$$

Equation 8: Turnover number, detailed as the total number of catalytic cycles completed per active site. Note: conversion is not in percent in this instance.

$$\text{Turnover frequency (TOF)} = \frac{TON}{\text{time}}$$

Equation 9: Turnover frequency, defined as the TON per unit time, thus has units of time⁻¹.

Through use of TON and TOF when reporting catalytic data, the activity of the catalyst can be evaluated as the quantity of the catalyst and substrate is taken in to account. The maximum TON achievable in a reaction is then at 100 % conversion, more simply determined by the ratio of substrate to catalyst. Turnover numbers enable for comparison between catalysts with different loadings. Thus in tandem with conversion and selectivity data, a catalyst can be evaluated for its ability to produce a desired product and the rate at which that occurs. It is still important to maintain the same ratio of substrate to catalyst even when intending to quote turnover numbers.

1.1.3 Classes of catalyst

There are two main classes of catalyst, homogeneous and heterogeneous, into which a catalyst can be placed. A homogenous catalyst is classified as being present in the same phase as the reagents. Therefore, mass transport is not normally rate-limiting if the solvent choice is suitable and the vessel well stirred. A heterogeneous system is defined as when the catalyst is in a different phase to the reagents. In this case, the mass transport becomes more important as the reactive species often have to diffuse through the system to the catalytic centre. In these instances, good mass transport is required for the substrate(s) to reach the active site and for removal of the product(s) following reaction in order to achieve fast reaction rates. Consequently, porous materials are widely employed to provide high surface areas and facilitate mass transport processes. The mixing of reagents throughout the support may not be as ideal as a homogeneous system and so the rate of reaction can be slowed in heterogeneous catalysts^[6].

The benefits and limitations to each catalyst type are summarised in Table 1. Biological catalysis, typically undertaken by enzymes, is sometimes given another sub-class of its own but can also be argued to be homogenous.

| Property | Heterogeneous | Homogeneous |
|-------------------|---|---|
| Phase | Solid, Liquid, Gas | Liquid |
| Temperature | Determined by the thermal stability of the material | Limited by the solvent medium |
| Synthetic control | Impregnation, deposition and anchoring techniques are more difficult to control. | Highly tuneable <i>via</i> synthetic pathway. |
| Mass transport | Lowered by requirement for substrates to diffuse through or adsorb onto surface environments to reach active site | High, diffusion high throughout the same phase |
| Active site | Structure and discrete nature can be more challenging to control | Predominantly organic, thus well-defined and reproducible. |
| Characterisation | Challenging, a combination of complex techniques is generally required | Common techniques such as NMR can discern structure easily |
| Re-use | Easily collected through filtration methodologies. Reactivation is needed in some occasions. | Separation from same phase reagents and is challenging. Aggregation can occur during use. |

Table 1: Comparison of the merits and disadvantages of heterogeneous and homogenous catalyst systems.

As shown in Table 1, one of the main benefits of heterogeneous catalysts is the ease of collection and reuse, even if they need to be reactivated, which can lower costs and so they are commonly favoured in industry. That is not to say that homogeneous catalysts are not industrially important, with estimates ranging from a 25-75 to 40-60 split (homogenous – heterogeneous) in those used commercially^[7]. Strategies for lowering the cost of homogenous catalyst re-use often focus on the redesign of the structure to aid separation following reaction or in the creation of heterogeneous versions.

1.1.4 Creation of heterogeneous catalysts

As highlighted in Table 1, homogeneous catalysts can suffer from aggregation during reaction which lowers activity and encourages the use of greater molar quantities in order to maintain yields. Following reaction homogeneous catalysts are dispersed throughout the reaction mixture and can even become embedded within the product itself, leading to expensive steps needed for recovery and reactivation. Development of heterogeneous versions to overcome these shortcomings is important. Not only is re-use easier but in some cases an increase in activity, selectivity and turnover numbers owing to the isolated single-site nature of the active sites created within the materials is seen. Site isolation is critical to activity as discrete, isolated active sites are able to function as efficiently as possible^[8,9]. The majority of properties of heterogeneous catalysts, detailed in Table 1, are dependent on the solid, insoluble component, commonly known as the support or framework. The formation of an active site on or within an insoluble support material can generally be undertaken through two different routes:

1. The support and catalytic entity are created separately and then combined;
2. The active sites are inherent to the support, by which they are incorporated in the material during the synthesis stage^[10].

1.1.4.1 Immobilisation of organic catalysts

The first route, listed above, is most often used for the creation of solid-supported organic and organometallic catalysts which are modified following reported activity in the homogeneous phase. *Organocatalysis* - the use of small organic molecules to catalyse organic transformations – has become a highly researched sub-section of catalysis since the early 2000s when work by List^[11] and Ahrendt^[12] first showed the benefits of organocatalyst use. List *et al* used L-proline, now one of the most commonly employed organocatalysts, to undertake the aldol reaction between acetone and an aldehyde with a 67 % yield of the desired product and good enantioselectivity, Figure 5^[11].

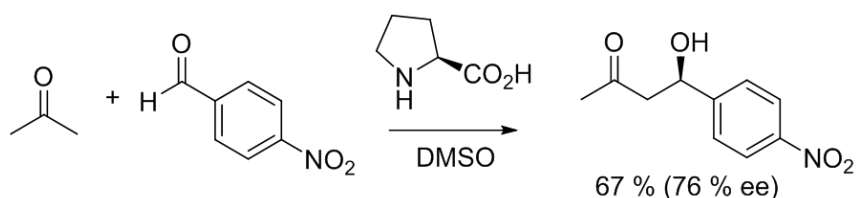


Figure 5: L-proline catalysed aldol reaction.^[11]

Organocatalysts have since been shown to have many advantages: they are easy to handle, facile to design and synthesise, have high selectivities, there are a large number of chiral options and they are mechanistically well understood and environmentally benign - the lack of metals within organocatalysts makes them attractive from a green standpoint^[13,14]. Reactions such as the previously mentioned aldol reaction but also Knoevenagel condensation, Diels-Alder, Michael addition and Baylis Hillman reactions are widely studied due to widespread use of the products in fine chemical applications for the pharmaceutical and perfume industries^[10,15,16].

Immobilisation then of organocatalysts on a support can theoretically maintain the benefits associated with these systems but with advantages of heterogeneous catalysts. Heterogenised versions of organic species can occur through covalent or non-covalent means – typically electrostatic interactions, Figure 6.

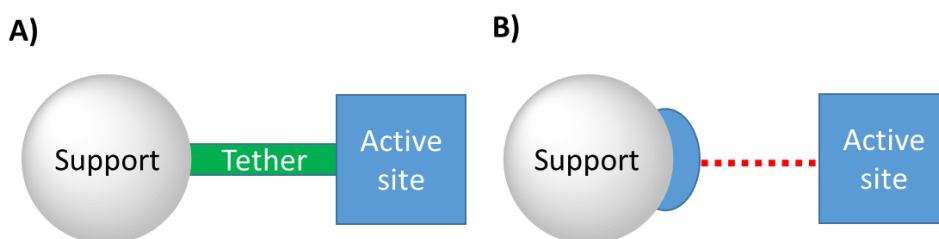


Figure 6: A) covalent attachment *via* a tether and B) electrostatic interaction.

Non-covalent immobilisation benefits from facile deposition of the material onto the support with little to no need for surface modification producing well-dispersed active sites which are partially labile (and can aid substrate interaction). However, because of this leaching of the catalytic centre can occur. Covalent anchoring typically prevents the leaching of the material as the robust nature of the covalent bonds induces high stability. Furthermore, this method can afford greater control over the location and loading of the organic material. To achieve covalent attachment alteration of the catalytically active homogeneous material is required in order for the support and active site to be linked by a tether, Figure 6A, a process which can negatively impact the catalytic activity.

Thus, when a covalent linkage is chosen, the choice of both support and tethering method is important^[17]. Covalent bonding of the catalytic species to the surface can occur through a variety

of means, see section 1.1.4.1.1, depending on the choice of support. Support selection is often particular to the catalytic system to be used and reaction to be undertaken with: solubility profile, cost, commercial availability, degree of functionalisation, and a possible involvement of the support backbone in the reaction all needing to be considered^[17]. The most common supports are an insoluble material which is cheap and readily available and to which functionalisation is facile so allowing for close control over immobilisation in order to produce discrete, catalytic, single-sites.

1.1.4.1.1 Mesoporous silica based organocatalysts

The creation of MCM-41 mesoporous silica^[18] allowed for the anchoring of organic moieties to the silanol (Si-OH) sites on the silica surface, but within a well-defined pore architecture. Mesoporous silicas are now commercially available in a range of pore sizes, 20 – 250 Å, through alteration of the synthesis procedure and so able to act as supports for organocatalysts. Covalent anchoring of organic species into the pores of silica occurs *via* the silanol groups which are found on the surface, see Figure 7. Not only is ease of functionalisation enabled, but the silanols can also have a role altering the chemical environment within the pore and aid the progression of reactions^[19].

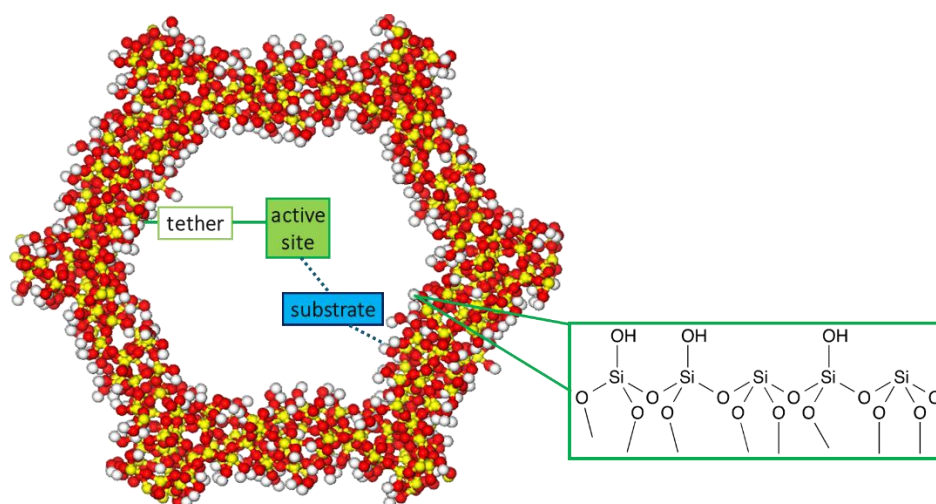


Figure 7: Diagrammatic representation of an organocatalytic moiety supported within the pore of a mesoporous silica, with silanol sites highlighted. Produced from reference to and adaption of Figure 16 from Thomas *et al*, *Angew. Chemie - Int. Ed.* **2005**, *44*, 6456–6482^[8].

The most common method of anchoring a tether onto a silica support uses trimethoxy or trimethoxysilane species. For trimethoxysilane, the methoxy groups are displaced by the silanols and a covalent bond is formed between the silica and the tether, the other end of which can be a range of different functionalities, see Figure 8. The selection of 'X', as per the notation in Figure 8,

will be dependent on the catalytic species which is to be anchored and how the two will be attached^[20].

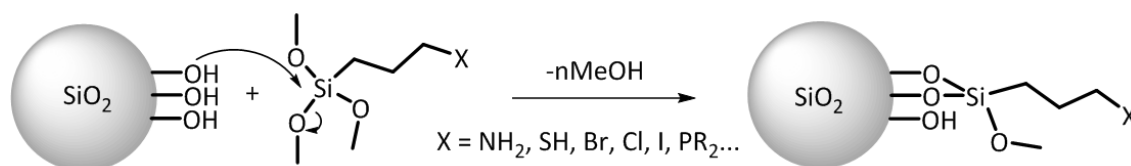


Figure 8: Methoxy displacement in trimethoxysilane tether resulting in covalent immobilisation.

The use of silica as a support for organocatalysts provides a number of benefits. Firstly, the ability to control the local chemical environment around the active site after covalent attachment onto silica is possible. The modification of the remaining silanols after immobilisation can be undertaken in order to fine tune the properties of the silica, with properties such as hydrophobicity able to be altered in this way. For example, if hydrophobicity shall enhance the reaction, then the number of silanol groups on the surface can be lowered through grafting organic compounds and the surface hydrophobicity will increase^[21,22]. Reagents such as $\text{RSi}(\text{OEt})_3$ and RSiCl_3 are popular silylating agents to functionalise the surface of the mesoporous silica^[23]. Furthermore, the structure of the environment around the catalytic centre is important, Jones *et al* elegantly showed that silica materials can control reactions through constriction of the pore size around an active catalytic centre^[24]. Through their use of MCM-41, which has an approximately 30 Å pore diameter, a concave environment around a bulky organometallic species was created. When contrasted with Cabosil, where the anchored species is in a convex environment, it was observed the organometallic complex on the MCM-41 had not only enhanced activity *versus* the homogeneous version but also that the constricted environment found in the MCM-41 allowed for greater enantioselectivity to be achieved than was obtained with Cabosil^[24].

Lastly, the large pore diameters possible for mesoporous silica enables the reaction of larger substrates but still within a controlled environment. In an early example by Maschmeyer *et al* MCM-41 was used to anchor a Ti metallocene for oxidation of bulky alkenes, such as pinene, and exemplified the promise of silica compared to other supports; in this case the material was able to oxidise bulky materials where microporous zeotype frameworks could not^[25].

The combination of silica and organic materials in some cases affords a system where the support and organocatalyst act in a synergist manner, as shown in the examples above. The key rationale to immobilisation onto silica was the ability to re-use the material with minimal activity loss. Proof of re-use capabilities was demonstrated by Dhar *et al*^[26] who used mesoporous MCM-41 supported L-proline to revisit the same reaction as List *et al*, Figure 5. Whilst immobilisation impacted both the yield and enantioselectivity the re-use of the catalyst, *via* facile collection, was

displayed and therefore clearly shows the benefits of immobilisation. A similar system by Calderon *et al*, again used MCM-41 supported L-proline to undertake different aldol reactions with re-use studies showing only minor yield decrease over three cycles, 45 to 40 %, hence validating the use of supported organocatalytic systems^[27].

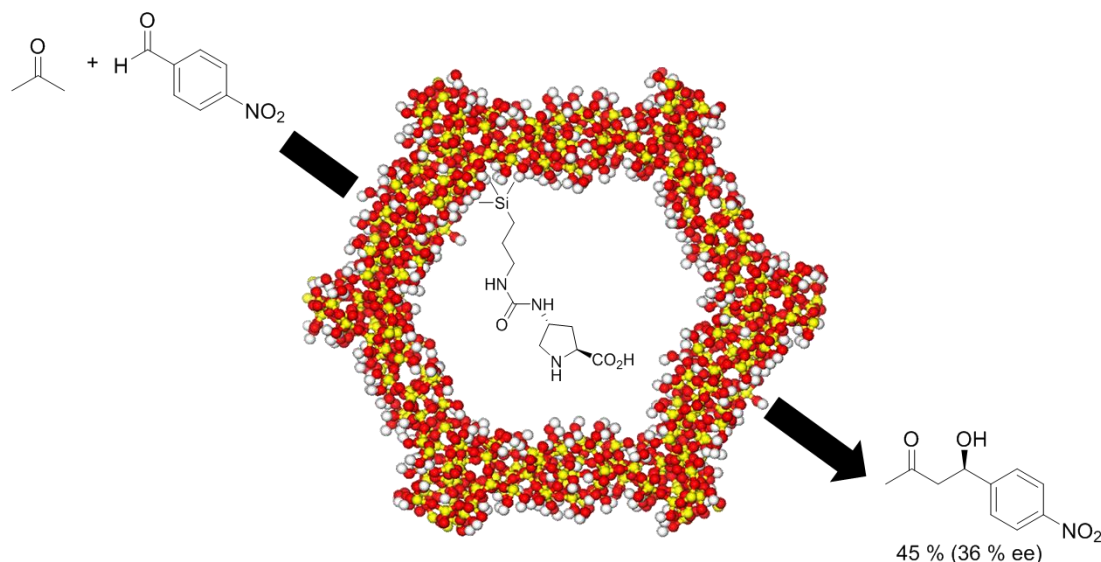


Figure 9: Representation of MCM-41 supported L-proline for an aldol reaction^[26].

1.1.4.2 Metal organic frameworks

For the second route detailed towards heterogeneous catalytic materials, 1.1.4, incorporation of the active site occurs during the synthesis stage to create a material where it is evenly distributed throughout the system. A huge range of catalysts have been produced by this route, amongst which the recent advances of Metal Organic Frameworks (MOFs) have shown huge scientific interest and potential.

MOFs are a class of *porous polymeric material, consisting of metal ions linked together by organic bridging ligands*^[28]. Their development in recent times has attracted immense attention owing to their flexible nature and relative ease of design^[29]. The linker, often a bi or multi-dentate carboxylate, or other heteroatom (such as nitrogen in ZIFs (Zeolitic Imidazolate Frameworks)) spans two or more metal atoms as part of the coordination sphere for both. Accordingly, the metal, either as a solitary atom or part of a cluster such as in UiO-66(Zr) (University of Oslo)^[30] and MIL-101(Cr) (Materials Institute Lavoisier)^[31], has multiple linker molecules bound to it propagating the structure, Figure 10. The capacity for differing MOFs is therefore extensive as there are innumerable conceivable combinations of metal and organic molecule which can link to form a framework as shown by the nearly 70,000 structures having been reported to date^[32]. Properties include but are not limited to: large internal surface areas, very low densities, and the

availability of uniformly structured pores and cavities leading to well-defined chemical environments, have allowed a variety of uses^[33–35].

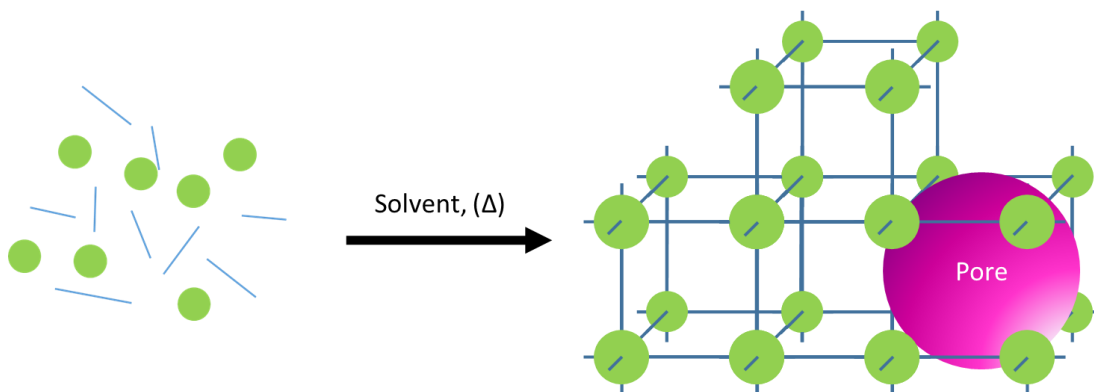


Figure 10: Diagrammatic representation of MOF synthesis, where green sphere indicates metal and blue line is the linker (bidentate).

Applications have been found in: gas storage and separation^[36,37] (of H_2 ^[38], CO_2 ^[39] and natural gas^[40]), gas sensing^[41], chemical sensing^[42], thin films^[43], biomedical applications^[44,45] and catalysis^[46–50]. For catalytic purposes they have been shown to be active as: single site^[51,52], supramolecular^[53] CO_2 utilisation^[54–56], oxidation^[57,58], enantioselective^[59] tandem^[60,61] and electro-^[62–65] and photo-catalysts^[66–69].

The range of products that can be achieved from MOFs acting in a catalytic capacity is accordingly large as both the linker^[70], metal nodes^[71] and post-synthetically added species^[72] can act as catalytic entities. The first report of MOFs acting catalytically was by Fujita *et al* where a cadmium MOF with a missing linker, and so an exposed metal site, was used to undertake the cyanosilylation of aldehydes^[73]. Production of catalytically active, exposed metal sites within well-defined architectures is then possible. It was found in 2006 that the dehydration of HKUST-1 leads to the exposure of coordinatively unsaturated sites (CUS), which are Lewis acidic in nature^[74]. One of the most important examples of CUS in MOFs is MIL-101(Cr) where the removal of water allows for uses in not only catalysis but also surface functionalisation, encapsulation and gas or small molecule adsorption^[75,76].

The heterogeneous nature of MOFs makes them attractive for industrial catalytic processes^[77,78] albeit that some of these applications are hindered by the reduced thermal and chemical stability of the MOF owing to the significant organic component. That said, there is now a growing list of highly stable MOFs present in the literature^[79], with ZIF-8 (Zeolitic Imidazolate Framework-8) the first example of a MOF to display exceptional chemical stability as it remains unaltered after suspension in boiling solvents: methanol, benzene, and water for up to 7 days and more remarkably in concentrated sodium hydroxide at 100°C for 24 hours^[80]. Cavka *et al* produced the

UiO-66 series of frameworks which display some of the highest thermal stabilities – up to 500 °C^[30]. These examples establish that that MOFs have the properties needed to be applied industrially, and indeed have been shown to be capable of industrially useful catalytic conversions when they are of sufficient stability^[81].

Imparting chemical and thermal stability into MOFs is therefore vital for their use in catalytic applications as is the creation of the required active site. Optimisation of MOFs for their desired application can be undertaken by a variety of means during the synthesis stages in order to maximise efficacy. Many MOF synthesis procedures are facile and allow for easy manipulation both before and after framework formation^[35]. Mono-carboxylic and strong acids that are weakly coordinating are used to modulate the synthesis of MOFs and improve properties and stabilities. Modulators work by either competitively coordinating with the metals or by suppressing the deprotonation of linkers therefore limiting the ability of them to coordinate. The competitive coordination is typically from mono-carboxylic acids which bind to the metal centre reducing the rate of nucleation which slows down crystal growth to produce highly crystalline products^[79], see Figure 11. Conversely, at reasonably high concentrations (10:1 benzoic acid: linker) the modulator can have the opposite effect and small, nano-scale MOF particles can be synthesised through sufficient concentration of the modulator to terminate crystal growth^[82].

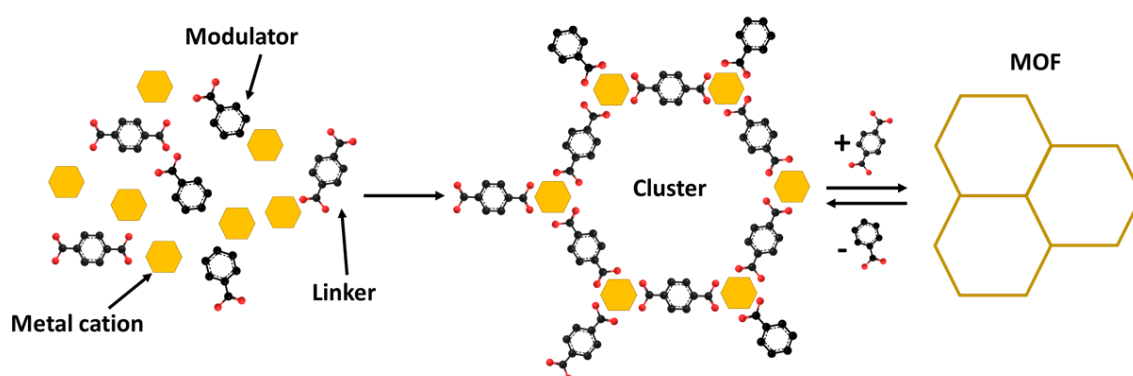


Figure 11: Representation of modulated synthesis of a MOF.

Post synthetic modification (PSM) of both metal and linker allows for additional functionality to be imparted onto MOFs^[83]. Modification of the linker allows for organocatalytic transformations to be undertaken. Most often, the incorporation of 2-aminoterephthalic acid is the starting point as the amino group enables further modification through reactions with anhydrides, isocyanates, aldehydes, acyl chlorides, alkyl bromides, and further more complicated variants to produce the required organic functionality^[79,83,84]. PSM of the metal can produce mixed metal MOFs if the framework coordination is sufficiently labile under the correct conditions. For example, MIL-101(Cr, 100 %) can be converted to a mixture of Fe and Cr nodes and the subsequent mixed metal variant was shown to be able to undertake the epoxidation of styrene to styrene oxide^[85].

Exchange has also been showed for some of the most stable frameworks, therefore allowing the most industrially relevant examples to be modified for greater activity, with post synthetic exchange for UiO-66 and ZIFs, as discussed earlier, having been reported by Kim *et al*^[86].

1.1.5 Green Chemistry and Sustainability

Sustainable processes are fundamentally linked with catalysis. Industrially, 25 % of the energy used in fine chemical synthesis is from the undertaking of catalytic processes which creates great opportunity to decrease energy consumption and environmental impact through efficiency improvements^[87]. Design of processes to be green is essential to industrial practices becoming more sustainable in the future, a goal that is especially pertinent given the ever-increasing need to reduce production of wastes, such as greenhouse gases, and curb unsustainable energy consumption^[88]. In order to attain such goals, new processes are often first considered using the Principles of Green Chemistry put forward by Warner and Anastas shown in Table 2^[89]. These principles simplified further by Poliakoff *et al* placing them into a mnemonic^[90] and summarised by in the following statement by Sheldon: *Green chemistry efficiently utilises (preferably renewable) raw materials, eliminates waste and avoids the use of toxic and/or hazardous reagents and solvents in the manufacture and application of chemical products*^[91].

| # | Principle |
|----|---|
| 1 | Waste prevention instead of remediation |
| 2 | Atom efficiency |
| 3 | Less hazardous/toxic chemicals |
| 4 | Safer products by design |
| 5 | Innocuous solvents and auxiliaries |
| 6 | Energy efficient by design |
| 7 | Preferably renewable raw materials |
| 8 | Shorter syntheses (avoid derivation) |
| 9 | Catalytic rather than stoichiometric reagents |
| 10 | Design products for degradation |
| 11 | Analytical methodologies for pollution prevention |
| 12 | Inherently safer processes |

Table 2: The twelve principles of green chemistry.

Adherence to these principles, Table 2, will ideally produce a process that is both green and efficient in its nature. Principle 9 is particularly enlightening as it explicitly states the need for catalysts in reactions and so conscientious design of a process based upon these principles is then well aligned with the production of active catalysts.

As discussed, homogeneous catalysts generally benefit from greater selectivity than heterogeneous analogues but are less utilised by industry^[7]. Heterogeneous catalysts, by contrast, are ubiquitous in industry due to ease of catalyst collection following reaction. Significant work is therefore being placed into the immobilisation of existing homogeneous catalysts or developing solid catalysts from the outset, as per the methodologies detailed above^[25,92–94]. In so doing, the process of catalyst recycling can be undertaken without the need for additional solvents and steps allowing for the production of fine and bulk chemicals whilst adhering to green practices^[95,96]. Moreover, combination of principles 1 and 6 would use waste and renewable materials as the feedstocks for industrial processes wherever possible. In this respect, an ideal target is carbon dioxide (CO₂) for use in the production of bulk and finer chemicals. Being a by-product of numerous industrial processes and naturally abundant, CO₂ is an attractive feedstock therefore use of it would be well aligned with the Green principles in Table 2. Consequently, this is an area which has been specifically targeted for research and development in recent years.

1.2 Carbon dioxide as a feedstock

Anthropogenic emissions of carbon dioxide, CO₂, are vast and increasing at an alarming rate. Climatic changes that excess CO₂ and other greenhouse gases are predicted to cause will have devastating effects on the planet making climate change one of the greatest environmental challenges of modern times^[97]. Consequently, research into the control and ultimately the decrease of CO₂ emissions and levels in the atmosphere is urgently required. Recent focus has therefore shifted to not only CO₂ capture and storage but ultimately, utilisation as well.

1.2.1 Fundamentals of reactions with CO₂

Carbon dioxide is a simple molecule; consisting of a single carbon atom bonded to two oxygens *via* two double bonds, with the carbon in its most oxidised form. It is therefore highly stable meaning reactions involving CO₂ necessitate the use of catalysts in order to overcome the considerable Gibbs energy of -394.4 kJ mol⁻¹ ^[98]. Activation and splitting of the CO₂ molecule are the most important steps in catalytic processes involving CO₂. The high stability necessitates the input of energy into the reaction system *via* either the use of high temperature and pressure conditions or high energy reagents, such as hydrogen^[99]. Nevertheless, reactions with CO₂ are possible through two general means. Either reduction of the carbon, and thus cleavage of the C=O bonds with new C-C or C-H bond formation is undertaken, leading to new molecule formation. Alternatively, utilisation can be achieved through CO₂ incorporation into other compounds, where the CO₂ structure is mostly maintained. Again, in order to achieve such conversion, activation of the CO₂ is crucial. Activation is possible under ambient conditions with the help of a solid state catalyst, the role of which is to adsorb CO₂ molecules and facilitate electron transfer to them^[100]. The energetics of the activation process – dependent on method of calculation – is variable between catalyst systems and reaction conditions, but estimated to be between 50 and 70 kcal mol⁻¹ ^[101–104].

1.2.2 CO₂ utilisation

Carbon dioxide is a C₁ source, therefore can be envisaged to be used as a building block in the production of larger, carbon based, chemicals. Unfortunately, exploitation of this highly abundant, economical and non-toxic source of carbon is low with only 110-120 Mt of CO₂ per year incorporated as a synthetic building block by industry^[97,105]. Most of this occurs through CO₂ incorporation into urea, salicylic acid and organic carbonates yet disappointingly, these routes still represent only a small fraction of the worldwide CO₂ emissions estimated to be around 0.03 % of

the total^[106]. A large array of CO₂ transformations can be undertaken and generally fall into one of the following categories:

- 1) Chemical, either by using hydrogen to produce hydrocarbons such as methanol, ethanol etc. and also non-hydrogen routes leading to carbonates and carbamates,
- 2) Photochemical, forming CO, formic acid and methane
- 3) Electrochemical, producing CO, formic acid and methanol;
- 4) Biological, enzymatic conversion to ethanol, sugar and acetic acid;
- 5) Reforming, using CO and H₂;
- 6) Inorganic, by incorporation (sequestering) into metal carbonates^[107].

It can be seen, as mentioned previously, that utilisation is restricted by the requirement of large energy inputs (electrochemical conversion) or high energy molecules (hydrogen). North *et al* highlighted that amongst these transformation options '*the synthesis of low energy target molecules, such as organic carbonates*' are particularly viable options as the epoxide is a high energy molecule^[105].

1.2.2.1 Cyclic carbonates

Cyclic (organic) carbonates are industrially attractive for use as green solvents^[108], additives to fuels^[109], cosmetics applications^[110], electrolytes for use in lithium ion batteries^[111] and as useful intermediates for the preparation of a large variety of larger molecular weight products^[110,112]. Traditional, and in some cases current, industrial methodologies for the production of cyclic carbonates use a reaction of phosgene with diols, Figure 12A^[113]. Not only does this method use phosgene, which is harmful, but it produces two moles of acid for each mole of cyclic carbonate synthesised^[106]. Methods that are less hazardous both in safety and environmental terms are therefore sought after.

One such route is the reaction between CO₂ and epoxides which is not only a 100 % atom efficient process but also, through incorporation of CO₂, utilises a waste product instead of producing one as shown in Figure 12B. The high energy epoxide provides the energy required for carbon dioxide utilisation, and so provides a much more sustainable method for the synthesis of cyclic carbonates.

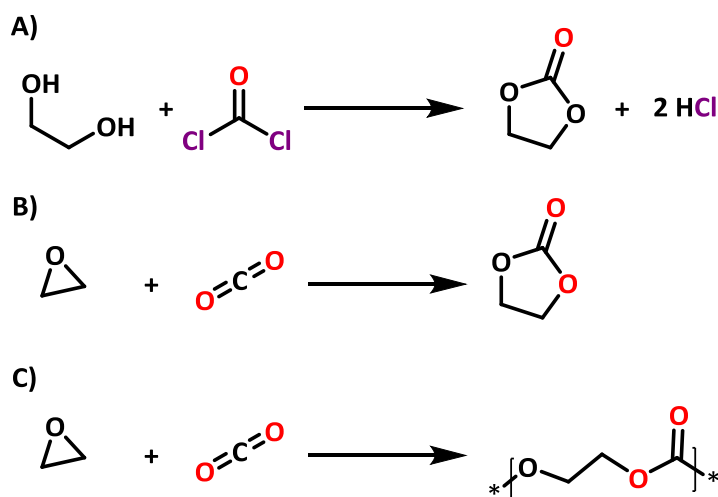


Figure 12: A) production of cyclic carbonate from a diol and phosgene B) 100 % atom efficient reaction of CO_2 and epoxides to form cyclic carbonate and C) production of polycarbonates (ethylene carbonate shown for all cases).

The reaction of CO_2 and epoxides can produce two different products, cyclic carbonates and polycarbonates. Polycarbonates, Figure 12C, find wide use as plastics owing to their impact resistance and optical transparency^[105]. Catalysts for polycarbonate synthesis are typically homogenous organometallics which often require the use of a co-catalyst to initiate the reaction, with tetrabutylammonium bromide (TBAB) a common choice^[114–119]. Production of the polycarbonate or cyclic carbonate is dependent on the mechanism the catalytic cycle goes through but also on the reaction conditions which are employed. Williams *et al* report that the cyclic carbonate is the thermodynamic product of the reaction^[115,120,121]. To produce the cyclic carbonate the catalyst shall initiate the reaction *via* one of two means, either: CO_2 activation occurs first, a carboxylate is formed that ring-opens the epoxide, or the epoxide ring opening occurs first^[122]. For the latter, the reaction pathway occurs with the catalyst ring-opening the high energy epoxide which proceeds to activate CO_2 . In order for this to occur the catalyst is most often required to have a nucleophilic component and a Lewis acidic component to attack the epoxide and stabilise the intermediate, respectively. This is shown in Figure 13 with TBAB acting as the catalytic component for the reaction as reported by North *et al*^[123].

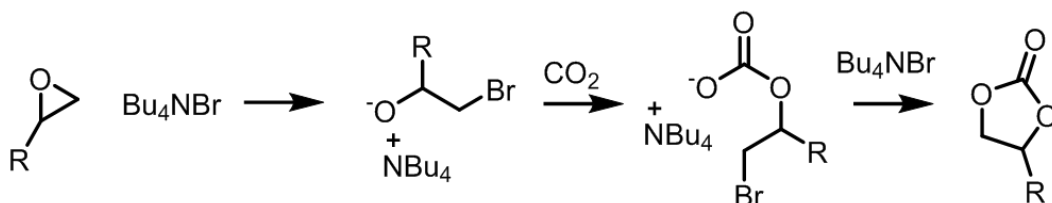


Figure 13: Known mechanism for cyclic carbonate production catalysed by TBAB.

Production of cyclic carbonates from CO₂ is not without its difficulties. Whilst cyclic carbonate synthesis from CO₂ is 100 % atom efficient this does not mean that it will automatically occur with a 100 % yield. Side reactions can occur leading to the formation of unwanted products.

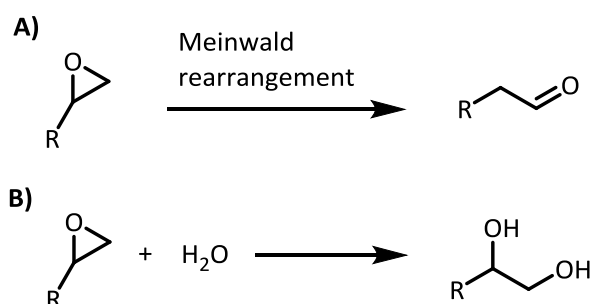


Figure 14: A) rearrangement of epoxide to aldehyde and B) diol formation from ring opening with water.

Shown above in Figure 14, are two common by-products formed during cyclic carbonate production, which must be minimised. The first, A), is the Meinwald rearrangement of the epoxide to the respective aldehyde. The second, B), occurs when there is moisture within the reaction system - either from solvents, reagents or catalyst – and ring opening of the epoxide can occur by water leading to the formation of a diol. Both by-products are undesirable, the latter is preventable by ensuring all components present for the reaction are dry. In the former, the rearrangement stems typically from the properties of the catalyst and so during the design stage this must be considered in order to minimise formation.

A wide range of materials have been employed for use as catalysts to promote the production of cyclic carbonates - both heterogeneous and homogeneous in nature. Given the proceeding arguments for the use of heterogeneous catalysts, these shall be focussed upon. Organocatalytic or majority organic based systems, have been shown to be applicable to cyclic carbonate production, with the flexibility afforded by organic systems allowing for the reactivity of the active site to be tuned. As a result, organic based or containing catalysts are a large sub-section within catalysts for cyclic carbonate production^[106,122,124].

1.2.2.2 Heterogeneous organocatalysts for cyclic carbonate production

Homogeneous salts, such as TBAB, are bifunctional in their role as catalysts to undertake the production of cyclic carbonates^[125] with both the anion and cation being shown to be implicit in the reaction mechanism as detailed above in Figure 13. This has led to the development of metal free systems which can be functionalised into heterogeneous analogues^[106,124]. Silica based catalysts are prevalent, owing to the ease of covalent attachment to the silanol (Si-OH) surface functionalities, as previously discussed. Silanol functionalisation via trimethoxy or ethoxysilane

species is a simple means to produce an anchored ion-pair, Figure 15, sometimes referred to as an ionic liquid, which mimics the mechanism of TBAB.

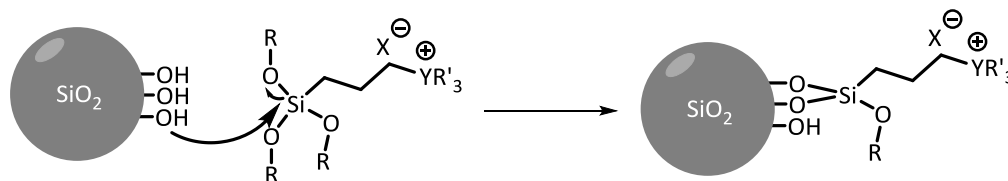


Figure 15: Depiction of silanol functionalisation resulting in covalent anchoring of ionic pair organic moiety to silica. Commonly $X = \text{Cl}, \text{Br}, \text{I}$ and $Y = \text{N}$ (either quaternary or part of an imidazolium ring) or P

It is most often the positively charged species that is anchored to the support and the anion which is labile. This can be explained when the general mechanistic pathway previously discussed is considered, shown in Figure 13. For the anchored catalyst an analogous pathway is followed: the anion acts as a nucleophile to undertake the ring opening of the epoxide leading to the intermediate species – the alkoxide – which is stabilised by the positive charge, now the anchored species. The anion is regenerated during closing of the ring leading to the cyclic carbonate. The anchoring of ion-pair organic-based systems is an elegant way of producing cyclic carbonates with a heterogeneous system and will be the focus of Chapter 3 of this work, where the state of the art for these systems will be summarised and discussed.

1.2.2.3 MOFs for CO_2 utilisation

MOFs are an attractive proposition for CO_2 utilisation, the high storage capacity of them for CO_2 provides scope for both capture and conversion to be envisaged. Capture and conversion of CO_2 with epoxides to cyclic carbonates within a MOF architecture has gathered increasing interest in recent years.

The first reported use of MOFs for cyclic carbonate production by Song *et al* used a MOF-5/*n*-TBAB system, with the latter acting as a co-catalyst, and achieved CO_2 conversion with a range of epoxides^[126]. Subsequently, this field has moved forward at remarkable speed with a growing number of different approaches reported. Manipulation of the MOF architecture has occurred in various guises, with both metal and linker being altered both during and after synthesis to promote greater catalytic ability. A summary of MOFs for the conversion of either styrene oxide or propylene oxide is detailed below.

| # | MOF name | Substrate | Reaction conditions | Co-catalyst | Yield (%) | Ref |
|----|---|-----------|------------------------|-------------|-----------|-------|
| 1 | MOF-5 | SO | 50 °C, 1 bar, 15 hrs | TBAB | 92 | [126] |
| 2 | MOF-5 | PO | 80 °C, 20 bar, 8 hrs | - | 1 | [127] |
| 3 | MOF-505 | PO | RT, 1 bar, 48 hrs | - | 48 | [128] |
| 4 | In-MOF ^a | PO | RT, 1 bar, 48 hrs | TBAB | 77.9 | [129] |
| 5 | MIL-101(Cr) | PO | RT, 8 bar, 24 hrs | TBAB | 91 | [130] |
| 6 | HKUST-1(Cu) | PO | RT, 12 bar, 48 hrs | - | 49.2 | [128] |
| 7 | Cu-MOF | PO | RT, 1 bar, 48 hrs | TBAB | 96 | [131] |
| 8 | ZIF-22 | PO | 120 °C, 12 bar, 2 hrs | - | 99 | [132] |
| 9 | Co-MOF ^a | PO | RT, 1 bar, 48 hrs | TBAB | 93.8 | [133] |
| 10 | [Zn ₆ (TATAB) ₄ (DABCO)- MOF | SO | 100 °C, 1 bar, 16 hrs | - | 89 | [134] |
| 11 | MOF-74(Mg) | SO | 100 °C, 20 bar, 4 hrs | TBACl | 95 | [135] |
| 12 | MOF-74(Co) | SO | 100 °C, 20 bar, 4 hrs | - | 96 | [136] |
| 13 | NU-1000(Hf) | SO | RT, 1 bar, 56 hrs | TBAB | 100 | [137] |
| 14 | Ni-TCPE1 | SO | 100 °C, 10 bar, 4 hrs | TBAB | 99 | [138] |
| 15 | UiO-66-NH ₂ | SO | 100 °C, 20 bar, 4 hrs | - | 96 | [127] |
| 16 | ZIF-8 | SO | 80 °C, 7 bar, 5 hrs | - | 43.7 | [139] |
| 17 | ZIF-68 | SO | 120 °C, 10 bar, 12 hrs | - | 93.3 | [140] |
| 18 | Co-MOF ^a | SO | 50 °C, 1 bar, 36 hrs | TBAB | 94.3 | [141] |
| 19 | FJI-C10 | SO | 80 °C, 1 bar, 48 hrs | - | 48 | [142] |
| 20 | NH ₂ -MIL-101(Al) | SO | 120 °C, 18 bar, 6 hrs | TBAB | 96 | [143] |
| 21 | MIL-101- NH ₂ (Al)@Fe ₃ O ₄ @SiO ₂ | SO | 100 °C, 1 bar, 9 hours | LiBr | 100 | [144] |
| 22 | Au/Zn-MOF | SO | 70 °C, 30 bar, 6 hrs | - | 97 | [145] |
| 23 | Gd-MOF | SO | 80 °C, 20 bar, 12 hrs | TBAB | 93.8 | [146] |

| | | | | | | |
|----|-------------|----|-----------------------|---|----|-------|
| 24 | UiO-67-ImBr | SO | 90 °C, 1 bar, 3 hrs | - | 51 | [147] |
| 25 | UiO-66-ImBr | SO | 120 °C, 1 bar, 24 hrs | - | 46 | [148] |

Table 3: Summary of MOFs used for styrene oxide (SO) or propylene oxide (PO) and CO₂ reactions.

^aMOF name unknown, the two Co MOFs have different structures.

As shown in Table 3, a wide range of MOFs have been synthesised and used for the conversion of CO₂ and epoxides to cyclic carbonates. The initial MOF-5 paper is shown in entry 1 and highlights one of the biggest downsides to MOF use – co-catalysts. Entry 2 clearly shows this as the same MOF-5 structure, when run under more harsh reaction conditions, displays barely any conversion when without the co-catalyst. To combat this an ammonium salt is often required to be used in conjunction with the MOF to aid the reaction to initiate the epoxide ring opening, again as previously detailed. The role of the MOF is to act as a Lewis acid for stabilisation of the intermediate alkoxide species. Recently, the use of TBAB and other co-catalyst use has been mitigated by incorporation of imidazolium species to the MOF linkers such as in entries 17, 24 and 25. In this case the ion pair is then inherent to the framework^[142,147]. Catalytic conversion has been seen to be possible at RT (entries 3-7, 9 and 13) showing that cyclic carbonates can be produced at room temperature, however, in all of these examples the reaction times were 24 hours or greater. The best results detailed in the above is that for entries 8 and 15 where ZIF-22 and UiO-66-NH₂ have been used.

It is clear that there is considerable opportunity for improvement in the use of MOFs as catalysts for CO₂ and epoxide reactions. Specifically, MIL-101(Cr), entry 5, has been amenable to modification and the required reaction times can be greatly improved. The current range of modifications present in the literature which have been made to MIL-101(Cr) for cyclic carbonate production from CO₂ and epoxides, will be detailed in Chapter 4 prior to discussion of the modifications performed on this MOF in this work to enhance its activity.

The flexibility of MOFs is apparent in Table 3, both through the wide range of MOFs detailed but also the modifications which have been made to them. Functionality has been imparted through metal and linker alteration but also through addition of nanoparticles and other species by encapsulation or deposition. The multiple chemical environments, which are subsequently formed, can be individually thought of as active sites for catalysis, therefore where multiple chemical environments are present then accordingly so are multiple active sites. The possibility to exploit all of the active sites opens up further avenues of research for MOFs to maximise the potential of them.

1.3 Tandem reactions

Improving catalytic efficiencies, reducing waste and using environmentally friendly reagents are the key factors of green chemistry^[149]. Cascade catalysis is attractive as a means of improving both catalytic efficiencies and reducing waste as the loss of material after each purification reduces the overall efficiency of a synthetic process. Methods for the preparation of multi-site solid catalysts in which a series of well-optimised, isolated active sites are present and able to catalyse different, successive reactions without the need for in-between product isolation are then sought^[150].

For successive reactions requiring a catalyst for each individual stage, two active sites are required. In a tandem reaction: A will transformed into B and then B into C (the final product) without the need to isolate B and purify it before the second reaction (as is the traditional route). Both examples are shown in Figure 16. For a tandem reaction, compound B is the intermediate in the reaction and will only be present for a relatively short period – depending on which of the two reactions has the faster rate - which can lead to the added benefits of lowering the chances of unfavourable side reactions occurring during a tandem process. Ideally then, a sole material will be able catalyse both reactions and so must possess dual functionality, as shown in Figure 16B.

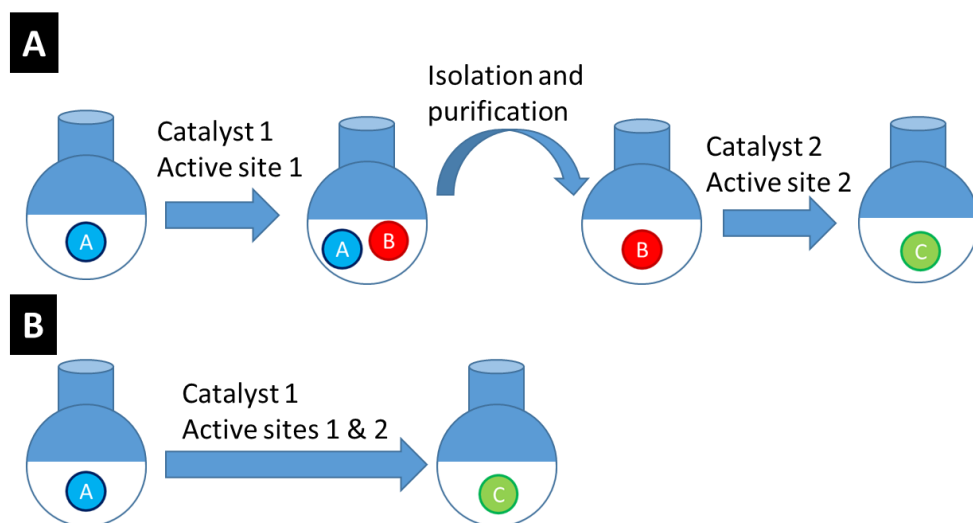


Figure 16: A) 'Traditional reaction route' of A to C *via* B using two catalysts, in two steps with isolation of B in-between. B) Tandem reaction route where A reacts to C catalysed by a catalyst with two active sites, without isolation of B.

The large variety of ways to manipulate MOFs, as described in the preceding sections, means that functionality within the material is not restricted to one environment. This then opens the door to scenarios where the MOF can undertake tandem or cascade catalysis reactions. A recent pair of reviews detailing MOFs as tandem catalysts highlighted the flexibility afforded by these systems to be able to undertake multiple reactions in this manner^[60,61]. The different properties within the

framework allow for the separate reactions to be undertaken with a selection of examples shown below, Table 4, in order to highlight the scope of variations.

| MOF | Reaction | Active sites | Ref |
|------------------------------|---|---------------------|-------|
| Au/MIL-53(Al) | Oxidation/esterification | NPs, acid | [151] |
| Zr-MOF-NH ₂ | Oxidation/Knoevenagel condensation | acid, base | [152] |
| Au-Pd/MIL-101(Cr) | Oxidation/aldol condensation | NPs, acid | [153] |
| Sc-MOF | Epoxidation/rearrangement | acid | [154] |
| MIL-101-NH ₂ (Al) | Deacetalisation/Knoevenagel condensation | acid, base | [155] |
| Pd@IRMOF-3 | Knoevenagel condensation/hydrogenation | base, NPs | [156] |
| UiO-66(Zr)-L(Ir) | Reductive amination/condensation/hydrogenation of imine | base, metal complex | [157] |
| Pd/MOF-5 | Aminocarbonylation | NPs, acid | [158] |
| Pd@MIL-101(Cr) | Isomerisation/hydrogenation | acid, NPs | [159] |

Table 4: Summary of different MOF materials, the tandem processes catalysed and the active sites employed.

The creation then of two or more different active sites, which are discrete from one another and of differing properties throughout MOF frameworks, is possible. The use of nanoparticles (NPs) based on or within MOFs is often used to catalyse one of the tandem reactions steps being undertaken, as shown in their prevalence in Table 4, leaving the framework to complete the other step of the tandem process. Methods of nanoparticle synthesis are a much researched area of catalysis and recently their combination with MOFs which can act as hosts, has proven to be a particularly promising area of heterogeneous catalysis^[160].

1.3.1 Gold Nanoparticles

Metal nanoparticles, especially those made from noble metals (Au, Ag, Pt and Pd) have shown great promise for use as catalysts, most often in oxidation reactions. Their ability to stabilise intermediates and facilitate electron transfer processes enables them to act in a catalytic manner, with gold nanoparticles gaining particular attention^[161–164] and heterogeneous versions active for a wide range of catalytic applications^[165].

1.3.1.1 Catalytic properties of gold

Nanoparticles, as classed by White *et al*, are materials which have one or more dimension in the range of 1 to 100 nm, be that length, width or thickness^[166]. Compared to the bulk analogue nanoparticles are attractive not only as their surface to volume ratio is large, but also because of the unique electronic properties that can occur at these dimensions; namely the change in the density of states and surface plasmon resonance comparative to the bulk material^[166]. The lowering of the density of electronic states is caused by the smaller number of atoms, because as you progress towards the nanoscale from the bulk *the energy continuum changes to produce more discrete energy levels*^[167], see Figure 17.

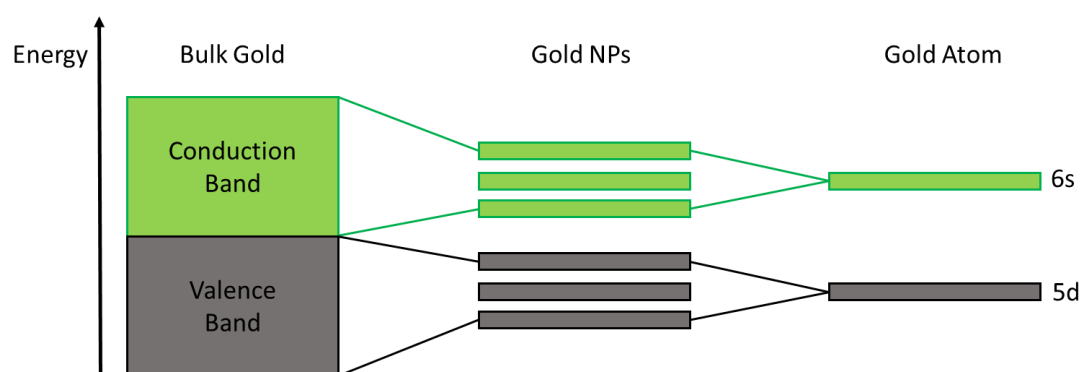


Figure 17: Energy level diagram for bulk, nanoparticle and atomic gold species tending towards discrete energy levels.

For gold nanoparticles the crossover point at which it loses its 'bulk metallic character' occurs when particles are between 5 nm and 2 nm and so the highest catalytic ability is observed within this range^[164,168], the exact point at which this occurs has not been determined and is a source of debate owing to the difficulty in producing monodisperse particles at such small sizes. With the loss of the metallic character, the particle tends towards behaviour of a molecule rather than a bulk metal. This lends to the alteration of chemical properties of the particle in a number of ways which cause and affect the catalytic activity.

The nanoscale size of the particles causes alteration of catalytic activity as *the way in which electrons are used to form metallic bonds determines the character of the free valences at the surface, hence the kind of chemisorption formed with the reactants*^[169]. In essence, the ability of nanoparticles to stabilise intermediate species improves as the size lowering tends towards the nanoparticle losing the 'bulk metallic character'. As the size of the nanoparticle decreases, the number of the atoms of the particle on the surfaces increases. For a nanoparticle of 10 nm, 12% of atoms in the particle are on the surface, whereas one of size less than 3 nm will have over 50 % of atoms on the surface^[170] as shown in the diagrammatic representation in Figure 18. Lowering

of the coordination number of a gold atom, as is the case for the surface atoms in a nanoparticle, increases the degrees of freedom for them and increases their ability to interact with substrate molecules. The greater number of atoms of low coordination number at the corners and edges of particles, are often claimed to be those which are the cause of the activity observed in catalytic reactions as these systems are readily able to interact with substrate molecules adsorbing onto the surface^[171]. The effect of size on catalytic ability has been summarised extensively by Haruta, with increase seen from 5 to 2 nm as aforementioned^[172]. Furthermore, oxidation state and influence of the support on the catalytic activity are also detailed. The effect of size was further displayed by an Au/TiO₂ system where an almost 10 fold increase in TOFs towards the oxidation of cinnamyl alcohol was seen when nanoparticles were decreased in size from 9.2 nm to 4.9 nm^[173]. The oxidation state of the gold required for catalysis has been shown to affect activity; with Au(0) suggested to be responsible for the activation of the substrate during oxidation reactions in tandem with *peripheral sites of the nanoparticles or clusters that are in contact with the surface of the support, which carry a net positive charge* and are responsible for the activation of the oxidant in the reaction^[162,165]. This also shows the importance of the support selection.

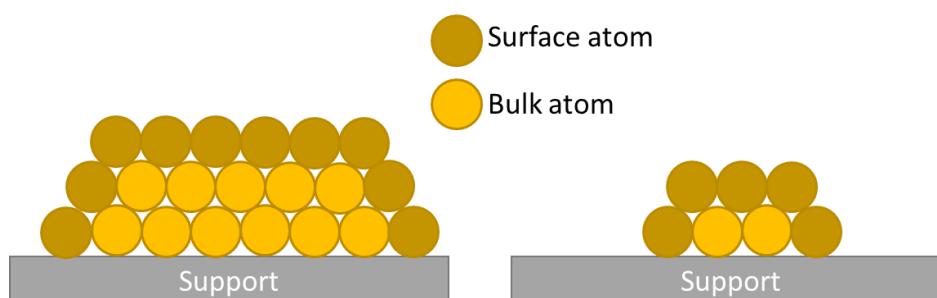


Figure 18: Representation of the increase in surface atoms as percentage of the total number of atoms within a nanoparticle as size decreases.

The size of the nanoparticle, as discussed, is critical to reactivity, hence a high degree of control is required during the synthesis stage in order to produce monodisperse particles of nanoscale size and so ensure that they are catalytically active.

1.3.1.2 Synthesis of gold nanoparticles

Control over nanoparticle size can be achieved through tailoring the environment that they are formed in, such as extrusion from a framework^[174,175] or by reduction in a colloidal solution^[176–178]. Colloidal methods require the use of stabilising agents such as surfactants^[179,180] or small coordinating molecules and polymers; organothiols^[181], PVA^[182], citrates^[183–186], and PVP^[187–190]. Micelles form around the metals salts controlling the size of the particles so that upon reduction (such as by NaBH₄) nanoparticles of specific size are formed. Control of size can be achieved

through varying the amounts of stabilising agent or manipulation of the temperature at which nanoparticle reduction occurs. During the synthesis of gold nanoparticles, the stabilising agents enable control through prevention of nanoparticle aggregation and precipitation. Strong Au-S bonds, as with organothiols, provides the interaction between the stabilising agent and the gold; whereas other types of capping agents rely on non-covalent interactions such as physisorption (PVP) or electrostatic interactions of ionised ligands (citrate)^[170]. A summary of some of the most common methods is detailed in Table 5. A modified PVP synthesis was used often later in this work.

| Method | Solvent | Reductant | Capping agent | NP size range (nm) | Ref |
|--------------------|---------|----------------------------|---------------|--------------------|-----------|
| B Brust– Schiffrin | Organic | NaBH ₄ | Organothiol | 2-10 | [181] |
| Turkevich | Aqueous | citrate | citrate | 10-40 | [185] |
| Perrault | Aqueous | hydroquinone | citrate | 50–200 | [186] |
| Murphy | Aqueous | ascorbic acid | CTAB | 10-40 | [180] |
| Polyol | Alcohol | Diols or NaBH ₄ | PVP | 2–200 | [189,190] |

Table 5: Summary of the most common routes to synthesis of gold nanoparticle in solution^[170].

As shown, the size of the nanoparticles produced can be closely controlled through the careful selection of solvent, capping agent and reductant but also temperature of the reaction. The ranges given in the above are the maximum and minimum possible for that method and not the size range of the particles produced. This close control of the particle diameter is crucial owing to the size related activity of the particles. Determination of size, and when required, the morphology of nanoparticles is commonly achieved by obtaining TEM images of the materials. In order for application in a re-usable manner, gold nanoparticles formed in the above methods are often deposited onto suitable supports to heterogenise them.

1.3.1.2.1 MOFs as gold nanoparticle hosts

Production of heterogenised gold allows for the collection of the material after use and also helps to protect the metal nanoparticles as they are highly susceptible to aggregation, and so deactivation, due to their high surface energies and strong Van der Waals interactions. Selection of the scaffold onto which they are heterogenised is important as in many cases the activity of NPs is drastically affected by the choice of support, which plays a key role in promoting reactions employing Au nanoparticles^[165,191].

Combination of MOFs with nanoparticles has yielded promising results and a huge variety of different metal NP-MOF materials have been produced^[192,193]. Choice of MOF is important as in many cases the chemical and/or thermal stability is insufficient to be maintained either after the NP synthesis stage, when applied to a catalytic process or both. The porous nature of MOFs means that the NPs are not exclusively restricted to deposition or formation on the surface.

In the most general terms the NPs can be situated in a number of locations when MOFs are used as the supporting material^[193]. The first, herein denoted NP/MOF, relates to when the NPs are situated upon the surface of the MOF. Typically this occurs when the nanoparticles are pre-formed using one of the above detailed methodologies, Table 5. Post-synthesis, the surface of MOFs are decorated with pendant carboxylic acid groups from incompletely bound linkers, and also possess heteroatoms on the linkers (such as N and O) which can form electrostatic interactions with the nanoparticles or the functional groups of the stabilising agents and cause the adhesion of the NP to the MOF. Alternatively, the NPs or other materials, can be situated within the framework, herein denoted NP@MOF^[193]. Nanoparticles can be incorporated into the structure by reduction of metal salts in the pores, or sequential growth of the framework around pre-synthesised nanoparticles. These two methods lead to often quite different materials and properties and so it is important to distinguish between the two as NP@ is often used interchangeably in the literature. Incorporation of NPs into the MOF synthesis leads to NP@MOF which are commonly within the centre of the MOF, so herein termed *encapsulated*^[160]. Whereas, those which are formed from the introduction of the metal to the pre-formed MOF and subsequently reduced within the pores and cavities will be denoted as being *impregnated*, see Figure 19.

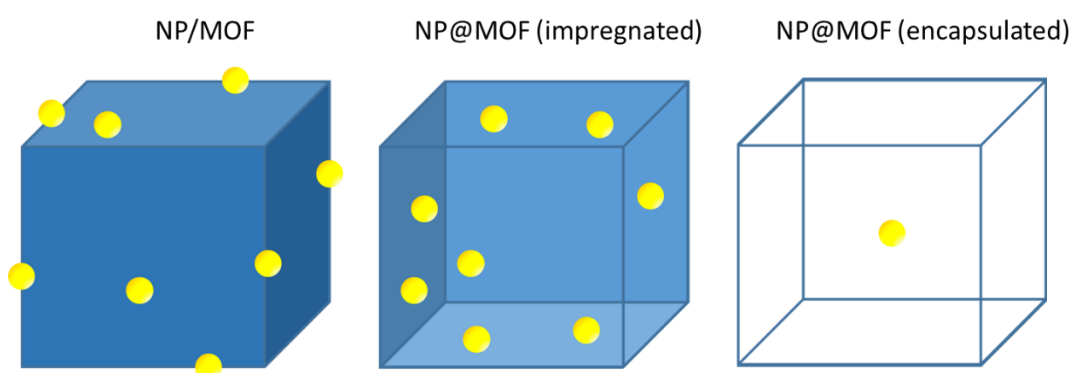


Figure 19: Visual representation of NP-MOF locations and nomenclature used.

For the NP/MOF and the encapsulated NP@MOF the NPs are pre-formed so control is achieved prior to deposition and the deposited species are well defined. The impregnation technique uses the structure of the MOF to dictate the NP size. This control is clearly shown for MOF based gold nanoparticles, Table 6, where very small NPs have been achieved on a range of frameworks. Au

NP-MOF hybrid materials have been employed widely for oxidation reactions, with alcohol oxidation in particular studied as it is of high industrial relevance. A selection of MOFs for benzyl alcohol oxidation are summarised below.

| # | Catalyst | NP size (nm) | Reaction conditions | Yield (%) | Ref |
|---|----------------------------|--------------|--|-------------------|-------|
| 1 | Au/MIL-53(Al) | < 1 | 80 °C, 5 bar O ₂ , 23 hrs, K ₂ CO ₃ . | 77 ^a | [151] |
| 2 | Au/ZIF-8 | 1 – 5 | 80 °C, 5 bar O ₂ , 24 hrs. | 80 ^a | [194] |
| 3 | Au/TiO ₂ @MOF-5 | 1 – 3 | 80 °C, 5 bar O ₂ , 0.5 hrs, K ₂ CO ₃ | 72 ^a | [195] |
| 4 | Au/MIL-101(Cr) | 2.3 | 80 °C, 1 bar O ₂ , 1 hr | 99 ^b | [196] |
| 5 | Au/MIL-101-PMA(Cr) | 2.5 | 80 °C, 1 bar O ₂ , 5 hrs, K ₂ CO ₃ | 65 ^b | [197] |
| 6 | Au/UiO-66 | 5 | 80 °C, 1 bar O ₂ , 10 hrs, K ₂ CO ₃ | 53.8 ^b | [198] |
| 7 | Au/UiO-66 | 7 | 100 °C, 5 bar O ₂ , 9.5 hrs | 94 ^b | [199] |
| 8 | Au@UiO-66-NH ₂ | 2.8 | 100 °C, 1 bar O ₂ , 1 hr | 93 ^b | [200] |
| 9 | Au@UiO-66-NH ₂ | - | RT white light irradiation, 1 bar O ₂ , 24 hrs | 30 ^b | [201] |

Table 6: Summary of Au/MOFs used for the oxidation of benzyl alcohol. ^aUndertaken in alcohol therefore ester product. ^bBenzaldehyde.

Au-MOF materials are then able to catalyse the oxidation of alcohols. Especially promising are entries 4 and 7-9, showing that a base is not always required for oxidation to occur with the UiO-66 based examples being highly interesting as they show this MOF is particularly amenable as a support without the need for base addition. A base is often used for formation of the alkoxide intermediate and so promotes reaction, but it introduces a homogeneous component and is often used in large quantities.

The oxidation abilities of Au NPs on MOFs then leaves the framework active sites available for catalysis, such as the other half of a tandem reaction. Within Table 4, the oxidation-Knoevenagel reaction is an interesting example. For this tandem reaction the aldehyde production from an alcohol occurs and then Knoevenagel condensation reaction is undertaken, Figure 20. The latter reaction, the Knoevenagel condensation is attractive as it involves C-C bond formation and so facilitates the introduction of functionality, through the variation of R₁, to an organic molecule with a carbonyl bond. This step requires a basic active site to deprotonate a methylene compound

which for MOFs is possible through the addition of amine functionalities to the MOF as detailed in 1.1.4.2.

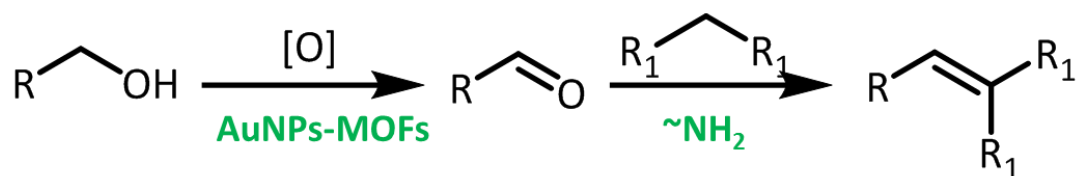


Figure 20: Route to Oxidation-Knoevenagel tandem reaction employing a MOF based system, active sites in green.

The Au NPs will then catalyse the oxidation of the alcohol, in an analogous manner to the materials reported in Table 6 and an amine on the linker of the MOF the conversion of the aldehyde to the condensation product. Combination of these two pathways it is possible and summarised in Figure 20. The tandem reaction is then imagined with the bifunctional MOF used two provide the two active sites required and this will be the focus of Chapter 5.

1.4 Aims and objectives

This thesis consists of 6 chapters. The proceeding part of Chapter 1 has laid out the rationale for the work which is about to be discussed, highlighting both the need for and possibilities of the different reactions and catalysts. The literature has shown the need for sustainable catalysts and that through careful design, highly active materials for challenging chemical transformations can be synthesised.

Chapter 2 will summarise the experimental techniques used in the production of this thesis, detailing the synthesis methods employed for production of the catalysts discussed and also detail the characterisation equipment used – explaining the key information each provide and how it allows for catalyst evaluation.

Chapter 3 will aim to produce a metal-free, heterogeneous organocatalyst based upon mesoporous silica for the production of cyclic carbonates from CO₂ and epoxides. The current state of art will be analysed with respect to immobilised organocatalysts for cyclic carbonate synthesis. Heterogeneous imidazolium species will be synthesised and evaluated for efficacy towards the aforementioned reaction. Through modification of the different aspects of the catalyst synthesis: pore diameter, loading of imidazolium, structure of the imidazolium (both the organic and anionic components will be altered) the catalytic ability of the material will be investigated in the hope of optimisation towards the desired application.

Chapter 4 will demonstrate the attempts to use the coordinatively unsaturated sites (CUS) present on metal organic framework MIL-101(Cr) for functionalisation and subsequent utilisation of CO₂. Anchoring of the imidazole structures from Chapter 3 onto the Cr-CUS of the framework will be undertaken and used to assess the viability of the MOF for CO₂ utilisation, again with epoxides, to produce cyclic carbonates. In combination with a modelling study, the activity of the framework will be explained through consideration of structure-property relationships that are occurring.

Chapter 5 will display the flexibility of MOFs to undertake multiple reactions due to the different chemical environments which can be created within them. UiO-66(Zr) will be introduced and used to produce a catalytic material capable of an oxidation-Knoevenagel condensation reaction. Careful manipulation of the catalyst synthesis to optimise the activity of the material will aim to produce high efficacy towards the reaction. Lastly, building on the work from Chapter 4, the use of MIL-101(Cr) to undertake a tandem reaction (epoxidation-CO₂ utilisation) will be shown.

Chapter 6 will summarise the findings of this work and propose directions in which the work should continue in order to fine tune the results and improve the materials researched herein.

Chapter 2 Experimental Techniques

2.1 Synthetic techniques

2.1.1 Mesoporous silica and hierarchically porous AIPO and SAPO based organocatalysts

2.1.1.1 Imidazole synthesis

1-(2,6-diisopropylphenyl) 1-H-imidazole, (diPrIm, see Table 7 for nomenclature), was synthesised *via* the methodology detailed below adapted from procedures by Medina *et al* and Liu *et al*^[202,203], 2,6-diisopropylaniline (9.13 mL, 43.5 mmol) in methanol (50 mL) was treated with glyoxal (40 % in H₂O, 5 mL, 43.5 mmol) for 16 hours at room temperature (RT). A yellow solution was observed after 30 minutes. Formaldehyde (37 % in H₂O, 6.47 mL) and ammonium chloride (4.65 g, 86.9 mmol) were added. The mixture was diluted using methanol (150 mL) and refluxed for 1 hour. Phosphoric acid 85 % (5.66 mL, 82.72 mmol) was added to the solution and the mixture further refluxed for 8 hours. The heat was removed and solvent volume reduced. The residue was cooled under ice then neutralised by potassium hydroxide (40 % solution) until pH 9. The crude product was extracted with dichloromethane, washed with brine and dried with magnesium sulphate. The mixture was separated into fractions using a silica column with a diethyl ether: ethyl acetate eluent. Fractions were tested using thin-layer chromatography and like fractions grouped together. The solvent was removed to obtain the purified product. Analysis of the purity and structure of the compound was undertaken through obtaining ¹H NMR spectra, see below for peak listing.

The synthesis of the remaining functionalised imidazoles was as follows. 1-(2,4,6-trimethylphenyl)-1-H-imidazole (MesIm) and 1-(*tert*-butyl)-1-H-imidazole (tBulIm) were produced using an analogous method to above but through alteration of the aniline/amine. For nPrIm and iPrIm, the following procedure was employed: Imidazole (2 g) and K₂CO₃ were added to MeCN (75 mL) and stirred at RT for 1 hour after which either 1-bromopropane or 2-bromopropane (2.76 mL) were added and the resulting solution refluxed for 24 hours. The solution was cooled and filtered through a glass funnel, to remove KHCO₃ and solvent removed by rotary evaporation. The resulting oil was dissolved in chloroform (40 mL) and washed with brine (4 x 10 mL) in a separating funnel. The pure product was isolated from the organic phase in each case after drying with magnesium sulphate and removal of the solvent by rotary evaporation. 1-methyl imidazole was purchased from Sigma Aldrich and used without further purification.

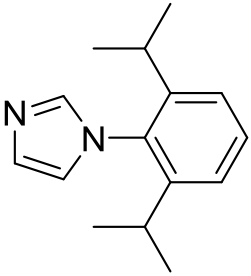
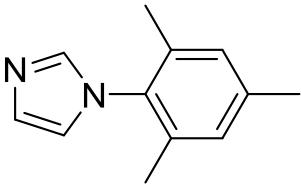
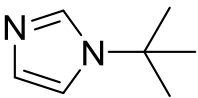
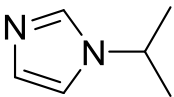
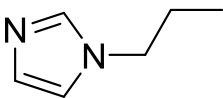
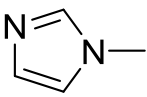
| Imidazole structure | Abbreviation | ^1H NMR tabulation |
|---|--------------|---|
|  | diPrIm | ^1H (400MHz, CDCl_3) δ 7.46 (1H, s), 7.43 (1H, d, J = 7.7 Hz), 7.24 (2H, d, J = 7.70 Hz) 6.9 (2H, s), 2.40 (2H, sept, J = 6.85 Hz), 1.14 (12H, d, J = 6.85 Hz). |
|  | MesIm | ^1H (400MHz, CDCl_3) δ = 7.39 (1H, s), 7.17 (1H, s), 6.90 (2H, s), 6.83 (1H, s), 2.27 (3H, s), 1.92 (6H, s). |
|  | tBulm | ^1H (400MHz, CDCl_3) δ 7.61 (1H, s), 7.04 (2H, s), 1.56 (9H, s) |
|  | iPrIm | ^1H (400MHz, CDCl_3) δ 7.53 (1H, s), 7.05(1H, s), 6.96 (1H, s), 4.34 (1H, sept, J = 6.72 Hz), 1.48, (6H, d, J = 6.72 Hz) |
|  | nPrIm | ^1H (400MHz, CDCl_3) δ 7.46 (1H, s), 7.05 (1H, s), 6.90 (1H, s), 3.89 (2H, t, J = 6.85 Hz), 1.80 (2H, dd, J = 7.34 Hz), 0.93 (3H, t, J = 7.34 Hz) |
|  | Melm | n/a 1-methyl imidazole was used as obtained from Sigma Aldrich. |

Table 7: Mono functionalised imidazole structures, abbreviation used and ^1H NMR tabulation.

2.1.1.2 Imidazolium synthesis

The conversion of the imidazole was undertaken in the following manner: The imidazole, diPrIm, (0.5 g, 2.6 mmol) was dissolved in acetonitrile (20 mL). To this (3-iodopropyl)trimethoxysilane (0.53 mL, 2.6 mmol) was added and the resulting solution heated to 90 °C for 7 hours. The heat and solvent were removed. The crude product was triturated with diethyl ether (15 mL) before drying under high vacuum to afford an orange oil. Analysis of the purity and structure of the compound was undertaken through obtaining ^1H NMR spectra. See below for peak listing. Collection of spectra was not undertaken for all of the imidazolium products formed from the above imidazole species for practical reasons.

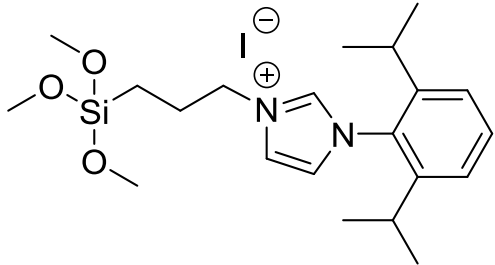
| Imidazolium structure | Abbreviation | ¹ H NMR tabulation |
|---|--------------|---|
|  | diPrIm(I) | ¹ H (400 MHz, CDCl ₃) δ 10.13 (1H, s), 7.74 (1H, s), 7.56 (1H, m), 7.32 (2H, m), 7.17 (1H, s), 4.83 (2H, t, <i>J</i> = 6.85 Hz), 3.60 (9H, s), 2.31 (2H, septet, <i>J</i> = 6.85 Hz), 2.15 (2H, quintet, <i>J</i> = 7.76 Hz), 1.21 (12H, d, <i>J</i> = 6.79 Hz), 0.73 (2H, t, <i>J</i> = 8.13 Hz). |

Table 8: Summary of peak positions and tabulations for diPrIm(I).

2.1.1.3 Imidazolium immobilisation *via* silanols

The silicas employed for grafting of the organocatalyst were commercial Grace-Davison silica with stated pore apertures of 250, 150, 60 and 30 Å (Sigma Aldrich). Synthesis of silica based imidazolium materials was as follows. The silica (varied) – 1 g – was placed into a round bottom flask along with toluene 30 mL and set to stir. To the stirred suspension the selected imidazolium was added (1 mmol) in order to obtain a maximum potential loading of 1 mmol g⁻¹. As such (0.611 g, 1 mmol) of the diPrIm(I), was added to the round bottom flask. The solution was set to stir for 10 hours at 120 °C. Following anchoring the solid was collected by filtration and placed into a soxhlet apparatus with dichloromethane as the solvent overnight. The catalyst was dried for further use.

Anchoring onto the silanol sites of the hierarchically porous materials was achieved *via* a similar method. HP SAPO-5 (1 g) was degassed and then suspended in toluene (60 mL). diPrIm(I) (0.5mmol) was added to the suspension and refluxed overnight. The solid was collected *via* filtration and then washed in a soxhlet using DCM.

2.1.1.4 Conversion to carboxylate *via* NHC

The imidazolium on silica (0.5 g) was weighed into a 3-neck RBF to which was affixed a nitrogen bubbler atop a condenser on the central neck, to each of the side-arms a septum was added. The RBF was charged with THF (40 mL, anhydrous). Typically, a 0.125 M solution of potassium hexamethyl hexamethyldisilazide (KHMDs) in THF (anhydrous) was made, with 1.2 equivalents (wrt to imidazolium loading) added to the stirred solution of the catalyst – under nitrogen. Upon addition a colour change from yellow to white in appearance of the solid was seen. After stirring for 15 minutes CO₂ was bubbled directly into the THF for 4 hours to produce the carboxylate

which was washed with THF and then dried. A tap prior to the nitrogen bubbler was used in order to control the flow rate of the CO₂ into the solution.

Attempts to remove the 'KI' were made through placing in the carboxylate materials into a THF soxhlet over 48 hours.

2.1.1.5 Catalytic testing

Reactions to test different aspects of the catalyst were undertaken, but in order to allow for comparison across studies followed the same general procedure. To a PEEK, liner 5 g of butylene oxide (equivalent moles used for substrate study) along with catalyst (100 mg, balanced for loading when comparing different R groups). This was then placed into a Parr batch reactor and the setup was pressurised to 20 bar CO₂ at room temperature. The reactor was vented and pressurised three times in order to obtain a complete CO₂ atmosphere (> 99 % CO₂). The reactor was heated to 115 °C (t = 0 when T = 115 °C) and stirred at 400 revolutions per minute (rpm) for 6 hours. Following cooling under ice the reactor was vented and mesitylene (3 g) was added as internal standard. The resulting solution was mixed thoroughly and centrifuged to remove the suspended catalyst. An aliquot of the supernatant analysed by NMR spectroscopy. Analysis *via* ¹H NMR was undertaken by through the procedure explained in section 2.2.5.

Analogous batch reactions were undertaken for the testing of the HP AlPO, SAPO and NHC materials. Specific reaction conditions can be found in Chapter 3 in the captions of each Figure.

2.1.2 Imidazole functionalisation of MIL-101(Cr)

2.1.2.1 Synthesis and purification of MIL-101(Cr)

MIL 101(Cr) was synthesised following a modified procedure of that reported by Jiang *et al*^[204] In a typical synthesis, 1 mmol of Cr(NO₃)₃·9H₂O was mixed with 1 mmol of terephthalic acid (C₈H₆O₄) in 265 mmol of deionised water and 1 mmol of HNO₃ in a Teflon beaker. The mixture was allowed to stir at room temperature for 1 hour. The black suspension was poured into a 23 mL Teflon liner and sealed in a steel autoclave vessel. The autoclave was transferred to a fan-assisted oven at 220 °C for 8 hours. The resulting solid was centrifuged (10 mins at 10k rpm) and then washed with 200 mL (5 x 40 mL) of ethanol. Product formed was a green solid with traces of white unreacted terephthalic acid. A 2-step activation procedure was used to remove the trapped terephthalic acid inside the pores. The green solid was stirred with 60 mL of boiling ethanol for 14 hours, followed by stirring with 80 mL of a 30 mM aqueous solution of NH₄F at 75 °C for 5 hours. The solid was recovered through centrifugation and washed with 100 mL of hot water. The purified MOF was

dried under vacuum at 160 °C overnight in order to remove physisorbed water from inside the pores.

1-methyl imidazole was purchased from Sigma Aldrich (>97 %) and used without further purification. Alternatively functionalised imidazoles were produced as per the procedure detailed above in section 2.1.1.1.

2.1.2.2 Grafting of imidazoles to MIL-101(Cr)

Imidazole-based molecular systems were grafted onto the coordinatively unsaturated chromium sites following a slightly modified procedure as reported by Hwang *et al.*^[205]. For a typical synthesis, MIL-101(Cr) (100 mg) was mixed with the substituted imidazole (0.1 mmol) in dry toluene (30 mL). The mixture was refluxed under N₂ atmosphere for 15 hours under stirring. The solid was collected through filtration onto a filter paper and placed into a Soxhlet extraction with dichloromethane overnight, to remove any imidazole within the pores that was not successfully grafted to a CUS.

2.1.2.3 Catalytic testing

A general procedure for the testing of the materials is shown in section 2.1.1.5 and was used to test the MIL-101(Cr) variants. Quantities used for each individual case will be detailed in Chapter 4 in the caption of the corresponding Figure.

2.1.2.4 Computational Modelling

Computational work was undertaken by Dr Liling Zhang of the Institute of High Performance Computing (IHPC), Agency for Science, Technology and Research (A*STAR). Two methodologies were employed to simulate and calculate computationally the MIL-101-Me system, in combination with the experimental work, Density Functional Theory (DFT) and Grand Canonical Monte Carlo (GCMC). The former performs calculations using an *ab initio*, first principles, approach and attempts to solve a simplified version of the Schrödinger equation – with assumptions applied to lessen the computational strain. GCMC is an approximation technique which uses repeated random sampling to determine the relative positions of atoms or molecules, where temperature, volume and chemical potential were fixed. A combination of both methodologies was used to determine the favourable location of atoms or molecules within the MIL-101(Cr) and MIL-101-Me structures during adsorption studies and under reaction conditions.

The MIL-101(Cr) structure was constructed based on experimental crystallographic data, followed by energy minimisation using Forcite in Materials Studio^[206]. The MIL-101-Me model was built by binding the imidazole to an unsaturated Cr site in the trimer of Cr₃O units giving an imidazole

loading of 1.3 mmol g^{-1} . To estimate the atomic charges of MIL-101(Cr) and MIL-101-Me, DFT calculation was performed on the Cr_3O trimer cluster. The cleaved bonds were terminated by methyl groups. Geometry optimisation was carried out in DMol3 using the BLYP correlation functional and DNP basis set. The atomic charges (listed in Table 9) were then obtained from the ESP charges by fitting the calculated electrostatic potentials. The bonding energy for imidazole grafted to unsaturated Cr site was also obtained from DFT calculation on Cr_3O trimer clusters with dispersion correction included using Grimme scheme^[207].

| Charge (q) | MIL-101 | MIL-101-Me |
|------------|---------|------------|
| Cr1 | 1.104 | 1.140 |
| Cr2 | 1.271 | 0.932 |
| Cr3 | 1.271 | 1.228 |
| O1 | -0.586 | -0.564 |
| O2 | -0.570 | -0.544 |
| F | -0.444 | -0.471 |
| C1 | 0.679 | 0.662 |
| C2 | -0.025 | -0.059 |
| C3 | -0.116 | -0.103 |
| H | 0.141 | 0.136 |
| N1-Im | - | -0.107 |
| N2-Im | - | 0.348 |
| C1-Im | - | -0.151 |
| C2-Im | - | -0.373 |
| C3-Im | - | -0.074 |
| C4-Im | - | -0.486 |

Table 9: Partial charges for atoms on MIL-101(Cr) and MIL-101-Me.

Grand Canonical Monte Carlo (GCMC) method was performed to simulate the adsorption of pure and mixed gases in MIL-101(Cr) and MIL-101-Me. The framework was assumed to be rigid and kept fixed during the simulations. The dispersion interactions of the framework atoms were modelled using the universal force field (UFF). CO_2 was represented as a three-site rigid molecule

and the partial charges on C and O atoms were 0.576e and -0.288e, respectively. The C-O bond length was 1.18 Å, for the remaining parameters see Table 10. The potential parameter for ethylene oxide was adopted from the TraPPE force field^[208]. GCMC was implemented by a source code from Jiang's group^[209], which was widely used for gas sorption in various MOFs.

| Site (adsorbate) | site | σ (Å) | ϵ/k_B (K) | Z (e) |
|------------------|------|--------------|--------------------|--------|
| CO ₂ | C | 2.789 | 29.66 | +0.576 |
| | O | 3.011 | 82.96 | -0.288 |
| N ₂ | N | 3.32 | 36.4 | 0.0 |

Table 10: Potential parameters and atomic charges of CO₂ and N₂.

DFT quantum mechanical modelling was undertaken on butylene oxide and carbon dioxide in MIL-101-Me using wb97xd functional with 6-31+G* basis set and Grimme's dispersion model.

2.1.3 MNPs/UiO-66-NH₂ for tandem reactions

2.1.3.1 UiO-66 synthesis

A typical synthesis for zirconium terephthalate MOF UiO-66 was also follows. In a 250 mL glass reaction bottle ZrCl₄ (0.640 g; 2.75 mmol), terephthalic acid (0.473 g; 2.85 mmol) and N,N'-dimethylformamide (40 mL) were added and sonicated for 5 minutes. Benzoic acid (3.36 g; 27.50 mmol) was added and the solution sonicated for a further 5 minutes until complete dissolution had occurred. The bottle was sealed and placed in a preheated convection oven at 120 °C for 48 hours, after which it cooled to RT naturally. Suspensions of the pale yellow product were collected by centrifugation at 10,000 rpm for 15 minutes. The supernatant was decanted off and the product washed twice with methanol (2 × 60 mL), collecting each time by centrifugation as before. Products were then dried ready for analysis or further experiments.

2.1.3.2 UiO-66-NH₂ synthesis

In a 100 mL glass reaction bottle ZrCl₄ (0.163 g; 0.70 mmol), 2-aminoterephthalic acid (0.13 g; 0.72 mmol) and N,N'-dimethylformamide (40 mL) were added and sonicated for 5. Benzoic acid (0.85 g; 7.00 mmol) was added and the solution sonicated for a further 5 minutes until complete dissolution had occurred. The bottle was capped and placed in a preheated convection oven at 120 °C for 48 hours, then allowed to cool to RT naturally. Suspensions of the pale yellow product were collected by centrifugation at 10,000 rpm for 15 minutes. The supernatant was decanted off

and the product washed twice with methanol (2×60 mL), collecting each time by centrifugation as before. Products were then dried ready for analysis or further experiments.

2.1.3.2.1 TEA and acetic acid modulated UiO-66-NH₂

Following the preparation detailed by Wang *et al.*^[133] to a RBF DMF (140 mL), TEA (0.1214 mL, 8 mmol) and 2-aminoterephthalic acid (0.108 g; 0.59 mmol) were added. The solution was stirred for 10 minutes before acetic acid (21 mL) was added and the reaction heated to 120 °C when ZrCl₄ (0.1401 g, 0.60 mmol, in 10 mL DMF) was added. The solution was stirred for 6 hours. The supernatant was decanted off and the product washed twice with methanol (2×60 mL), collecting each time by centrifugation as before. Products were then dried ready for analysis or further experiments.

2.1.3.3 Deposition of NPs on/in UiO-66

In all of the following methods UiO-66 and UiO-66-NH₂ are interchangeable and were used in equivalent quantities.

2.1.3.3.1 PVP stabilised Au NPS on UiO-66

In a 150 mL RBF methanol (80 mL), HAuCl₄ solution (0.38 mL; 10.61 mg/mL in H₂O) and polyvinylpyrrolidone (PVP) solution (0.20 mL; 6.50 mg/mL in H₂O) were added and stirred vigorously. To the rapidly stirred solution, a freshly prepared aqueous solution of NaBH₄ (0.51 mL; 0.1 M) was added dropwise over a period of 3 minutes, then left to stir for a further 2 hours.

For a 1 wt. % loading of Au NPs, UiO-66 or /UiO-66-NH₂ (200 mg) was added to the stirred Au NP sol and left to stir for 24 hours. The pink-purple powdered product was collected by centrifugation at 10,000 rpm for 15 minutes, the supernatant decanted and washed twice with methanol (2×40 mL), collected by centrifugation each time as before. Products were then dried ready for analysis or further experiments.

An analogous procedure was used for Pd and Pt NP formation using solutions of K₂PtCl₄ and K₂PdCl₄ (as solutions of approximately 10 mg/mL).

2.1.3.3.2 Impregnation of Au NPs in UiO-66

To a RBF methanol/hexane (10 mL) and UiO-66 or /UiO-66-NH₂ (200 mg) and stirred for 10 minutes. HAuCl₄ solution (0.38 mL; 10.61 mg/mL in H₂O). The suspension was stirred overnight before a freshly prepared aqueous solution of NaBH₄ (0.51 mL; 0.1 M) was added dropwise over a period of 3 minutes, then left to stir for a further 2 hours.

The pink-purple powdered product was collected by centrifugation at 10,000 rpm for 15 minutes, the supernatant decanted and washed twice with methanol (2×40 mL), collected by centrifugation each time as before. Products were then dried ready for analysis or further experiments.

2.1.3.3.3 Encapsulation of PVP stabilised Au NPs in UiO-66

Following a modified version of the preparation by Gu *et al.*^[201] PVP capped Au NPs were produced as per 2.1.3.3.1 before collection *via* centrifugation (14k rpm, 30 mins). To an autoclave liner Acetic acid (4.8 mL, 80 mmol) and 2-aminoterephthalic acid (0.0635 g; 0.35 mmol) were added in DMF (28 mL) and stirred. Following 10 minutes of stirring, ZrCl_4 (0.0817 g; 0.35 mmol) was added. The NPs were re-suspended in 1 mL of methanol and added to the reagent mixture during which the solution was bubbled constantly with Ar. After 5 mins of bubbling the vessel was sealed and placed into a pre-heated oven at 120 °C for 48 hours.

The powdered product was collected by centrifugation at 10,000 rpm for 15 minutes, the supernatant decanted and washed twice with methanol (2×40 mL), collected by centrifugation each time as before. Products were then dried ready for analysis or further experiments.

2.1.3.4 Catalytic testing of MNP/UiO-66(-NH₂)

The general reaction case was as follows, to a RBF was measured catalyst, reactants, chlorobenzene (as an internal standard) and tert-butanol as a solvent in varying concentrations, see Chapter 5. The RBF was immersed in a preheated oil bath at 70 °C with stirring and left for the desired amount of time. Samples were extracted at varying time intervals, centrifuged and capped in a vial for GC analysis. For exact reaction conditions relating to specific studies see caption on the corresponding Figure or Table associated with it.

2.1.4 MIL-101(Cr) for the epoxidation of styrene

2.1.4.1 Modulated synthesis of MIL-101(Cr)

MIL 101(Cr) was synthesised following a modified procedure of that reported by Jiang *et al.*^[204] In a typical synthesis, 1 mmol of $\text{Cr}(\text{NO}_3)_3 \cdot 9\text{H}_2\text{O}$ was mixed with 1 mmol of terephthalic acid ($\text{C}_8\text{H}_6\text{O}_4$) in 265 mmol of deionised water and 1 mmol of HNO_3 in a Teflon beaker. Benzoic acid was added in (100 and 50 mol %) to two of synthesis mixtures with amount related to the terephthalic acid amount. The mixture was allowed to stir at room temperature for 1 hour. The black suspension was poured into a 23 mL Teflon liner and sealed in a steel autoclave vessel. The autoclave was

transferred to a fan-assisted oven at 220 °C for 8 hours. The resulting solid was centrifuged (10 mins at 10k rpm) and then washed with 200 mL (5 x 40 mL) of ethanol.

2.1.4.2 Au/MIL-101(Cr) and Au@MIL-101(Cr)

To a RBF hexane (10 mL) and MIL-101(Cr) (200 mg) and stirred for 10 minutes. HAuCl_4 solution (0.38 mL; 10.61 mg/mL in H_2O). The suspension was stirred overnight before a freshly prepared aqueous solution of NaBH_4 (0.51 mL; 0.1 M) was added dropwise over a period of 3 minutes, then left to stir for a further 2 hours.

The dark green product was collected by centrifugation at 10,000 rpm for 15 minutes, the supernatant decanted and washed twice with methanol (2×40 mL), collected by centrifugation each time as before. Products were then dried ready for analysis or further experiments.

2.1.4.3 Epoxidation catalytic reactions

Epoxidation reactions were run using a 2-neck RBF (25 mL) to which MIL-101(Cr) (various, 25 mg), TBHP (5.5 M in decane, 1 mL), styrene (0.5 g, 4.8 mmol), chlorobenzene (0.1 g, ITSD) and acetonitrile (5 mL) were added. The reaction was heated to 80 °C and sampled hourly for quantification of products *via* GC, the sample was centrifuged to remove the solid catalyst before an aliquot removed for injection.

A repeat of the above was undertaken without the addition of catalyst in order to obtain a value for the blank reaction.

2.2 Characterisation Techniques

Characterisation of catalysts is hugely important. It allows for the understanding of how they function through the determination of structure property relationships and enables optimisation through careful material design. A wide range of characterisation techniques have been employed during the course of this work to assess the properties of the materials synthesised and how they act under catalytic test conditions. The following table states, in the simplest terms, the relevant information which was gleaned from each methodology, before they are each described in greater detail and related to the materials which were used to analysed in the subsequent Chapters.

| Technique (abbreviation) | Information obtained |
|--|--|
| X-ray Diffraction (XRD) | Determination of crystallinity and phase purity of catalyst framework. |
| N ₂ and CO ₂ gas sorption (BET etc.) | Surface area, pore diameter, pore volume and gas capacity measurements. |
| Thermogravimetric Analysis (TGA) | Thermal stability of the material, therefore the maximum operating temperature and loading of organic species. |
| Thermogravimetric- Mass Spectroscopy (TG-MS) | Identification of decomposition products lost during each of the mass loss stages of TGA. |
| Nuclear Magnetic Resonance (NMR) | Compound structure of organic species and analysis of reaction progression. |
| Solid state NMR (ssNMR) | Determination of structure and local chemical environment of solid materials. |
| Ultra violet –visible spectroscopy (UV-vis) | Characterisation of metal species and ligands <i>via</i> electronic transition observation. |
| Near Infrared (NIR) | Observation of vibrational modes. |
| Fourier Transform Infrared (FT-IR) | Observation of vibrational modes within molecules and materials, chemical bonding and environment can be observed. |
| X-ray photoelectron Spectroscopy (XPS) | Identification of oxidation states, local chemical environments and elemental analysis. |

| | |
|--|--|
| Gas Chromatography (GC) | Separation of compounds in a reaction mixture for subsequent quantification. |
| Gas Chromatography – Mass Spectrometry (GC-MS) | Identification of unknown components within a reaction mixture through analysis of fragmentation patterns and m/z values. |
| Scanning Electron Microscopy (SEM) | Imaging of material surfaces and morphology of samples (typically > 100 nm). |
| Transmission Electron Microscopy (TEM) | Imaging of material surface and morphology at very high magnification for nanomaterials such as NPs (typically < 100 nm). |
| Inductively Couple Plasma – Optical Spectroscopy (ICP-OES) | Elemental analysis of all elements present within the analysed sample. |
| Elemental Analysis (EA) | CHNS % weight percentages within a sample. |
| Electron Paramagnetic Resonance (EPR) | For systems with unpaired electrons, the local environment can be studied, typically with respect to metals and their ligands, such as Cr(III). |
| Density Functional Theory (DFT) | Calculation of optimised ligand geometry and atomic charges as well as calculation of epoxide and CO ₂ binding sites and molecular orbital interactions between reagents and framework. |
| Grand Canonical Monte Carlo (GCMC) | Simulation of small molecules within framework structures and determination of favourable binding sites. |

Table 11: Summary of the techniques used and information obtained during material evaluation.

2.2.1 X-Ray Diffraction (XRD)

X-Ray Diffraction allows for determination of crystalline phases, phase purity and crystallinity of generally a powdered solid sample. A monochromatic x-ray source bombards the sample following which a detector senses any diffracted x-rays. In order for the signals to be analysed the x-rays incident on the sample must impinge in a constructive manner, as displayed in Figure 21, or no signal will be observed. The source and detector are rotated around the sample at angle θ and as such when diffracted x-rays are observed they are displayed as 2θ against signal intensity. The pattern of 2θ values can then be related to the crystal structure of the material mathematically by Bragg's law.

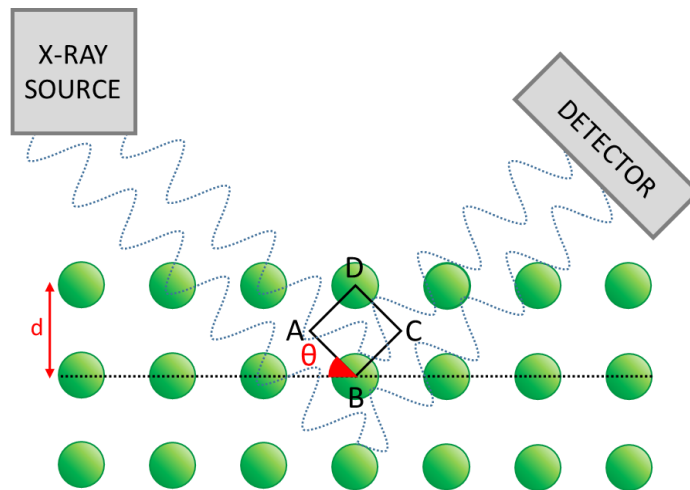


Figure 21: Diagrammatic representation of constructive diffraction of X-Rays

Bragg's law, see below for derivation, relates the lattice planes and crystal structure to the pattern observed. The detected x-rays scatter off neighbouring lattice planes of the material studied, therefore will have travelled a distance which is an integer value away from another x-ray impinging onto the detector.

$$n\lambda = AB + BC$$

Thus, $AB = CD$ as per Figure 21, which gives, from the above, $n\lambda = 2AB$. Given that $\frac{AB}{d} = \sin\theta$ then the final form, Bragg's Law can be defined as, with d equal to d_{hkl} .

$$n\lambda = 2d \sin\theta$$

Equation 10: Bragg's Law.

The above equation can be used to not only describe the distances between the lattice planes but also their orientation with respect to the origin of the unit cell. A unit cell is defined as the smallest 3D cell from which the repeating structure is reproducible by translation. Miller indices are used to identify different planes of atoms and so the atomic and micro-structure of a sample found. The indices (hkl) define where a plane intersects along abc within a unit cell, i.e. $\frac{a}{h}$, $\frac{b}{k}$ and $\frac{c}{l}$ as per, Figure 22. The vector d_{hkl} is used then to determine where the diffraction peaks will occur for a material also known as the spacing between the planes within the material^[210].

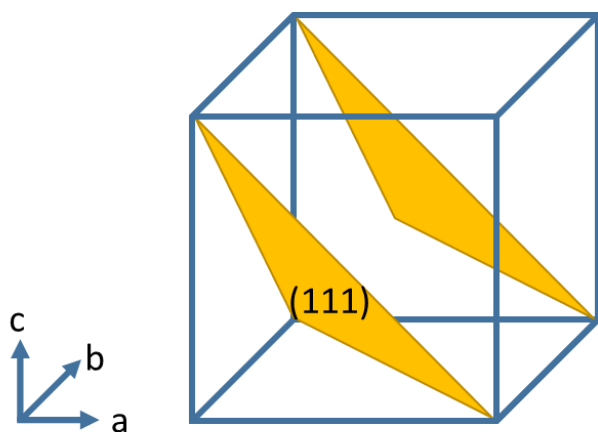


Figure 22: Representation of a unit cell (fcc) with (111) plane shown.

Primarily, an XRD pattern allows for the crystallinity as purity of a material to be determined. A material of repeating structure will produce a unique diffraction pattern which is a key identifier in confirming a synthesis has been completed successfully. For the work undertaken in the following Chapters XRD was used to confirm the structural details of powdered samples. Rietveld refinement was used in order to do so, it is a whole pattern refinement in which the experimentally collected pattern is compared with a calculated pattern, based on an optimisation algorithm. The refinement requires a known structure, often this is in the form of a pattern from the literature. In the latter Chapters this reference pattern shall be plotted with the experimental patterns to allow comparison.

The following shows the refinement of the AlPO-5 structure as discussed in Chapter 3 using a database pattern of the structure for the refinement, Figure 23.

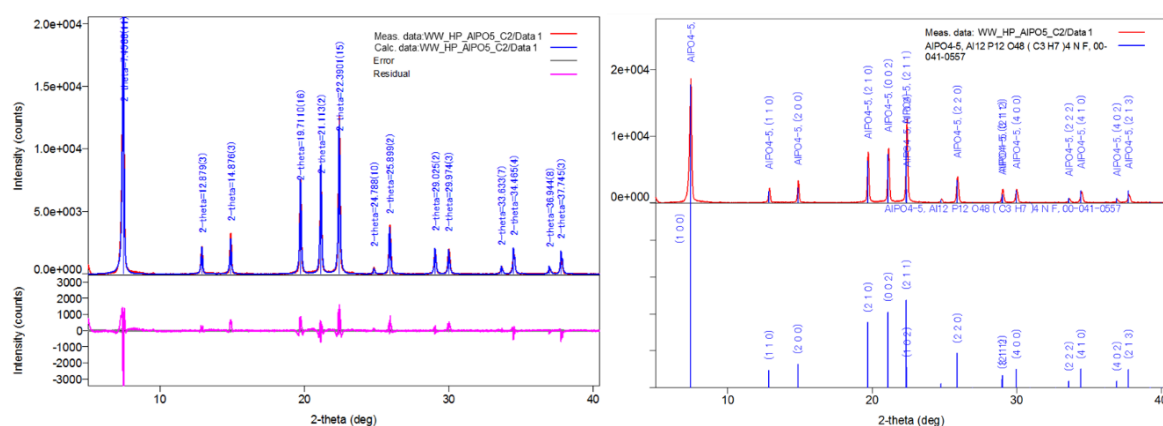


Figure 23: Refinement of HP AlPO-5 using AlPO-5 literature reference (blue) to refine experimental pattern (red).

The refinement of the above structure in the above led to the indexing of the pattern as seen which confirmed the phase purity and crystallinity of the material. An analogous procedure was

used for all other structures analysed by XRD and shown in the subsequent Chapters to confirm correct structure and phase purity of them.

2.2.1.1 XRD Equipment details

X-Ray diffraction (XRD) was collected on Bruker D2 Phaser with non-monochromatic Cu K α radiation ($\lambda = 1.5406 \text{ \AA}$). Samples were prepared by grinding into a fine powder and mounted in a sample holder.

2.2.2 Surface analysis *via* gas adsorption

Methodologies of measuring gas adsorption are very useful in the design and evaluation of catalytic materials as more often than not they are porous. The measurement of the amount of gas adsorbed on a solid material at a given temperature and a range of pressures allows for the determination of surface area, pore volume, pore size distribution as well as the overall isotherm. Nitrogen is commonly used as an adsorbate at $-196 \text{ }^\circ\text{C}$ and is the adsorbate used within this thesis unless stated otherwise.

There are three different classifications for pore diameter within the context of physisorption - as set by IUPAC in 1985^[211]:

1. pores with widths exceeding about 50 nm are called macropores;
2. pores of widths between 2 nm and 50 nm are called mesopores;
3. pores with widths not exceeding about 2 nm are called micropores.

An isotherm is collected through measurement of the amount of gas adsorbed (preferably in either mmol g^{-1} or $\text{cm}^3 \text{ g}^{-1}$) over a range of equilibrium relative pressures (p/p_0), where p_0 is the saturation pressure of the pure adsorptive at the operational temperature. Prior to analysis the sample is degassed thoroughly in order to remove any solvents or smaller molecules within the sample. The shape of the isotherm provides information on the characteristics of the material studied. Thommes *et al* proposed new classifications for isotherm shape and detailed how they relate to the type of porosity present^[212].

In Chapters 3 and 4 mesoporous materials, silica and MIL-101(Cr) are investigated. For these materials the nitrogen isotherm has the type IV shape but with subtly different characteristics. For silica based materials, the pore size is large, so a Type IVa isotherm, as per Thommes *et al*, is observed along with a hysteresis, due to capillary condensation. For the MIL-101(Cr) a type IVb isotherm is to be expected as the pore width is less than 4 nm, below which it is reported that completely reversible isotherms are observed^[212,213]. In Chapter 5 the UiO-66 material is

microporous and a shape similar to a type II, reversible isotherm is expected. The two types expected to be observed with the materials studied in Chapter 3 and 5 are shown below in Figure 24, the isotherm of MIL-101(Cr) shall have the hysteresis shifted to lower relative pressures.

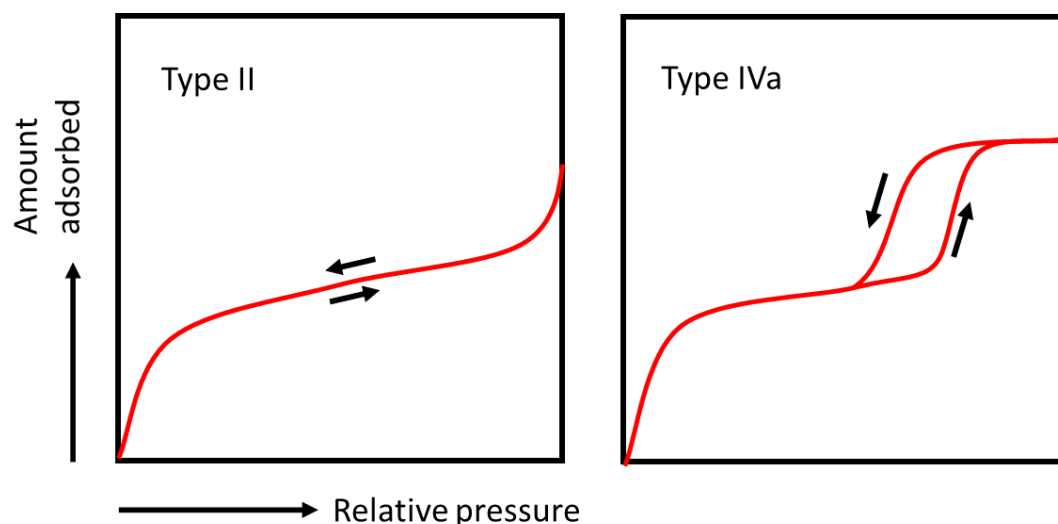


Figure 24: Representation of the characteristic shape of Type II and Type IVa isotherms, produced with reference to Thommes *et al*^[212].

There are two different types of model to describe adsorption of a molecule to a surface. The Langmuir model describes the formation of a monolayer occurring at low pressures as the surface sites are the most favourable, with multilayer adsorption at higher pressures. The Brunauer Emmett Teller (BET) model realises that multilayer formation will occur before a complete monolayer has formed, and so is more realistic in its approach, Figure 25.

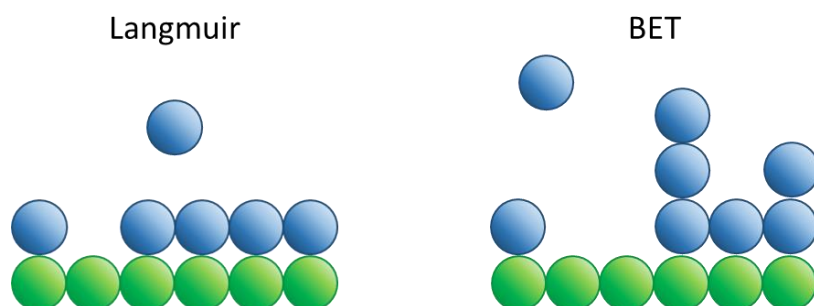


Figure 25: Langmuir and BET gas adsorption theories, whereby the Langmuir model shows solely monolayer formation and the BET model shows the formation of multiple layers prior to monolayer occurrence.

For determination of the surface area, the Brunauer Emmet Teller (BET) method^[214] is most commonly used with mesoporous materials and was used for the surface area determinations in Chapter 3-5, it makes the following important assumptions^[215,216].

1. Adsorption of the first adsorbate layer occurs on a range of surface sites with equal energy.
2. Second layer adsorption only occurs on the first layer of adsorbates, the third on the second layer and so on, when the pressure equals the saturation pressure an infinite layer of adsorbates is present.
3. The rate of condensation and evaporation are equal at the equilibrium point for each layer.
4. The first adsorbed layer will have an enthalpy of adsorption that is equal to the Langmuir case; however the following adsorbed layers will have equilibrium constants that are equal.

This produces the BET equation:

$$\frac{p/p_0}{n(p - p_0)} = \frac{1}{n_m C} + \frac{C - 1}{n_m C} (p/p_0)$$

Equation 11: BET equation whereby p is pressure, p_0 is standard pressure, n_m is the volume of gas required to form a monolayer, V is volume of gas adsorbed at pressure P and finally C is the BET constant.

For the region of $0.05 - 0.3 p/p_0$ for type II and type IV isotherms, such as those to be studied in this work, a straight line is obtained from the plot of $\frac{p/p_0}{n(p - p_0)}$ against p/p_0 and allows for the calculation of the capacity of the monolayer which has formed, i.e. the surface area. From the intercept and gradient the surface area can be found:

$$n_m = \frac{1}{G + I}$$

Equation 12: Equation for monolayer determination whereby the gradient (G) = $\frac{C-1}{n_m C}$ and the intercept (I) is equal to $\frac{1}{n_m C}$

The BET surface area is then calculated from the monolayer capacity once the mass of the material being studied is factored in as well as the size of the adsorbent (the cross sectional area, σ , for N_2 is usually taken to be 0.162 nm^2)^[212].

$$S (BET) = \frac{n_m N_{Av} \sigma}{\text{sample mass}}$$

Equation 13: Determination of surface area whereby N_{Av} is Avogadro's constant, and σ is the cross sectional area of the sorbent.

Owing to the assumptions made and errors inherent in use of the BET method, caution must be made when determining surface areas for porous materials, as detailed by Rouquerol *et al*, especially microporous materials^[217].

Determination of the size of pores and the distribution of them is undertaken using the Barret-Joyner-Halenda (BJH) method was used to determine the pore sizes of materials studied, in combination with the Kelvin equation.

$$\ln\left(\frac{p}{p_0}\right) = \frac{-2\gamma V}{(r_p - t_c)RT}$$

Equation 14: Modified Kelvin equation where γ is the surface tension of the adsorbent, V is the molar volume, r_p is the pore radius and t_c the thickness of the adsorbed multilayer film^[212].

From the Kelvin equation it can be seen that the pressure at which the hysteresis occurs can be derived and as the relative pressure where the pore condensation occurs depends on the pore radius, this can also be found using the following: $r_p = r_k + t_c$. Therefore pore distribution can be calculated, and r_k is the Kelvin radius, the vapour radius around the meniscus formed by condensation within the pore.

Other adsorbents can be useful in order to determine the capacity of a material for them. With regards to the work in this thesis the determination with respect to CO₂ utilisation, CO₂ is then a useful sorbent to use. The amount of CO₂ uptake for the MIL-101(Cr) materials was investigated by dosing the samples with CO₂ over the range of pressures from 0 – 1100 mbar. The mol adsorbed per unit mass of the catalyst was then calculated and could be compared with literature values for other sorbent materials.

2.2.2.1 Gas adsorption equipment details

N₂ and CO₂ isotherms were collected on Micrometrics ASAP 2020 Automatic High Resolution Micropore Physisorption Analyser. CO₂ measurements were collected at room temperature using a water bath. All samples were outgassed at 150 °C for 6 hours prior to measurement.

2.2.3 Thermogravimetric Analysis (TGA)

Thermogravimetric analysis is a simple yet powerful tool that allows for the determination of thermal properties. A sample, of known mass, is heated under a flow of air or nitrogen and the mass loss profile over time is recorded. The temperature at which the samples begins to thermally degrade can then be determined. If the material has an organic component to it then the mass

loss observed relates to the loading of the organic species. Typically a plot of temperature against mass, normalised to remove an initial loss (corresponding to water or solvent), is reported. The first derivative is often used to isolate discrete mass loss events within the degradation.

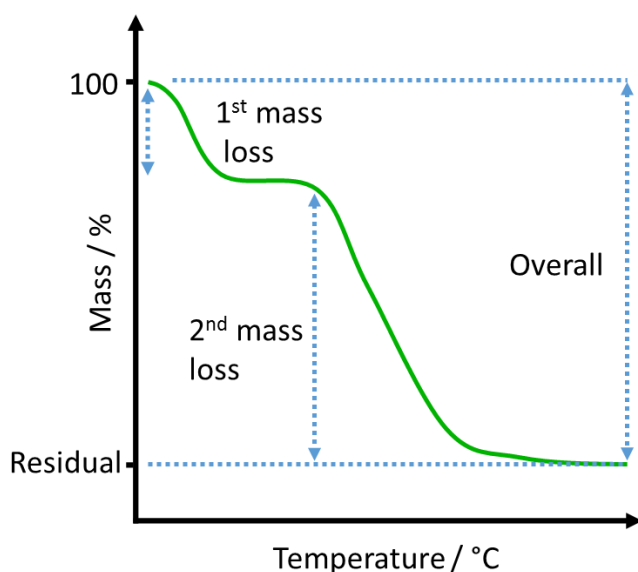


Figure 26: Diagrammatic representation of a TGA curve with labels affixed

TGA is of particular interest when working with catalysts as the maximum working temperature of the material can be found but also it can be used as a secondary method of loading calculation. For example, for the determination of an organic component the mass loss percentage will correspond to the amount of the organic present within the material, thus if structure is known then loading can be calculated. Alternatively, the addition of an inorganic component, such as metal nanoparticles to a MOF, is quantifiable. The overall weight loss of the material will decrease as the inorganic component is larger, therefore the difference between the residuals, see Figure 26, will be caused by the inorganic component added.

2.2.3.1 TGA equipment details

Thermogravimetric analysis (TGA) measurements were obtained on the TA Instruments Thermogravimetric analyser, TGA Q500. Analysis was normally undertaken in air (50 mL/min) at 10 °C/min ramp rate. The curves for each of the samples were normalised for solvent loss before 100 °C. This was completed through setting the starting mass to 100 % at the region where the peak on the derivative plot returned to a neutral gradient.

2.2.4 Thermogravimetric mass spectroscopy (TG-MS)

Coupling of mass spectroscopy to thermogravimetric measurements allows for the identification of the mass loss peaks occurring within a TGA curve. Additionally, TG-MS can analyse small

molecules adsorbed or bonded reversibly to a material. The sample is heated, in a carrier gas and the gas stream is fed into a mass spectrometer for analysis. The coupling of the two systems then, with careful selection of the ramp rate to ensure the decoupling of mass loss peaks, means that the individual decomposition stages are the molecular structure of each part to be identified.

TG-MS was used in the analysis of the NHC-CO₂ materials produced in Chapter 3 in order to observe and confirm the removal of CO₂ from the material and so prove that the carboxylate intermediate had been produced, m/z 44 was studied for this purpose.

2.2.4.1 TG-MS equipment details

Analysis of CO₂ removal was achieved by a Netzsch Libra TG-209 coupled to a QMS-403C MS system the TG component was undertaken in air at 2 °C/min ramp rate.

2.2.5 Nuclear Magnetic Resonance (NMR) Spectroscopy

Nuclear magnetic resonance (NMR) spectroscopy allows for the observation of different chemical environments within a sample. The sample, in solution, is spun within a magnetic field and as long as the nuclei of interest has nuclear angular momentum spin quantum number, I , greater than zero then it can be observed. Where the nucleus has no spin, then it is not observable. For those which do possess a spin quantum number above 0, upon placement in a magnetic field, B_0 , the nucleus is no longer be degenerate and adopts a defined number of possible orientations ($2I+1$). These orientations are restricted by the selection rule $\Delta m = \pm 1$, whereby m is equal to the spin state of the nucleus. Irradiation of the sample by electromagnetic radiation (200-900 MHz) occurs, with the greater the energy applied, the greater the difference between the two states, Figure 27. As such, the resolution of the instrument depends on the size of the magnetic field applied.

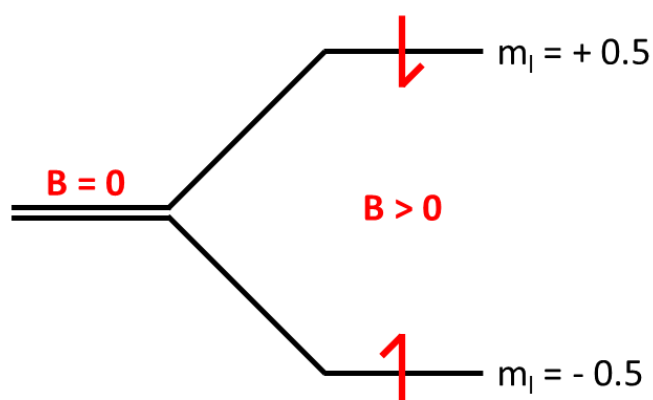


Figure 27: Diagrammatic representation of a nucleus with spin $I > 0$ in a magnetic field, $B > 0$.

Orientations are shown with different energies ($2I+1$ (labelled m_I) orientations are possible).

Within a molecule being observed by NMR each nuclei is not isolated from other nuclei within the molecule and so the magnetic field actually felt by that nuclei is slightly different from that of the applied external magnetic field. The chemical environment of a nuclei consequently alters the position of its absorbance, known as chemical shift, δ . A standard, such as tetramethylsilane (TMS) is used in order to reference the size of the shift which is governed by shielding and de-shielding by neighbouring groups or atoms. For a proton (^1H) spectra de-shielding will shift peaks to higher values, such as those for an aldehyde proton (9-10 ppm). Conversely, shielding, such as longer alkyl chains, will see lower chemical shift values (1-3 ppm).

NMR was used as the primary method of quantification in the conversion of CO_2 and epoxides to cyclic carbonates. The reactions were run under solvent free conditions so a relatively uncomplicated NMR spectra was obtained. The epoxide and cyclic carbonates have well defined peaks which are easily monitored as they appear discretely to one another. Following reaction mesitylene was added as an internal standard (ITSD). An internal standard for NMR quantification is hereby defined as one which is internal during the collection of the spectra, and not during the course of the reaction. Use of such a standard allows for the determination of the mass balance of the reaction being studied. No calibration is required when using NMR for quantification as the peak integral is directly proportional to the concentration as all nuclei being studied are observable by the spectrometer.

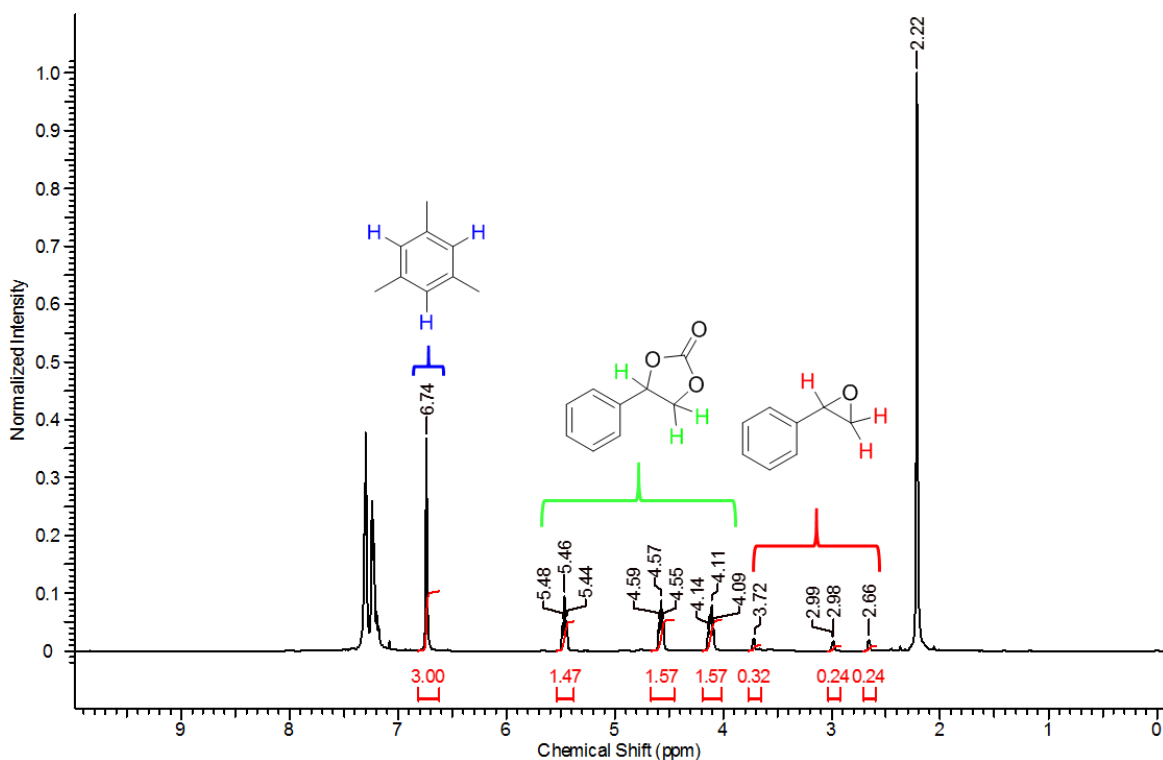


Figure 28: ^1H NMR spectra of the reaction of styrene oxide to styrene carbonate, with mesitylene added following the reaction.

The calculation of conversion and selectivity values was undertaken with the following methodology for the work undertaken in Chapters 3 and 4. A known mass of ITSD was added to the reaction mixture and was assumed to be well mixed throughout, an aliquot was taken, centrifuged and the supernatant analysed. Unless explicitly stated deuterated chloroform (CDCl_3) was used as the NMR solvent. Mesitylene was used as the ITSD as it has only two proton environments which can be reliably measured and do not overlap with either of the product or starting material peaks, see Figure 28. The aromatic peak, 6.8 ppm, was selected as the ITSD peak to be integrated. The labelled peaks for the epoxide and cyclic carbonate are shown on Figure 28, all three peaks are integrated for both and the values averaged. For mesitylene the peak *circa* 6.8 ppm equates to three protons and so the integral is divided accordingly and the ratio between that value and the cyclic carbonate and epoxide integrals used. The molar quantity of each is then calculated as follows.

The mass of the ITSD was set as an absolute value.

$$A \text{ (mol)} = \text{ITSD (mol)} \times \left(\frac{nH \text{ (ITSD)}}{nH \text{ (A)}} \right) \times \left(\frac{\text{integral (A)}}{\text{integral (ITSD)}} \right)$$

Equation 15: Means to determine moles of A within an NMR solvent, given the moles of the ITSD, the integrals ITSD and A and the number of protons (nH) for each.

As per Equation 15, the moles of A are obtained through accounting for by the value of the integral and the number of protons present in the environment of each peak. The moles of the ITSD is required for the calculation, therefore the accuracy of the weighing and the assumption the resulting solution is well mixed are key. Two values for conversion are obtained. One is conversion based upon the amount of the starting material weighed into the reaction vessel. The other is normalised conversion, which is the sum of the moles calculated from Equation 15 applied to all components identified within the reaction mixture. The difference between the total moles in each case is the mass balance for the reaction. The conversion values reported in this work as determined by NMR are normalised conversion values.

Purity and structure of synthesised materials in the work was determined using NMR with chemical shift, integral and splitting pattern used in order to identify the compounds produced. For analysis, see synthetic techniques (section 2.1 and Chapter 3)

2.2.5.1 NMR equipment details

Nuclear Magnetic Resonance (NMR) experiments were performed with a Bruker AVII400 FT-NMR Spectrometer. Experimental ^1H spectra were acquired in CDCl_3 solvent with TMS serving as

internal standard ($\delta = 0$) at 400 MHz (9.4 T) at room temperature, for all samples. Spectra were processed using ACD Labs ^1H NMR Processor Software.

2.2.6 Solid state NMR

NMR is a highly useful technique for investigation of the chemical environments within solid materials as well as solutions. Solid state NMR follows many of the same principles to solution NMR and can be used to study nuclei with nuclear angular momentum spin quantum number, I , that is greater than zero. However, unlike in solution NMR where the anisotropy is overcome due to the averaging caused by the random movement and rotation of the sample, thus a spectra containing sharp transitions is observed, this is due does occur in solid materials.

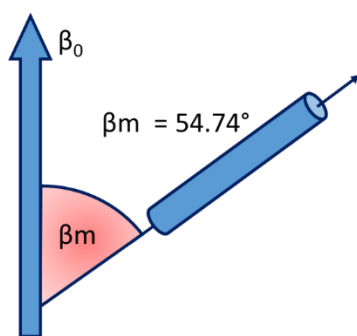


Figure 29: Depiction of magic angle spinning NMR

In a solid sample the lack of random motion leads to very broad, often indistinct spectra to be collected. Magic Angle Spinning (MAS) NMR is used to overcome this in order to collect sharp, well resolved spectra. The broadening of the signal due to the lack of sample orientation towards the magnetic field is solved by MAS NMR by spinning the sample at a specific angle. The magic angle, 54.74° , derives from the value of θ required to satisfy $3\cos^2\theta - 1 = 0$. With this orientation the average angular dependence goes to zero and allows for the sharpening of the NMR peaks allows for collection of NMR spectra of solid samples with comparable resolution to that of solution NMR^[218].

Unlike solution NMR the concentrations within solids, such as organocatalysts on silica, are sometimes very low so difficult to detect. In cases like these, cross polarisation (CP) can be used to achieve better peak resolution. When protons are present within a sample they can be used to boost the signal for other studied nuclei. The application of electromagnetic radiation to the protons is transferred onto the nuclei to be observed and signals are then enhanced. This method unfortunately prevents any quantitative measurement as the peak integral will no longer be directly proportional concentration, having been boosted.

Solid state NMR is then key to the characterisation of catalysts and particularly for organocatalytic materials which have been covalently bound to silica^[219,220]. Collection of ^{29}Si spectra allows for the detection of the Si-C environment which is indicative of covalent anchoring of the organic moiety to the support. This environment is significantly shifted from the bulk silica peaks, Table 12.

| Environment | Chemical shift / ppm |
|-------------|----------------------|
| Si-O-Si | -110 |
| Si-OH | -100 |
| Si-C | -50 to -75 |

Table 12: ^{29}Si chemical environments and characteristic chemical shifts, chemical shifts are approximate for reference and based upon those from Chapter 3 and those reported by Baccile *et al*^[221].

The Si-C peak position is given as a range as the exact value depends on the number of the methoxy groups which are displaced. ^{13}C NMR is also commonly collected with solid state NMR, and can be interpreted in an analogous manner to solution based ^{13}C .

2.2.6.1 MAS NMR Equipment details

EPSRC UK National Solid-state NMR Service at Durham undertook the ^{29}Si and ^{13}C NMR experiments on the silica based materials.

2.2.7 Ultraviolet – Visible Spectroscopy (UV-vis)

Ultra-Violet – Visible Spectroscopy (UV-vis) is the monitoring of the absorption of visible and ultraviolet electromagnetic radiation (200 – 800 nm) which can provide valuable information on materials such as oxidation state and molecular structure. The transitions observed correspond to the transition of an electron between electronic energy levels and can be metal-metal, ligand to metal or metal to ligand charge transfers. For a transition to occur it must be allowed by the spin and Laporte selection rules. The spin selection rule states that a spin allowed transition does not change the multiplicity and the Laporte selection rule that the only allowed transition in a centrosymmetric molecule must be accompanied by a change in parity, this rule is disregarded for tetrahedral complexes. The UV-vis spectra of inorganic compounds, such as transition metal (TM) complexes, originate from electronic d-d transitions. As a gaseous species the d orbitals of a metal are degenerate, when ligands are coordinated to the metal splitting of the orbitals occurs dependent on the geometry and the ligand. The largest gap between the now different energy

orbitals is known as the crystal field splitting, Δ . The greater Δ , the greater the energy (E) needed to promote the electrons therefore the shorter the excitation wavelength, λ , which is required to cause the promotion to occur. The size of the crystal field splitting depends on the nature of ligand. Ligands are ordered by crystal field splitting by means of the spectrochemical series.

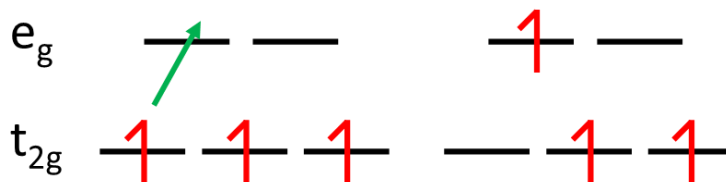


Figure 30: Schematic representation of a d-d transition in d^3 Cr(III).

For the d^3 system, as per MOF MIL-101(Cr(III)), a d-d transition can occur from any one of the t_{2g} orbitals (d_{xy} , d_{xz} and d_{zy}) to the e_g (d_{z^2} and $d_{x^2-y^2}$) set, Figure 30. Transitions are low in intensity as they are forbidden by the Laporte selection rule. For Cr(III) two d-d transitions are observed in the UV-Vis spectra. Filling of the d_{z^2} causes electron density to increase further in the z axis orientated orbitals, so electron repulsion is increased and promotion requires higher energy^[222].

UV-vis was used to study both the UiO-66(Zr) and MIL-101(Cr) MOF systems. For MIL-101(Cr) there are two transitions observed in the UV-Vis spectra, for UiO-66 there are no transitions as it is a d^0 species, the amine version has a transition relating to nonbonding to antibonding molecular orbital electronic transition of the linker, gold nanoparticle were deposited onto UiO-66 which themselves are detectable *via* UV-vis. The typical peaks and their positions for these materials are shown in Table 13 below to aid discussion in later Chapter.

| Material | Peak | Peak position / cm^{-1} (nm) | Ref |
|------------------------|---|---------------------------------------|-------|
| MIL-101(Cr) | d-d transition (${}^4A_{2g} \rightarrow {}^4T_{2g}(F)$) | approx. 18000 (555) | [223] |
| | d-d transition (${}^4A_{2g} \rightarrow {}^4T_{1g}(F)$) | approx. 23000 (434) | [223] |
| UiO-66-NH ₂ | n to π^* (Ligand to ligand) | 30395 (329) | [224] |
| Gold Nanoparticles | SPR (size dependent) | 19230 - 17241 (520-580) | [225] |

Table 13: Summary of UV-vis peak positions for MIL-101(Cr), UiO-66-NH₂ and Au NPs.

2.2.7.1 UV-vis equipment details

UV-vis-NIR of the MIL-101(Cr) material were collected by Enrica Gianotti, Chiara Ivaldi and Ivana Miletto in Alessandria, Italy. Diffuse Reflectance UV-Vis-NIR spectra were recorded using a Perkin Elmer Lambda 900 spectrometer equipped with a diffuse reflectance sphere attachment, using

specially designed cells permanently connected to a vacuum line to perform adsorption-desorption in situ measurements.

The remaining UV-vis spectra were collected using specially a modified sample holder on the UV-Visible-NIR Range Microspectrophotometer, CRAIC Technology QDI2010.

2.2.8 Fourier Transform – Infrared Spectroscopy (FT-IR)

FT-IR spectroscopy allows for the observation of different chemical environments. It can be employed to either directly analyse the sample in question or in combination with a probe molecule in order to identify certain characteristics of a material. A sample is irradiated with radiation in the infrared (IR) region, between $4000 - 400 \text{ cm}^{-1}$ which causes the excitation of the molecule leading to vibrations of the covalent bonds which are present. A vibrational mode is observable *via* FT-IR only if the vibrations that occur change the dipole moment. The energy of the transition is determined through use of the Schrödinger equation, solved for a diatomic example of the harmonic oscillator, whereby $\nu_m = \frac{1}{2\pi c} \sqrt{\frac{k}{\mu}}$ and μ (the reduced mass of each end of the bond in question) $= \frac{m_1 m_2}{m_1 + m_2}$.

$$E_n = (v + \frac{1}{2})h\nu_m$$

The vibration frequency is dependent on the masses of the two atoms on either end of the bond so leading to the force constant of the bond (k), see Figure 31. The frequency, ν_m , will be high when the bond is rigid and so has a large k value but also when the effective mass of the oscillator is low. Frequencies of vibrations measured can be related to different functional groups as each functional group will have specific masses and bond lengths, impacting vibration frequency. Typically conversion of the frequency to wavenumbers plotted against the absorbance value which was measured at the point^[222].

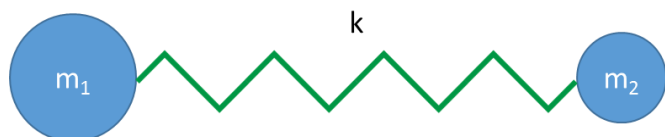


Figure 31: Hooke's Law whereby a diatomic molecule is seen to be two masses, m_1 and m_2 connected by a spring with a force constant of k .

Description of different stretches uses the following nomenclature with typically the bond being referenced being in brackets e.g. (X-Y). and the type of stretch proceeding it. For this body of work the following are used to describe stretch type, Table 14.

| Vibrational modes | Symbol |
|-------------------|------------|
| Symmetric | ν |
| Asymmetric | ν_{as} |
| Bending | δ |
| in/out of plane | γ |

Table 14: Nomenclature used to describe different stretching modes.

FT-IR can be used in collaboration with a probe molecule which allows for certain characteristics of the material to be studied. For the work undertaken the Lewis acidity of the MIL-101(Cr) is of interest and so deuterated acetonitrile (CD_3CN) is employed as a probe molecule to study the alteration of Lewis acidity between different samples. Acetonitrile used due to the medium strength Lewis base character which promotes interaction with Lewis acid sites. The deuterated version is used due to the Fermi resonance effect associated with CH_3CN that splits the peak into two components and makes deconvolution difficult^[226].

The shift of the $\nu(C\equiv N)$ is observed to determine Lewis acid strength. The nitrogen electron acts as a Lewis base and therefore the position of the band alters depending of the strength of the interaction. For example, the $\nu(C\equiv N)$ wavenumber increases upon a strong interaction with a Lewis acid up to a shift of maximum 75 cm^{-1} ^[227]. Monitoring of the shift can determine the strength of a Lewis acid site.

To aid discussion in later sections, some of the key vibrations which are relevant to the synthesised materials as reported in the literature or recorded are detailed below.

| Material | Vibration | Wavenumber / cm^{-1} | Ref |
|-----------------|---|-------------------------------|-------|
| NHC- CO_2 | $\nu(CO_2)$ | 1662 | [228] |
| Imidazole | $\nu(C-H)$ | 3118 | - |
| UiO-66- NH_2 | ν and $\nu_{as}(NH_2)$ | 3515 and 3390 | [229] |
| | $\delta(NH_2)$ | 1629 | [229] |
| | $\nu(C-N)$ | 1340 and 1257 | [229] |
| Carboxylate MOF | $\nu_{as}(COO)$, $\nu_s(COO)$ and $\nu(C-C)$ | 1800 - 1300 | - |

Table 15: Summary of key IR vibrations and peak positions.

2.2.8.1 FT-IR equipment details

Fourier Transform – Infrared Spectroscopy (FT-IR) spectra of the MIL-101(Cr) material were collected by Enrica Gianotti, Chiara Ivaldi and Ivana Miletto in Alessandria, Italy. Spectra of self-supporting pellets were collected under vacuum conditions (residual pressure <10⁻⁵ mbar) using a Bruker Equinox 55 spectrometer equipped with a pyroelectric detector (DTGS type) with a resolution of 4 cm⁻¹. CD₃CN was adsorbed at room temperature using specially designed cells that were permanently connected to a vacuum line to perform adsorption-desorption in situ measurements. FT-IR spectra were normalised with respect the pellet weight and, whenever specified, are reported in difference-mode by subtracting the spectrum of the sample in vacuum from the spectrum of the adsorbed molecules.

All other FT-IR spectra were collected using KBr discs and analysed on a Perkin Elmer Spectrum 2000, between 400 – 4000 cm⁻¹ at a resolution of 4 cm⁻¹. Samples were degassed prior to analysis.

2.2.9 X-ray Photoelectron Spectroscopy (XPS)

XPS is a surface sensitive technique which can be used to identify the elements present within a sample (Li-U detectable). Information on the chemical environment in which the respective element exists can be found. XPS is a surface sensitive technique, therefore only analyses the composition of the sample to a maximum sampling depth of 10 nm, max penetration.

XPS occurs with the bombardment of a sample, in ultra-high vacuum, with x-rays sufficient in energy to eject electrons, typically from the inner core of the element. The x-rays are of a specific wavelength that results in the emission of photoelectrons. If the energy is sufficient, the electron will be ejected with quantifiable kinetic energy (KE) that is then measured by the instrument. The overall KE of an ejected electron will be equal to the energy of the incident photon minus the binding energy (BE), as this is required to be overcome for ejection to occur, generally binding energy is reported as this is more useful, see Equation 16.

$$BE = h\nu - KE - \phi$$

Equation 16: Determination of binding energy (BE) of the ejected photoelectron where $h\nu$ is the incident photon energy (h = Planks constant, ν = frequency), KE is the kinetic energy of the ejected photoelectron and ϕ is the work function of the spectrometer.

The binding energies obtained in XPS are highly specific to the electron which was emitted from the nucleus. The peaks resulting from the emissions are assigned spectroscopic labelling based on the respective quantum numbers related to the electron emission, and are thus related to orbital splitting. The spectroscopic notation of a peak is denoted in the form $n\ell j$ where n is the principal

quantum number, l is the angular momentum quantum number (a value for l of 0 = s, 1 = p, 2 = d etc.) and j is the spin-orbit coupling. Peaks are observable as doublets for p, d and f shells (as these energy levels have non-zero angular momentum quantum numbers. The ratios between the sizes of the doublets are seen as $p = 1:2$ $d = 2:3$ and $f = 3:4$ and occur due to spin-orbit coupling.

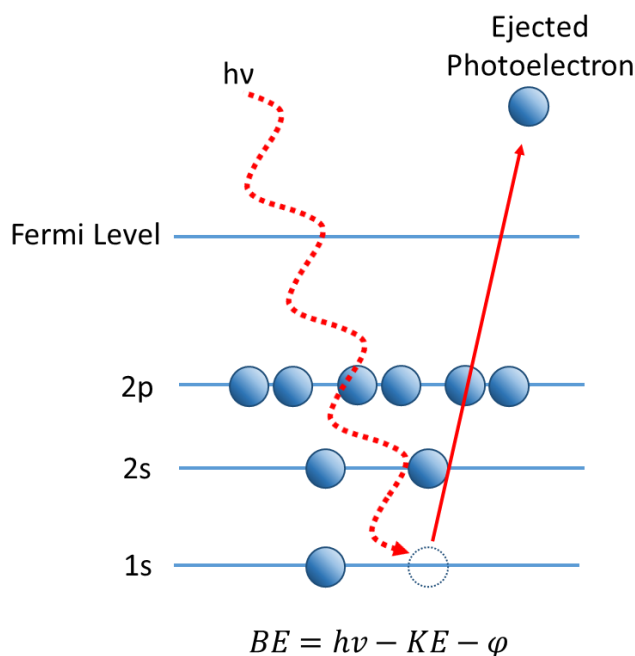


Figure 32: Representation of photoelectron emission from the 1s level.

As such, properties that affect the binding energy of an electron - oxidation state for example - can be probed. The energy of a core level electron within an atom is highly specific to that element, therefore the unique energy of the ejection allows for elemental detection. The nature of the chemical bonding of that specific element is obtained from the subtle differences which the bonding imparts on the binding energy. Therefore, within the binding energy region of an element the position of the peak will shift determinably dependent on oxidation state.

Binding Energy (BE), usually plotted for XPS, is inversely proportional to the KE as it allows for comparison between different instruments – the KE is dependent on the source. It is normal to plot the x-axis in reverse order as then the binding energy increases away from the KE 'zero'. Survey spectra are low resolution scans over the entire spectrum of the KE of a photoelectron, Figure 33. Higher resolution scans are then collected of the specific KE regions applicable to each element observed within the survey scan in order to allow for discrete peaks to be resolved.

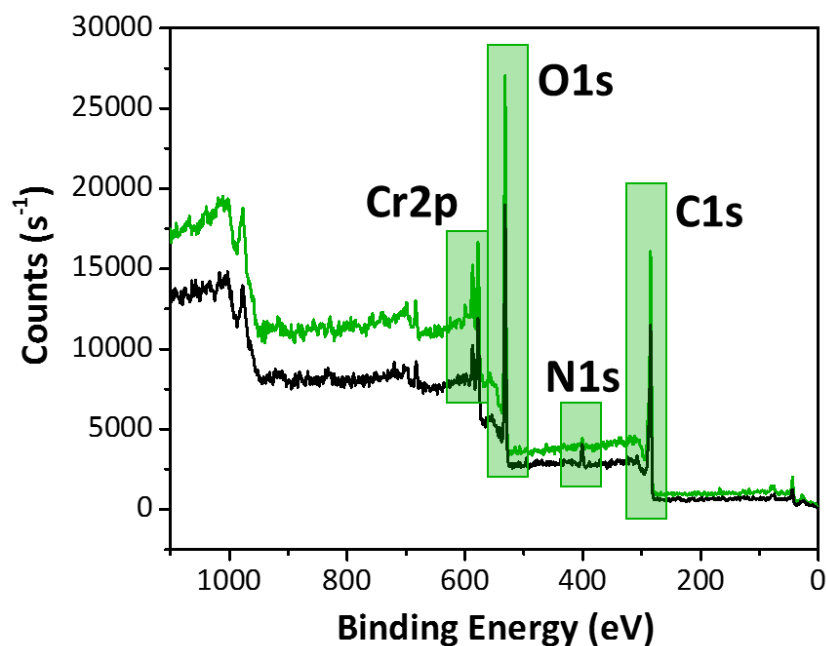


Figure 33: Exemplar XPS spectra displaying Cr2p, O1s, N1s and C1s peaks as labelled.

Besides the determination of the elements present and the chemical state of them, the amounts of each element within a sample can be quantified. The intensities of the signals relating to individual elements relative to one another enables their percentage in the sample to be calculated. Elemental analysis calculations *via* XPS requires that the peaks are represented by a mathematical equation that can be used to define the peak height, area and full-width half maximum (FWHM), a process known as fitting. Fitting undertaken in this work had the following applied to each sample: for the energy splitting between peaks of a doublet the splitting value was forced according to literature, but the peak positions allowed to vary; the ratio between peaks was held constant according to the multiplicity of the spin-orbit state and finally the FWHM maximum of peaks within a region was fixed but allowed to vary across different samples with the same region. The high resolution spectra were fitted with linear and Shirley backgrounds before peak analysis.

2.2.9.1 XPS equipment details

For this work XPS was used for elemental detection and oxidation state identification. A Thermo Scientific Theta Probe XPS equipped with a monochromatic Al K α X-ray ($h\nu=1486.7$ eV) source was employed for the collection of spectra. The x-ray spot size 400 μm in diameter with an x-ray incident angle fixed to 30° relative to the surface. For the survey scans were the step was 1 eV with a pass energy of 200 eV. The higher resolution scans of specific regions step = 0.1 eV and pass energy = 40eV. The Advantage software package was used to analyse the XPS data and undertake peak fitting.

2.2.10 Gas Chromatography (GC)

Gas chromatography (GC) is a technique which separates out the components of a mixture in the gas phase allowing for them to be individually identified and quantified. The separation of the components employs both a stationary phase, the column, and a mobile phase, the carrier gas. As shown in Figure 34 the sample is injected into the injector port, typical held at a sufficiently high temperature to vaporise the majority of the component mixture to be analysed, from which it is carried into the oven by the carrier gas (He) flow.

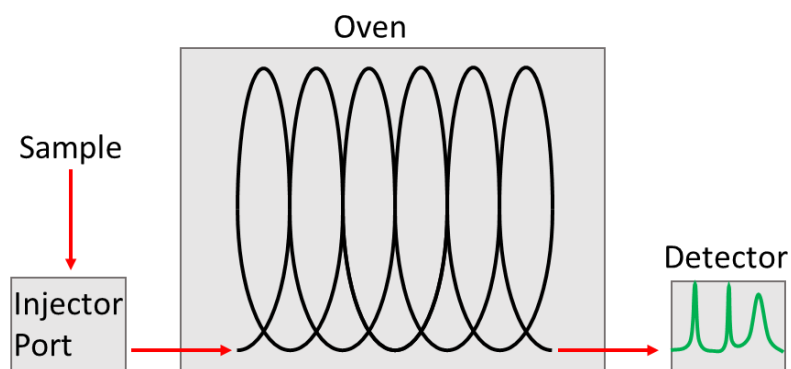


Figure 34: Schematic of Gas Chromatography system

Upon entrance to the oven the components pass through a pre-column which removes any high boiling point species which would have sufficient retention to not pass through the main column. Once at the column the mixture will separate due to boiling point and interaction with the column, stationary phase. Transported by the carrier gas the species within the injected mixture will elute typically in order of boiling point as separated entities. Species exiting the column enter into the detector of choice. A flame ionisation detector (FID) operates through the detection of ion which occur during the combustion of an organic compound, the signal given off is then a related to the amount of the compound within the mobile gas stream and allows for each, now separate, component within what was previously a mixture, to be quantified.

Unlike techniques such as NMR whereby the signal received by the instrument is proportional to the concentration of the entity providing it, GC requires calibration in order for quantitative analysis. In GC analysis, two compounds of different structure but equimolar amount will not provide the same signal from a FID – be it the peak height or peak area of the response. Therefore the peak area (the more accurate indicator of signal value than peak height) to molar ratio seen is differently for most compounds at the fluctuation in current is proportional to the rate of ionisation the value of which is determined by the concentration of the component and its ionisation potential. Back calculation of molar quantities within samples can be achieved then

following the construction of a calibration curve to discover the retention factor (R_f) of each component.

Calibration of the GC was undertaken as follows so enabling the monitoring of reaction progression over time.

| Sample Code | Cinnamyl Alcohol (C) | | Internal Standard | | Molar ratio |
|-------------|----------------------|-------------|-------------------|-------------|-------------|
| | mass (g) | moles (mol) | mass (g) | moles (mol) | C/IS |
| 7696-24-C1 | 0.0227 | 0.000169188 | 0.0582 | 0.000517058 | 0.327213744 |
| 7696-24-C2 | 0.0465 | 0.000346575 | 0.0631 | 0.00056059 | 0.618233107 |
| 7696-24-C3 | 0.0882 | 0.000657375 | 0.0462 | 0.000410448 | 1.601604477 |
| 7696-24-C4 | 0.101 | 0.000752776 | 0.0509 | 0.000452203 | 1.664685728 |
| 7696-24-C5 | 0.1552 | 0.001156741 | 0.047 | 0.000417555 | 2.770272709 |

Table 16: Analyte and internal standard masses and corresponding molar quantities then converted to ratio. C and IS in this instances relate to cinnamyl alcohol and internal standard respectively.

| Peak Area 1 | | Peak Area 2 | | Peak Area 3 | | Average | | Peak Ratio |
|-------------|------------|-------------|------------|-------------|------------|------------|------------|------------|
| C | IS | C | IS | C | IS | C | IS | C/IS |
| 610322.98 | 3112860.12 | 624834.98 | 2830485.50 | 573026.28 | 2719100.35 | 602728.08 | 2887481.99 | 0.2087383 |
| 1038538.30 | 2968259.40 | 1099097.83 | 2965869.41 | 1164480.37 | 2912846.91 | 1100705.50 | 2948991.91 | 0.37324806 |
| 1875587.31 | 2127669.22 | 1941465.96 | 2102312.00 | 2000727.77 | 2063582.24 | 1939260.35 | 2097854.49 | 0.92440174 |
| 2147675.50 | 2318256.08 | 2121235.70 | 2266414.73 | 2145365.58 | 2229101.64 | 2138092.26 | 2271257.48 | 0.94136938 |
| 3122905.99 | 1992277.02 | 3238548.39 | 1958156.95 | 3112694.55 | 1924643.67 | 3158049.64 | 1958359.21 | 1.61259978 |

Table 17: Peak area responses for triplicate measurement of each calibration solution and calculated peak ration of analyte to standard. C and IS in this instances relate to cinnamyl alcohol and internal standard respectively.

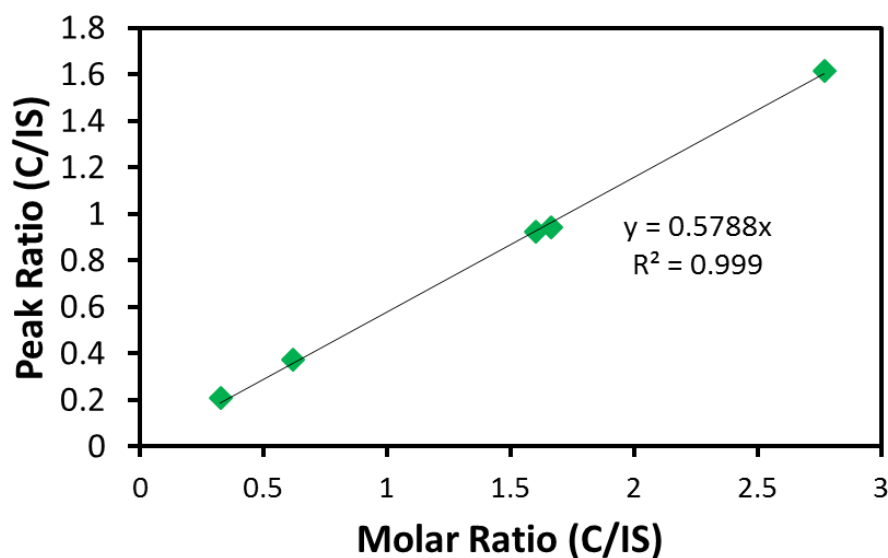


Figure 35: Example calibration curve based off the data displayed in Table 16 and Table 17, where

In this work, GC is used predominantly for analysing samples of catalysis reactions by monitoring conversions of starting materials and yields of products. Quantitative analysis is facilitated by performing calibrations with an internal standard to determine response factors (R_f) of each component in the system. A graph of peak area ratios against molar ratios, Figure 35, gives a straight line where the gradient is the R_f . This value can then be applied in the following two equations to determine the moles of the desired component as follows.

$$\frac{\text{peak area (A)}}{\text{peak area (IS)}} = R_f \frac{\text{moles (A)}}{\text{moles (IS)}}$$

Equation 17: Relationship between peak areas of and moles of components adjusted by the R_f value. A and IS stand for analyte (to be determined) and internal standard respectively.

Therefore Equation 17 rearranged leads to the following, Equation 18, whereby the moles of the component to be studied can directly calculated. The use of the internal standard allows also for the mass balance of the reaction to be studied giving an indication of the percentage of the total compounds detected and analysed.

$$\text{moles (A)} = \frac{\text{moles (IS)} \times \text{peak area (A)}}{R_f \times \text{peak area (IS)}}$$

Equation 18: Rearranged equation to find the concentration of an analyte from the peak area response recorded with R_f value applied. A and IS stand for analyte (to be determined) and internal standard respectively.

This was the main method used for the quantification of components in the reactions undertaken in Chapter 5 and so determination of the conversion and selectivity of the oxidation and Knoevenagel reactions studied.

2.2.10.1 GC equipment details

Samples were analysed by GC-FID (Gas Chromatography-Flame Ionisation Detector) using a Perkin Elmer Clarus 480 fitted with an autosampler. Components were identified against known commercial standards where possible.

2.2.11 Gas Chromatography-Mass Spectrometry (GC-MS)

A Mass Spectrometer (MS) is commonly coupled to a Gas Chromatography system resulting in a GC-MS. Mass spectrometry detectors are highly useful, particularly in the detection of by-products from reactions – especially oxidation reactions. A GC-MS fundamentally consists of a MS which is attached to the gas outlet of the GC creating the coupled system.

A quadrupolar MS instrument works as follows. It has four rods which are set up to have opposing rf and dc fields on the oppositely positioned rods. As the ions enter, they pass down the chamber passing between each of the four rods which are having voltages swept. Sweeping of the voltages separates the ions based on m/z values, whereby M is the mass and Z is the charge number of the ion, as the vast majority of the ions are singly charge then then ions are separated by their mass. The outlet gas stream enters the ion chamber *via* an ion source which is continually analysed. As each, now separated, component exits the column, an increase in ions is detected and so results in a peak which has associated mass spectrum corresponding to the ions detected. As each compound will fragment differently dependent on its structure then the pattern displayed in the mass spectra, along with the highest m/z value can identify compounds and is particularly useful for unknown determination^[230,231]. GC-MS was employed for the qualitative determination of by-products for oxidation reactions as the MS software used had access to the NIST database for referencing.

2.2.11.1 GC-MS equipment details

GC-MS analysis was undertaken by manual injection (2 μ L) into a Agilent Technologies 7890A GC system with a boiling point column which was coupled to an Agilent Technologies 5975C inert MSD. Components were identified against known commercial standards where possible.

2.2.12 Electron Microscopy

Imaging of samples is important in catalysis in order to better understand key principles such as structure property relationships. For samples of very small size, optical microscopy is not possible, and so electrons are utilised instead. Electron microscopy provides far greater resolution owing to the much smaller wavelength of the electrons. Consequently, the resolution of electron microscopy is limited by the wavelength of the electron, also known as the de Broglie wavelength.

$$\lambda = \frac{h}{p}$$

Equation 19: The de Broglie equation where h is Planck's constant, and p is the relativistic momentum of the electron and λ is the wavelength.

As seen in Equation 19, the momentum of the electron is important, therefore through acceleration of the electron an increase in the resolution is obtained through the decrease of the wavelength and, in so doing shapes and sizes of samples down to the nanometre scale can be resolved.

2.2.12.1 Scanning Electron Microscopy (SEM)

Scanning electron microscopy (SEM) is an imaging technique which allows the size, morphology and in some cases topology of materials to be determined. It is a powerful tool which allows the sample in question to be visually observed and can be especially usefully for catalysis to correlate size and shape characteristics to catalytic activity.

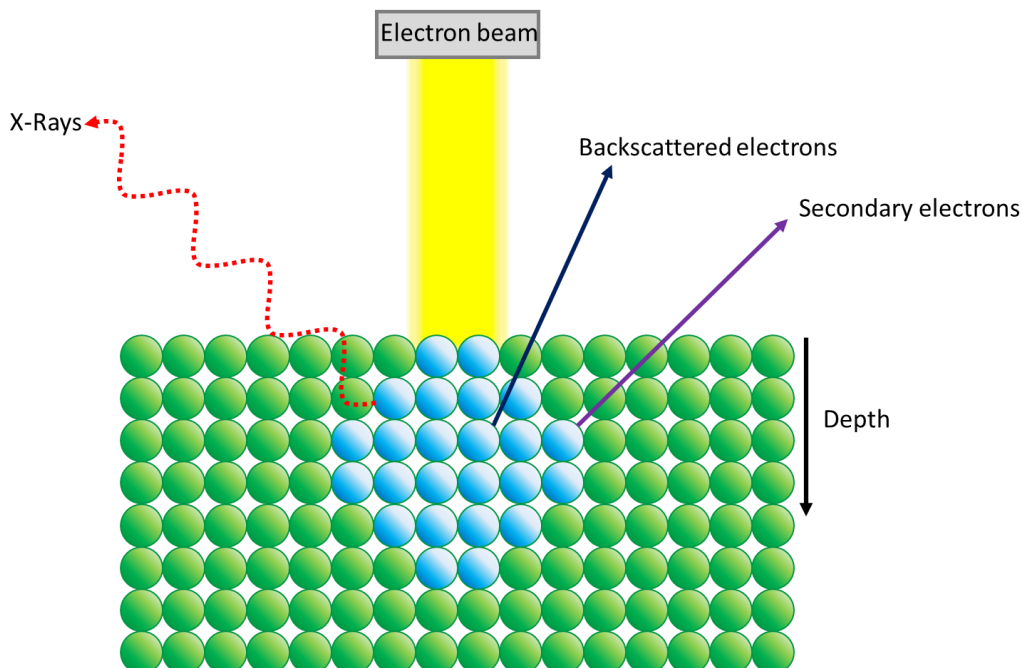


Figure 36: Schematic representation of scanning electron microscopy

A focussed electron beam scans over the sample and in so doing an image of the subject is created *via* the detector. The bombardment of the surface with the electrons of 5-50 keV with a spot size of 5-50 nm causes a variety of signals to be returned as the sample is scanned to a depth of up to 1 μm – x-rays, backscattered and secondary electrons. Of these the emission of secondary electrons is most important and occurs when the electron beam causes emission of the valence electrons. The energy of the secondary electrons is small, thus only the surface emissions are seen as those expelled within the bulk are re-absorbed. This allows for the surface characteristics of the sample to be determined. The most common method of detection is known as secondary electron imaging (SEI) and uses these low energy electrons. As the surface of a sample changes with respect to the electron beam, the shape of the electron penetration, Figure 36, alters. This produces a change in the number of secondary electrons which are detected, with the lowest amount when the sample surface is orthogonal to the electron beam and highest when the sample is angled. The change in the secondary electron quantities across a sample is seen as contrast, producing an image. For this to happen the sample must be conductive and so it is commonplace to sputter samples with gold prior to imaging to aid this. Lack of conduction within a sample leads to charging and image distortion.

SEM images were collected of the MOF samples which were synthesised and subsequently modified in the latter chapters of this work. The size of a material can profoundly alter catalytic ability thus collection of SEM images aided the MOF discussions in Chapters 4 and 5 which employ post synthetic modification techniques in order to manipulate the properties of framework. Key to this is that the modification stage does not meaningfully alter the framework which SEM imaging can be used to determine.

2.2.12.1.1 SEM Equipment details

Scanning Electron Microscopy (SEM) was conducted on JEOL FESEM JSM6700F using carbon tape and 20 second gold sputtering to aid imaging.

2.2.12.2 Transmission Electron Microscopy (TEM)

TEM is used when the size of the sample to be studied has sizes that are sufficiently small that they exceed the capabilities of SEM magnification. This is particularly useful when studying metal nanoparticles with sub 10 nm dimensions that are commonly employed for oxidation processes.

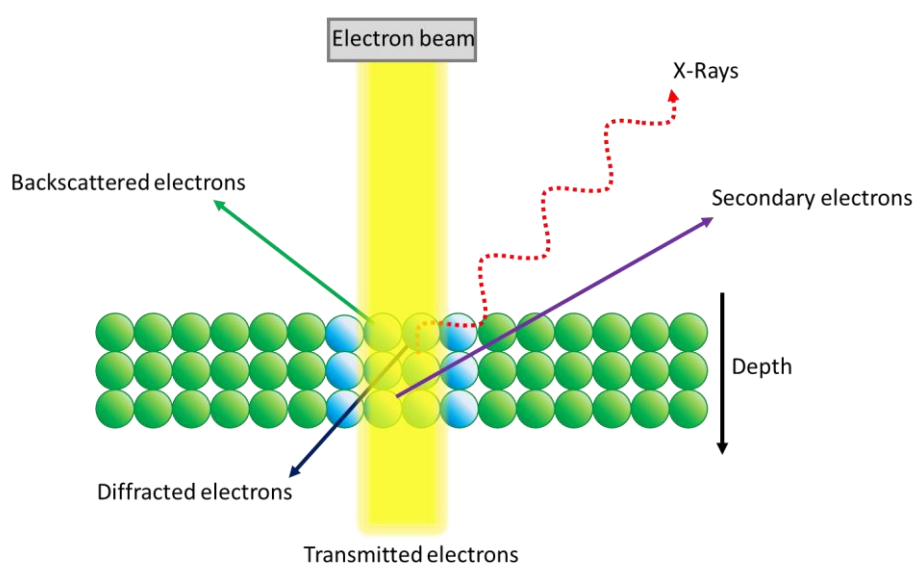


Figure 37: Electron beam transmission through a sample with depiction of different electron scattering occurrence.

TEM is similar to SEM except that it analyses the transmitted electrons through the sample, rather than those which are reflected. In order for transmittance to occur the sample has to be relatively thin and so generally sample of small, 200 nm or less, size is investigated. Lighter elements will allow for a greater proportion of the electron beam to pass through, unaltered to impinge on the detector and emit a photon, building an image. Therefore, the heavier the element the darker that part of the image as a smaller amount of the electron beam will pass through, see Figure 37.

For the work in Chapter 5 then, where nanoparticles of Au, Pd, and Pt were investigated for oxidation ability, TEM was useful. The heavier elements of the nanoparticles *versus* the MOF meant allowed for them to be visualised and quantified for size. This was critical to evaluating performance as it is intrinsically linked to the size of nanoparticle.

2.2.12.2.1 TEM Equipment details

TEM images were collected with the help of Hui Rui Tan at IMRE using the Philips CM300 FEGTEM instrument with samples prepared by suspension of the MOF in methanol and then dispersing onto a carbon coated copper TEM grid.

2.2.13 Inductively Coupled Plasma – Optical Emission Spectroscopy (ICP-OES)

ICP-OES analysis was undertaken by Medac Ltd. In order to undertake the calculation of TON is vital to know the concentration of the catalytic species in the material to be studied. The elemental composition of the catalyst can be determined by the use of ICP-OES in order to determine the ratios between the different elements present. Prior to analysis the materials are digested by a strong acid in order to break apart and dissolved the sample. The solution containing a known amount of the sample is then propelled into an Argon plasma as an aerosol. The high temperature plasma causes the excitation of the atoms present within the sample which subsequently emit photons upon relaxation which are specific to the energy levels of the excited element, allowing it to be identified. The intensity of the signal will be proportional to the concentration of each element within the solution, therefore in combination with an appropriate calibration curve and the mass of the sample used quantitative analysis is achievable.

2.2.14 Elemental Analysis

Carbon, hydrogen, nitrogen and sulphur (CHNS) elemental analysis was undertaken to calculate the loading of the imidazole and imidazolium species on MIL-101(Cr) and silica/HP materials respectively. To determine the amounts present a sample of known mass is burned at 900 °C within a high oxygen atmosphere in order to produce the combustion products of CO₂, H₂O, NO or NO₂, and SO₂. The combustion products separated in by gas chromatography before entering a thermal conductivity detector which measures the amount of each, by changes in the thermal conductivity of the column output with respect to a reference flow of carrier gas (He or Ar). The thermal conductivity will be reduced when an analyte passes through the gas flow and so can be accordingly detected with the use of a reference material and a calibration.

2.2.14.1 EA equipment details

Elemental Analysis was collected on Thermo Scientific Flash EA 1112 Series (CHNS), with sulfanilamide used as the standard for calibration purposes. Samples analysed during work undertaken in Southampton were analysed by Stephen Boyer of London Metropolitan University.

2.2.15 Electron Paramagnetic Resonance (EPR) Spectroscopy

Electron paramagnetic resonance is a useful tool if the sample to be studied contains unpaired electrons within the system. As such, free radicals, triplet states and transition metals with odd numbers of electrons can be studied. Electrons have spin angular momentum, as per 2.2.5, which generates a magnetic field. EPR uses microwave radiation to promote transitions between energy levels. Unlike typical spectroscopy techniques where a constant magnetic field is applied and the electromagnetic radiation is then varied, EPR maintains the electromagnetic radiation frequency constant and scans the magnetic field. A signal is then produced when the magnetic field becomes equal to that of the two spin states of the electron, i.e. the energy difference of them matches that of the radiation. An electron is spin $\frac{1}{2}$ therefore the orientations are $m_s = +\frac{1}{2}$ and $m_s = -\frac{1}{2}$ which within the magnetic field become two energy levels: $E_{\frac{1}{2}} = \frac{1}{2} g_e \beta B_0$ and $E_{-\frac{1}{2}} = -\frac{1}{2} g_e \beta B_0$, as shown in Figure 38.

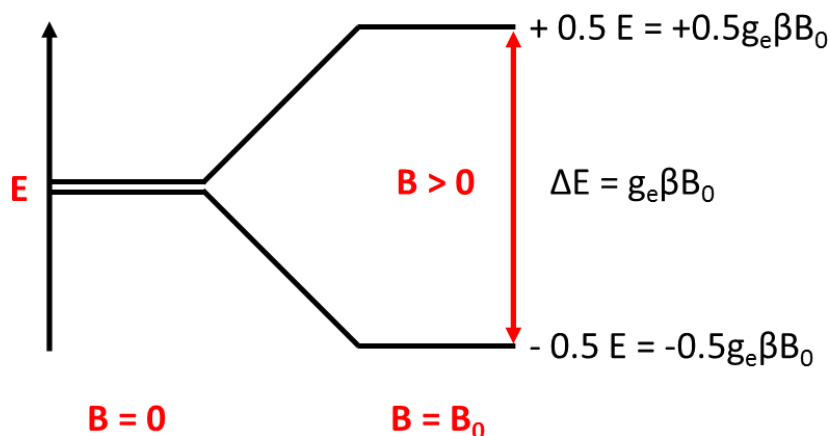


Figure 38: Spin state energies as a function of the magnetic field B_0 , β is the Bohr magneton and g_e is the spectroscopic g -factor.

When within a molecule an electron has orbital angular momentum, approximately zero when in the ground state. Interaction between the ground state and excited states, creates orbital angular momentum to the ground state and so spin-orbit coupling contribution. This is often said to be proportional to intrinsic spin angular momentum and so they are combined to give $\Delta E = g\beta B_0$ as g_e becomes g ^[232]. Determination of the value of g is obtained through rearrangement as $\Delta E = h\nu$, and

β and B_0 are known. In solids the lack of anisotropy means the g-factor changes as the sample is rotated. Ligands around a metal atom will produce a different g-factor if they are unequal. The g-factors are measured along the principal axis system, and are labelled g_x , g_y and g_z ^[233]. For a system where the ligands are equal then $g_x = g_y = g_z$ and the line shape will be sharp as the magnetic moment is equal in all directions, Figure 39. Alteration from this result in change in the line shape, therefore line shape informs on the local environment. G then is comparable to the 'chemical shift' of NMR where it will depend on the particular ion, oxidation state, coordination number and ligands.

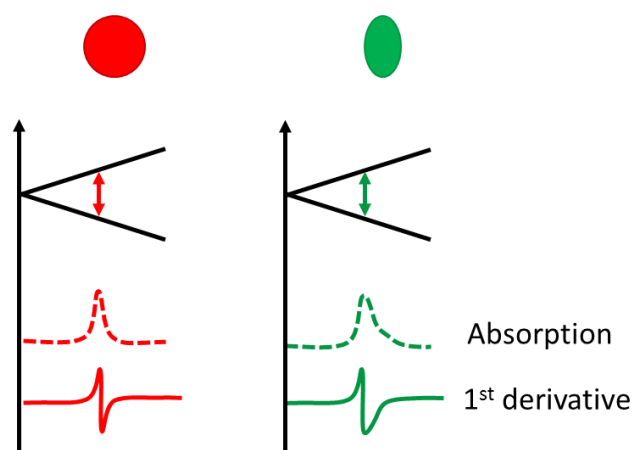


Figure 39: Schematic representation of g tensor and the EPR absorption and 1st derivatives which result from this. Spherical system (red), whereby $g_x = g_y = g_z$ and axial system (green) whereby, $g_x = g_y < g_z$.

EPR is therefore sensitive to alterations in the local environment of the unpaired system being studied. For Cr(III), being d^3 , it has three unpaired electrons, so can be readily observed by EPR. The alteration of the local environment around the chromium differed upon imidazole addition and so was analysed to determine whether, as expected, line broadening occurred. The first derivative of the adsorption is typically shown when presenting EPR data, with the magnetic field strength (B , gauss) as the x-axis as this is varied, and the energy, E on the y.

2.2.15.1 EPR equipment details

Dr Stuart Elliott is thanked for help with the EPR measurements at the University of Southampton. Electron Paramagnetic Resonance (EPR) X-band detected continuous wave (CW) EPR spectroscopy experiments were performed on a Bruker EMX MicroX spectrometer (microwave frequency 9.86 MHz) with built-in frequency counter, at ambient temperature and pressure. Experimental parameters for spectral detection were as follows; microwave power = 1.8 mW, modulation amplitude = 0.1 mT, and modulation frequency = 100 kHz. Spectra were recorded using Bruker Xenon software, and were processed in Mathematica.

Chapter 3 Harnessing silanols for heterogeneous, organocatalytic CO₂ utilisation

Special acknowledgements:

I would like to acknowledge the following colleagues for their collaboration and assistance with the work in this chapter.

Dr Matthew Potter: School of Chemistry, University of Southampton, Southampton, UK. For his help with the testing of carboxylate materials under high pressures.

Dr Stephanie Newland: School of Chemistry, University of Southampton, Southampton, UK. For preparation of the blank HP-AIPO materials used as supports.

Jack Parsons: School of Chemistry, University of Southampton, Southampton, UK. For assistance with collection of kinetic data on butylene carbonate reaction rates.

Prof. Enrica Gianotti: Università del Piemonte Orientale, Alessandria, Italy. For collection of the FT-IR on the HP AIPO based organocatalysts.

The solid state NMR facility at Durham University is thanked for help with the ¹³C and ²⁹Si measurements and their help with analysis and subsequent CP spectra collection.

3.1 Heterogeneous organocatalysts for CO₂ utilisation

Heterogeneous organocatalysts which produce cyclic carbonates from CO₂ and epoxides can most often be placed into one of three general categories: phosphonium salts, ammonium salts and imidazolium salts - including N-heterocyclic systems. The anion is most often a halide. A wide range of supports are present in the literature as well as anchoring methods^[234]. Silica based catalysts are prevalent, owing to the ease of covalent attachment to the silanol (Si-OH) surface functionalities, as discussed in section 1.1.4.1.1 and displayed again in Figure 40 for reference.

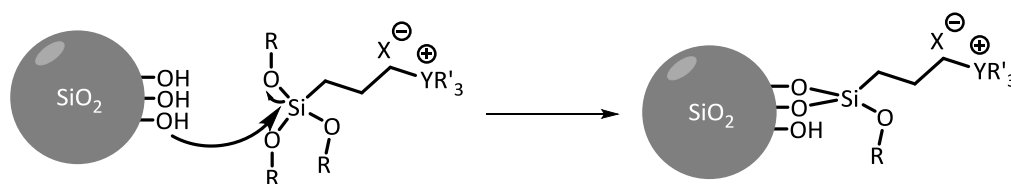


Figure 40: Depiction of silanol functionalisation resulting in covalent anchoring of ionic pair organic moiety to silica. Commonly X = Cl, Br, I and Y = N (can be part of an imidazolium ring) or P.

Heterogeneous organocatalysts have displayed promising results coupled with the traditional benefits associated with a solid catalyst: recyclability, synergy between support and active site and lowered experimental costs^[22]. Additionally, they provide the possibility of undertaking the reaction in solvent, metal and co-catalyst free conditions^[234]. The need for a co-catalyst is largely removed through use of ionic pair species, with the anion commonly initiating the reaction, as per the discussion in Chapter 1. The different categories of heterogeneous organocatalysts have merits and drawbacks to them with imidazolium versions having been reported to show very promising, high activities.

3.1.1 Heterogeneous phosphonium catalysts

Phosphonium based materials mostly rely on the charge balancing anionic species to act as the nucleophile, with the positive phosphonium centre stabilising intermediates. A summary of immobilised phosphorous based materials for cyclic carbonates is detailed in Table 18, with focus on propylene oxide (PO) as the substrate, to aid comparison.

| Cation | Anion | Support | Conditions | | | | Conv (Sel) (%) | Ref |
|-------------------------------|-------|-----------------------------|------------|--------|-----------------------|----------------|-------------------|-----------|
| | | | Cat (mol) | T (°C) | CO ₂ (bar) | t (hrs) | | |
| ^a PBu ₃ | Cl | Polystyrene | 5.0 | 150 | 50 | 6 | 93 (99) | [235] |
| PBu ₃ | Cl | Fluorinated polymer | 1.0 | 150 | 80 | 8 | 99 (97) | [236] |
| PBu ₃ | Br | Silica | 1.0 | 90 | 10 | 6 | 99 (99) | [237] |
| PBu ₃ | I | Silica | 1.0 | 100 | 10 | 1 ^c | 99 (98) | [238] |
| PPh ₃ | Cl | ^d PPIL-co-PEGDMA | 0.2 | 140 | 30 | 3 | 99.6 (100) | [239,240] |
| PPh ₃ | Br | ^e PEG | 5.0 wt. % | 100 | 27 | 3 | 60 (99) | [241] |

Table 18: Overview of supported phosphonium catalysts. ^an-butyl chain. Propylene oxide substrate for all entries. ^cFlow conditions. ^d Poly(4-vinylbenzyl-tributylphosphorous-co-ethylene dimethacrylate). ^ePoly(ethylene glycol). Conv = conversion, Sel = selectivity.

Good yields of propylene carbonate are shown for phosphonium catalysts yet, reaction conditions typically employed involved high temperatures and/or pressures. In many cases, loss of activity was reported over successive cycles, as the halide is required for the key step of epoxide ring opening it is likely loss of this *via* leaching is the main reason for deactivation^[238–240]. Of the polymer supported variants PPIL-co-PEGDMA based phosphonium showed superior activity which was maintained over 5 cycles, the greater activity of PPh₃ over PBu₃ the cause of the increased activity^[239,240]. The fluorous support used by Song *et al* is novel in that it dissolves into scCO₂ so is homogenous during the reaction but ultimately recyclable, so a catalyst which bridges the homogeneous-heterogeneous gap by having merits of both^[236].

Silica based phosphonium organocatalysts display higher activity versus the polymer supported variants and temperatures used are lower. The silanol groups which remain following the anchoring process have been shown to activate the epoxide in a synergistic manner as depicted in Figure 41, and is applicable to other silica supported catalysts^[234,238].

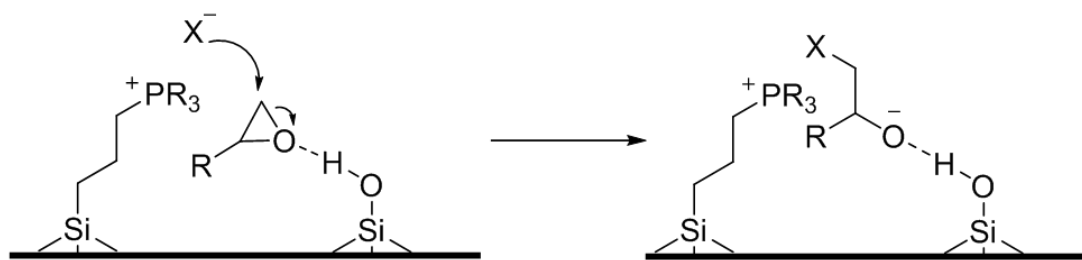


Figure 41: Possible acceleration mechanism on the synergistic hybrid catalyst, proposed by Takahashi *et al*^[238].

This was one of the reasons proposed by Takahashi *et al* to explain the impressive activity over a long timescale which was reported and shows the benefits of a flow reactor based system^[238].

3.1.2 Heterogeneous ammonium catalysts

There are several routes to the production of ammonium based heterogeneous catalysts. As with phosphonium based catalysts the ammonium provides stabilisation of the intermediates, whilst the anion, typically a halide, undertakes ring opening. Recyclable variants were first reported by Du *et al* as well as description of substituents effect with activity following the trend of $\text{NR}_3 > \text{NHR}_2 > \text{NH}_2\text{R} > \text{NH}_2$. Production of the ammonium species upon a solid support, such as silica, is ordinarily completed by one of the following facile processes, Figure 42^[234].

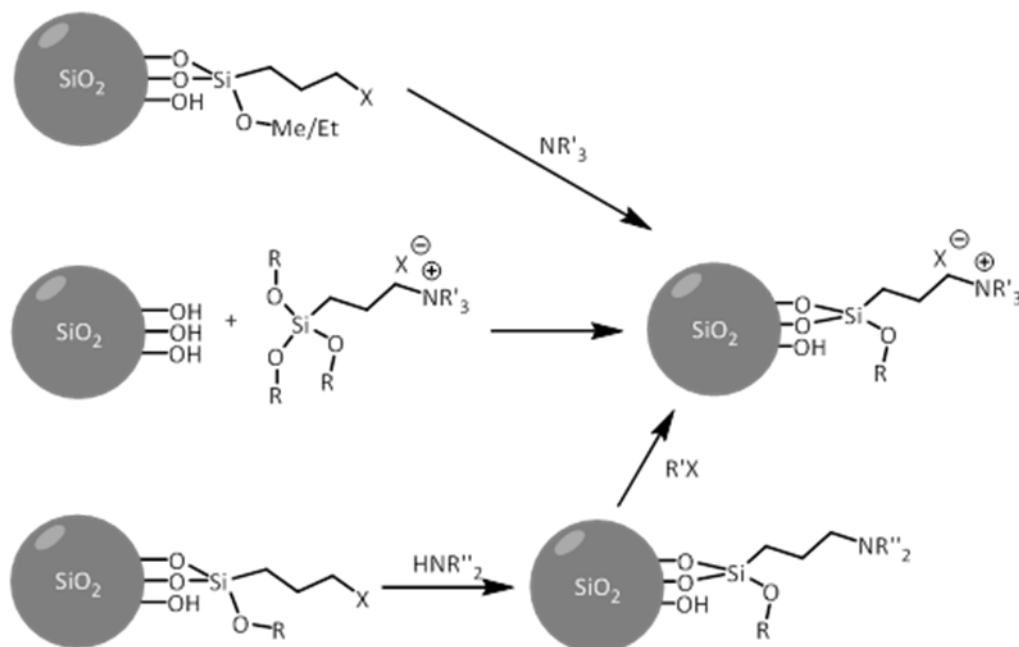


Figure 42: Depiction of three common routes to ammonium based organocatalysts for CO_2 coupling to epoxides. Note: this methodology is applicable to imidazole and imidazolium creation.

Silica supports have the aforementioned benefits of silanol groups for epoxide activation, but also, as with the examples discussed previously with respect to MCM-41, they provide well defined environments around the active site to promote further possible synergy *via* spatial confinement and manipulation of hydrophobicity.

| Cation | Anion | Support | Conditions | | | | | Conv (Sel) / % | Ref |
|--|-------|----------|------------------|-------------|--------|-----------------------|---------|-------------------|-------|
| | | | Sub | Cat (mol) | T (°C) | CO ₂ (bar) | t (hrs) | | |
| NMe ₃ | Cl | PS | PO | 5.0 | 100 | 80 | 12 | 97 (99) | [242] |
| NMe ₃ | I | Chitosan | PO | 1.7 | 160 | 40 | 6 | 100 (99) | [243] |
| NEt ₃ | Cl | MCM-41 | ^a AGE | 1.0 | 110 | 7.5 | 10 | 69.5 (88.5) | [244] |
| EtN((CH ₂) ₂ OH) ₂ | Br | PS | PO | 2.0 | 110 | 20 | 3 | 92 (99) | [245] |
| ^b NBu ₄ | Br | Silica | PO | 1.0 | 150 | 80 | 8 | 99 (97) | [246] |
| NMe ₃ | I | Chitosan | PO | 1.6 | 120 | 12 | 6 | 88 (99) | [247] |
| NMe ₃ | Cl | Chitosan | PO | 0.4, 0.4 KI | 80 | 7 | 4 | ^c 89 | [248] |

Table 19: Summary of immobilised quaternary ammonium organocatalysts. ^aAGE = allyl glycidol ether. ^bPrecipitated and dried. ^cYield (%)

Ammonium based examples in Table 19, showed near complete conversion and selectivity in most cases, however the use of harsh conditions would appear to be often required. The polystyryl supported ammonium showed good activity, however only at harsh, high (80 bar) CO₂ pressure and 12 hours reaction time^[242]. Whilst complete conversion and minimal reduction over successive cycles (5) was reported for the NMe₃.chitosan based variant, high temperature (160 °C) was used^[243]. Contrary to this, a later report on chitosan based analogues from Tharun *et al*, using a novel microwave synthesis method, did maintain activity over four cycles^[247] whilst higher yields were produced on a chitosan support by Besse *et al* however KI was needed as a co-catalyst^[248].

Silica supports produced varied results and comparison is tricky owing to different experimental conditions with respect to the cations, anions and temperatures and pressures used. Udayakumar *et al* employed lower pressures, however lower conversion and selectivity were observed, which they rationalised on the basis of the acidity of the MCM-41 support^[249]. For acidity effect on selectivity see section 0.

Overall, quaternary ammonium ionic liquids show the ability to catalyse the CO₂ and epoxide coupling, but required harsh conditions in the majority of instances yet the improvements in

quaternary nitrogen species has led to the use of imidazolium species for CO₂ and epoxide reactions as they allow for less harsh reaction conditions to be employed^[106,250].

3.1.3 Heterogeneous imidazolium catalysts

Immobilisation of imidazolium/ionic liquids material (that are nitrogen based) has yielded a large variety of materials able to produce cyclic carbonates from CO₂ and epoxides^[106,250] owing to the flexibility in anion and R₁ group, Figure 43. The anion and cation are important to consider because the mechanism for imidazolium materials is usually as follows: the anion, often a halide, will ring open the epoxide, whereby the resulting alkoxide (stabilised by the imidazolium) reacts with CO₂ leading to halide ejection following ring formation^[123,234]. Consequently, both anion and imidazolium can affect the rate of the reaction as they are involved in the initiation of reaction and stabilisation of intermediates respectively.

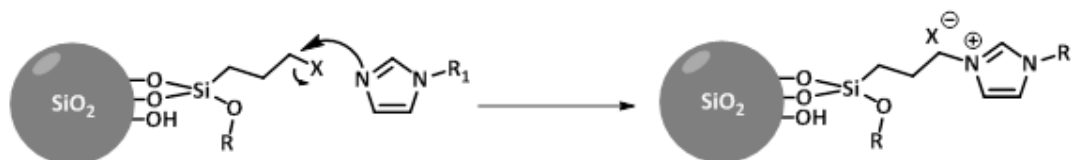


Figure 43: Imidazolium salt produced upon immobilisation to a silica support.

Therefore, a range of differently structured heterogeneous imidazolium examples have been produced^[234,250,251] and summarised in Table 20 and Table 21. The high activities displayed by these materials have led to significant advancement in CO₂ coupling to epoxides since the first report by Peng and Deng^[252]. Immobilisation on organic based supports, as reviewed by Song *et al.*^[250], has shown promise - particularly those which act in a homogeneous manner but with the separation capabilities of heterogeneous materials, Table 20.

| Cation | Anion | Support | Conditions | | | | | Conv (Sel) (%) | TON | Ref |
|--------------------|-------|------------------|------------|-------------|--------|-----------------------|---------|-------------------|-------|-------|
| | | | Sub | Cat (mol %) | T (°C) | CO ₂ (bar) | t (hrs) | | | |
| Im ⁿ Bu | Cl | Cellulose | PO | 1.2 | 110 | 18 | 2 | 99 (98) | 82.5 | [253] |
| MeIm | Cl | PEG | AGE | 3.2 | 120 | 19 | 4 | 90 (99) | 41.2 | [254] |
| EtIm | Br | CS | PO | 1 | 110 | 20 | 4 | 99 (99) | 99 | [255] |
| Im ⁿ Bu | Cl | IL-poly (DVB) | PO | 0.7 | 110 | 60 | 7 | 92.8 (yield) | 137.3 | [256] |
| diol-Im | Br | PS | PO | 0.2 g | 130 | 20 | 3 | 98 (99) | - | [257] |
| H-Im | I | PS | PO | 1.41 | 140 | 25 | 3 | 99 (99) | 70 | [258] |
| EtIm | Br | FDU | PO | 0.5 | 110 | 10 | 3 | 99 (99) | 198 | [259] |

Table 20: Polymer supported imidazolium moieties for cyclic carbonate production. PO = propylene oxide, AGE = Allyl glycidol ether, CS = Cytosan, DVB = divinylbenzene, PS = polystyrene.

The turnover numbers (TON) for the catalysts allow easier comparison, and where possible the data for the reaction using PO has been summarised. The activity of the imidazolium materials show clear improvement on the ammonium and phosphonium catalysts previously discussed. The work by Zhang *et al* displayed the highest TON value, 198, using a highly ordered mesoporous FDU (Fudan University) polymer. The porous nature of this material provides greater surface area available for catalyst immobilisation and restrictive pore size – approximately 70 Å – enables close control over the chemical environment around the active sites as they are encompassed by the support. The large number of phenolic hydroxyl groups present were proposed to aid reaction in an analogous manner to silanols^[259].

As porosity can be seen to be crucial, then the use of inorganic supports, such as silica are attractive. As per Chapter 1, mesoporous silica is non-toxic, cheap and readily obtainable. Moreover, immobilisation onto silanol OH groups on the surface is easily undertaken making it an ideal support for imidazolium species. Additionally, unlike the polymer supported structures, Table 20, silica allows for control over the support structure – the folding of polymer systems or the variance in natural polymers such as chitosan or cellulose means full control over these materials is not possible. It is known for organocatalytic systems that are heterogenised to silica that it can have a profound effect on the activity^[260]. As such, synergistic effects between the support and organic component are often reported as well as the benefits of site isolation that

enhance catalytic ability^[8]. For these reasons, the control afforded by silica is useful. A selection of silica based imidazolium materials is detailed in Table 21, with propylene oxide values quoted where possible to aid comparison.

| Cation | Anion | Support | Conditions | | | | | Conv (Sel) (%) | TON | Ref |
|---------------------|-----------------|------------------------------------|------------|-------------------|--------|-----------------------|---------|-------------------|-------|-------|
| | | | Sub | Cat (mol %) | T (°C) | CO ₂ (bar) | t (hrs) | | | |
| EtIm(Poly) | Br | SBA-15 | PO | 1 | 150 | 100 | 3 | 80 (99) | 189 | [261] |
| ⁿ Bulm | Br | TEOS | AGE | 0.8 | 110 | 35 | 6 | 92 (98) | 129.1 | [262] |
| EtIm | Br | MCM-41 | SO | 0.3 | 140 | 40 | 4 | 98 (99) | 142.4 | [263] |
| ⁿ Bulm | Br | MCM-41 | AGE | 3.7 | 110 | 18 | 6 | 99 (98) | 26.6 | [264] |
| Poly-Im | Cl | SiO ₂ /PIL ^a | PO | 0.05 ^b | 110 | 10 | 3 | 94 (99) | 104.4 | [265] |
| ⁿ BuMeIm | BF ₄ | SiO ₂ ^c | PO | 1.8 | 160 | 80 | 4 | 96 (99) | 53.3 | [266] |
| Poly-EtIm | Br | SiO ₂ /PIL | PO | 50 | 80 | 5 | 0.5 | 99 (99) | 1.98 | [267] |
| MeIm | Cl | SiO ₂ | PO | 2.5 | 130 | 40 | 6 | 41 (38) | 16.8 | [268] |
| EtIm | Br | SiO ₂ | PO | 12 wt. % | 120 | 20 | 3 | 86 (95) | 336 | [269] |
| Im | n/a | SiO ₂ | PO | 10 wt. % | 130 | 6 | 10 | 99 (99) | 170 | [270] |

Table 21: Summary of silica immobilised imidazolium organocatalysts for cyclic carbonate production. ^aPolymer covalently linked to silica (PIL = Poly ionic liquid). ^b0.05 wt. % not mol %. ^cNot covalently bonded, deposited by physical interaction. SO = styrene oxide.

The silica based imidazolium species display high activity. Reaction times are low for the examples in Table 21, with the exception of the last entry which is included as the imidazole is not quaternised. This is interesting as it shows the necessity for the anion – given the relatively long reaction time for reaction completion but also shows that imidazole species are able to catalyse the reaction. Despite the high conversion values displayed, the need for further understanding and optimisation of immobilised imidazolium species can still be seen. For some, high pressure (>20 bar) or temperature (> 120 °C) are still employed and the TON values reported or calculated are relatively modest as catalyst: substrate amounts were often within an order of magnitude to one another. The work of Su *et al*^[259] returned an impressive TON of 336 relative to the other examples, whilst the low reaction time and high yield reported in the recent work by Martínez-Ferraté *et al* is due to the 50 mol % of catalyst used, so low TON value^[267].

Recent reports have indicated that the presence of one or more OH groups leads to heightened yield of cyclic carbonates. Publications from Whiteoak *et al*^[102], Anthofer and Wilhelm *et al*^[271,272] and another from Hardman-Baldwin *et al*^[273] showed that in combination with a tertiary ammonium salt (TBAI), OH groups within the organic moiety significantly increase activity both with and without the presence of imidazolium, ammonium or phosphonium. Understanding of the mechanism of this could produce the next group of metal-free heterogeneous organocatalysts for CO₂ utilisation.

As shown, the literature provides a huge range of imidazolium variants which are able to catalyse the reaction successfully. Turnover numbers remain low in the majority of cases and the most active examples of immobilised imidazolium species are those which use the addition of metal salts. For example Xiao *et al* used zinc chloride to produce a 96 % yield of propylene carbonate at a TOF of 2741 hr⁻¹^[274]. The use of a homogeneous salt counteracts the benefits of an immobilised system and so despite the high activity these reports will not be covered but are summarised in a review by Cokoja *et al*^[234]. Production of more active organic moieties in order to bridge the clear activity gap between metal based and non-metal catalysts for cyclic carbonate synthesis, without the metal salt use, is needed.

Only brief comment has been passed in many cases on the true effect of the support on the capabilities of the catalyst as often supports are not fully defined in terms of their properties^[234]. More recent examples in the literature have started to discuss the effect of silica and other supports that are highly active,^[275] indicating that the careful selection and/or design of a support which would enhance the catalytic ability, synergistically, rather than simply being a means for immobilisation could improve activity. Imidazolium species are quaternary ammonium salts but being 5-membered ring systems means that functionalisation is constrained to the groups on the two nitrogens, one of which is typically employed for anchoring to the support. Nevertheless, flexibility is still afforded by the other nitrogen. The catalyst structure is also changeable by varying the anionic counter-ion.

3.1.3.1 N-Heterocyclic carbenes

Finally, imidazolium species lend themselves to formation of N-heterocyclic carbenes (NHCs) a stable form of carbene which were first described by Arduengo *et al*^[276]. Through a deprotonation of the methylene bridging the two nitrogens, an electron pair is both gained and lost from the carbon almost simultaneously and concurrent to the breaking of two bonds. The resulting species is a neutral carbon atom with 6 electrons – four bonding and two unpaired electrons, a carbene, see Figure 44.

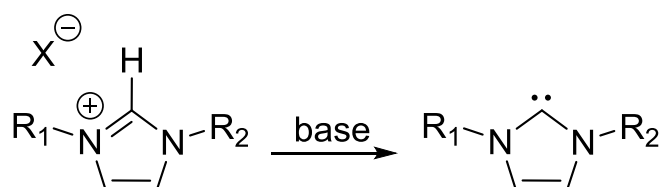


Figure 44: N-heterocyclic carbene formation following deprotonation of an imidazolium

Introduction of CO₂ was shown to be reversible and caused the formation of a stable carboxylate by Duong *et al*^[277] and shortly after the ability of the carbene to catalyse the reaction of CO₂ with epoxides was reported,^[278,279] as upon introduction to the NHC, the CO₂ is converted to an activated form, the carboxylate, Figure 45. This allows it to react onwards in a CO₂ utilisation reaction with an epoxide to produce a cyclic carbonate. The carbene acts as the catalytic entity as it is reformed in a CO₂ atmosphere and the catalytic cycle continues.

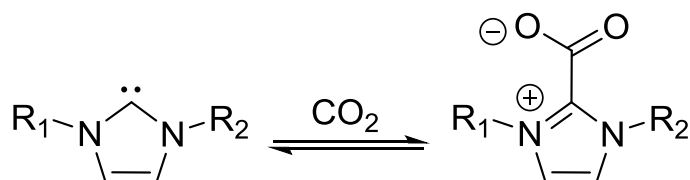


Figure 45: Carboxylate formation following introduction of a CO₂ atmosphere to the carbene

Heterogenised versions such as polymers containing NHCs have been reported and shown to be active for CO₂ capture^[280] and subsequent reaction with epoxides^[281]. Immobilisation on silica supports, such as on MCM-41 has been reported with activity for a range of epoxides^[228] A review by Yang and Wang summarised the use of NHCs for carbon dioxide capture, fixation, and activation^[282]. The reported heterogeneous examples employing metal-free NHCs required long reaction times (24+ hrs) to ensure complete conversion^[228,281].

3.2 Aims and objectives

The aim of this Chapter is to achieve the immobilisation of a range of imidazolium species onto mesoporous silicas, *via* pendant silanols, in order to effectively catalyse the reaction between CO₂ and epoxides. The current literature shows the good activity for these systems, however it is commonly reported that high temperature, pressures, long reaction times or relatively high amounts of catalyst are required (as evidenced by low TON values) and so efforts shall be focussed on improving the efficacy of the imidazolium species. The silica based catalysts produced will be characterised by a wide range of techniques in order to determine the structure and properties of both support and organic moiety enabling conclusions being drawn with regard to the structure property relationships that are occurring.

Consideration will be given to both the support and the imidazolium structures in order to better understand the effect that the design of them has on catalytic turnover. The imidazolium will be altered in terms of R group, anion and loading on the silica whereas the silica pore diameter will be changed to determine the effect on the rate of the reaction. Overall, the most active variant will be screened for efficacy in catalysing a range of epoxides. Additionally, when altering the support, the type of support itself will be investigated with hierarchically porous materials (HP-AIPOs) also considered given the presence of silanol sites within the mesopores and the additional support functionalities that are possible with these more complicated materials. The re-use of heterogeneous supports is crucial in order to validate the need for immobilisation therefore, where possible post-catalysis characterisation will be undertaken and the samples tested through re-use.

Lastly, imidazolium species are capable of being converted to N-heterocyclic carbenes (NHCs) as shown in Figure 44, therefore attempts to produce the carboxylate, NHC-CO₂⁻ as depicted in Figure 45, will be made and once confirmed through characterisation the material tested in the epoxide and CO₂ reaction.

3.3 Mesoporous silica based imidazolium organocatalysts

3.3.1 Characterisation of silica anchored imidazolium

Confirmation of structural retention post immobilisation of the imidazolium but also the support is key to the activity of the organocatalytic component. A range of techniques were used to determine the structure of the organic moiety following its addition to silica. Solution NMR analysed the structure prior to anchoring, and solid state NMR was used to confirm retention post-synthesis. Solid state NMR was not obtained for all silica based catalysts synthesised, owing to the time constraints for these measurements. Structures and catalyst variants will have individual characterisation plotted, rather summary and discussion to save repetition.

Nomenclature for the range of different imidazolium species and structures affixed covalently to mesoporous silicas is detailed in Figure 46 and Table 22. The 150 Å silica was used as the support during variance of the structure and anion of the imidazolium. The diPr imidazolium (diPrIm) was used as the organic component when varying the silica support and the anion.

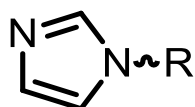


Figure 46: Imidazole with R group depicting where functionality differs.

| R = | Melm | nPrIm | iPrIm | tBulm | MesIm | diPrIm |
|-----------|------|-------|-------|-------|-------|--------|
| Structure | | | | | | |

Table 22: Summary of R group functionality along with naming convention used, with respect to Figure 46.

Column purification yielded the diPrIm, MesIm and tBulm variants. The purity and structure of diPrIm was checked using ^{13}C and ^1H NMR. Further spectra were obtained of the intermediate oil obtained from the reaction of the imidazole with the trimethoxysilane both to check for retention of structure and efficacy of the purification step with ether. As an example, the characterisation and analysis of these stages with diPrIm is detailed below. For the remaining imidazole analogues tabulation and assignment of NMR peaks can be found in Chapter 2.

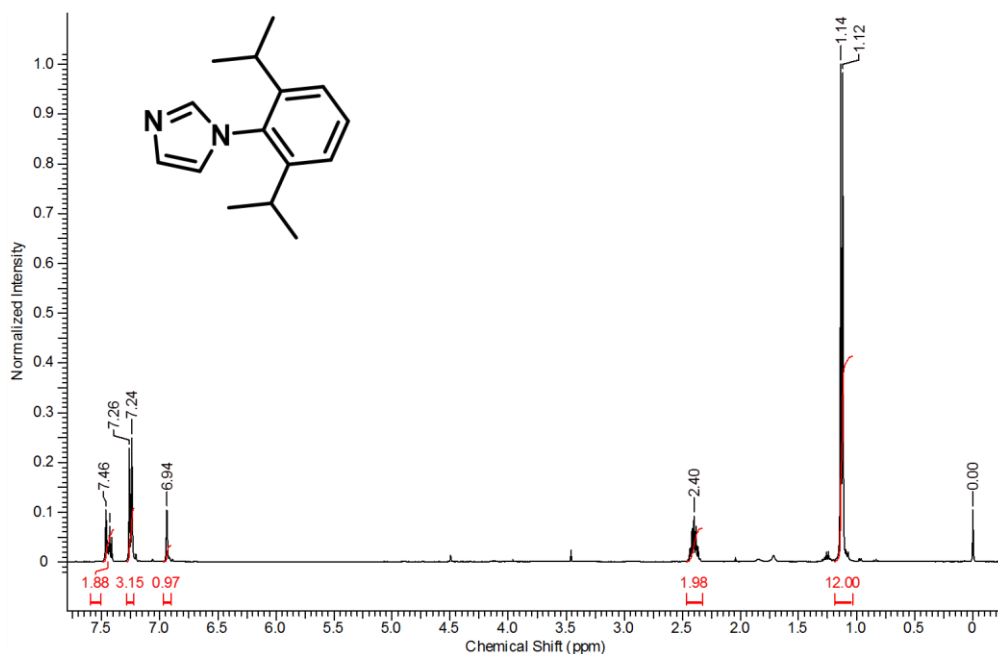


Figure 47: ^1H NMR spectra of diPrIm (inset) with peak labels and associated integrals. 400 MHz, CDCl_3 , TMS reference

Column chromatography yielded the diPrIm, shown in Figure 47, inset. The doublet at 1.13 ppm corresponds to the 12H of the iso-propyl groups, split by the C-H of the middle carbon which itself accounts for the septet at 2.40 ppm from the reverse splitting. The imidazole ring protons and those on the phenyl ring account for the remaining 6H, additional integral value is attributable to the CDCl_3 peak which overlaps. Minimal impurities are present in the spectra, validating the purification methodology.

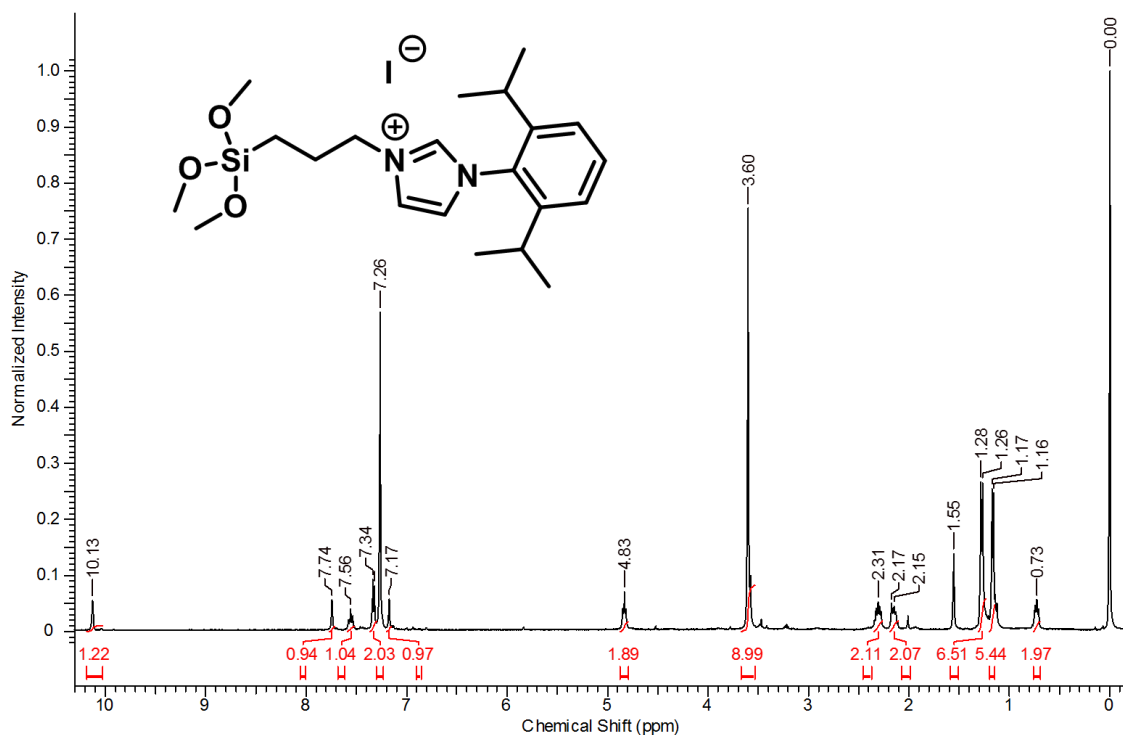


Figure 48: ^1H NMR spectra of diPr-imidazolium, diPrIm(I), formed from reaction with (3-iodopropyl)trimethoxysilane (structure inset). 400 MHz, CDCl_3 , TMS reference

The reaction of (3-iodopropyl)trimethoxysilane with diPrIm afforded the product shown (inset in Figure 48). The propyl chain components are shown in the ^1H NMR spectrum as: the triplet at 0.73 ppm from the CH_2 bound to the Si; the multiplet at 2.16 ppm from the middle CH_2 and the N bound CH_2 of the propyl linker appears as a triplet at 4.83 ppm. The trimethoxy singlet appears at 3.60 ppm, equivalent to 9H. Imidazolium formation is confirmed by the large shift of the imidazole ring CH in-between the two nitrogen atoms, at 10.13 ppm, owing to the formation of the ionic species. The phenyl and imidazole ring C-H peaks occur in the range of 7-8 ppm, totalling 5H. Methyl groups of the isopropyl ring substituents appear as two doublets, indicating non-equivalence upon imidazolium formation. Creation of the trimethoxy species enables the covalent anchoring of the imidazolium onto a solid support, Figure 49, *via* a facile process.

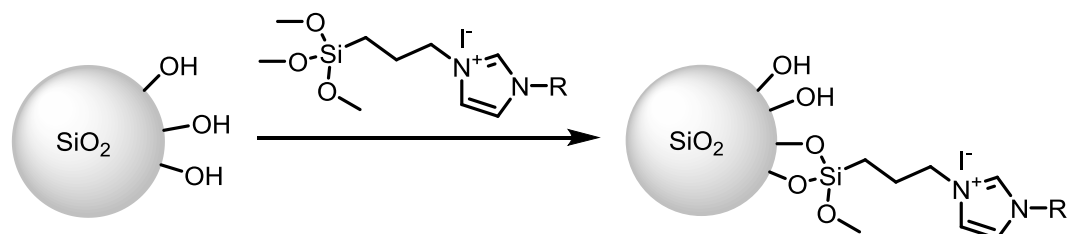


Figure 49: Diagrammatic representation of covalent anchoring of imidazolium species to silica, *via* pendant silanols.

Given the activity shown by imidazole derivatives in the literature, careful design and manipulation of the catalyst environment will be undertaken in order to produce a highly active heterogeneous CO₂ utilisation catalyst for cyclic carbonate production.

3.3.2 Coupling of carbon dioxide and epoxides

Design and optimisation began with proof of concept reactions combined with a kinetic study. Methyl imidazolium with an iodide counter ion on silica (MeIm(I)/SiO₂) was synthesised, as the imidazole is commercially available and so the catalyst could be easily produced *at scale*.

Sampling of the reaction was not possible *in-situ* due to the nature of the batch process at pressure therefore to obtain data on the initial behaviour of the reaction each time-point in the below plot is a separate reaction using fresh catalyst each time.

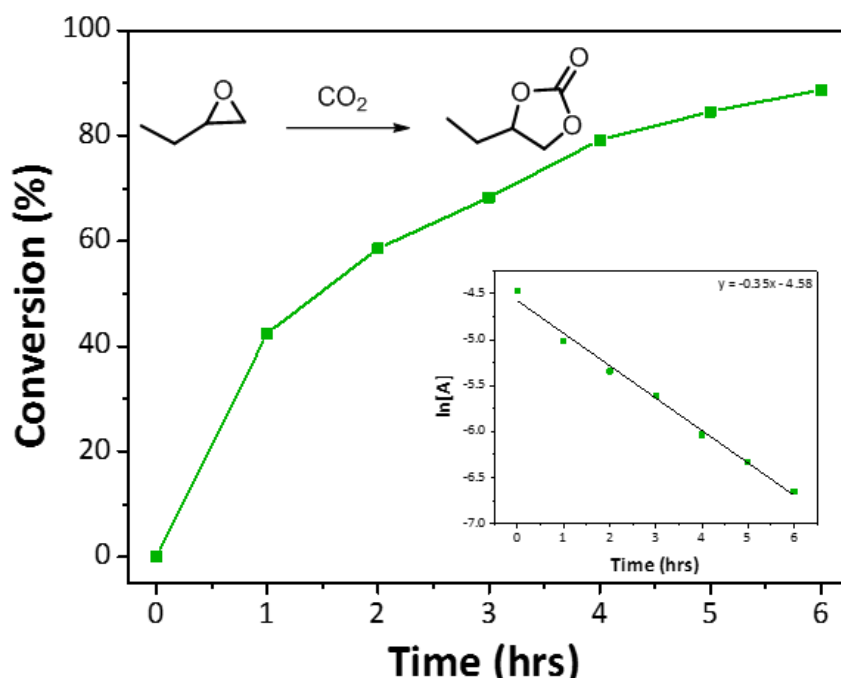


Figure 50: Conversion of butylene oxide to butylene carbonate (shown) over time by 1-methylimidazolium on silica (MeIm(I)/SiO₂). Reaction conditions: 115 °C, t = as per x axis, 20 bar CO₂, 5 g butylene oxide, 0.1 % catalyst, solvent free. Analysed by ¹H NMR, mesitylene as ITSD. Inset: plot of ln[butylene oxide] versus time.

It can immediately be seen that the methyl imidazolium is a successful catalyst for the reaction. At a low loading (0.1 %) the 40 % conversion after one hour is impressive and has a TOF value of 383, higher than the majority of reported values for analogous systems from the literature discussion above. Selectivity towards the cyclic carbonate product was above 99 % in all of the 6 hr reactions undertaken for Figure 50.

A plot of $\ln[A]$ produces a straight line, indicating the reaction is first order with respect to the concentration of the substrate. Jutz *et al* undertook a thorough study whereby cyclohexene oxide conversion to cyclohexene carbonate, also observed first order kinetics with respect to (wrt) the epoxide; it must be noted the catalyst system is different here^[121]. Another comprehensive study by North *et al* determined first order reactivity wrt to [epoxide], again with a different catalytic system^[123]. Undertaking the reaction at further temperatures would allow for the activation energy to be calculated for the reaction with the catalyst allowing for a quantitative means to examine reaction rates of differing catalysts alongside TONs, the 115 °C and 20 bar CO₂ reaction conditions were selected as these appeared to be the average of literature values employed.

The preliminary results show clearly that the anchoring of the imidazolium material creates a silica based catalyst active in the production of the cyclic carbonate product, and at high yield. Optimisation by variance of the catalyst characteristics was subsequently undertaken.

3.3.2.1 Investigation of pore diameter alteration

It is known that pore diameter can affect catalytic turnover; Newland *et al* and Xuereb *et al* describe alteration of pore dimensions within which organocatalytic material is anchored^[21,260]. Jones *et al* discussed the manipulation of pore aperture in order to provide constraint around the active site and in so doing compelled the reaction to occur in a particular manner^[24].

With this in mind a series of alternate pore diameter mesoporous silicas were considered for the imidazolium anchoring. Silicas of 30, 60, 150 and 250 Å as well as Cabosil (fumed silica, nominally non-porous) as a comparison, with diPrIm(I) anchored *via* silanols were synthesised. The pore size distribution before anchoring was measured and compared to the manufacturers quoted diameter, see appendix Figure A2, for an exemplar distribution for the 30 Å variant where close agreement with the quoted manufacturer's value was confirmed and shown across all silica variants.

| Support | Loading / mmol/g |
|---------|------------------|
| 30 Å | 0.41 |
| 60 Å | 0.51 |
| 150 Å | 0.33 |
| 250 Å | 0.49 |
| Cabosil | 0.58 |

Table 23: Loading of diPrIm(I) on various silica supports, determined by CHN analysis using the nitrogen value for calculation

Theoretical loading of 0.5 mmol g^{-1} was attempted for all supports. Actual loadings, based on nitrogen percentage from CHN values are displayed in Table 23. Any excess of the imidazolium oil used in the anchoring was assumed to have been removed *via* the DCM soxhlet wash that was employed. Nitrogen was the element of choice for the loading calculation as the imidazolium is the only source of nitrogen in the final anchoring procedure. Thermogravimetric analysis (TGA) was used to assess the ability of elemental analysis for the loading calculation. A comparison of elemental analysis and TGA mass loss percentages is displayed in Table 24.

| Catalyst | EA / % | TGA / % | Difference [%] |
|----------|--------|---------|----------------|
| 30 Å | 12.22 | 13.72 | 1.50 |
| 60 Å | 15.20 | 16.72 | 1.52 |
| 150 Å | 10.13 | 12.28 | 2.15 |
| 250 Å | 14.60 | 15.33 | 0.73 |
| Cabosil | 17.17 | 19.48 | 2.31 |

Table 24: Comparison of elemental analysis and TGA weight loss percentages for the range of pore diameter catalysts and Cabosil, diPrIm imidazolium for all. TGA mass loss curves normalised to 100 °C.

The elemental analysis (EA) percentage values in Table 24 are the mass losses that would be expected from a TGA measurement, based upon the loading calculated from the elemental analysis. The difference quoted is the modulus of the elemental analysis theoretical value minus that of the measured TGA value. For all cases, the difference is small, giving validity to the loading calculations. The loading is critical as it forms the basis of turnover number calculations that are to be used to evaluate differences between alternate catalysts, therefore the validity of the loading is crucial to the conclusions drawn using this metric. As the data was normalised to 100 °C this does not account for all of the solvent that could be present and may account for some of the differences tabulated. The TGA loss is greater in all cases so it is likely not all the solvent/small molecules are removed prior to 100 °C, additionally, there is inherent error in choosing the temperature at which peaks are deemed to start, even when use of the first derivative is applied.

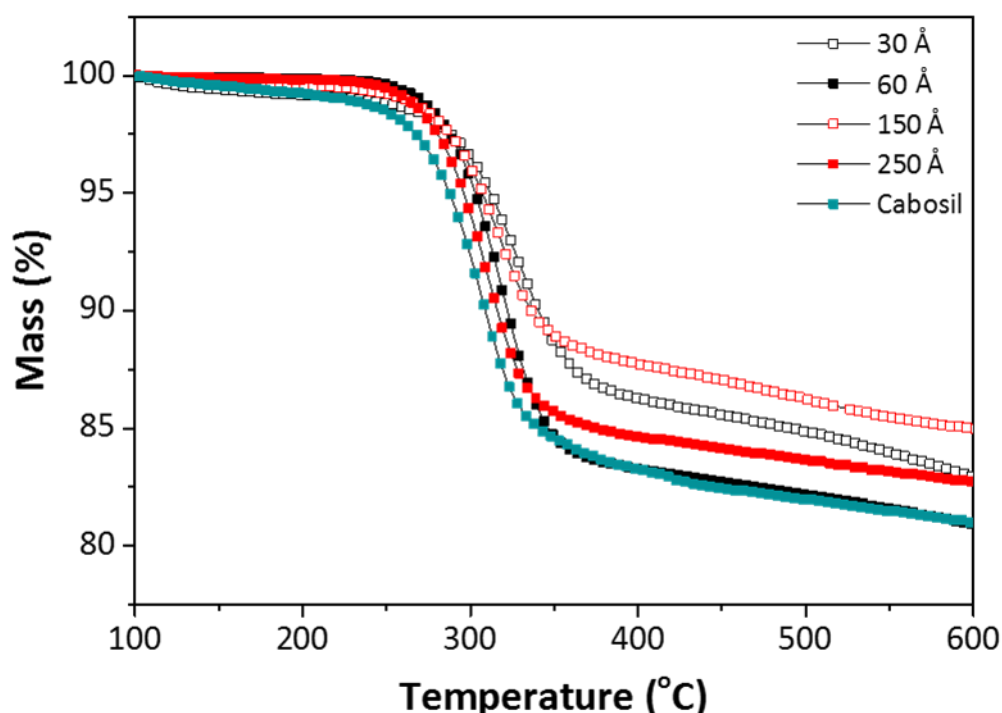


Figure 51: TGA curves for diPrIm(I) anchored onto different pore diameter silica supports. The curve was normalised to 100 °C in all cases. Conditions: range 30-900 °C, ramp rate 10 °C/min, Air flow: 50 mL/min.

The thermogravimetric data, Figure 51, also allows for the maximum working temperature of the materials to be found, seen to be almost identical for all at 225 °C. The first derivative, see appendix Figure A3, was used to find the initial point of inflection and thus the maximum working temperature. Above this temperature the degradation of the material would begin to inhibit any reaction being catalysed.

Absolute confirmation of covalent binding was attained with solid state NMR probing the ^{29}Si and ^{13}C environments. Si-C and C-Si bonding environments in the respective spectra would validate the experimental methodology and confirm anchoring.

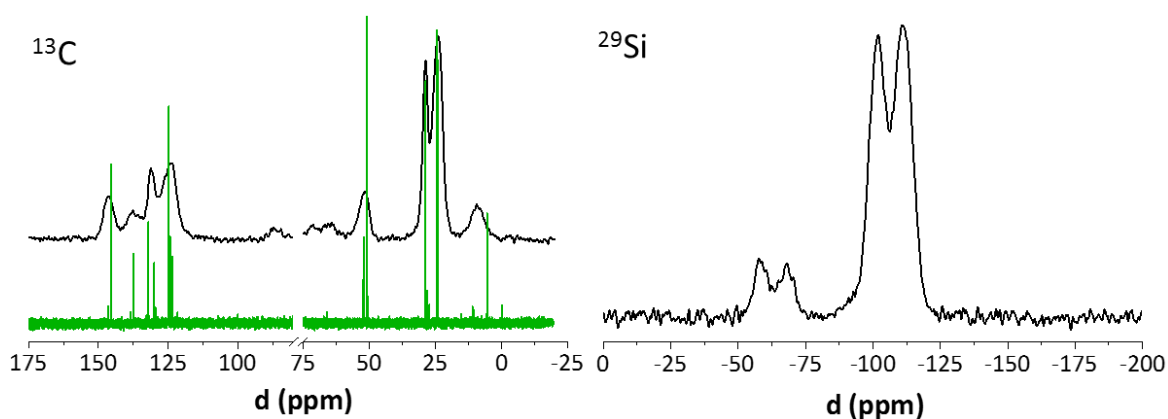


Figure 52: ^{13}C solid state CP NMR (black, diPrIm(I)/ $\text{SiO}_2(150 \text{ \AA})$) and solution (green, diPrIm(I) oil) NMR spectrum (left) and ^{29}Si solid state CP NMR for diPrIm(I)/ $\text{SiO}_2(150 \text{ \AA})$. **Note:** the region of 75 – 80 ppm has been omitted from the ^{13}C spectrum to remove the large CDCl_3 present in the solution spectrum in order to adjust the scale to aid comparison.

The ^{29}Si spectra contains two key environments, the peak at -111 ppm relates to the Si-O-Si and the peak at -102 ppm relates to the Si-OH environments inherent to the bulk structure of the silica framework. The region relating to the Si-C environment is between -70 and -50 ppm. The peaks shown are characteristic of R-Si(O) $_3$ species, typical of the trimethoxy group and confirms the covalent attachment to the mesoporous silica *via* silanols. These could not be observed in the direct excitation (DE) spectra, see appendix Figure A1, so their intensity is exaggerated relative to the Si(OSi) $_4$ signal of the framework at -111 ppm through the use of cross polarisation (CP) experiments. Multiple peaks are observed due to different amount of methoxy substitution occurring. Specifically, the peaks at -57 and -69 ppm correspond to the R-Si(OSi)(OH) $_2$ and (OSi) $_3$ Si-R environments respectively - confirming covalent anchoring of the organocatalyst.

Within the ^{13}C spectra, peaks at *circa* 10 and 50 ppm are assigned to the CH_2Si and $\text{CH}_2\text{-N}$ environments in the linker with the alkyl-chain CH_2 discernible at 22 ppm as the shoulder peak. The peaks at 28 ppm, are the isopropyl group carbons which functionalise the phenyl ring. Signals between 110 and 140 ppm account for the aromatic carbons of the phenyl ring. The appearance of these peaks within the solid state NMR spectra, mimicking that of the solution spectra, is confirmation that the structure of the imidazolium is unaltered during the anchoring process. The peak shift observed for the silica bonded carbon in the trimethoxy imidazolium is different to that of the heterogenised version as the methoxy groups are displaced by silanols upon heterogenisation thus altering the chemical environment the carbon observed.

Ideally, affixing a material to a mesoporous support should have as minimal an effect on the porosity as possible. For this study, retention of porosity is key to pore diameter effect evaluation. Significant alteration of the pore size upon anchoring of the organic moiety would prevent

meaningful conclusions on about the influence of the support on activity being made. Nitrogen adsorption experiments, pre and post-anchoring were undertaken to determine any significant change.

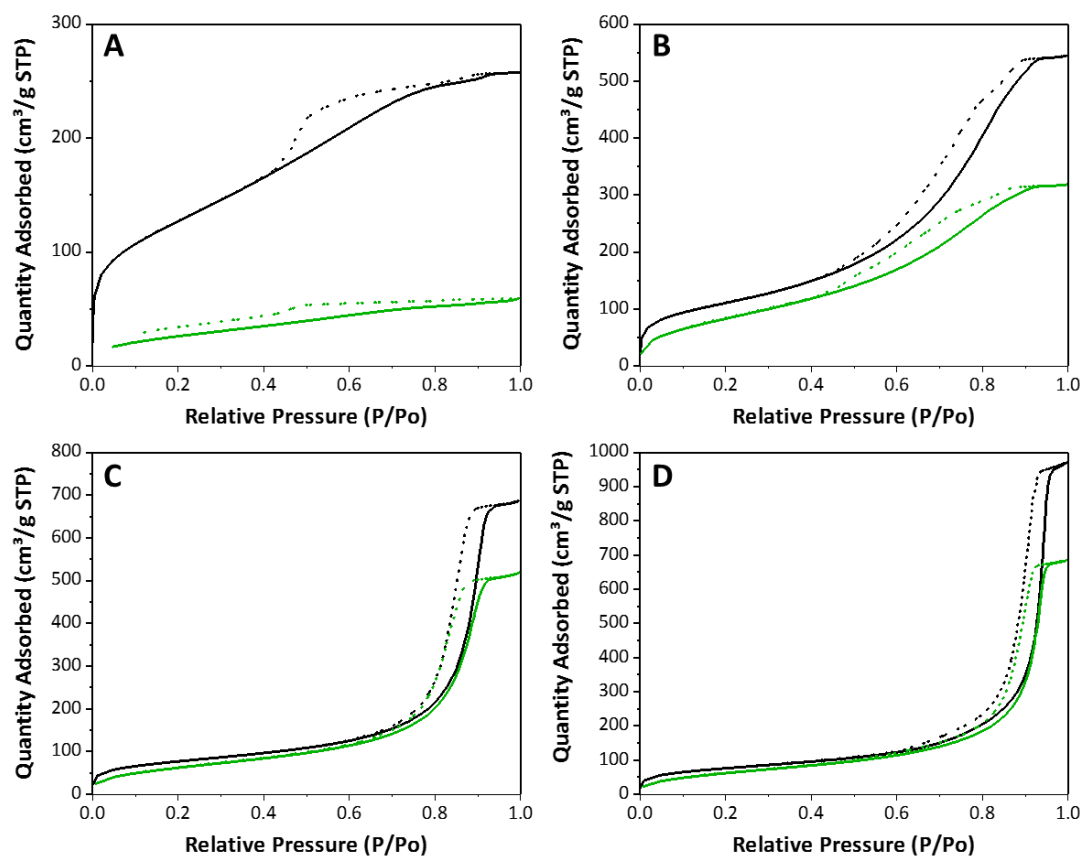


Figure 53: N₂ adsorption and desorption isotherm for A) 30 Å B) 60 Å C) 150 Å and D) 250 Å mesoporous, in all cases blank silica (black), diPrIm/SiO₂ (green), adsorption isotherm (solid) and desorption isotherm (dotted).

In all variants of pore diameter a decrease was observed for pore volume, surface area and adsorption capacity upon anchoring. The surface area and volume decrease imply anchoring to the walls of the mesopores, so allows for the effect of the local environment on the activity of the imidazolium to be observed. The 30 Å diPrIm(I) exhibited a large drop in the surface area compared to the blank, $458 \pm 2 \text{ m}^2/\text{g}$ to $98 \pm 1 \text{ m}^2/\text{g}$ decrease, thus the porosity was impacted to a large extent by anchoring.

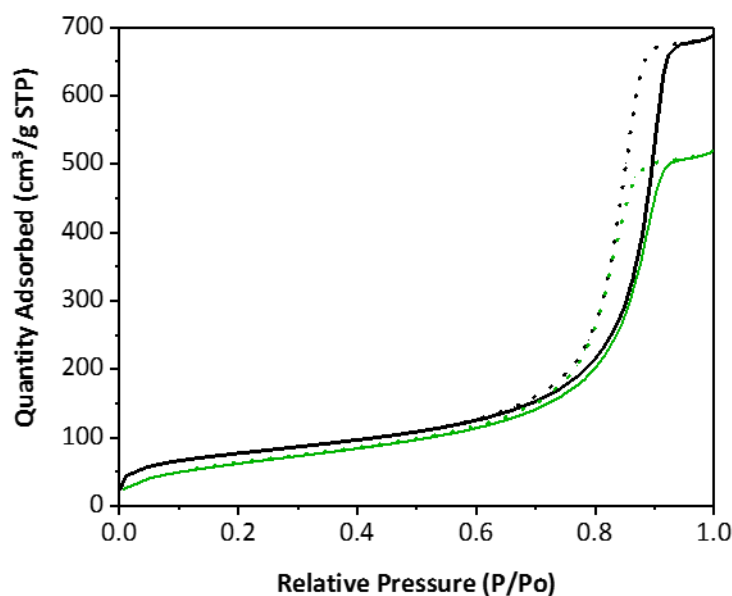


Figure 54: N₂ adsorption and desorption curves for blank mesoporous SiO₂(150 Å) (black), diPrIm(I)/SiO₂(150 Å) (green), adsorption isotherm (solid) and desorption isotherm (dotted).

As an example: the 150 Å SiO₂ the adsorption and desorption curves for both the blank and the functionalised silica, are shown in Figure 54, and form a type IVa isotherm as described by IUPAC^[212]. Initial adsorption occurs on the walls of the mesopore followed by the occurrence of pore (capillary) condensation. Capillary condensation occurs with a H1 hysteresis which is expected given the pore diameter of greater than 4 nm with delayed condensation occurring in the adsorption isotherm due to the stability of the adsorbed layer^[212]. A final plateau is seen for both the blank and the imidazolium functionalised silica following condensation. Adsorption quantities are lower for the diPrIm(I)/SiO₂(150 Å) than the blank silica, as would be expected for the introduction of an organic moiety into the silica pore, occupying volume within the pore. Crucially, mesoporosity is maintained within the silica therefore enabling active site access for any reagents.

| Material | Surface area (BET) / m ² /g | Pore volume / cm ³ /g |
|-------------------------------------|--|----------------------------------|
| unmodified SiO ₂ (150 Å) | 271 ± 2 (300) | 1.11 (1.15) |
| diPrIm(I)/SiO ₂ (150 Å) | 236 ± 2 | 0.85 |

Table 25: Surface area and pore volume measurements on SiO₂ and diPrIm(I) functionalised SiO₂.

Values in brackets in the unmodified silica row are quoted from manufacturers specifications¹.

It can be seen that, as expected the surface area and pore volume both decrease upon anchoring of the diPr imidazolium (I) to the mesoporous silica. The measurements for the blank compare favourably to those of the manufacturer, see Table 25, therefore giving confidence in the values being experimentally obtained but also any relationship between the pore diameter and catalytic activity. Pore volume decrease versus the blank indicates that the anchoring is occurring within the mesopores of the silica, rather than on the outer walls. Surface area decrease is solely attributed to organic materials anchoring to the silanols.

Each material was tested for efficacy for styrene carbonate production. The unanchored imidazole, as a homogeneous catalyst, was tested to show the effect the formation of the imidazolium has on the reactivity. Each support had a different loading, as determined by elemental analysis, so the mass of substrate was maintained and the catalyst varied to be equimolar across each support. This allows for the best comparison of the catalysts *via* turnover frequency (TOF) which gives the best measure of differing activities between the diameters. For this metric, initial rates of reaction offer the best insight into catalyst ability as substrate concentration has not been lowered sufficiently to become a limitation to turnover therefore lower reaction times were used, rather than attempting reaction completion. Each of the different catalysts were tested twice and an average obtained of the two results (except the 30 Å which is an average of three).

¹Silica gel high-purity grade (Davisil Grade 643), pore size 150 Å, 200-425 mesh (Sigma Aldrich: <https://www.sigmaaldrich.com/catalog/product/sial/236810?lang=en®ion=SG>)

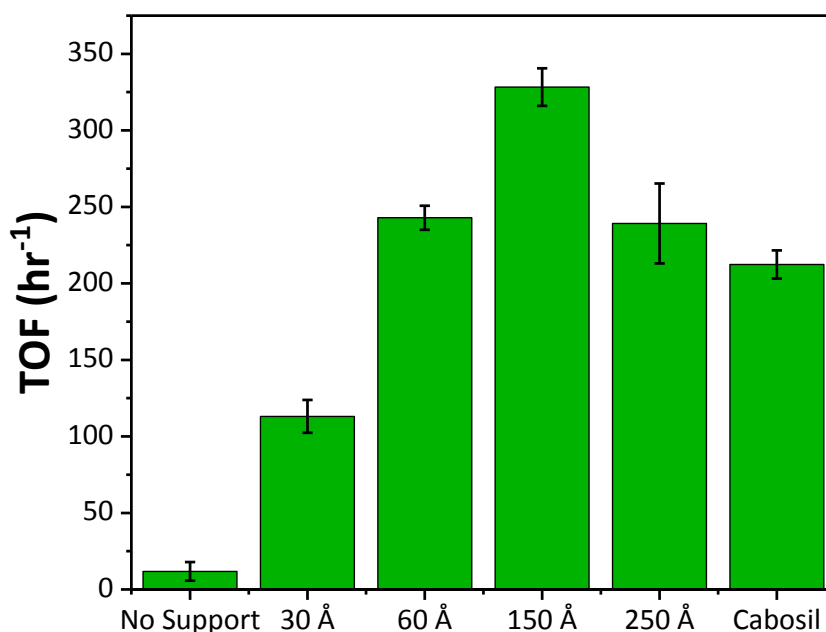


Figure 55: Average turnover frequency numbers for styrene oxide to styrene carbonate conversion over a range of pore diameter silica supports. Reaction conditions: 115 °C, 2 hours, 20 bar CO₂, 5 g styrene oxide, 0.1 % diPrIm(I)/SiO₂ (No support is diPrIm(I) at 0.1 %). Analysed by ¹H NMR, mesitylene as ITSD. Standard deviation shown based upon two measurements.

The homogeneous diPrIm shows ability to catalyse the reaction, however the TOF of 11.8 hr⁻¹ is far lower than the anchored variants. The highest activity is displayed for the 150 Å silica supported catalyst. At the smaller pore diameter (30 Å) it would be expected that the smaller pore size may become blocked during reaction and could account for the lower reaction rates; recycle tests would be able to confirm this, see section 3.3.2.6 for discussion. The Cabosil showed a similar ability towards styrene carbonate formation as the 250 Å silica, which could indicate that above a certain pore diameter no benefits are seen to activity. However, it must be stated that the pore size distribution was not consistent for the 250 Å following anchoring upon this silica. Over several iterations of the same anchoring technique the final material using the 250 Å support displayed considerable variance in pore size distribution, see appendix Figure A2. If this batch of support was degrading by some route then it would provide explanation for the similarity between it and the fumed silica analogue, Cabosil, if the pores are no longer intact or have become altered.

The 150 Å aperture support showed superior performance compared to the others. This diameter would appear to display a synergy between the pore diameter and the organocatalyst whereby the combination of the organocatalyst with the support lends to enhanced CO₂ utilisation. Caution must be used when drawing conclusions as other factors such as the catalyst loading,

which plays a key role in causing site isolation, often provide key contributions to catalytic ability. This is especially relevant to the example shown above given the material displaying the greatest TOF (150 Å) had the lowest loading in this instance. A loading study, section 3.3.2.4, was undertaken as a result, yet the performance of the 150 Å silica resulted in this support being used in further attempts to understand and optimise the system.

3.3.2.2 Expansion of substrate scope

A range of different terminal epoxides were tested to evaluate the flexibility of the catalyst and also to discern any effect of epoxide substituents upon the rate of the reaction and give an indication of the catalyst mechanism. The effect of chain length, steric bulk and electron withdrawing and donating groups upon conversion and selectivity is then quantified.

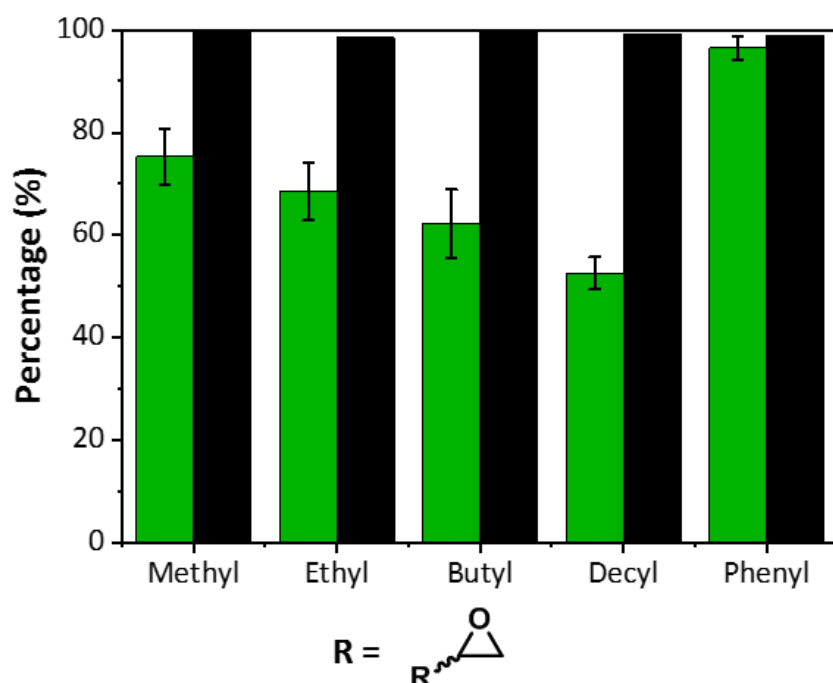


Figure 56: Average Conversion (green) and selectivity (black) values for the coupling of CO₂ with various epoxides. Reaction conditions: 115 °C, 6 hours, 20 bar CO₂, 5 g epoxide, 0.1 % diPrIm(I)/SiO₂(150 Å). Analysed by ¹H NMR, mesitylene as ITSD. Standard deviation shown based upon two measurements.

Figure 56 shows the catalyst (diPrIm(I)/SiO₂) is highly capable of catalysing the coupling of CO₂ to a range of terminal epoxides. The selectivity in all cases was high, > 98 %, indicating that the catalyst is able to convert the epoxide to almost exclusively the desired, cyclic carbonate product. A trend of lowered activity is seen with increasing chain length associated with the epoxide, though TOF analysis can be used to determine the true nature of this. The use of styrene oxide (R = phenyl) displayed a seemingly higher than expected conversion. This can be explained by the

electron withdrawing effect of the phenyl ring and conversely may explain the lowered activity with chain length of the linear alkane epoxides^[283], Figure 57.

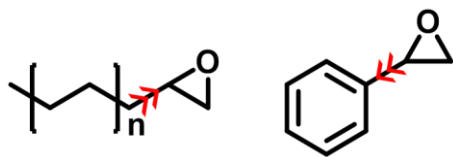


Figure 57: Depiction of electron donating effect and electron withdrawing effect of linear alkane and phenyl epoxide R groups respectively.

It can be theorised that the linear chains *via* the $+I$, inductive effect, will place electron density onto the carbons of the epoxide. Therefore, the polarisation of the C-O bond in the 'linear' epoxide will be minimised with increasing chain length, ultimately making the epoxide less reactive to the nucleophile (I^-) so lowering the TOFs seen for the reaction. Conversely, the $-I$ effect of the electron withdrawing phenyl group enhances the existing polarisation of the C-O epoxide bond, thus explaining the high conversion observed for styrene oxide. One final possibility is the favourable interaction of the catalyst aromatic ring and styrene oxide ring, such as pi-pi stacking that may cause substrate closer proximity to the nucleophile. The effect of the chain length on reactivity can be further seen in Figure 58.

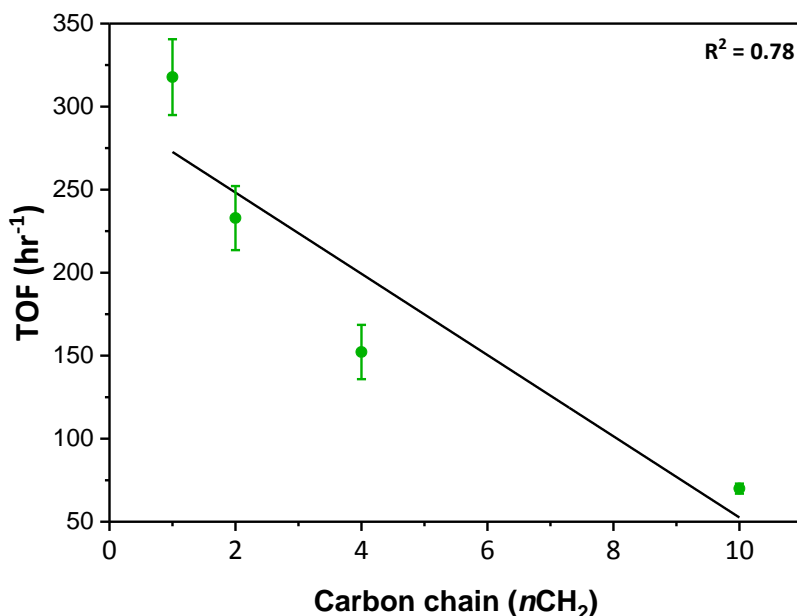


Figure 58: Comparison of epoxide side chain length and TOF. Trendline applied to data with correlation shown. Reaction conditions: 115 °C, 6 hours, 20 bar CO_2 , 5 g epoxide, 0.1 % diPrIm(I)/ SiO_2 (150 Å). Analysed by 1H NMR, mesitylene as ITSD. Standard deviation shown based upon two measurements.

The trend observed in Figure 58 shows indicates lower conversion with increasing chain length. A study by Castro-Gomez *et al* suggested that steric bulk of the epoxide also contributes to reaction rates so must be considered, with the carbon that is the nucleophile reacts with affected by the epoxide side groups^[284]. Overall, the diPrIm(I)/SiO₂ showed good ability over a range of epoxides to produce cyclic carbonate from CO₂, indicating it is a highly flexible catalyst for the production of cyclic carbonates from terminal epoxides. A non-terminal or di-substituted epoxide, cyclohexene oxide, was trialled and 5 % conversion was observed over a 6 hour time period, indicating this hindered system is not readily accessible to the catalytic component.

3.3.2.3 Investigation of imidazole functionality alteration

Alternate R groups, with respect to the imidazole, were synthesised and tested for efficacy in the CO₂ and epoxide coupling reaction. Udayakumar *et al* discussed the effect of the substituents on the nitrogen, such as steric bulk and *+I* and *-I* inductive effects^[244]. Multiple characterisation techniques confirmed the successful synthesis and anchoring of the imidazole and subsequently imidazolium structures onto the silica, similar to the aforementioned, see Chapter 2 for NMR tabulation.

To test the effect of the R groups all other conditions were maintained throughout to aid comparability. In all cases the selectivity towards the carbonate was greater than 95 %. Two main side products were identified - the diol and a small amount of the isomerisation product, the aldehyde.

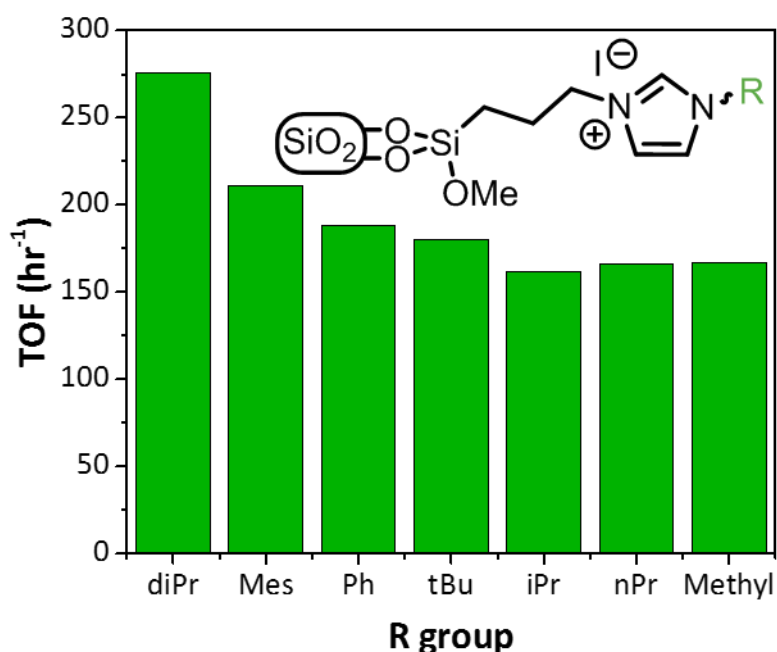


Figure 59: TOF values for styrene carbonate formation by differently functionalised silica anchored imidazolium catalysts, inset: catalyst structure with R group location.

Reaction conditions: 115 °C, 6 hours, 20 bar CO₂, 5 g styrene oxide, 0.1 % RIm(I)/SiO₂(150 Å) . Analysed by ¹H NMR, mesitylene as ITSD.

There is no distinct trend seen for the alteration of the imidazole R group, see Figure 46 and Table 22 for structure clarification, when errors are considered. However, what is apparent is that elevated TOF values occur with the use of aromatic, phenyl ring derivatives on the imidazolium. The reasoning for this was not fully understood. The proposed mechanism requires intermediate stabilisation by the imidazolium, as such the distribution of the positive charge around the structure is likely to affect the intermediate stages of the catalytic cycle thus, theoretically, affect the rate of reaction. Steric bulk of the R group is another factor to be considered as, the ability of the intermediate to be stabilised will rely on proximity of the substrate.

Similarly to the study of the effect of different pore diameters, the results here indicate that the loading of the catalyst influences the catalytic ability more so than the structure as there is a strong correlation between loading and conversion. If structure was critical then the same loading of two different structures would give appreciably different conversions and therefore TOF values over the same time period. Conversely, if loading was important then differing loading could give the same conversion. If this is found to be true then either the loading upon the silica, the anion, or both are the key components of the imidazolium catalyst rate determination.

3.3.2.4 Imidazolium loading study

Loading variation of the diPrIm on the 150 Å silica support was used to understand how the concentration of imidazolium on the silica surfaces affects the catalytic ability. Site isolation is well known to be a key component and therefore requirement of heterogeneous catalysis^[8]. Percent CHN analysis confirmed the range of loadings to be investigated for the study, shown on the below plot.

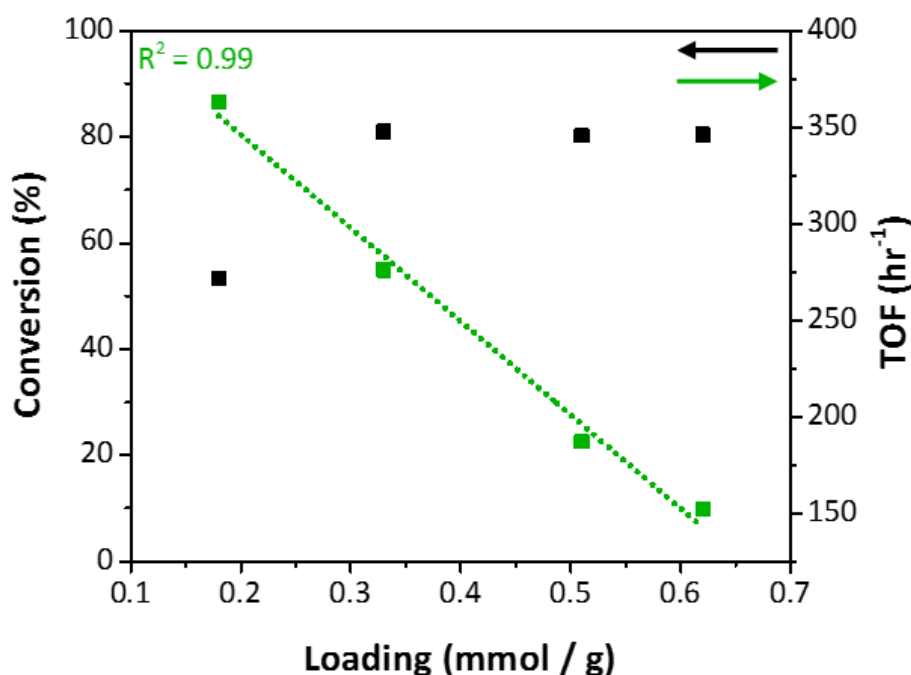


Figure 60: Conversion (black) and turnover frequency (TOF, green) for diPrIm(I)/SiO₂(150 Å) for a range of loadings. Reaction conditions: 115 °C, 6 hours, 20 bar CO₂, 5 g styrene oxide, 0.1 g catalyst. Analysed by ¹H NMR, mesitylene as ITSD.

It can be clearly seen that different loadings of the catalyst produce similar conversion values. Were the loading of the catalyst to not affect the catalytic ability then the conversion value would have been seen to increase proportionally with the amount of the catalyst present. The 0.62, 0.55 and 0.33 mmol/g loading all return approximately 80 % yield after 6 hours, Figure 60, therefore loading influences catalytic activity. The 0.18 mmol/g variant produces the highest TOF value (363 hr⁻¹) and an impressive TON of 2181 but conversion is noticeably lower.

In the 0.18 mmol/g variant each individual site is highly active but from a practical point of view a trade-off between activity and the yield obtained is needed for optimisation. Whilst a lower loading has been shown to produce sites of greater individual catalytic ability, the amount of support required increases proportionally with loading decrease. Therefore, the mass of catalyst used becomes increasingly high for these low organic content variants providing the need for a middle ground. The idealised scenario in the above would appear to be the a loading around that of the 0.33 mmol/g catalyst where the high yield is maintained whilst using less organocatalytic material to do so.

3.3.2.5 Reaction dependence on the anion

The anion was varied and the structure maintained. The diPr imidazolium was synthesised with iodide, bromide, chloride and bistriflimide as the counter-ion. In the first three cases the synthesis

was altered so that the trimethoxysilane species in each case contained the desired anion element (i.e. for chloride the starting material was (3-chloropropyl) trimethoxysilane) and was thus present following the imidazolium creation. For the bistriflimide - used because it is bulky and only weakly nucleophilic owing to the highly stable nature of the anion - post-synthetic anion exchange was undertaken. ^{19}F NMR was used to confirm exchange, see appendix Figure A4, for NMR and bistriflimide structure. Presence of a peak in the ^{19}F spectra confirmed the exchange in combination with the ^1H spectra whereby the imidazole ring peaks and the closest CH_2 were both shifted in comparison with the same protons within the diPrIm(I) variant of the ionic liquid/oil prior to anchoring, see Figure 48. Activity for each was tested with butylene oxide as the epoxide producing butylene carbonate.

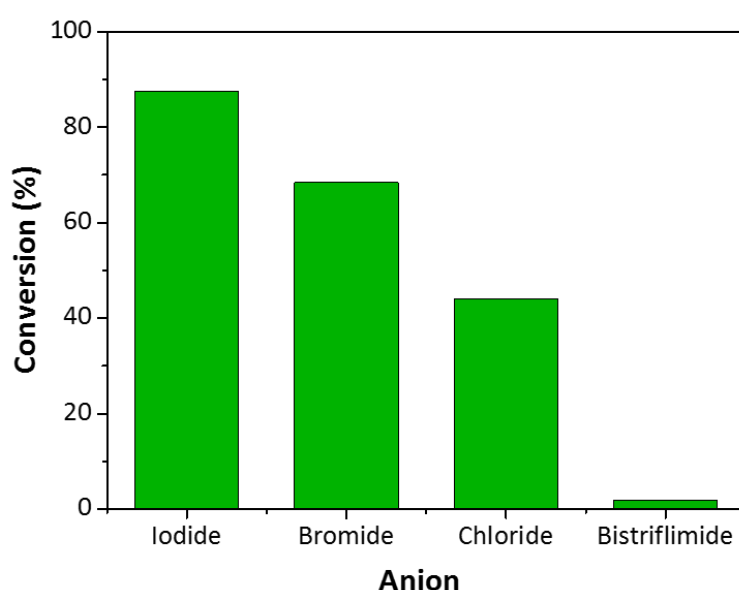


Figure 61: Conversion values of CO_2 and butylene oxide to butylene carbonate with diPrIm/ SiO_2 (150 Å) and different anions. Reaction conditions: 115 °C, 6 hours, 20 bar CO_2 , 72 mmol butylene oxide, 0.1 mol % loading catalyst. Analysed by ^1H NMR, mesitylene as ITSD.

As seen in Figure 61, the anion of choice has a marked effect on the conversion which is obtained. The iodide provides the highest conversion with 87 % followed by bromide (68 %) then chloride (44 %). The bistriflimide (1.8 %) shows a low conversion percentage, comparable with that of the blank reaction. In all cases the reactions progressed with greater than 98 % selectivity towards the butylene carbonate product, even in the bistriflimide instance.

The catalytic ability of the halide anions is a combination of nucleophilic character and leaving group ability^[285,286] $\text{I}^- > \text{Br}^- > \text{Cl}^-$ therefore during the reaction the faster loss of halide from the intermediate will allow for a faster catalytic cycle to occur leading to greater turnover numbers. This is in line with results observed for homogeneous ionic liquid systems^[287] whereby the same

trend was observed for imidazolium cations and was attributed to the nucleophilic character of the anion under the catalytic conditions and also similar silica based versions^[288]. The bistriflimide is only weakly nucleophilic and also bulky therefore theoretically will not undergo the ring opening stage as readily and so therefore acts as a control for the study, similar to the use of PF_6 and BF_4 by Ghazali-Esfahani *et al.*^[289]. It must be stated that this trend is not always observed, and conflicting reports are present in the literature where bistriflimide displays high activity which is attributed to the interaction energy between cation and anion being lowest for NTf_2^- which allows it greater freedom to act in a nucleophilic fashion^[290]. For this work, based on, the results shown it is believed that the bistriflimide is sufficiently bulky to be prevent the intermediate structures being stabilised by the imidazolium if the bistriflimide does act in a nucleophilic manner. The mechanism for the catalyst can therefore be considered to be as shown in Figure 62, in line with the conclusions made and is very similar to the mode of action previously described for immobilised TBAB in earlier sections.

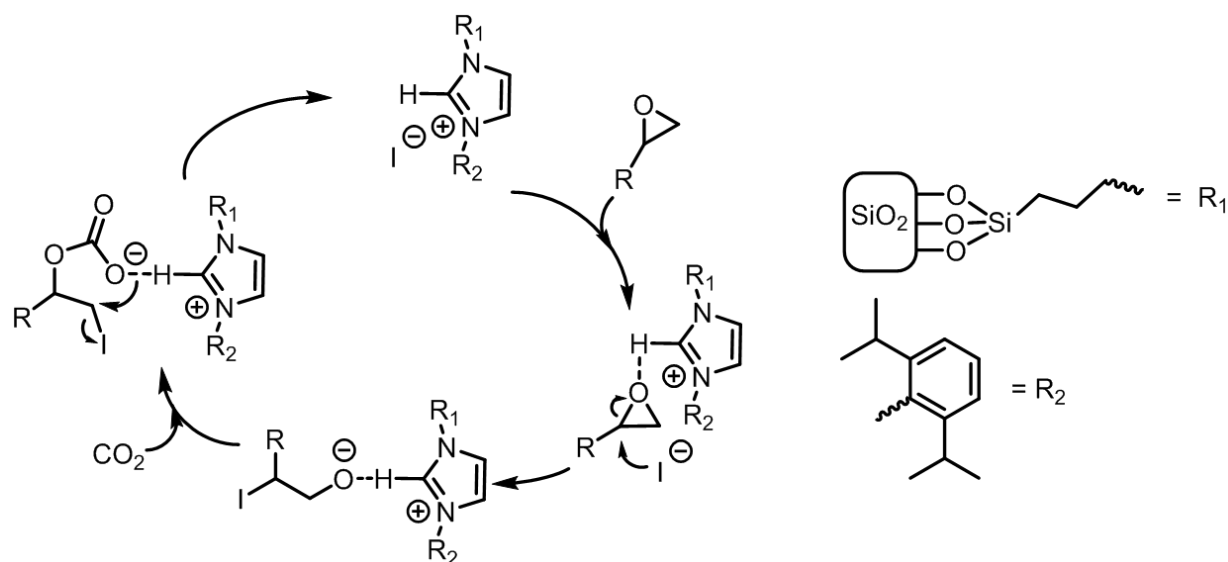


Figure 62: Mechanism of cyclic carbonate formation, catalysed by diPrIm(I)/SiO₂.

In the above, the iodide counter ion, acting as the nucleophile, ring opens the epoxides which is held near to the imidazole ring. The imidazole stabilises the intermediate which then itself attacks the CO₂. Ring closing occurs with the formation of the five membered ring of the cyclic carbonate product and ejection of the iodide as the leaving group. Regeneration of the iodide is key as it then allows for a further ring opening step to occur and subsequent catalytic propagation of the reaction.

3.3.2.6 Recycle tests

To determine the viability of the catalyst for reuse, successive cycles of the same catalyst were undertaken. The catalysts used for section 3.3.2.1 were employed, as pore diameter may

influence the degradation of the materials. If blocking of the pores is occurring then a larger (i.e. 250 Å) mesoporous support should enable more cycles at higher retained activity. The 250 Å and 30 Å variants were chosen to study this. Each was collected, washed, reused and evaluated for activity for the same reaction each time. TOF was selected as the metric for comparisons to normalise for differing masses of catalyst and substrate – the ratio of which was maintained throughout as catalyst amounts dropped across the multiple trials.

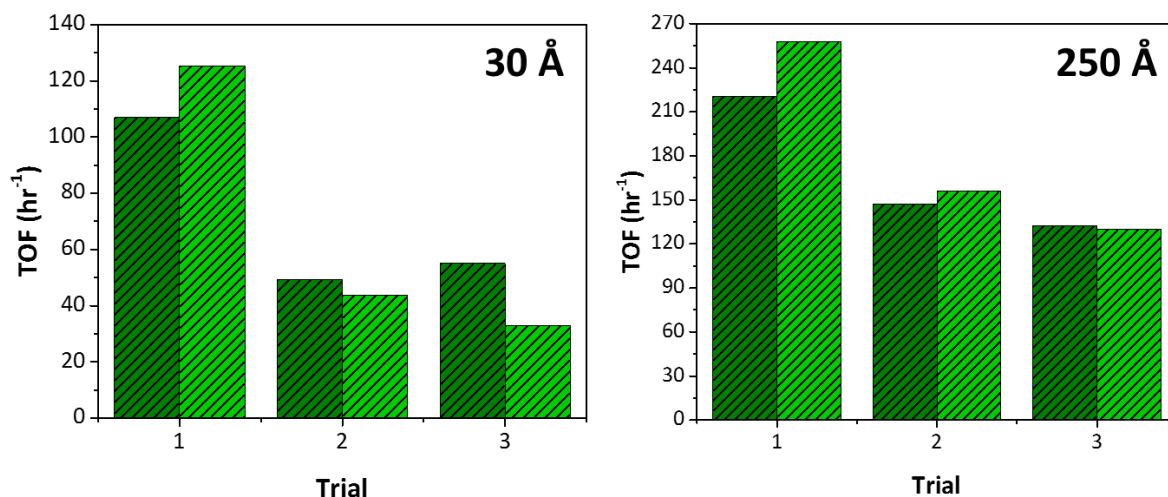


Figure 63: Recycle study on 30 and 250 Å diPrIm(I)/SiO₂. 1st trial reaction conditions: 115 °C, 2 hours, 20 bar CO₂, 5 g styrene oxide, 0.1 mol % diPrIm(I)/SiO₂. Analysed by ¹H NMR with mesitylene as ITSD. For collection and washing details, see experimental section. Light and dark green indicate each batch was tested twice.

High selectivity was maintained (> 99 %) for both catalysts over the re-use cycles, conversion dropped significantly following the 1st cycle – shown by the TOF values, as they are a function of conversion. The loss of activity over several cycles seen is highly discouraging for a theoretically heterogeneous catalyst. If the silica is becoming blocked then this correlates with the activity loss shown being more pronounced in the smaller, 30 Å, pore. The testing of the intermediate pore diameters, 60 and 150 Å is needed to confirm these results, especially given the aforementioned potential reliability issues with the 250 Å support. The 2nd and 3rd trials show similar activity for the 30 Å pore diameter and the same is seen for the 250 Å variant. This implies that the loss of activity could be from leaching and that after the first cycle non-anchored catalytic material that was present was removed during reaction therefore in subsequent cycles activity was maintained as the amount of catalytic materials was a constant. This is an unexpected outcome as the synthesis stage employed a soxhlet wash for this purpose and the covalent grafting is sufficiently robust to withstand the reaction conditions.

In order to determine the validity of these two hypotheses, post catalytic characterisation was undertaken on some of the used catalysts. Elemental analysis was obtained of the 30 Å catalyst prior to and after use and is shown in Table 26. If leaching of the organic component has occurred to a significant extent the loading based on the nitrogen content would show an appreciable decrease when contrasted to the as synthesised sample.

| Catalyst | C / % | H / % | N / % | Loading / mmol g ⁻¹ |
|--------------------|-------|-------|-------|--------------------------------|
| 30 Å | 8.76 | 1.64 | 1.14 | 0.41 |
| 30 Å after trial 1 | 14.15 | 1.53 | 1.21 | 0.43 |

Table 26: Elemental CHN % before and after use for the 30 Å diPrIm(I)/SiO₂. Loading calculated based off the nitrogen content of the material.

This was not seen. The loading of the organocatalyst does not change significantly, based on the nitrogen content and as there are no other possible source of nitrogen that can be introduced in either the reaction or the washing stages it is concluded that the organic component has withstood use in the reaction. An appreciable increase in the carbon content is observed. Increase of the carbon content within the framework would indicate that either the reagent or product is becoming trapped within the pore and not removed during the washing of the collected functionalised silica undertaken in-between cycles. A decrease in activity would be associated with this as it would restrict access to the active site of fresh substrate in the subsequent trials, giving evidence to the theory that pore blockage is occurring and is the cause of the activity reduction.

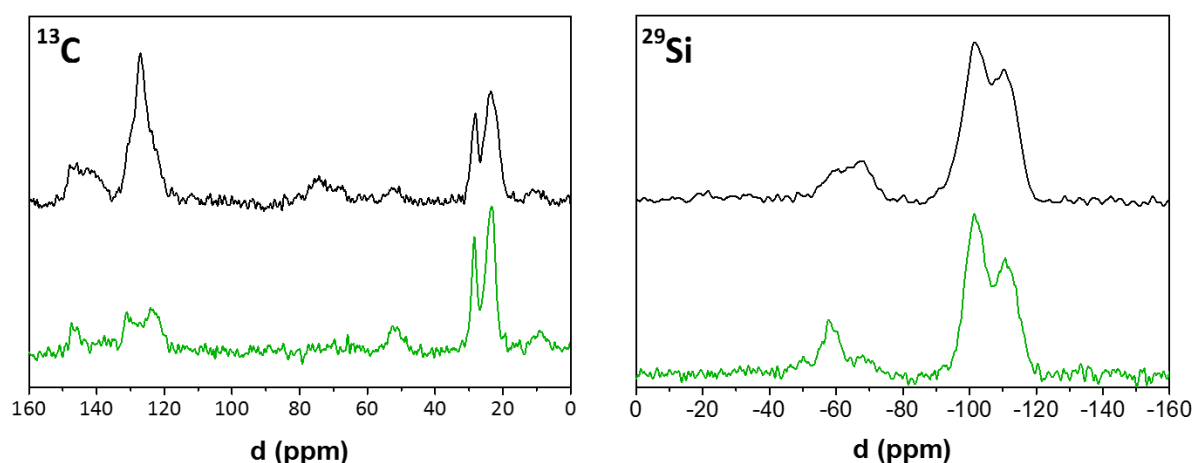


Figure 64: ¹³C solid state NMR for as synthesised diPrIm(I)/SiO₂ 30 Å (green) and diPrIm(I)/SiO₂ 30 Å post catalysis/recovered (black) and ²⁹Si solid state NMR for as synthesised diPrIm(I)/SiO₂ 30 Å (green) and diPrIm(I)/SiO₂ 30 Å post catalysis/recovered (black). In all cases the spectra are CP not DE in order to resolve all peaks clearly.

Collection of solid state NMR indicated that the organocatalyst was still present and structurally intact on the silica following a second use of the catalyst. The C-Si environment is distinguishable in the ^{13}C spectra at *circa* 10 ppm and the Si-C environment at approximately -68 ppm in the recovered catalyst ^{29}Si spectra (black line). Structural retention of the organic moiety is shown by the carbon spectra, with the continuance of the key environments in the recovered material being seen. Additional peaks are seen and assigned to styrene oxide which was used as the starting material epoxide for the catalyst analysed. The peak at 75 ppm is typical of a C-O environment which can be attributed to the epoxide or a product of, the increase in the existing peak at 125 ppm accounts for the styrene oxide aromatic carbon environments. Given that the collected catalyst was washed thoroughly with DCM several times and dried, this observation suggests the pores are being blocked in some capacity by a reagent or by-product which is not easily removed. Such occurrence would limit the ability of catalyst, going some way to explaining the decrease in yields seen over successive cycles.

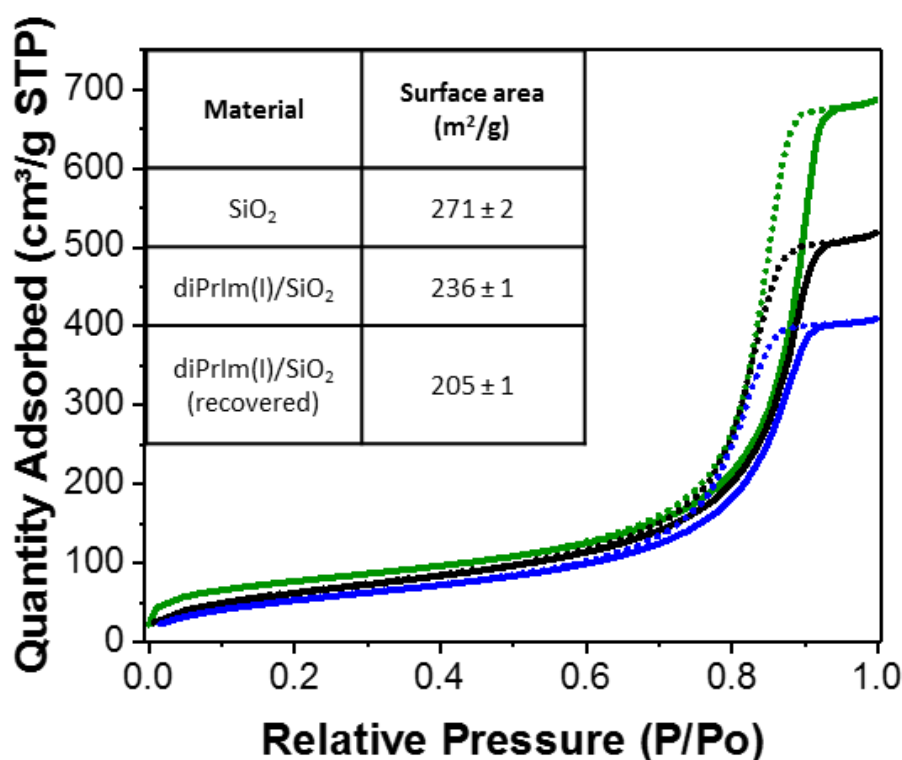


Figure 65: N₂ adsorption and desorption isotherms for SiO₂ (black), diPrIm(I)/SiO₂ (green) and diPrIm(I)/SiO₂ recovered (blue). Silica was 150 Å for all. Inset: BET surface areas for the three materials.

To determine the occurrence of the pore blockage and the extent of it, a reaction was run with the 150 Å diPrIm(I)/SiO₂ on a large enough scale to allow for gas sorption studies and TGA to be undertaken on the material collected post-catalysis. The 150 Å was used, whilst this is not ideal as it was not employed for the recycle studies above, given the uncertainty in the results obtained

from the pore distribution study, the 250 Å version was ruled out. The analysis showed that capacity and surface area decreased upon use of the catalyst as shown in Figure 65. Given the solid state NMR and elemental analysis results, assumed to be also applicable to this different variant, and which indicated the presence of styrene oxide, or a variant of, becoming trapped or bound to the framework the reduction in the porosity of the material shown in Figure 65 is expected. Retention of mesoporosity is shown, given the hysteresis in the recovered sample. The TGA curve of the catalyst material, Figure 66, following use and washing (4 x 10 mL dichloromethane), showed a different profile to the as synthesised catalyst. The earlier loss is likely to be the substrate, styrene oxide, and occurs at a similar temperature to the boiling point of 194 °C (Sigma-Aldrich, 97 %). The latter loss peak starting at approximately 400 °C is unknown but it could be a higher molecular weight by-product or similar with a strong interaction with the framework.

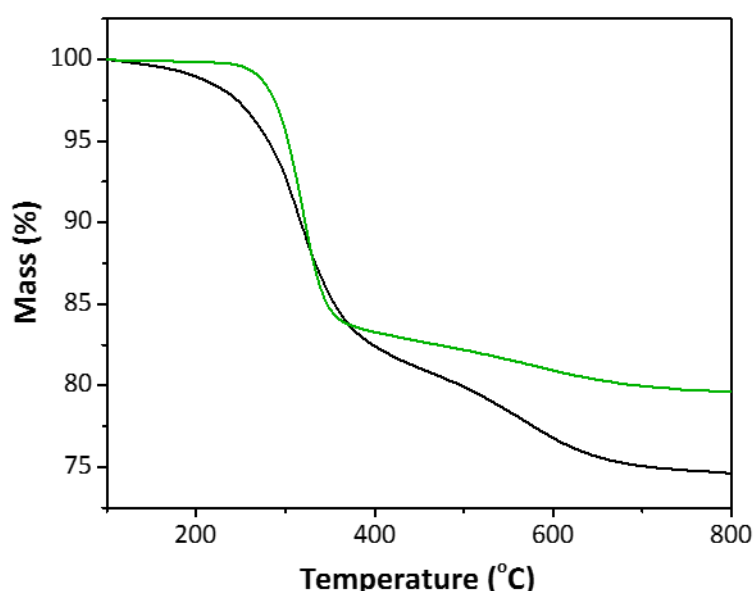


Figure 66: TGA curves for as synthesised diPrIm(I)/SiO₂ (150 Å, green) and diPrIm(I)/SiO₂ following a single use and washing with DCM (150 Å, black). Conditions: range 30-900 °C, ramp rate 10 °C/min, Air flow: 50 mL/min

From the recycle tests activity decline upon recycling is then apparent. Any use of these silica based materials for a significant number of cycles then requires a robust strategy to reactivate them following use as one of the most important aspects of a heterogeneous catalyst is the ability of it to be not only easily collected, but also successively re-used. Further characterisation of the catalysts post reaction is therefore important in order to determine the reason for catalytic activity loss. The CHN % analysis indicated that the loading of the organic component is not decreasing, and the solid state NMR showed that the organic moiety is intact following catalysis. A strategy to employ solely the organic part of the imidazolium (rather than in combination with the

halide) as the catalytic component is therefore desirable and could theoretically overcome some of the issues observed and attributed to causing the large loss of activity within the imidazolium systems. This was investigated in the experiments trialled in section 3.5.

3.4 Hierarchically porous supports

Given the results of the pore size study and literature reports where synergy from anchoring and the support itself were observed, other supports were trialled. Whilst silica supports possess the silanol groups required for functionalisation the non-ordered arrangement of the mesopores hampers mass transport and they generally have low thermal stabilities. Conversely, hierarchically porous silicoaluminophosphates (HP-SAPOs) have much higher thermal stability, are an ordered framework with discrete, but interconnected, micro and mesopores that aid mass transport^[291]. Critically, the synthesis of the HP-SAPOs creates silanols exclusively within the mesopores allowing for the anchoring of organic components *via* the methodology aforementioned. There are a few reports of functionalisation of zeolites in the literature whereby an organic species to such supports have been covalently bound for catalysis purposes^[292–295] but no current reports have been found for HP aluminosilico or aluminophosphates. A recent article showed the use of mesoporous TS-1 to undertake the conversion of CO₂ and an epoxide (epichlorohydrin)^[296]. Furthermore, doping of metal species within the framework is well documented^[9] and would add a second catalytic functionality to the material – which could be exploited for a tandem or cascade process.

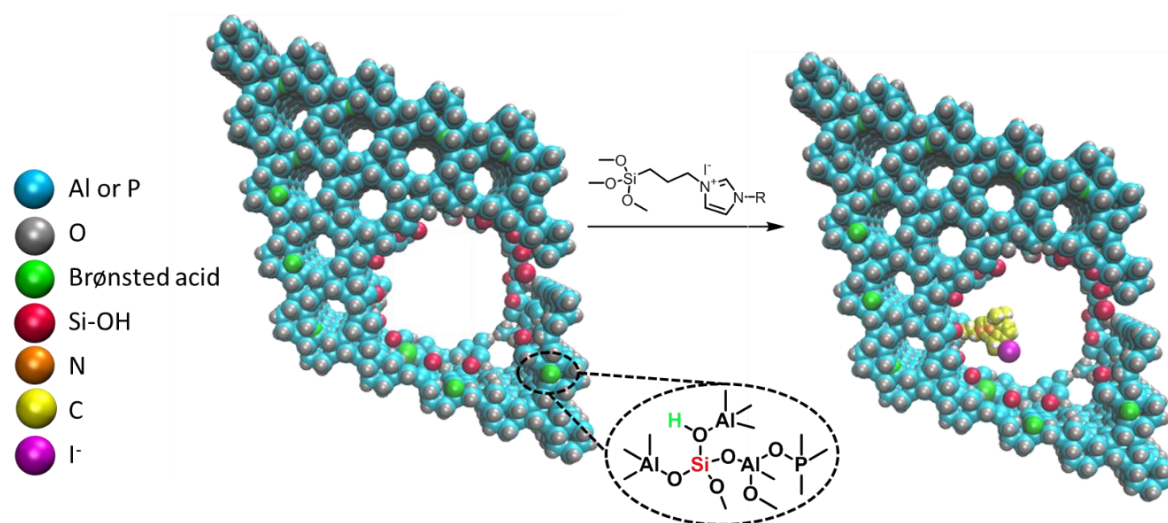


Figure 67: Diagrammatic representation of imidazolium grafting to HP SAPO-5, anchoring location depicted as within the mesopore, and isomorphous Si doping within the framework. R = 2,6-diisopropylphenyl.

Immobilisation of the ionic liquid, imidazolium, was undertaken by an analogous procedure to that of the anchoring to silica as shown in Figure 67. The diPrIm imidazolium was selected for anchoring as this had the greatest data collected on it from the purely silica based catalyst and nominally displayed the highest activity. Post synthetic characterisation was compared to the

blank material to discern any physical or chemical alteration the attachment process had on the material.

Elemental analysis probing for nitrogen content was undertaken, showing 0.69 % N which relates to a 0.25 mmol/g loading of the imidazolium anchored onto the surface. Given the significant carbon percentage seen, 7.63 %, the CHN strongly indicates an organic component has been introduced to the HP-SAPO-5. The shift in the expected ratios between carbon, hydrogen and nitrogen is ascribed to trapped solvent within the structure likely due to the microporous component.

Powder XRD was crucial to determine that the anchoring stage did not significantly alter the framework structure. Any detrimental effects of the anchoring technique on the framework could remove the aforementioned advantages the material may have over the silica supported versions. No noticeable difference was found in the XRD patterns, Figure 68, with no extra peaks observed within the pattern for the immobilised organocatalyst, indicating the retention of both crystallinity and phase purity of the sample post immobilisation (see XRD section of Chapter 2 for exemplar Reitveld refinement). The retention of the crystallinity indicates that the structure remains and so the ordered nature of the interconnected micro and mesopores is preserved.

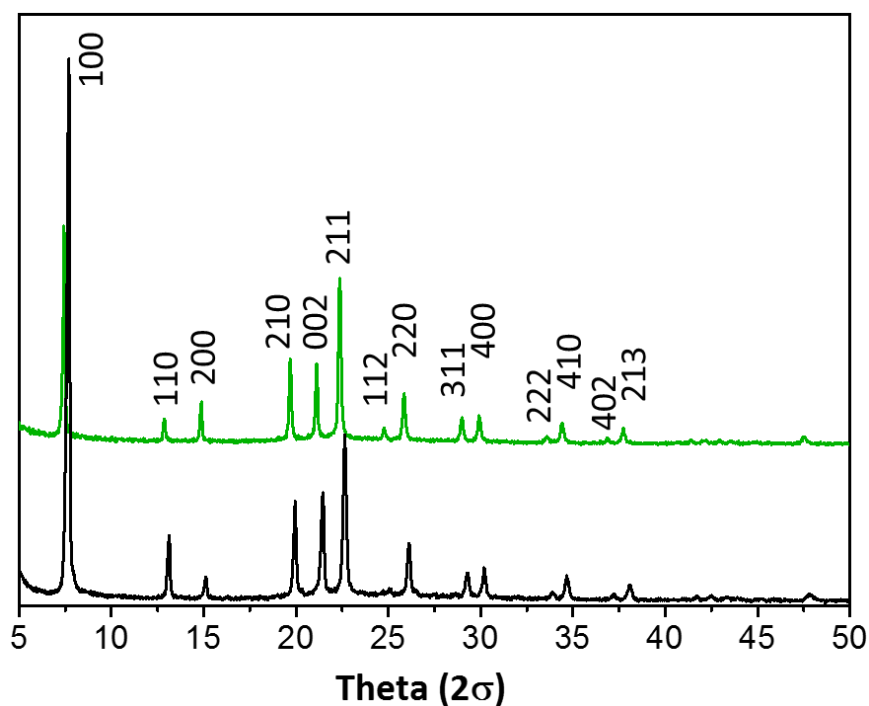


Figure 68: Powder XRD of diPrIm(I)/HP-SAPO-5 (green) and HP-SAPO-5 (black) to show retention of structural integrity. Patterns stacked to aid comparison.

Further confirmation can be obtained with collection of a low angle XRD scan, whereby a broad peak in the low angle region (2θ less than 5°) is indicative of mesopore presence.

Both the starting framework and modified version are phase pure and crystalline suggesting that anchoring organic moieties has not affected the structure significantly. Conversely, the framework could have had an adverse effect on the structure of the organic moiety, therefore characterisation of the organic component of diPrIm(I)/HP-SAPO-5 was completed.

FT-IR of the functionalised material was able to discern the key features of the imidazolium following attachment to the silanols of the HP framework.

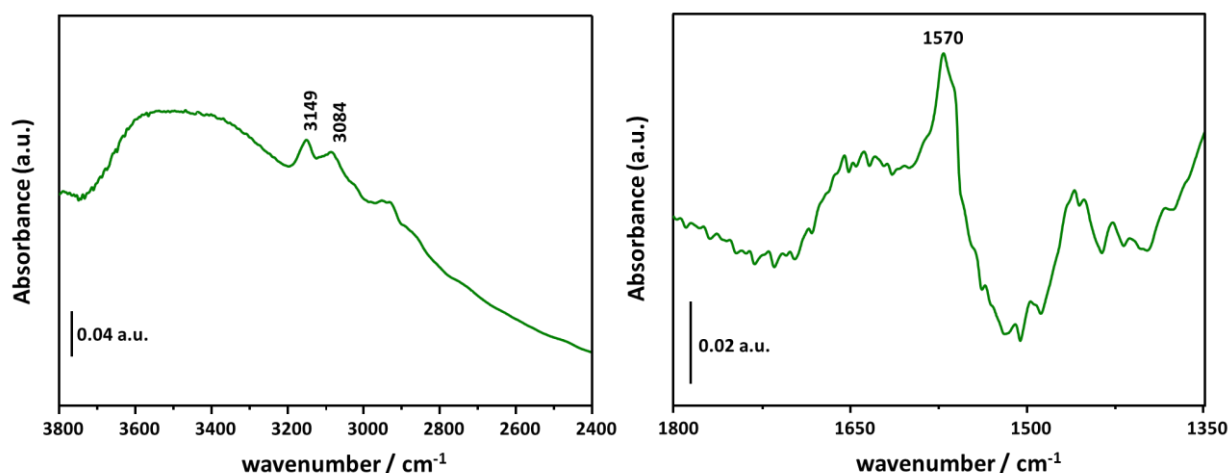


Figure 69: FT-IR spectra of diPrIm(I)/HP-SAPO-5 with regions 3800-2400 cm^{-1} and 1350-1800 cm^{-1} shown to aid peak identification. Obtained as a KBr disc at RT, sample degassed beforehand.

The region of 3700 - 3200 cm^{-1} displays a broad peak due to hydrogen bonded silanols both with each other and/or with any residual water molecules that were not removed from the framework prior to analysis. Despite this, the typical imidazole C-H stretches of the ring are still observable and present at 3149 and 3084 cm^{-1} . In the 1350 to 1800 cm^{-1} range (right, Figure 69) the imidazole ring stretch is seen at 1570 cm^{-1} with other signals in this region from the C-H bending, C=C and C=N of the imidazole ring. Given the intensive washing stages employed in the synthesis stage and the characteristic peaks which were seen in the FT-IR it is reasonable to conclude that the imidazolium has been incorporated into the HP framework.

To determine the nature of the interaction between the imidazole and the HP framework, solid state NMR probing ^{13}C and ^{29}Si was obtained. Covalent bonding, occurring with displacement of the methoxy groups, results in the formation of an additional environment in the ^{29}Si spectra from the Si-C bond with the reverse C-Si also seen in the ^{13}C spectra.

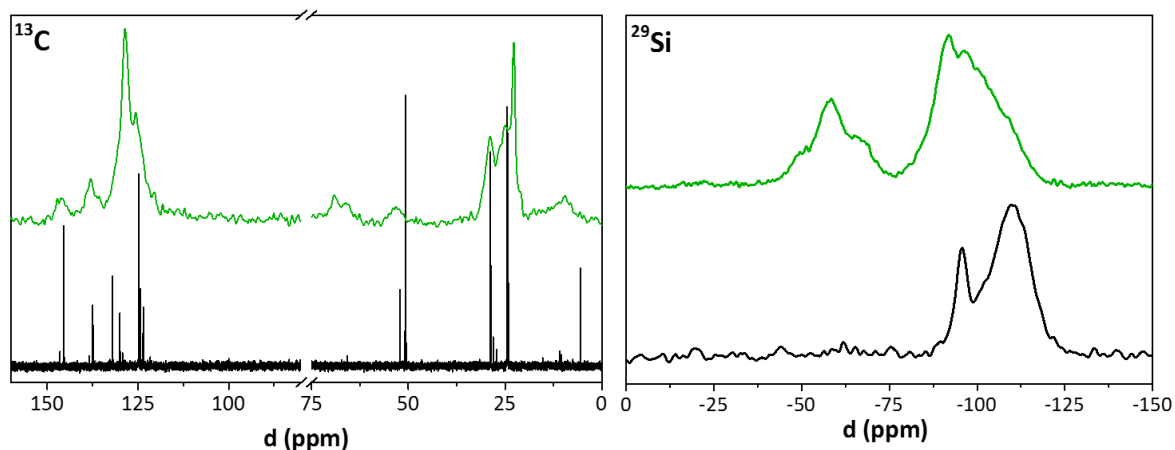


Figure 70: Solution ^{13}C spectrum for diPrIm(I)-trimethoxysilane oil (black) and solid state ^{13}C of diPrIm(I)/HP SAPO-5 (green), left. ^{29}Si solid state NMR of diPrIm(I)/HP SAPO-5 (green) and as synthesised HP SAPO-5 (black), right. **Note:** the region of 75 – 80 ppm has been omitted from the ^{13}C spectrum to remove the large CDCl_3 solvent peak to aid comparability. ^{29}Si NMR was obtained by CP.

Retention of structure is observed from the ^{13}C spectra, the peaks at approx. 10 and 52 ppm are assigned to the CH_2Si and $\text{CH}_2\text{-N}$ environments in the linker with the alkyl-chain CH_2 discernible at 22 ppm as the shoulder peak. The remaining peaks, 125 -150 ppm, indicate the structure remains intact on anchoring, see section 3.3.1 for full analysis. ^{29}Si experiments showed the presence of the silanol handles for functionalisation are present within the mesopores of the HP SAPO-5 material before imidazolium attachment as the peak at -110 ppm is the Si-O-Si environment and the peak at -95 ppm relates to the Si-OH. Si-C peak appearance in the diPrIm functionalised analogue confirms covalent anchoring.

As with the exclusively silica based system, the maintenance of porosity following post synthetic modification is key with the HP materials. Nitrogen adsorption studies, both prior and after the addition of the imidazolium were used to understand the location of the covalent anchoring and determine the effect on the framework surface area and porosity.

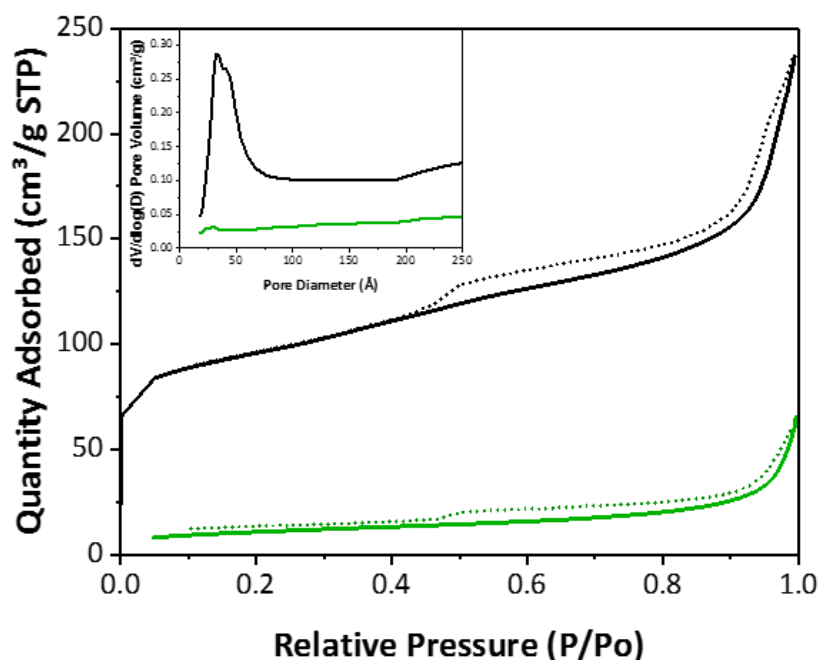


Figure 71: N₂ isotherm for HP SAPO-5 (black) and diPrIm(I)/HP SAPO-5 (green), inset: pore distributions for HP SAPO-5 (black) and diPrIm(I)/HP SAPO-5 (green). Adsorption isotherm (solid line) and desorption isotherm (dotted line).

The pore distribution indicates that blocking of the mesopores has almost completely occurred upon anchoring of the organic component, however, the type II isotherm indicates that the mesoporosity is maintained, as the H2 hysteresis is still observable in the diPrIm(I)/HP SAPO-5. The surface area of the imidazolium variant, $37 \pm 1 \text{ m}^2/\text{g}$, is considerably lower than that of the blank framework, $315 \pm 4 \text{ m}^2/\text{g}$. This result, in combination with the pore distribution would indicate that the location of the organic moiety is within the mesopores of the HP material, accounting for the considerable drop in isotherm values for the proposed catalyst, almost to the extent of pore blockage.

The conversion of styrene oxide to styrene carbonate was studied to probe the ability of the diPrIm(I)/HP SAPO-5 catalyst. Additionally, the blank framework was trialled under batch conditions in order to determine the benefits of the post synthetic modification stage.

| Catalyst | Conditions | Conversion / % | Selectivity / % | |
|-----------------------------------|---|-------------------|-----------------|----------|
| | | | Carbonate | Aldehyde |
| HP SAPO-5 | 24 hours, 20 bar CO ₂ , 115 °C, 5 g SO | 99 | - | 34 |
| diPrIm(I)/HP SAPO-5 | 2 hours, 20 bar CO ₂ , 115 °C, 5 g SO | 36 | 26 | 74 |
| diPrIm(I)/SiO ₂ (30 Å) | 2 hours, 20 bar CO ₂ , 115 °C, 5 g SO | 55 | 98 | 2 |

Table 27: Summary of styrene oxide to styrene carbonate by HP SAPO-5 and silica based material with similar pore distribution. Analysed by ^1H NMR, mesitylene used ITSD.

The catalysis results show that the production of the cyclic carbonate product is possible with the diPrIm(I)/HP SAPO-5 material synthesised, Table 27. However, the framework appears to promote the rearrangement of the epoxide to the aldehyde, resulting in far lower selectivity towards the cyclic carbonate desired product when compared against the purely silica analogue. The blank HP-SAPO-5 was tested and in a 24 hour batch reaction, it was seen that complete conversion was obtained but no styrene carbonate was detected *via* NMR of the reaction solution. The aldehyde was observed with 34 % selectivity towards it shown. The rest of the products were instead high molecular weight by-products, largely formed due to the acid sites present within the framework. Covalent attachment of the imidazolium within the mesopores *via* the silanol groups was not only successful but also returned a catalyst capable of CO_2 utilisation at reasonable rates, TOF was 51 hr^{-1} , based on the organic component. Poor selectivity with respect to the cyclic carbonate stems from the acidity of the framework promoting rearrangement of the starting material with reasoning for this as follows. Yet, these results clearly demonstrate that the imidazolium is key in forming the desired, cyclic carbonate, product and therefore the design strategy presented did produce an active heterogenised catalyst that is covalently anchored on a HP SAPO-5 framework, shown in the characterisation.

Newland *et al* discussed the role of the dopant and silanol groups in the overall acidity of the framework^[291]. It was shown that the acidity of the HP SAPO-5 is from both the Brønsted acid centres within the micropores and acidic silanols in the mesopores. It is a combination of the two that acted as the catalytic active sites for the reaction reported, the Beckmann rearrangement. It was seen that interplay between these two sites was the reason behind the high activity shown by the material which acted as a weak acid catalyst^[291]. This can explain the results shown in the above. The anchoring of the organic to the silanols in the imidazolium version may lower the acidity of the framework sufficiently, *via* capping of the silanols, and prevent the formation of larger molecular weight products driven by the higher acidity. However, the acidity in this case is not lowered to an extent that the rearrangement is prevented and so still occurs. Therefore, the aldehyde selectivity increase with the imidazolium is explainable if the anchoring lessens the acidity. This allows for cyclic carbonate formation to occur as the active sites are now accessible to the substrate and not blocked by the higher molecular weight products that form when the acidity is greater.

There are several possibilities to mitigate this to produce a higher yield of the cyclic carbonate. Capping of the remaining silanol groups which were not used for anchoring may further mitigate

some of the framework acidity. This can be done with a facile technique, Figure 72, undertaken after post-synthetic grafting of the imidazolium.

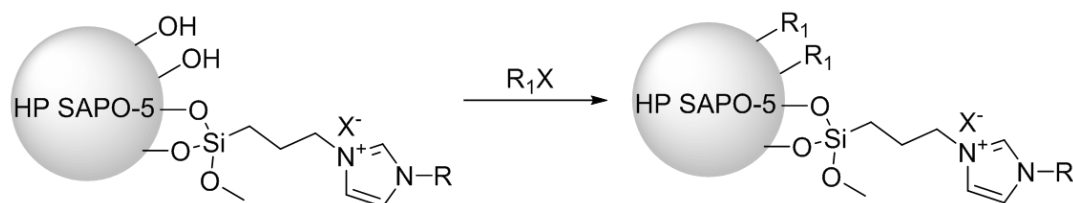


Figure 72: Proposed capping method to reduce the number of silanols present in the framework mesopores after imidazolium grafting.

This method does not address the Brønsted acid sites which would still be present. Therefore, an alternative approach is needed. The isomorphous substitution of Si for P in the HP SAPO-5 creates the Brønsted acid sites, Figure 74, therefore modulation of the acidity is possible with other substitutions or none. Consequently, a range of different elements can be explored as dopants to tune the activity of the catalyst^[9]. The benefit of doping is the creation of a further active site to those in the mesopores. As such, it could be envisaged that a tandem reaction of alkene epoxidation^[297,298], catalysed by the introduced metal species, followed by CO_2 utilisation could be undertaken in the future. However, prior to this, improvement in the selectivity towards the carbonate is more important.

Consequently, HP AIPO-5 was synthesised and the diPrIm species was accordingly grafted to it, Figure 73, with the lower framework acidity intended to improve the selectivity. The removal of the Si dopant removes the source of the Brønsted acidity. Therefore the selectivity of the HP AIPO-5 should improve towards the cyclic carbonate versus HP SAPO-5 for the version with the anchored organocatalyst.

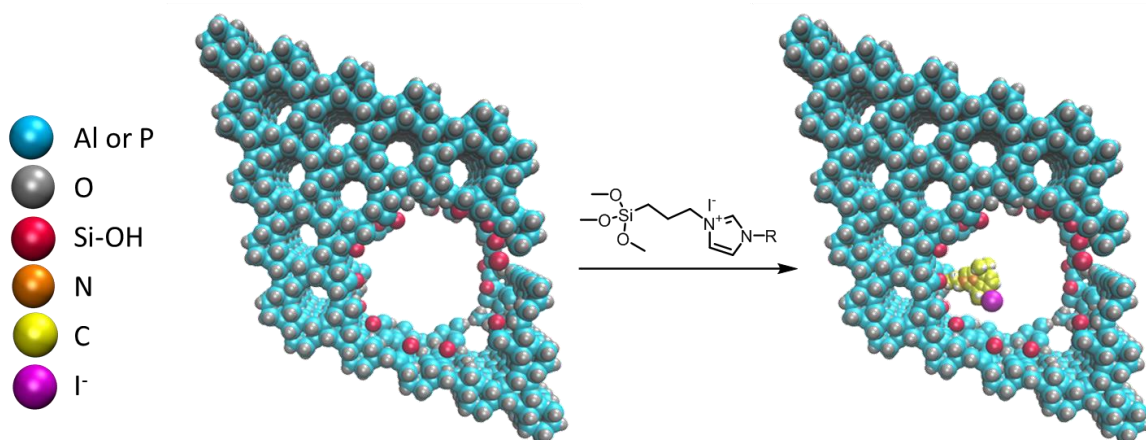


Figure 73: Diagrammatic representation of imidazolium grafting to HP AIPO-5, anchoring location depicted as within the mesopore. R = 2,6-diisopropylphenyl.

Reduction in acidity versus that of the SAPO stems from the following, as previously alluded to. In the SAPO the Si is situated in the site normally occupied by P, creating a charge imbalance over the course of the framework, Figure 74.

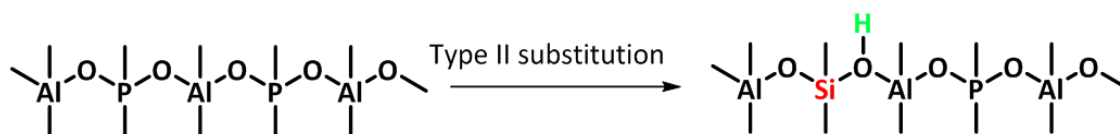


Figure 74: Representation of isomorphous substitution of P with Si, leading to Brønsted acid site creation in the SAPO (right) as opposed to the AlPO (left).

To address this a proton acts as a balance, and therefore the isomorphous substitution of Si for P introduces the Brønsted acid site depicted as a green sphere in Figure 67 and above, Figure 74. As the AlPO does not have such substitution it has a lower overall acid strength than observed in the SAPO, as shown by Newland *et al* via FT-IR studies^[291]. The grafting procedure produced diPrIm(I)/HP AlPO-5 using silanols present for functionalisation which remain from surfactant removal.

| Material | C /% | H /% | N/% | Loading/ mmol/g |
|---------------------|------|------|------|-----------------|
| diPrIm(I)/HP AlPO-5 | 6.78 | 1.29 | 0.29 | 0.11 |

Table 28: CHN % values for the diPrIm(I)/HP AlPO-5, with loading calculated from the nitrogen percentage.

Given the low CHN values of the diPrIm(I)/HP AlPO-5, Table 28, and the low conversions observed for the HP SAPO-5 materials, Table 27, longer reaction timescales were employed. Again, the blank framework was tested. Conversion of 77 % occurred with the unmodified framework and no carbonate product observed, as was expected.

| Catalyst | Conditions | Conversion / % | Selectivity / % | | TON |
|---------------------|--|----------------|-----------------|----------|------|
| | | | Carbonate | Aldehyde | |
| diPrIm(I)/HP AlPO-5 | 24 hours, 20 bar CO ₂ , 115 °C, 5g SO, 0.1 g catalyst | 72 | 88 | 12 | 1178 |
| HP AlPO-5 | | 77 | - | 87 | - |

Table 29: Summary of styrene oxide to styrene carbonate by HP AlPO-5 and silica based materials. TON based upon organic component. Analysed by ¹H NMR, mesitylene used ITSD.

The aldehyde, phenylacetaldehyde, was identified as the main component of the blank framework, HP AlPO-5, reaction mixture. Non-identified components, owing to multiple indiscrete peaks, were assumed to be similar to the of the HP SAPO-5 blank framework – higher molecular

weight by-products. The selectivity towards the aldehyde was shown to have increased for the blank HP AlPO-5 framework. This can be rationalised as the amount of high molecular weight products decreased. Therefore, following the conclusions drawn from the HP SAPO-5 data, the higher selectivity towards the aldehyde is from the lessened occurrence of the other side-reactions – the production of the higher molecular weight products because the overall framework acidity is now lower. Consequently, the rearrangement is the predominant reaction that is occurring.

The diPrIm(I)/HP AlPO-5 showed an impressive TON of 1178 with improved selectivity towards the carbonate product (88 %) resulting in a 63 % yield after 24 hours. The improved selectivity of the HP AlPO-5 analogue would appear to confirm that removal of the Brønsted acid sites improves the carbonate production as the formation of higher molecular weight products does not as readily occur. The imidazolium catalytic active sites are therefore not blocked so allowing for formation of the carbonate.

A range of different acid strength HP frameworks would need to be tested to definitively prove these conclusions as well as absolute proof of the predicted changes to the framework acidity upon imidazolium grafting. These initial findings indicate that the HP AlPO framework is a viable host for the imidazolium organic moieties and with further careful design could be engineered, even to surpass the catalytic ability of the silica organocatalysts discussed in section 3.3. Organic functionalisation of the HP silicoaluminophosphates and aluminophosphates is relatively novel and could prove to be an exciting avenue for not only CO₂ utilisation but also wider use for organocatalysed transformations. Further to this, the ability of the framework to, as previously mentioned, host other active sites creates greater still opportunities for catalytic pathways to be explored.

Another support, metal organic framework (MOF) MIL-101(Cr) was also explored as a host for the imidazole or imidazolium functionalities. This work is detailed extensively in Chapter 4.

3.5 Immobilised N-heterocyclic carbenes

Section 3.3.23.3 detailed that anchoring imidazolium species onto mesoporous silica produced a variety of heterogeneous catalysts effective in the production of cyclic carbonates from CO₂ and epoxides. The ability of the catalysts was shown to be influenced by the loading of the organocatalyst, pore size of the silica and the counter anion of the imidazolium. It was shown that the latter, the counter ion is the most important factor with catalytic ability $I^- > Br^- > Cl^-$, mirroring that of leaving group ability owing to C-X bond strength as the iodide bond is longer, therefore weaker. It was seen that on re-use the activity of the catalyst lowered dramatically over successive cycles, assumed to be from loss of the anion within the silica framework and substrate or product retention within the framework. Such dramatic activity decrease hinders the use of these materials in their current form as effective heterogeneous catalysts in the production of cyclic carbonates from CO₂.

However, the same structures lend themselves to the formation of N-heterocyclic carbenes, as discussed in section 3.1.3.1.

3.5.1 Characterisation

Deprotonation was undertaken on the silica based ionic liquids (imidazolium) produced and tested in section 3.3, followed by introduction of CO₂ to form the carboxylate. Specifically, the Melm, iPrIm, tBulm and MesIm versions were used. The characterisation for the Mes analogue is discussed. The carboxylate was found to be air stable and so allowed for characterisation and catalytic testing to be completed. A combination of XPS, FT-IR, TGA and TG-MS techniques confirmed the synthesis of the carboxylate. Formation of the carboxylate is easily detectable through IR due to the strong C=O and C-O bands.

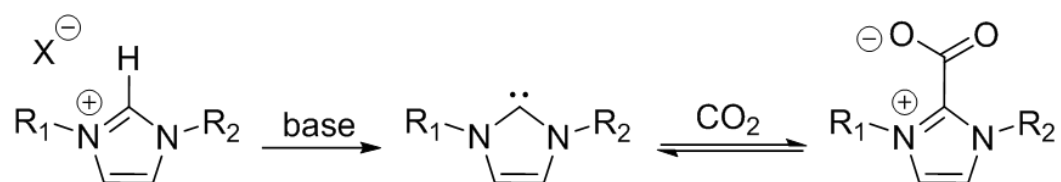


Figure 75: Imidazolium deprotonation to form the respective carbene followed by carboxylate formation upon introduction of a CO₂ atmosphere.

The framework contributes a number of peaks to the spectra, Figure 76A (below) the peaks at 800 cm⁻¹ and 950 cm⁻¹ (seen as shoulder on the Si-O-Si stretch) relate to Si-O symmetric stretch and Si-OH respectively. The large peak *circa* 1100 cm⁻¹ is the silica framework stretch of Si-O-Si and the broad peak at approximately 3200 - 3800 cm⁻¹ corresponds to the and Si-OH and any adsorbed

water on the sample. A further O-H bending stretch is seen at 1622 cm^{-1} . The imidazolium grafted to the silica causes the addition of the peak at 3144 v(C-H) with further peaks expected for C-H vibrations but are obscured by the large Si-O-Si framework peak.

In the carboxylate spectra, Figure 76A and B (green), characteristic peaks for the framework and imidazole peaks are evident with the addition of those relating to the carboxylate. The O-H bending stretch is observed at 1622 cm^{-1} in Figure 76A, is lost under the strong $\nu_{\text{as}}\text{CO}_2$ 1653 cm^{-1} which can be clearly seen and the appearance of this is indicative of the formation of the carboxylate species following: deprotonation of the imidazolium and successive carbene and carboxylate formation (upon CO_2 introduction). This is in close agreement with the work of Zhou *et al* where a di-substituted imidazolium on MCM-41 was used for carboxylate formation with FT-IR showing a peak at 1662 cm^{-1} [228]. Figure 76B also displays the same $\text{MesCO}_2/\text{SiO}_2$ material but after it was placed into a soxhlet apparatus (THF) overnight to wash the material. This was undertaken as an attempt to purify the material following the carboxylation, see latter XPS section for further details. It can be seen that the carboxylate feature at 1653 cm^{-1} remains, therefore the structure and presence of the CO_2 activated by the carbene is preserved.

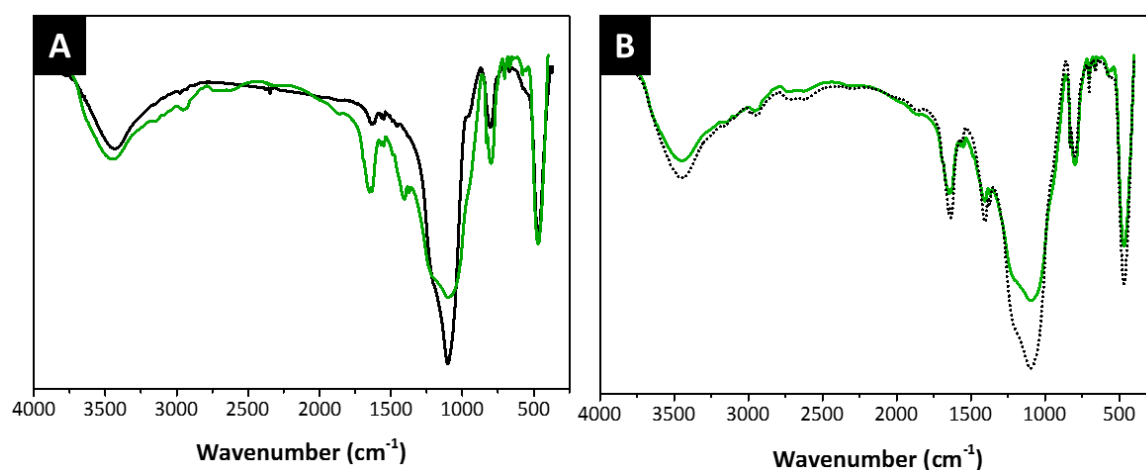


Figure 76: A) FT-IR of $\text{MesIm}/\text{SiO}_2$ (black) and $\text{MesCO}_2/\text{SiO}_2$ (green) prepared as KBr discs. B) FT-IR of $\text{MesCO}_2/\text{SiO}_2$ (green) and $\text{MesCO}_2/\text{SiO}_2$ following soxhlet washing (black dots) prepared as KBr discs. Data normalised for comparison.

XPS can further indicate the formation of the carboxylate as this is resolved as an additional peak within the C1s region. The spectra were referenced to the adventitious carbon peak at 284.4 eV therefore analysis of the C1s region is qualitative in nature. The Si2p doublet was observed as a single asymmetric peak rather than two discrete peaks, owing to the high energy used. No Si-C environments were discernible – taken to be masked beneath the larger Si-O-Si bulk peaks.

The C1s region displays the adventitious (C-C) carbon peak with the shoulder peak of this correlating to C-O, which is seen in both the imidazolium and the carboxylate. An additional peak at 289.5 eV relating to the C=O environment is seen within the carboxylate sample. This feature is indicative of the formation of the carboxylate, given the absence of this in spectra collected on the imidazolium.

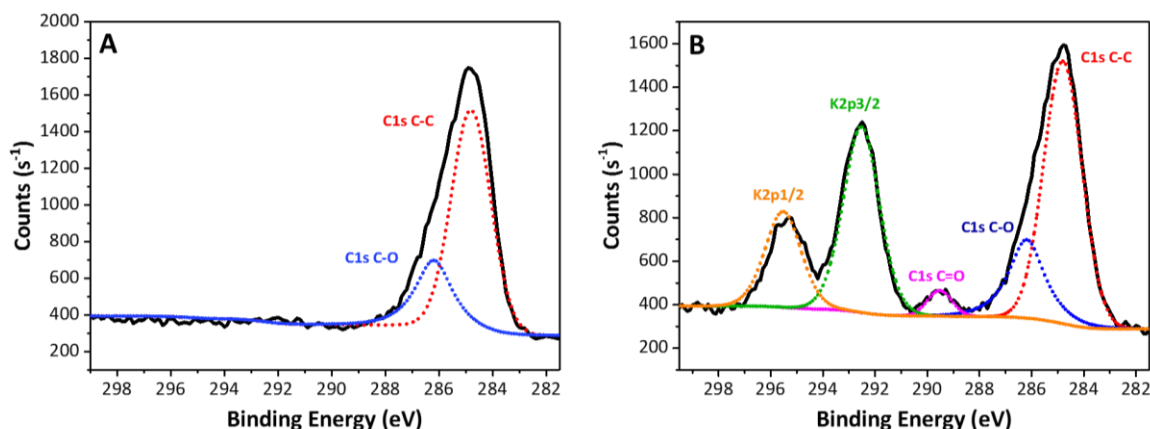


Figure 77: C1s and K2p regions of A) MesIm(I)/SiO₂ and B) MesCO₂/SiO₂. Raw data (black) with fittings labelled in associated colour.

However, the C1s region also shows a doublet ascribed to K2p with set spin orbit coupling of 2.8 eV. Whilst unexpected, the presence of potassium within the sample can be attributed to the base, potassium *tert*-butoxide, which was used in the deprotonation step of the synthesis. It is clear that a significant amount of potassium from the base remains, which, will presumably be as KI in this instance given that iodide was the counter-ion for the precursor imidazolium. The K2s peak was also seen in the survey scan *circa* 378 eV as well as the doublet for iodine at 619 eV, indicating that the by-product of the deprotonation is KI as predicted.

| Sample | Si / % | K / % |
|--------------------------------------|--------|--------|
| MesIm(I)/SiO ₂ | 33.37 | < 0.01 |
| MesCO ₂ /SiO ₂ | 32.47 | 4.00 |

Table 30: ICP-OES results from Medac Ltd. showing the presence of potassium following the carboxylate synthesis stage.

Potassium iodide was still present following extensive washing in a THF soxhlet, Figure 77B, in attempt to remove it from the system. Further confirmation of the potassium was obtained through ICP-OES, Table 30, a more detailed analysis is needed to confirm the nature of this and whether some of the potassium is potassium iodide. This would be problematic for the catalytic results as KI can be catalytic in the production of cyclic carbonates^[107,248]. If KI is found to be

present, then a simple solution to this would be to use a different trimethoxysilane in the synthesis/or employ an ion exchange step which would remove the iodide and so prevent further complications.

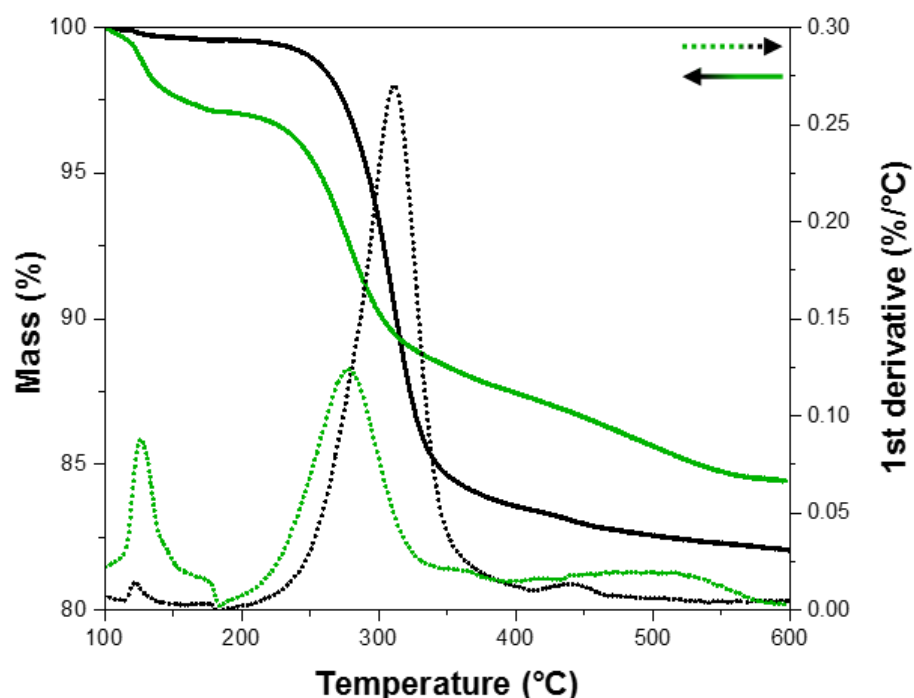


Figure 78: Thermogravimetric measurement of MesIm/SiO₂ (black) and MesCO₂Im/SiO₂ (green), 1st derivative also shown MesIm/SiO₂ (black dots) and MesCO₂Im/SiO₂ (green dots)

A combination of thermogravimetric analysis (TGA) and thermogravimetric-mass spectrometry (TG-MS) techniques were used to unequivocally identify and prove the formation of the carboxylate. TGA of the imidazolium and the carboxylate produced distinctly differing decomposition profiles to one another, Figure 78. Both had a solvent loss prior to 100 °C which was removed following normalisation to this temperature. The imidazolium showed minimal mass loss in the region from 100 to 225 °C following which there is a sharp drop attributed to the breakdown of the organic species and its removal from the silica, total mass loss for the imidazolium system was 17 % which compares favourably with that expected - the loading was calculated to be 0.42 mmol g⁻¹ from CHN elemental analysis.

The 'carboxylate' version shows an earlier loss than the imidazolium, at approximately 120 °C. This theoretically would be the release of CO₂ captured by the carbene. The next derivative peak starts at almost the same temperature as the degradation of imidazolium. This would be expected given the similar structure following CO₂ loss. The overall loss for the carboxylate, including decarboxylation, is 15.5 %. The difference with respect to the imidazolium can be explained in two ways; firstly the loss is lowered for the carboxylate as the iodide, a heavier element, is no longer

present therefore the mass of the anchored component is lower despite the addition of CO₂. However, this is unlikely when the XPS data is considered. Therefore more likely is the inorganic component of the material is larger, due to the KI, so does not decompose under TGA, as a result the organic component is smaller.

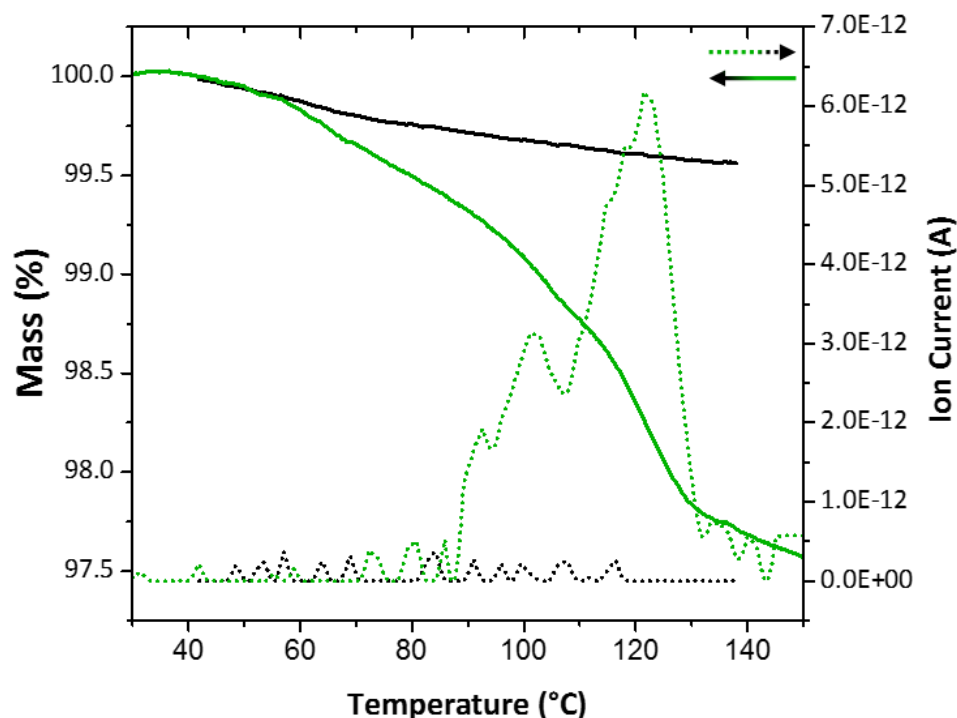


Figure 79: Thermogravimetric MesIm/SiO₂ (black) and MesCO₂Im/SiO₂ (green) and mass spectrum data for m/z of 44 for MesIm/SiO₂ (black dots) and MesCO₂Im/SiO₂ (green dots).

TG-MS was used to identify the initial mass loss peak for the carboxylate material, Figure 79. The mass spectrometer scanned through m/z values from 0 to 90 with a particular focus on m/z 44 (CO₂). The m/z of 44 trace increased appreciably over the initial mass loss region of the carboxylate which has been highlighted in Figure 79. Over the equivalent temperature region for the imidazolium there was no appreciable change in the ion current for m/z 44, indicating that CO₂ was not present in the decomposition stream. A lower decarboxylation temperature to that observed under the TGA measurement was attributed to the TG-MS setup being under vacuum unlike the TGA which operates under a carrier gas flow. No other species were detected by the mass spectrometer in significant quantity during this time, Figure 80, with the exception of m/z 18, 17 and 16. The m/z of 16 peak is fragmentation of the removed CO₂ molecule but also from water which accounts for the peaks at m/z 17 and 18. Water was present consistently throughout the measurement – it was concluded that either the sample, the instrument gases or both were not completely dry. Complete drying of the carboxylate versions to obtain water removal from the sample is experimentally challenging given the low decarboxylation temperatures observed.

Fragmentation of the CO_2 should appear as a peak at m/z 28. This was not observed as a large amount of nitrogen was present in the background signal and meant the relatively minute signal from CO_2 fragmentation was removed during background subtraction.

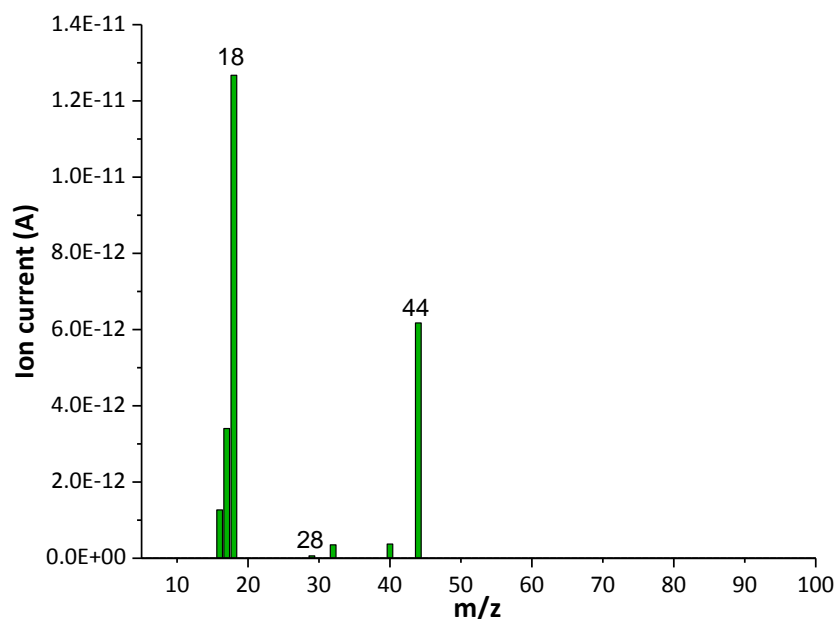


Figure 80: Mass spectrum snapshot for $\text{MesCO}_2/\text{SiO}_2$ when $T = 120\text{ }^\circ\text{C}$ (approximate ion current peak maximum for $m/z = 44$)

Therefore the loss in the TGA can be said to be the decarboxylation as confirmed by the TG-MS technique. The carboxylate has been synthesised successfully.

3.5.2 Catalytic testing

After characterisation indicating the formation of the carboxylate the materials tested for efficacy in the CO_2 and epoxide reaction with comparison made to the imidazolium materials which they were synthesised from. Three of the variants were tested initially across a range of R groups, with the MesIm not in sufficient quantity following characterisation to be tested.

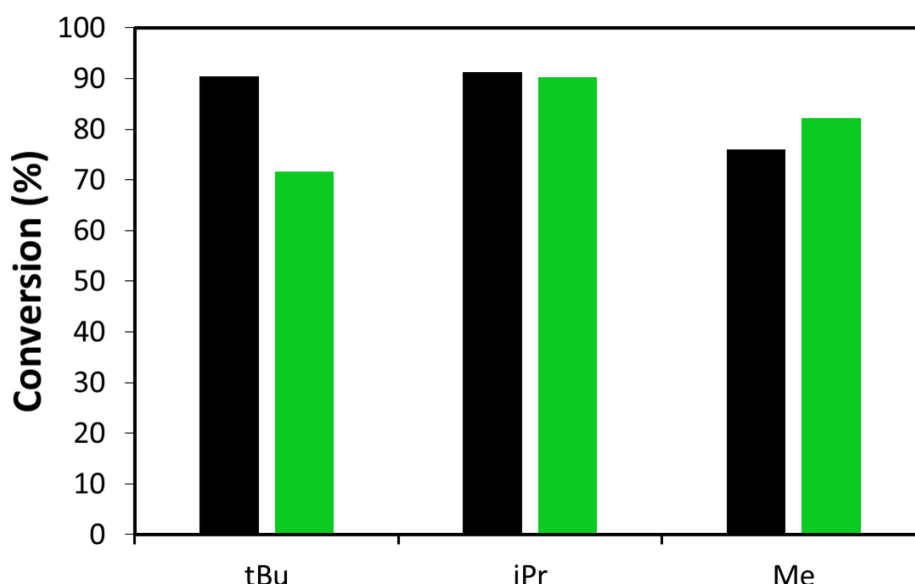


Figure 81: Conversion values of butylene oxide by Me, iPr and tBu materials, imidazolium (black) and carboxylate (green) for all cases. Reaction conditions: 115 °C, 6 hours, 20 bar CO₂ at RT, 72 mmol butylene oxide, 0.1 % mol loading catalyst. Analysed by ¹H NMR, mesitylene as ITSD.

Mixed results were obtained upon testing of the materials, Figure 81. The carboxylate materials are active for the reaction in all cases, with the methyl imidazole based carboxylate showing a greater conversion than that of the imidazolium. It was envisaged that the R group would have a pronounced effect on the catalytic ability as it determines the stability of the carboxylate, through being one of the reaction intermediates. This can be considered in two ways, either a low stability of the carboxylate means it would be highly reactive or it may be that such high instability leads to insufficient lifetime to undertake the reaction at the elevated temperatures used. This was rationalised by Zhou *et al.*^[278] for a homogeneous di-substituted system by assessment of the thermal stability. They concluded that the thermal stability of the system is related to the activity, as the final stage of the reaction, see Figure 82, requires the cleaving of the C_{carboxylate}-C_{carbene} bond; the strength of which determines the stability. Also it was seen that in the presence of CO₂ the thermal stability of the carboxylate is maintained, therefore it can be said that the carboxylate would have a sufficient lifetime to ring open the epoxide^[278]. High resolution TGA of the decarboxylation then may be able to determine the thermal stabilities with respect to the R group across the range of materials synthesised and so be able to analyse or explain any trend in reactivity shown.

The carboxylate methodology is interesting as the NHC formed directly activates CO₂. The CO₂ and epoxide reaction therefore occurs *via* a different catalytic pathway to the halide catalysed route which was depicted above, Figure 62, which relied on the ring opening of the epoxide. With this

variant, the carboxylate undertakes the ring opening of the epoxide, followed by the ring formation of the 5-membered cyclic carbonate ring which results in the reformation of the carbene, Figure 82. The critical step in the continuation of the catalytic cycle is the regeneration of the carboxylate from the carbene reacting with another CO_2 to activate it.

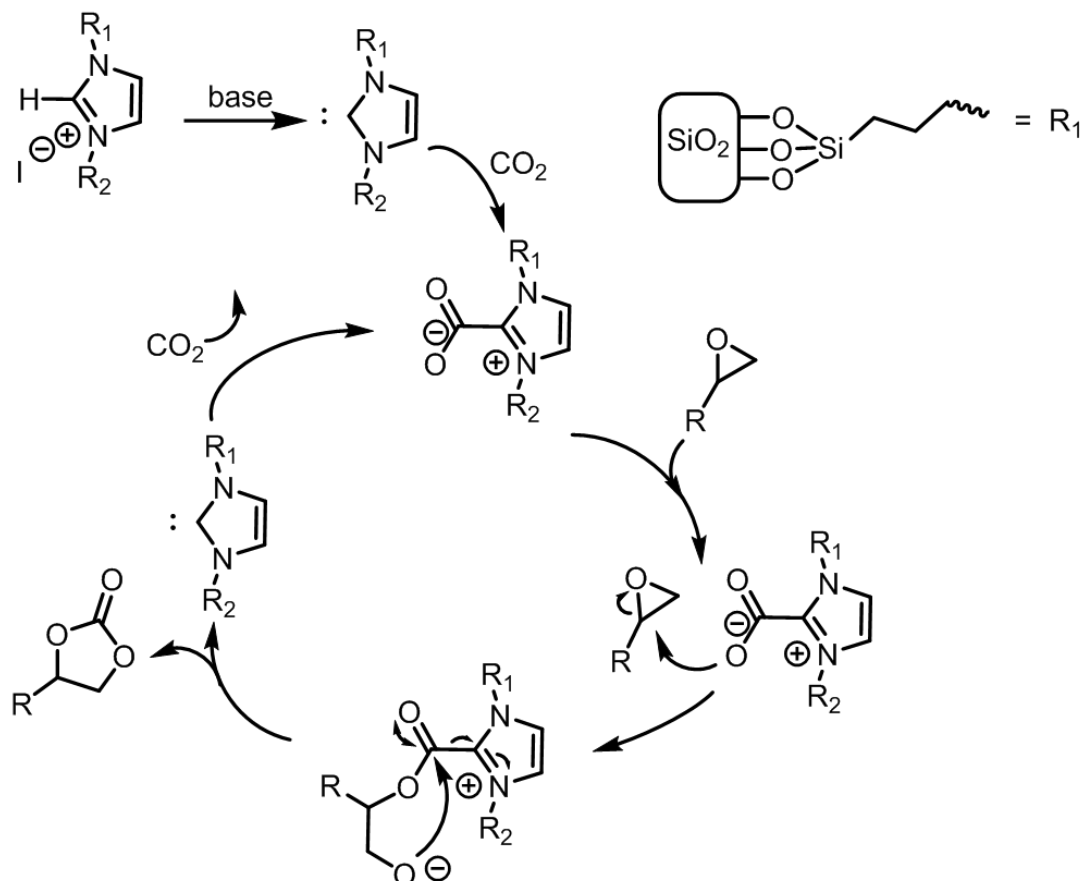


Figure 82: Proposed mechanism for the carboxylate catalyst. R_2 equal to structure shown in Table 22.

The alternate pathway of the carboxylate compared to the imidazolium may provide access to different reactions with carbon dioxide or allow for cyclic carbonate synthesis from using a greater substrate scope than with the imidazolium, such as non-terminal epoxides.

However, the ambiguity in the current catalysis results obtained - despite the high activity of the variants tested to date – necessitates further optimisation of the synthesis and characterisation procedures. Iodide removal needs to be undertaken and a means to quantify and ensure the completed conversion of the imidazolium to the carboxylate *via* the carbene found, solid state NMR and TG-MS may be able to achieve this.

3.6 Future work and conclusions

3.6.1 Silica based imidazolium organocatalysts

Combination of imidazolium species with silica supports created heterogeneous organocatalysts which could catalyse the reaction of epoxides and CO₂. The cyclic carbonate product was obtained in high yield owing to the high conversion and selectivity values observed, and given the low catalyst quantities used, resulted in large turnover numbers. The materials synthesised were extensively characterised to confirm that the organic component structure was retained during and after the synthesis processes and was found to be covalently bound to the silica support *via* a facile methodology. Substrate, imidazolium structure, pore diameter, anion and loading were altered to investigate the effect of the changes on the rate of carbonate production, with the latter two parameters seen to have the largest influence on activity. The best result was obtained for a 0.33 mmol/g loading of diPrIm(I)/SiO₂(150 Å) which at 0.1 mol % returned 81 % yield (4.05 g of cyclic carbonate) after 6 hours reaction time. High TOF values of 363 hr⁻¹ and TON of 2181 were seen, which are, to our best knowledge, higher than those reported in the current literature for metal free, heterogeneous organocatalysts under solvent free conditions.

However, whilst initial cycles produced high TOF and yield values, re-use showed the activity of the silica based materials decreased significantly. Characterisation of expended catalysts indicated that either the substrate or product or both were becoming trapped within the porous structure and lowering reaction rates in sequential cycles. The organic content was shown to be maintained, however it was theorised that iodide content may have decreased. Further studies on the used material, specifically ICP-OES are needed and would confirm this.

3.6.2 HP AlPO-5 based imidazolium organocatalysts

The viability of HP-AlPO and SAPO materials for CO₂ utilisation was proven. Covalent anchoring of imidazolium species within, specifically, the mesopores of the material was confirmed and shown to occur with no degradation of the host or organic components. The selectivity towards the desired product was revealed to be hindered by the acidity of the framework. Through dopant, Si, removal in the creation of HP AlPO-5 a reduction in the acidity was achieved, producing a variant which afforded a 63 % yield of the carbonate over a 24 hour reaction with improved selectivity when compared to the HP SAPO-5 version. These materials show great promise as they have much higher thermal stability and mass transport capability than the silica variants owing to the interconnected micro and mesopores. Further work with these materials would focus on the continued improvement of the selectivity of the catalysts to achieve values similar to those seen

for the silica systems. Routes to improve selectivity further have been documented in the proceeding discussion in this Chapter with the capping of the remaining silanol groups after the covalent anchoring suggested.

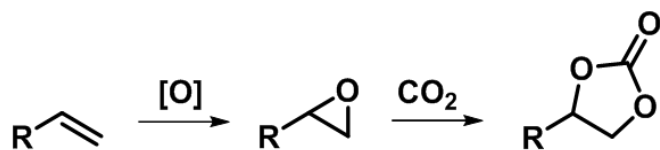


Figure 83: Proposed tandem reaction to produce cyclic carbonates from olefins

Once optimised for the production of cyclic carbonates, the HP AlPO-5 support should be fully exploited as it has greater scope for modification than mesoporous silica. The ability to carefully design microporous AlPO structures for specific functions is well documented^[9] and so the organic component produces multiple functionality within the HP material. It can consequently be envisaged that a tandem reaction taking advantage of the multi-functional nature could be achieved. A candidate reaction for this is to convert an alkene to a cyclic carbonate *via* the epoxide, Figure 83. Recent literature has shown proof of concept for this tandem reaction to be undertaken but often the reactions were treated individually^[299,300]. The capability for the epoxidation has been proven with the TiVAIPO-5 bimetallic system and so a starting point has been established for the individual stages of this process with variants of the same support^[298]. It would be highly desirable if this was achievable as a one pot, cascade reaction employing a single, bifunctional catalyst, in an environmentally friendly manner. Some consideration to this reaction has been given in Chapter 5, albeit with a different catalyst.

3.6.3 Heterogeneous NHCs

Cycloaddition of CO₂ into epoxides was successfully undertaken with NHCs produced from silica based imidazolium moieties. A range of characterisation unequivocally validated the synthesis technique in formation of the carboxylate. XPS observed the C=O environment of the CO₂⁻ and TG-MS detected the removal of the CO₂ upon thermal treatment of the sample. The results of the catalytic data were promising, in that the cyclic carbonate was obtained in high yield (up to 90 % in 6 hours) as conversion and importantly selectivity were high.

However, presence of potassium in the XPS spectra and in ICP-OES measurements, led to the conclusion that KI, a known catalyst for the reaction, is produced and retained in the silica as a by-product of the deprotonation stage. The use of an alternative trimethoxysilane species or, as discussed above, ion exchange to remove the iodide presence prior to NHC synthesis would prevent the formation of the KI. The percentage of the imidazolium converted to the carboxylate

was not quantified, use of solid state NMR in future work would be useful to determine this through observation of the change in chemical environments that occurs with the formation of the CO₂ adduct. Alternatively, a quantitative assessment using TG-MS could be undertaken through comparison against known inputs of CO₂ pulsed into the MS functionality. These problems are required to be solved for improvement in the current state of the materials shown here.

Also required to be considered is: for the conversion of epoxides and CO₂ to cyclic carbonates using NHCs, the sensitivity to water is currently a significant hindrance to the synthesis stage, but also would affect the catalytic and recycle ability through re-protonation of the carbene. A paper from Tasci *et al*^[301] provided a possible new avenue for NHC use. A silver-NHC was shown to be able to be used with minimal loss of activity over 7 cycles for cyclic carbonate formation, even without the use of a co-catalyst. A metal-NHC, silver based or otherwise, could potentially overcome the issues involved with the aforementioned methodology and as the NHC is anchored, allow for easier recycling of the system. A notable benefit is the formation of the Ag-NHC directly from the introduction of Ag₂O and the imidazolium. For the work discussed in this chapter this is advantageous for two key reasons. Firstly, the ability of the Ag-NHC to be formed from the imidazolium removes the need for a base to be used, thus removing the by-products, such as KI, which complicated the methodology. Secondly, the free carbene does not appear to be present as an intermediate in the system discussed by Tasci *et al* and therefore this prevents the opportunity for re-protonation from water or other proton sources present within the system. The combination of a metal and the NHC system can then undertake the reaction, an Ag/NHC system for cyclic carbonate production from propargylic alcohols has also been recently reported^[302]. Careful monitoring of any leaching would be needed if this were to be employed.

Appendix A

A.1 ^{29}Si CP and DE solid state NMR

Detection of the Si-C environment indicative of the covalent bonding of the imidazolium to the silica support *via* the propyl linker required the use of cross polarisation in order to produce a visible peak in the spectra as the loading of the organic on the support is low, as per elemental analysis.

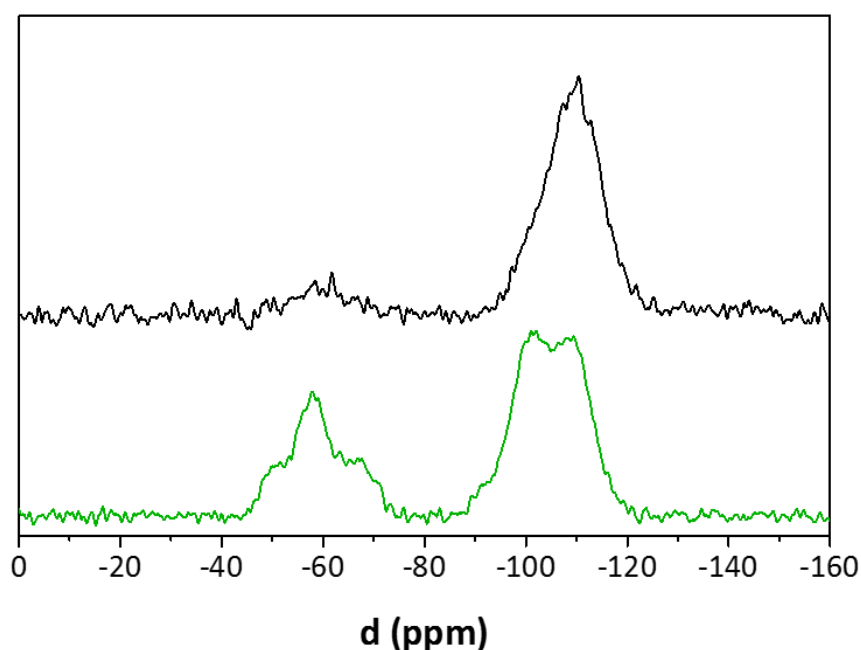


Figure A1: Cross Polarisation (green) and Direct Excitation ^{29}Si spectra for diPrIm(I)/SiO₂ to show the requirement for CP measurement.

The use of CP prevents the use of spectra for quantitative analysis of the loading *via* NMR.

A.2 Pore size distributions

A check on the pore distribution of the silica used in the pore diameter study was undertaken to confirm the values used were similar to that quoted by the manufacturer.

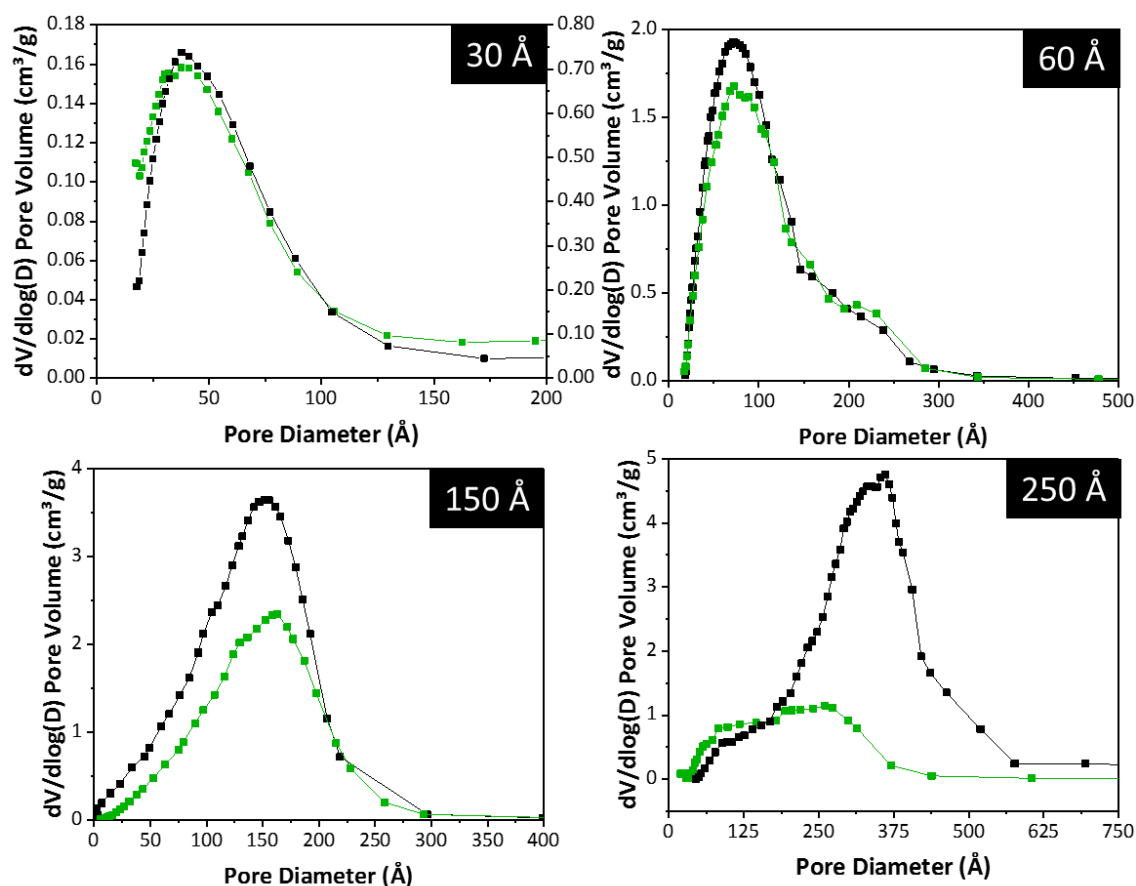


Figure A2: BJH Pore size distributions for 30, 60, 150 and 250 Å blank silica (black) and diPrIm(I)/SiO₂ (green) as labelled. RHS y-axis for 30 Å relates to the blank silica (black), plots stacked to aid comparison.

A.3 TGA curves of pore diameter catalysts

Thermal degradation temperature and loading of the range of difference pore diameter catalysts was found from the TGA following the data being normalised.

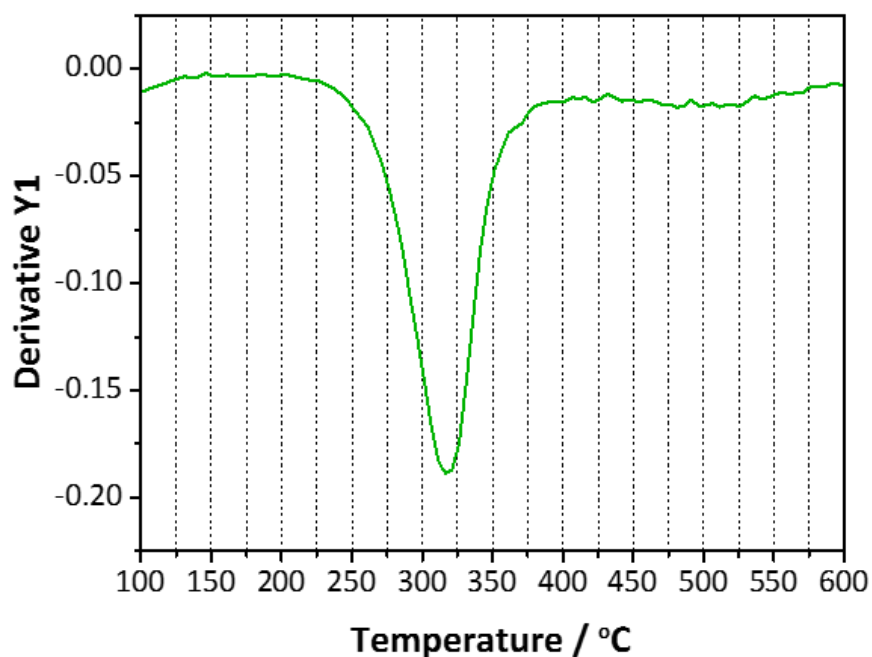


Figure A3: 1st derivative of mass % for diPrIm(I)/SiO₂ 150 Å.

The first derivative being used to find the point of inflection of the curve and so the maximum working temperature.

A.4 NMR confirmation of anion exchange

Confirmation of anion exchange to bistriflimide was confirmed by ¹⁹F and ¹H NMR. Complete exchange was assumed as there was only a single peak observable in the ¹H spectra relating to the C-H proton which is highest shifted and relates to that between the two nitrogens of the ring (at 8.68 ppm, shifted from 10.13 ppm in diPrIm with iodide as counter ion).

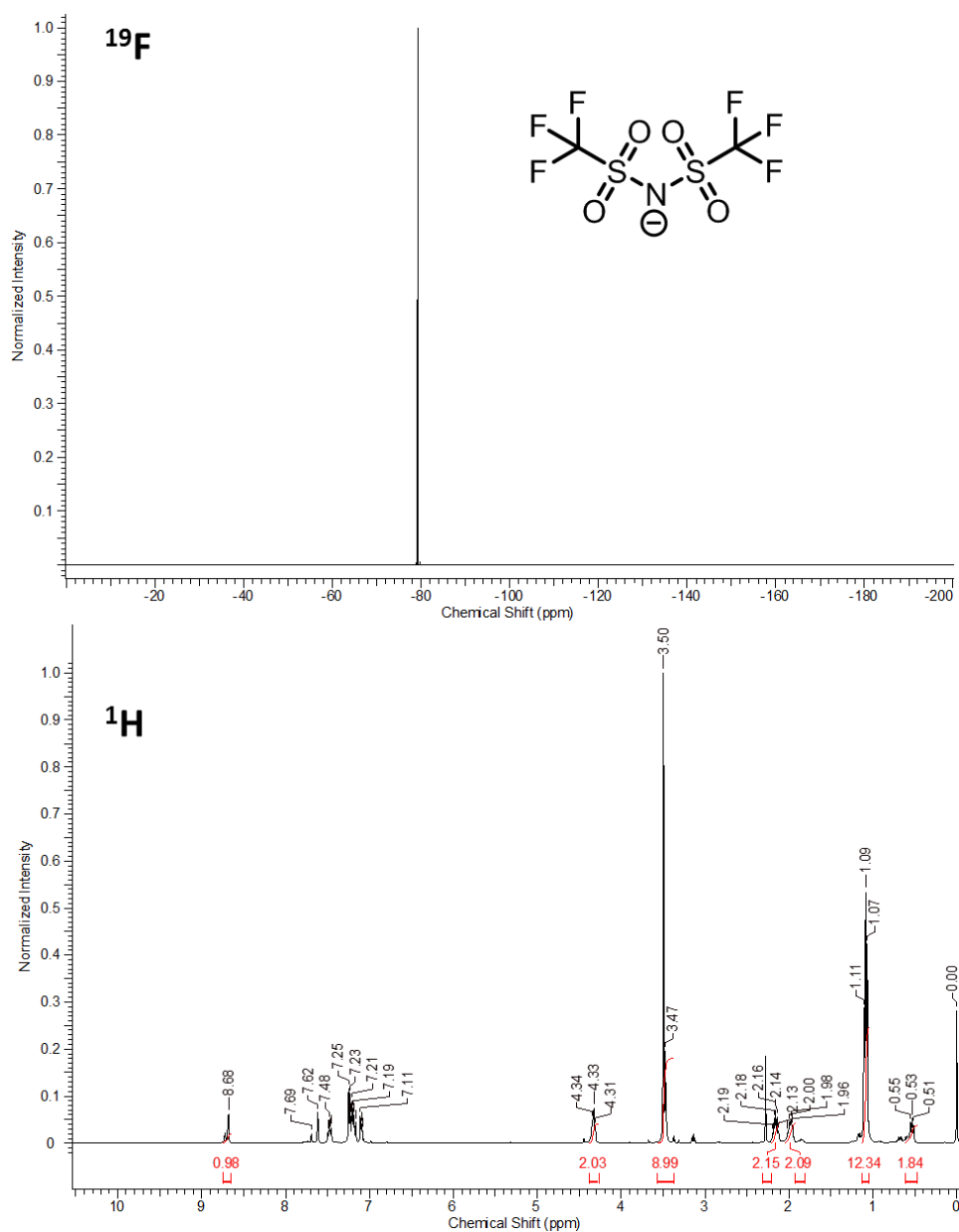


Figure A4: ^{19}F NMR spectra of trimethoxy diPrIm(Ntf₂) with bistriflimide structure inset (top) and ^1H spectra of trimethoxy diPrIm(Ntf₂).

Presence of a peak in the ^{19}F spectra confirmed the exchange in combination with the ^1H spectra whereby the imidazole ring peaks and the closest CH₂ shifted.

Chapter 4 Imidazole functionalised MIL-101(Cr) for enhanced CO₂ utilisation

Special Acknowledgements:

The following special acknowledgements recognise the contributed work of colleagues and collaborators to the presented content of this chapter.

Dr Zhang Liling: Institute of High Performance Computing (IHPC), Agency for Science Technology and Research, Singapore: For undertaking simulations on MIL-101(Cr) and variants including GCMC and DFT work.

Dr Matthew Potter: University of Southampton, UK: For assistance with characterisation and discussion on MIL-101-Me materials.

Daniel Stewart: University of Southampton, UK: For help with catalysis and characterisation on the MIL-101-Me materials

Prof. Enrica Gianotti: Università del Piemonte Orientale, Italy: For analysis of the MIL-101-Me materials with UV-vis, FT-IR and NIR techniques.

4.1 Introduction to MIL-101(Cr)

4.1.1 Structure and properties

MIL-101(Cr) (MIL, Material Institut Lavoisier) is a Metal Organic Framework consisting of chromium trimers and terephthalate (BDC, 1,4-benzenedicarboxylate) linkers with a structural formula of $\text{Cr}_3\text{F}(\text{H}_2\text{O})_2\text{O}(\text{BDC})_3 \cdot n\text{H}_2\text{O}$ in an MTN zeotype structure with cubic unit cell (89 Å, $F d-3m$ space group)^[303], where n is approximately equivalent to 25^[31]. It has attracted a large amount of attention due to its large surface area and pore volumes, resulting in it displaying great promise in a range of applications including but not limited to: separation^[304,305], gas adsorption^[306–311], catalysis^[52,75,76,205,312,313], photocatalysis^[67,314,315] and encapsulation^[34,316].

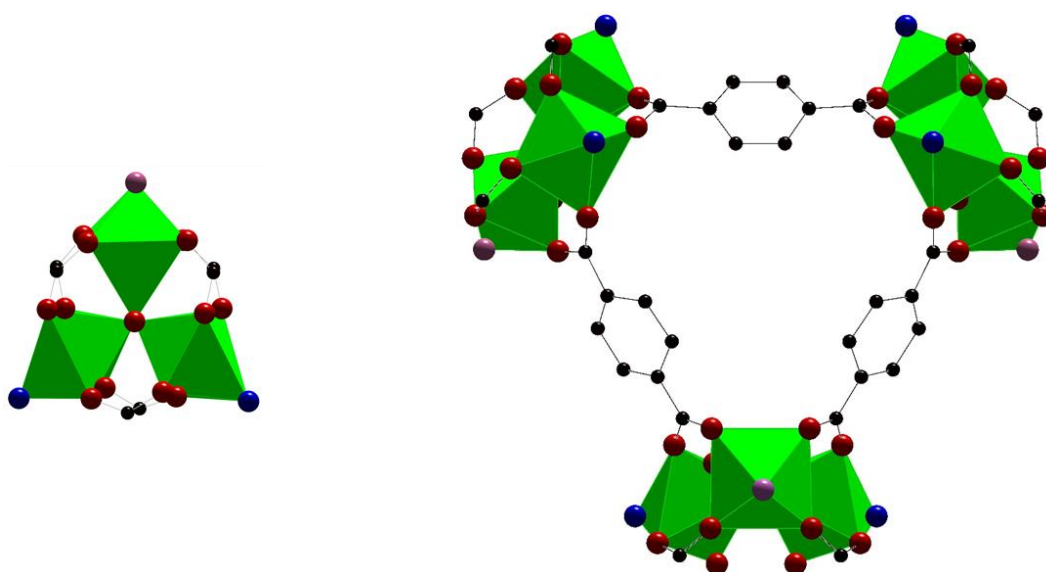


Figure 84: Single Cr_3O trimer (left) and three Cr_3O trimers depicting interconnectivity by terephthalate linkers (right). Only O-C-O depicted of outward facing terephthalate linkers. Oxygen (red), chromium shown as octahedral environment (green) fluorine/hydroxyl (pink), carbon (black) and oxygen of water (blue).

The chromium in the framework is present as clusters, with each chromium (III) ion in an octahedral environment as part of a Cr_3O trimer, Figure 84 (left). Within the trimer, each chromium has four oxygens from different terephthalate ligands, a bridging μ_3 oxygen (which connects the three chromium atoms of the cluster) and finally a fluorine or oxygen which is from water or a hydroxyl group and occurs to the μ_3 oxygen. The terephthalate link trimers to each other and in so doing propagate the MOF structure. Two cage structures, are formed from the expansion of the interconnected trimers to produce the framework.

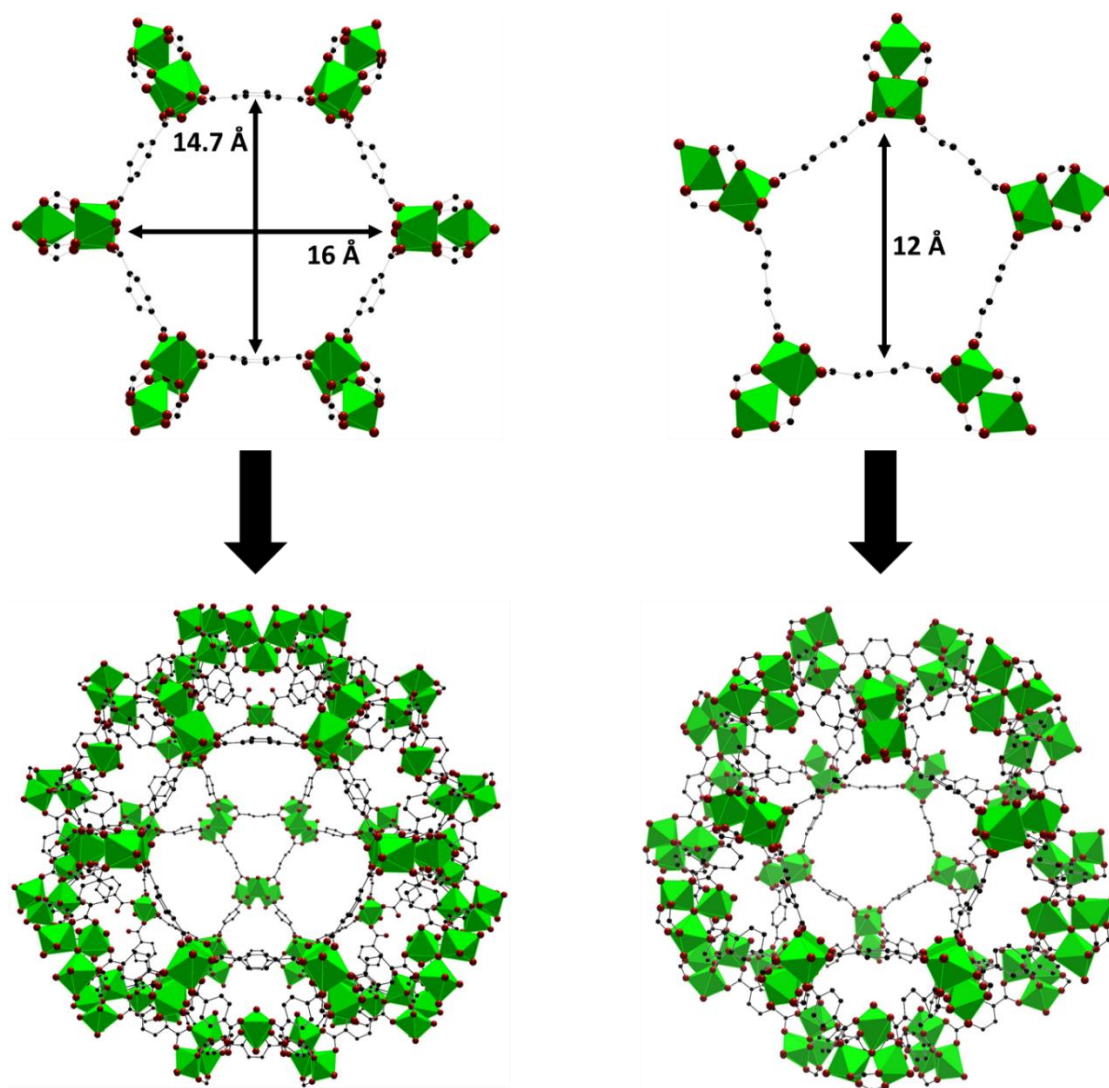


Figure 85: Hexagonal and pentagonal windows, with dimensions shown (top). Cage structures formed as part of MTN zeotype structure (bottom). Oxygen (red), chromium as octahedral environments (green) and carbon (black).

The larger of these cages contains both pentagonal and hexagonal windows resulting in a pore diameter of 34 Å (3.4 nm), Figure 85 (left). The smaller pore is made up of solely pentagonal windows and has an internal pore diameter of 29 Å (2.9 nm) and appears twice as often through the framework as the larger cage. Interconnectivity between the two cages occurs from the supertetrahedral units, which themselves are microporous in nature and have windows of 8.6 Å in diameter. The pentagonal window has an opening of 12 Å with the asymmetrical, hexagonal window aperture 14.7 by 16 Å, Figure 85^[75]. The large size of the pores allows access throughout the framework to a large multitude of adsorbates, reagents or otherwise and results in a high surface area with values of greater than 4000 m²g⁻¹ ^[31]. Additionally, that MIL-101-(Cr) is stable both chemically and thermally, up to 275 °C for the latter, makes it attractive for a range of applications as aforementioned, but most notably for gas adsorption and catalytic purposes^[31].

4.1.2 CO₂ adsorption and catalysis

MIL-101(Cr) is well suited for applications involving carbon dioxide with reports showing it has not only a high capacity for CO₂^[309,317,318] but also shows selective uptake versus other gases indicating preferential affinity for CO₂^[319]. Furthermore, with addition of amines or other nitrogen containing compounds to the framework to further improve to the CO₂ uptake is possible^[320,321]. More recently, a range of catalytic applications have been discovered for MIL-101(Cr), with not only capture but utilisation of CO₂ in a comparable manner to that of other MOFs possible, see Chapter 1 for tabulation of MOF and CO₂ utilisation activities. The activity of unmodified MIL-101(Cr) towards the cycloaddition of CO₂ and epoxides was first shown by Zalomaeva *et al*^[130] and further demonstrated showed by Kim *et al*^[127]. Following these results, a range of modified MIL-101(Cr) have been produced, see Table 31. Notably, Taherimehr *et al* incorporated phosphotungstic acid and produced styrene carbonate in combination with a co-catalyst (TBABr)^[322]. Co-catalyst free conversion was attained by Ding *et al* using ionic liquids which were encapsulated within the pores of the framework forming (ILs)@MIL-101(Cr)^[323]. Imidazolium species affixed on the linker of MIL-101(Cr) has been described by Liu *et al*^[324], Liang *et al*^[142] and Ma *et al*^[56] with varying degrees of success, with the latter two examples employing neither co-catalyst or solvent. These results are summarised below in Table 31.

| Catalyst | Conditions | Substrate | Co-catalyst | Yield / % | Ref |
|---|--|-----------------|-------------|-----------|-------|
| MIL-101(Cr) | 8 bar CO ₂ , 25 °C, 48 hrs, SF ^a | Styrene oxide | TBABr | 95 | [130] |
| MIL-101(Cr) | 20 bar CO ₂ , 100 °C, 4 hrs, chlorobenzene | Styrene oxide | - | 63 | [127] |
| MIL-101(Cr)[PTA] ^b | 8 bar CO ₂ , 25 °C, 24 hrs, SF | Styrene oxide | TBABr | 42 | [322] |
| polyIL@MIL-101(Cr) | 1 bar CO ₂ , 70 °C, 48 hrs, Acetonitrile | Styrene oxide | - | 81 | [323] |
| ⁿ HexImBr-MIL-101(Cr) | 8 bar CO ₂ , 80 °C, 4 hrs, DCM | Propylene oxide | - | 93 | [324] |
| EtImBr-MIL-101(Cr) | 1 bar CO ₂ , 80 °C, 48 hrs, SF | Styrene oxide | - | 48 | [142] |
| (ⁿ Bu) ₄ NBr-MIL-101(Cr) | 20 bar CO ₂ , 80 °C, 8 hrs, SF | Propylene oxide | - | 99 | [56] |

Table 31: Summary of MIL-101(Cr) based catalysts for CO₂ and epoxide coupling. ^aSolvent free.

^bphosphotungstic acid

Given the long reaction times, co-catalyst and/or solvent use of the above examples there is scope for improvement in the use of MIL-101(Cr) for CO₂ insertion into epoxides leading to cyclic carbonate formation.

4.1.3 Coordinatively unsaturated sites (CUS)

The water molecules which act as ligands to complete the chromium octahedral coordination environments can be removed under heating and/or vacuum at, or above, 423 K. Each chromium cluster, possesses two water ligands, that when removed results in two coordinatively unsaturated sites (CUS) per trimeric Cr(III)^[205], Figure 86.

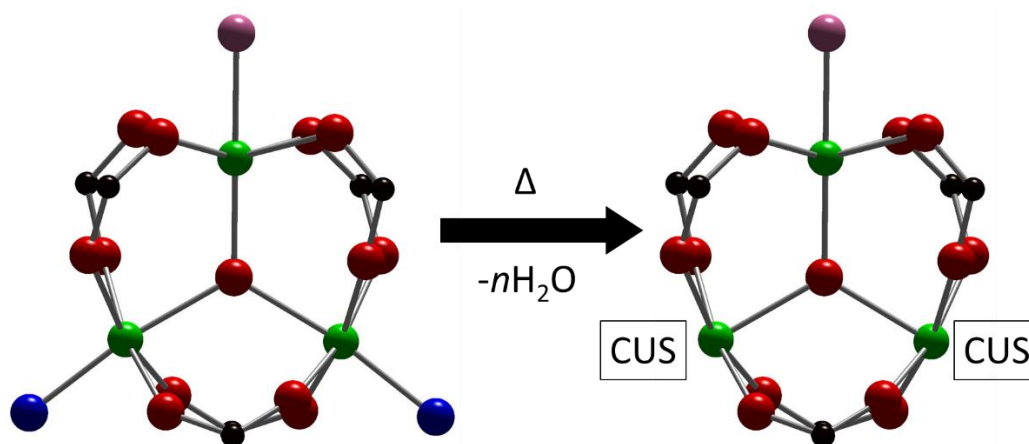


Figure 86: Representation of Cr₃O trimer water removal to create coordinatively unsaturated sites (CUS). Oxygen (red), chromium (green) fluorine/hydroxyl (pink), carbon (black) and oxygen of water (blue)

The CUS in the framework are handles for functionalisation as they enable the introduction of a selected ligand to be undertaken and grafted to the vacant sites created by dehydration of the framework. Hwang and Hong *et al*^[75,205] showed that amine groups, with ethylenediamine reported, can be grafted onto the open metal sites of the chromium by a facile post synthetic modification (PSM) technique. Accordingly, it can be envisaged that other nitrogen containing compounds have the potential for grafting onto the framework and thus, the MIL-101(Cr) framework can be envisaged to be a support for imidazole species, given their known ability to undertake CO₂ reactions.

The propensity of MIL-101(Cr) to catalyse CO₂ and epoxide reactions in combination with imidazolium species based on the linker has been reported, Table 31. However, imidazole incorporation *via* the CUS of MIL-101(Cr) has not, and so provides an opportunity to produce an enhanced CO₂ utilisation catalyst.

4.2 Aims and objectives

MIL-101(Cr) will be investigated to enhance the existing CO₂ adsorption and utilisation properties. The removal of the water from the framework structure will be undertaken creating coordinatively unsaturated sites to which a variety of functionalised imidazoles will be grafted.

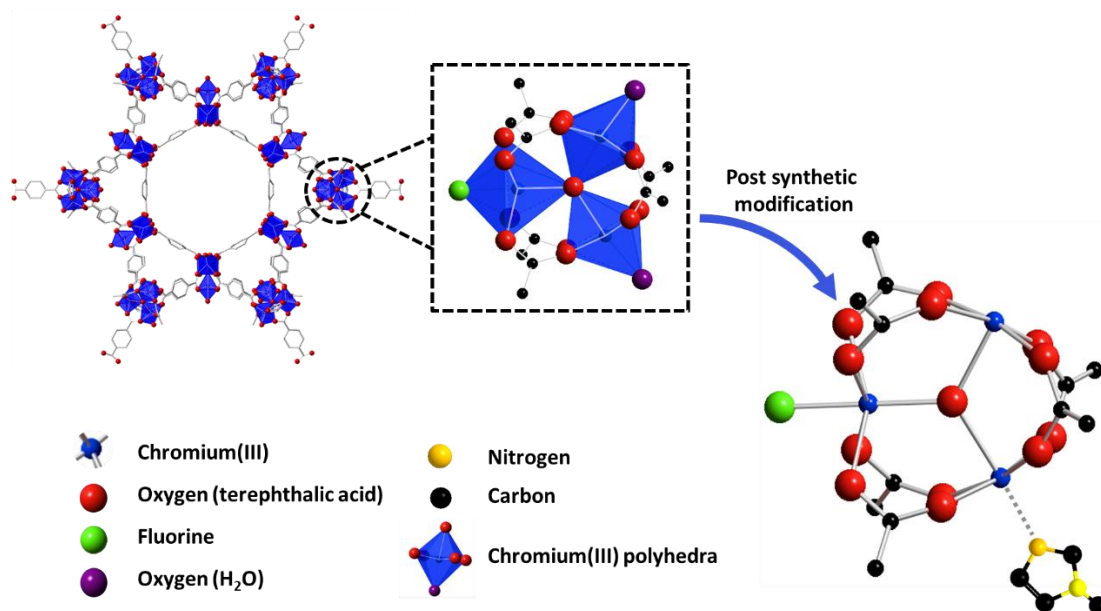


Figure 87: Diagrammatic representation of dehydration of MIL-101(Cr) followed by post synthetic modification by functionalisation of the created CUS with an imidazole.

The subsequently formed hybrid material will be tested for efficacy in CO₂ utilisation reactions, namely the coupling of CO₂ with epoxides to form cyclic carbonates as shown in Figure 88.

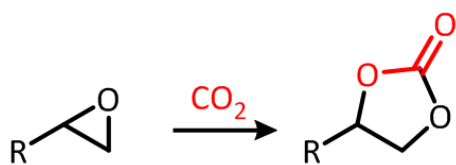


Figure 88: Insertion of carbon dioxide into an epoxide forming a cyclic carbonate

A range of characterisation techniques will be used to probe and rationalise any structure property relationships or synergy between support and imidazole that are observed.

4.3 Results and discussion

A range of imidazoles were grafted to MIL-101(Cr) and tested for activity in CO₂ cycloaddition to epoxides. The results and discussion shall focus on the MIL-101(Cr) produced from 1-methyl imidazole being grafted to the CUS, herein denoted MIL-101-Me. This was selected due to the commercial availability, ease of characterisation and marginally improved results versus the other analogues of the 1-methyl imidazole variant. It should be made clear here that the modelling work displayed and discussed in the forthcoming section was undertaken by Dr Liling Zhang to aid the understanding of the workings of the MIL-101-R materials (where R relates to imidazole functionality, as per Chapter 3).

4.3.1 Characterisation

MIL-101(Cr) was synthesised *via* a hydrothermal technique, followed by washing in ethanol and a dilute NH₄F solution. After these washing stages the light green powder was dried and this material was used as the basis of the grafting procedures and as the MIL-101(Cr) (blank) sample for testing and analysis. Characterisation of the materials produced was two-fold: firstly structural integrity was analysed to ensure the desired physical properties (e.g. porosity, thermal stability, crystallinity and morphology) of the MIL-101(Cr) were not significantly altered through the modification procedure. Secondly, analysis of the binding of the imidazole was probed, to understand the catalytic benefits of the heterogenisation of the imidazole with the MIL-101(Cr) species in combination with a computational study.

High resolution imaging of the framework crystals used a field emission scanning electron microscope (FESEM) in order to document not just the morphology of the framework crystals, but also any significant surface features, if visible at SEM magnification. The SEM images obtained of the MIL-101(Cr) synthesised using a hydrothermal and additive free methodology (typically HF is used in the synthesis) showed small clustered particles with a mixture of irregular and spherical shapes contrary to the morphology documented widely in the literature, Figure 89A.

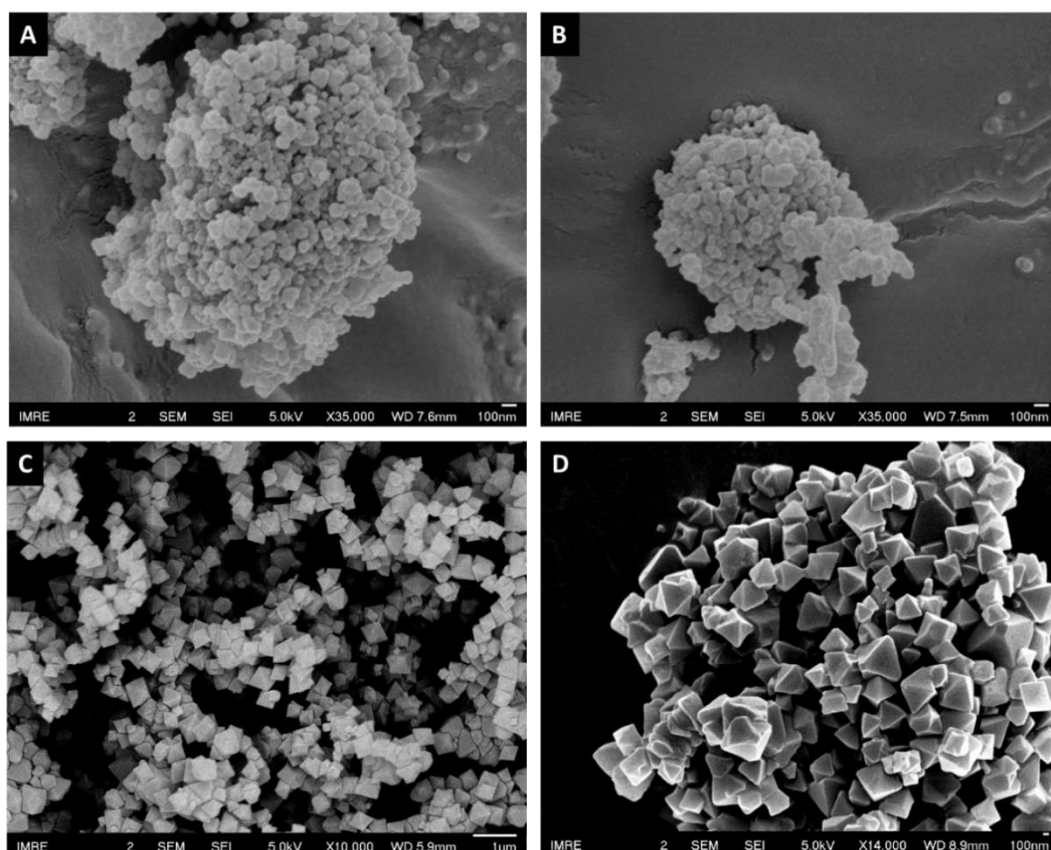


Figure 89: FESEM images of A) MIL-101(Cr) hydrothermally synthesised with no additive (after ethanol and NH_4F treatment) B) MIL-101-Me by PSM on sample synthesised with no additive C) MIL-101(Cr) with HNO_3 additive (after ethanol and NH_4F treatment) and D) MIL-101-Me by PSM on batch synthesised with HNO_3 additive. Samples gold coated for 20s prior to imaging.

PSM on this occurred with minimal effect on the morphology of the sample, as shown through Figure 89A and B, validating the methodology to be used. Whilst XRD of these initial samples displayed the correct x-ray pattern, the observation of a different morphology *via* SEM and the small size of the particles seen, indicated that the crystal growth was not occurring correctly during the synthesis. The HF used in the traditional synthesis provides fluorine which acts as a mineralising agent to promote crystal growth^[325] and also lowers the pH which is thought to improve crystal formation, although the exact reasoning is not known, leading to the formation of large MIL-101(Cr) crystals^[75]. An alternative preparation based on that of Jiang *et al*^[319] and Zhao *et al*^[326] using nitric acid was undertaken, resulting in the MIL-101(Cr) shown in Figure 89C and the XRD shown Figure 90. Powder X-ray diffraction on these analysed the crystal structure; the MIL-101(Cr) species showed a crystalline diffraction pattern with no extra peaks which compared favourably to literature values and that of the simulated pattern generated from the literature^[31]. Refinement undertaken on collected pattern confirmed the structure of the material, peak

labelling within Figure 90 is not shown, owing to the individual reflections often not appearing discretely.

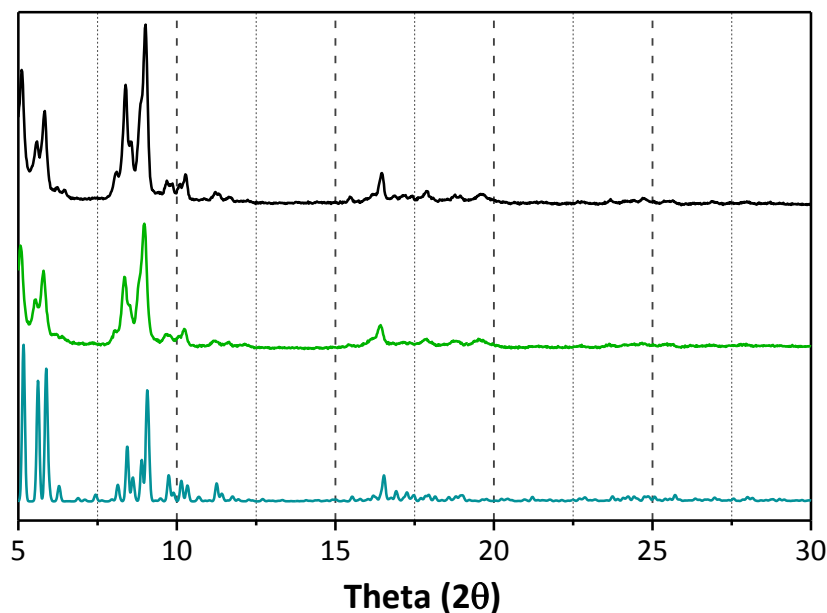


Figure 90: Powder XRD patterns of MIL-101(Cr) simulated (blue), MIL-101(Cr) with HNO₃ (green) and MIL-101-Me (black). Y values offset for comparison.

Following post synthetic modification (PSM) there is no observable variation in XRD pattern indicating the structure is retained during the grafting process. Similarly, imaging of samples produced using nitric acid as an additive displayed morphologies in correlation with those first reported by Lebedev *et al*^[327] with the as synthesised MIL-101(Cr) displaying octahedron crystals with particle sizes in the range of 400-500 nm. Partial collapse of the MIL-101(Cr) and analogues was observed under FESEM conditions therefore extensive imaging to determine size distribution was not possible, see appendix Figure B1^[327]. The use of nitric acid was therefore employed in all further synthesis procedures in order to obtain the correct morphology. As with the additive free synthesis it can again be seen that after performing the post-synthetic modification, there is little visible change in the particles, all of which maintain the same size and shape. It can also be seen that the faces are still smooth, showing that the particles have not degraded, and mechanical defects have not been introduced to the surface by the PSM process, in agreement with recent literature where PSM has been undertaken^[328–331] as shown in Figure 89D.

| Entry | Sample | BET surface area (m ² /g) |
|-------|--|--------------------------------------|
| 1 | MIL-101(Cr) (post EtOH and NH ₄ F) | 2585 ± 101 |
| 2 | MIL-101-Me ^a | 1750 ± 67 |
| 3 | MIL-101(Cr) (HNO ₃ , AS) | 2860 ± 88 |
| 4 | MIL-101(Cr) (HNO ₃ , post EtOH and NH ₄ F) | 3513 ± 84 |
| 5 | MIL-101-Me (HNO ₃) | 2372 ± 118 |

Table 32: BET surface area values for MIL-101(Cr) variants showing the effect of HNO₃ addition and washing cycles. ^aSynthesised from entry 1.

Further evidence promoting the use of nitric acid in the synthesis was gained when the two synthesis methods are compared by N₂ adsorption studies. The selection of synthesis methodology is validated, both in the use of nitric acid and the employment of ethanol and NH₄F washing stages. Comparison of the surface areas of the two methodologies, Table 32, shows the benefits of the nitric acid use – the values are greatly improved for the MIL-101(Cr) produced with nitric acid, entry 4 compared to MIL-101(Cr) the hydrothermal synthesis without additive, entry 1. Figure 91 clearly shows the benefits of the washing stages used, indicating that a significant amount of unreacted starting product was present within the framework following the hydrothermal synthesis, this is further apparent from comparison of the surface areas, Table 32 entries 3 and 4 based on the isotherms shown in Figure 91.

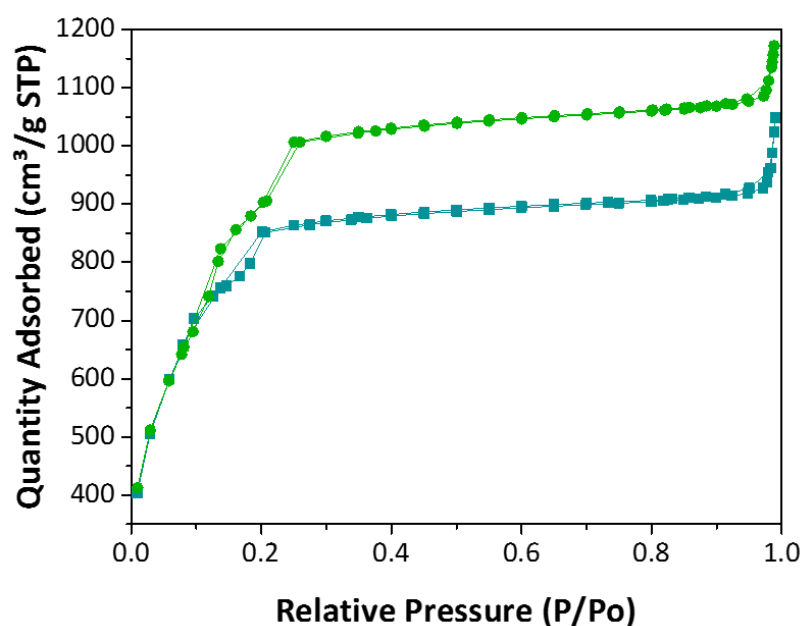


Figure 91: N₂ adsorption and desorption isotherms of MIL-101(Cr) as synthesised (blue) and MIL-101(Cr) following ethanol and NH₄F washing (green).

For the MIL-101(Cr) after the washing stages the isotherm shows high uptake and a slight hysteresis as expected given the mesopores which the MIL-101(Cr) structure possesses. A reversible type IVb isotherm is therefore produced as the sub-4 nm pore diameters tend towards condensation at lower P/P_0 values^[212]. PSM incorporation of the imidazole shows an appreciable effect on the porosity and surface area of the MIL-101(Cr), Figure 92 and Table 32 (entry 5).

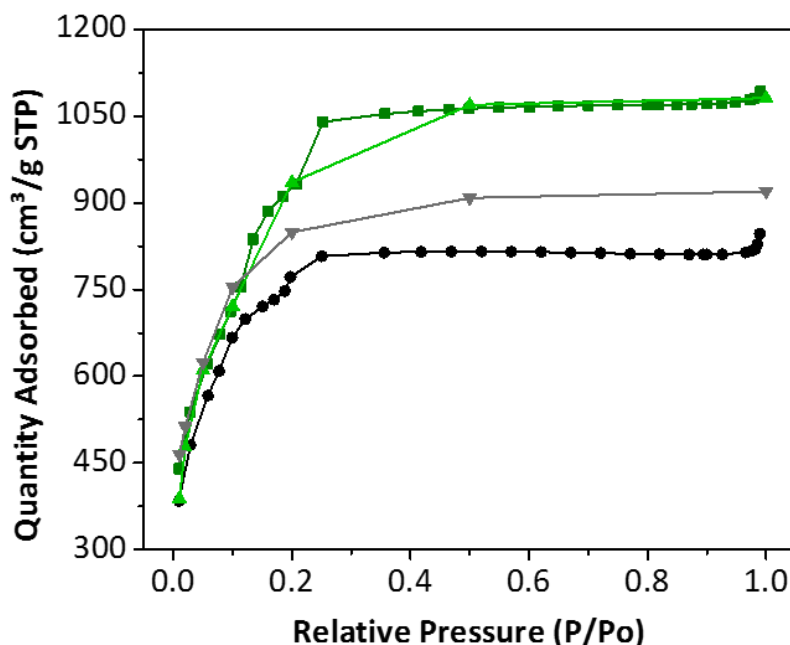


Figure 92: N_2 adsorption isotherms for MIL-101(Cr) (green), MIL-101-Me (black), MIL-101(Cr) simulated (light green) and MIL-101-Me (grey)

The capacity of the MIL-101-Me is lowered compared to the blank framework, as expected given the removal of the relatively small water ligand and replacement with an imidazole. The pore volume of $1.7 \text{ cm}^3 \text{ g}^{-1}$ for the MIL-101(Cr) decreased by 22 % upon formation of MIL-101-Me, as the imidazoles occupy the framework sites and extend into the pores. Crucially though, the framework still retains significant porosity after PSM with the mesoporosity along with the high surface area observed. Therefore, access to the imidazole species throughout the framework during catalysis is possible. Gas adsorption studies, experimentally and computationally, were completed to understand the effect of the imidazole grafting on both N_2 and CO_2 isotherms. The experimental and computational values are seen to be in very good agreement for nitrogen adsorption, for the MIL-101(Cr) framework, Figure 92. However, differ noticeably for the MIL-101-Me variant. The reasoning for this is unknown, but given the experimental value is lower it can be attributed to additional solvent or other molecules being trapped within the framework after PSM leading to the lower values measured highlighting the importance of the washing cycles employed, as has already been shown markedly in the study of the ethanol and NH_4F washes previously.

Determination of the loading of the imidazole is critical. A loading of 1 mmol/g of the imidazole was attempted to be grafted onto the CUS of the MIL-101(Cr) framework during the PSM stage. For each sample produced, elemental analysis CHN % measurement was taken to determine the amount of imidazole successfully grafted to the framework. As with the silica work in Chapter 3, the nitrogen content was used as the means of loading calculation as it was assumed to be the only source of nitrogen following washing. Confirmation of this assumption was needed as the precursor species during synthesis was chromium nitrate and nitric acid was also used, therefore the imidazole is not the sole possible source of nitrogen in this synthesis procedure.

| Sample | % / C | % / H | % / N | Loading/ mmol g ⁻¹ |
|-------------|-------|-------|--------|-------------------------------|
| MIL-101(Cr) | 34.46 | 2.78 | < 0.10 | 0.00^a |
| MIL-101-Me | 40.57 | 3.41 | 2.68 | 0.96 |

Table 33: Elemental analysis for MIL-101(Cr) and MIL-101-Me samples. Loading (mmol g⁻¹) based upon nitrogen percentage. ^aNitrogen content below detection limits so assumed to be zero.

Based then upon the nitrogen content the MIL-101-Me sample, shown in Table 33, had an imidazole loading of 0.96 mmol g⁻¹. Nitrogen content was shown to be a reliable indicator of imidazole amount, given the result obtained for the MIL-101(Cr) sample whereby the nitrogen content *via* CHN % was below the detection limits of the instrumentation. This implies that no or very little nitrogen from the framework synthesis is retained - in close agreement with literature values and procedures when nitrogen containing compounds are introduced to the framework^[332]. To enable greater confidence in this calculation further determination with other techniques was used to confirm the loading.

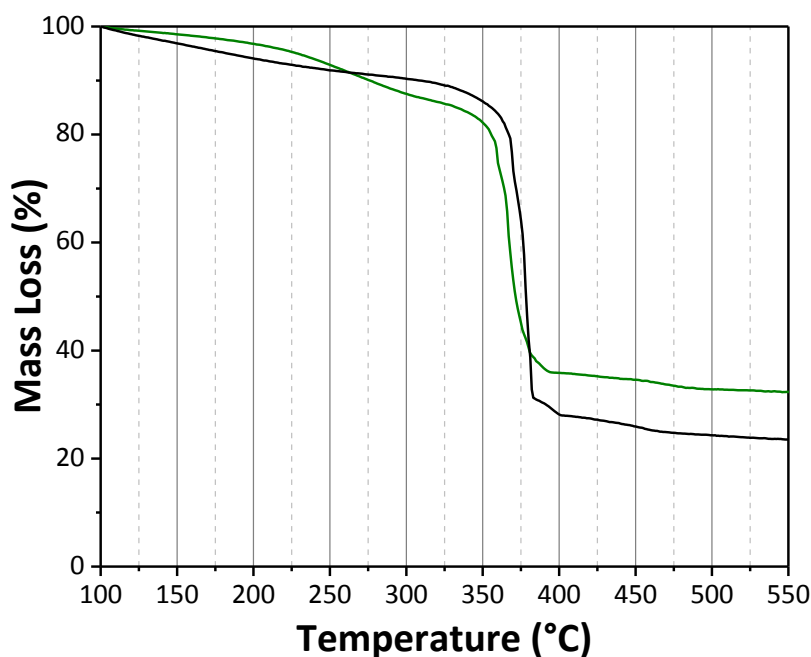


Figure 93: TGA profiles for MIL-101(Cr) (green) and MIL-101-Me (black), taken in air at 10 °C/min ramp rate.

Thermogravimetric analysis (TGA) studies evaluated the thermal tolerance of the MIL-101(Cr) and also loading of the MIL-101-Me material. The TGA curves, Figure 93, show the MIL-101-Me to have very similar thermal stability as the blank framework, if not nominally higher. The overall mass loss is greater for the MIL-101-Me analogue as the addition of the imidazole alters the ratio between the metal and organic components causing the metal to be a smaller proportion of the overall. No extra mass loss peaks are seen in the MIL-101-Me so the loss of the imidazole occurs at the same time as the degradation of the framework, beginning around 325 °C, which implies it is strongly bound. TGA also provided a secondary method of calculating the loading of the imidazole, which is important given the possibility of error in the EA measurements from impurities within the framework or moisture. The TGA curve was normalised to account for the majority of the initial mass loss attributed to residual solvent and, or water (in this instance set as the loss observed prior to 100 °C). The loading calculated from the TGA was found to be 0.93 mmol g⁻¹ based on mass losses between 250 °C and 475 °C determined from analysis of the first derivatives of each data set in combination with the work of Hong *et al.*^[75]. This figure is in good agreement with the calculated value from elemental analysis, Table 33.

However, upon obtaining ICP-OES analysis the calculation of the imidazole loading based on the nitrogen amount observed in CHN analysis was found to be more complicated. Values for the CHN as well as chromium and fluorine are shown in Table 34. Firstly from the results it can be seen that the NH₄F wash is successful in introducing fluorine into the framework during the washing and treatment stages of the synthesis. Given the general formula of MIL-101(Cr),

$\text{Cr}_3\text{F}(\text{H}_2\text{O})_2\text{O}(\text{BDC})_3 \cdot n\text{H}_2\text{O}$, it would be expected that the F percentage would be approximately 1.6 % if n is taken to be 25. In reality the amount measured is higher than this but if n is lower than 25 then the ratios would shift.

Disappointingly and contrary to the results obtained for the CHN detailed in Table 33, there is a significant amount of nitrogen seen in the blank MIL-101(Cr) framework, assumed to be from the nitric acid used in the synthesis which then situates in the CUS instead of a water ligand. Whilst this could be a one-off anomaly for this sample which was analysed (unfortunately a different batch to that of Table 33) if still present within the framework at the same level following the PSM process then this would boost the calculated loading by approximately 0.3 mmol/g – a highly significant amount given the proposed use of 1 mmol/g loading of the imidazole species. To rectify this a blank subtraction could be employed by the systematic recording of the nitrogen levels from ICP-MS for each MIL-101(Cr) batch in order to obtain the value by which the imidazole amount would be increased by and provide a more certain value for the loading.

The chromium amounts seen are similar to the theoretical values calculated - 21.74 % and 19.51 % for MIL-101(Cr) and MIL-101-Me (1.12 mmol/g) respectively. That of the MIL-101-Me is slightly lower, which would be anticipated given the increased organic component. The chromium amount is not comparable to the residual amount for the TGA curves as these were undertaken in air and so the amount of the residual mass present as an oxide is unknown.

| Sample | C / % | H / % | N / % | Cr / % | F / % |
|-------------|-------|-------|-------|--------|-------|
| MIL-101(Cr) | 35.97 | 3.51 | 0.87 | 22.71 | 2.19 |
| MIL-101-Me | 36.15 | 3.05 | 3.14 | 21.62 | 2.50 |

Table 34: Carbon, hydrogen, nitrogen, chromium and fluorine percentages as determined by ICP-OES for MIL-101(Cr) and MIL-101-Me.

Investigation of the nitrogen discrepancies observed was completed using x-ray photoelectron spectroscopy (XPS). The nitrogen region would be expected to yield one additional peak following PSM, given the additional of the imidazole. Peaks were observed in the expected regions in both the MIL-101(Cr) and MIL-101-Me which correspond to the framework, as shown by the survey scan, Figure 94A. The framework contributes the peaks in the Cr2p and C1s regions as shown in Figure 94B and C. The Cr2p region shows the characteristic doublet expected for Cr(III), the Cr2p_{1/2} was not fitted owing to the issues with determining speciation fitting of the Cr2p_{1/2} peak as per literature guidance^[333]. The Cr2p_{3/2} peak at 577.51 eV is similar to the average value reported by Biesinger *et al*^[334]. Given the presence of F and other O ligands which they report to cause the binding energy to be higher and lower respectively than that of exclusively Cr(OH)₃ which the

experimental value obtained matches closely, the position measured is likely due the effect of the multiple different ligands for each Cr(III). The peak position of 577.58 eV for the MIL-101-Me Cr2p_{3/2} shows the continuation of the Cr environment as minimal difference was observed for between the C1s and Cr2p regions of MIL-101(Cr) and MIL-101-Me. A wider scan of the Cr 2p region did not allow for the definitive observation of a discrete Cr-N interaction associated with the imidazole attachment to the framework.

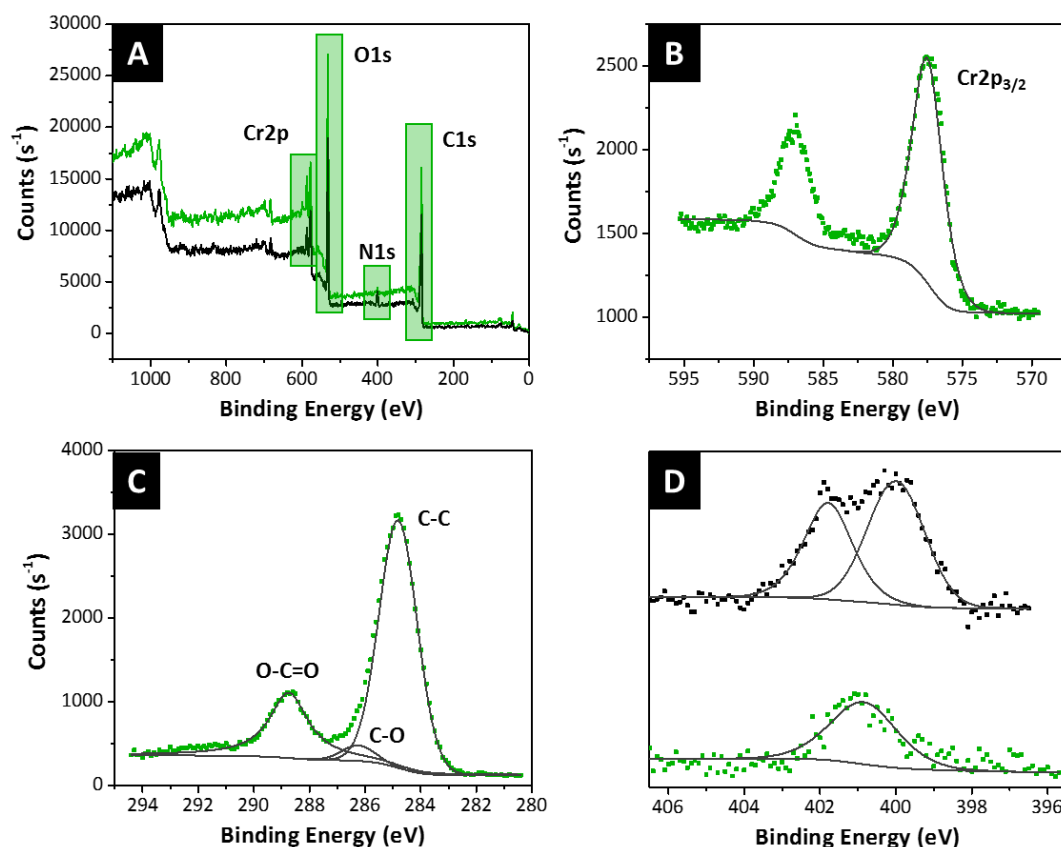


Figure 94: XPS spectra for A) Survey scan of MIL-101(Cr) (green) and MIL-101-Me (black) with regions highlighted, B) Cr2p region of MIL-101(Cr), C) C1s region of MIL-101(Cr), D) N1s region of MIL-101(Cr) (green) and MIL-101-Me (black). For B-D raw data is shown as data points.

The C1s region, Figure 94C, displayed the C-C adventitious carbon peak which the value of was set to 284.4 eV and used as a reference. Also observable are the C-O seen as a shoulder of the C-C peak and O-C=O contribution that relate to the terephthalate linker of the framework. Finally, a small peak is observable on the survey scan for both materials at *circa* 685 eV which corresponds to the F1s relating to the Cr-F interaction^[334] present within the framework. The N1s scans, Figure 94D, showed a clear difference for between the MIL-101(Cr) and the MIL-101-Me. The MIL-101(Cr) showed a single peak at 400.85 eV which, given the results for the ICP-MS showing nitrogen present after synthesis, can be ascribed to be sourced from either the nitric acid or the ammonium (fluoride). A second environment is observable at 401.79 eV for the MIL-101-Me

indicating the presence of another nitrogen environment within the sample. Given the characterisation results already discussed this is taken to be from the imidazole.

From this it can be seen there is a measurable amount of nitrogen within the MIL-101(Cr) framework. However, owing to the ICP-OES being undertaken externally the results from it required a significantly longer timescale than those of EA and TGA. It was decided that the latter two techniques would be used for loading determination as they were in agreement and readily available. It is clear that this is not ideal and further investigation is needed to understand why the different values have occurred. Therefore for the use of EA for loading calculation the following assumption has been made: the nitrogen content of the MIL-101(Cr) is consistent across synthesised batches and so the nitrogen content will have the same effect across all MIL-101-R analogues resulting in the effect of it to be normalised and any differences in catalytic ability can then be assumed to result from the imidazole itself.

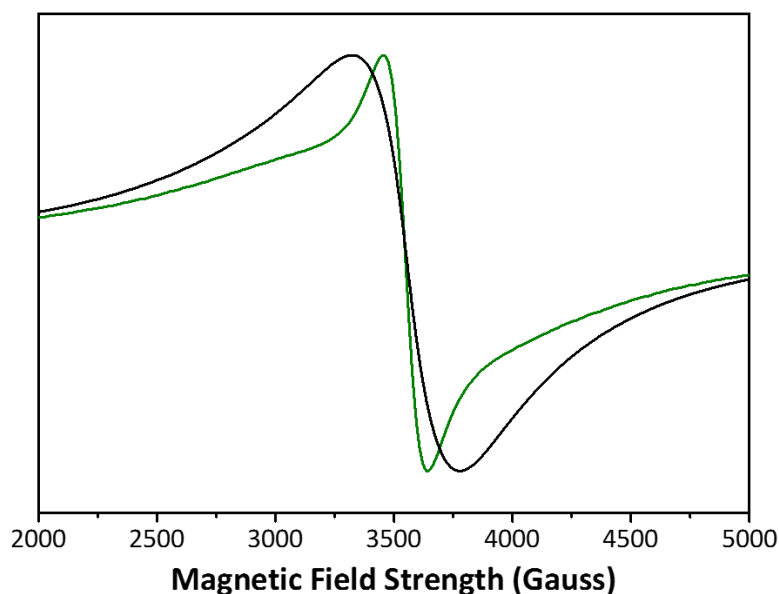


Figure 95: X-band continuous wave (CW) detected EPR spectra of MIL-101(Cr) (green) and MIL-101-Me (black) recorded at ambient temperature and pressure.

To probe the location of the imidazole in MIL-101-Me electron paramagnetic resonance (EPR) was used. Within the Cr_3O metal clusters of the framework, the chromium sites exist as octahedral Cr(III) , d^3 species, in the high spin arrangement, therefore possessing three unpaired electrons. The presence of these unpaired electrons makes EPR a powerful technique to probe differences in the environment surrounding the chromium metal centres. The EPR obtained for the bare MIL-101(Cr) (Figure 95, green) is in good agreement with previously published literature and shows a broad splitting pattern, centred at 3500 G^[316]. The position of this band is indicative of the pseudo-octahedral environment of high-spin chromium d^3 species. The broad shape is attributable to the lack of symmetry in the ligands surrounding the chromium atoms. Upon

binding of the imidazole to MIL-101(Cr) there is a distinct change in the EPR spectrum as the MIL-101-Me (Figure 95, black) signal is noticeably broader. This behaviour indicates a change in the coupling constant of the EPR signal, signifying a change in the electron spin–spin state of the active chromium species caused by the presence of a different neighbouring nuclei compared to the bare MIL-101(Cr), such as imidazole addition^[316]. The addition of a further ligand will reduce the average symmetry around the chromium atoms of the framework, leading to a less uniform averaged environment with the MIL-101-Me analogue and hence a broadening of the EPR signal.

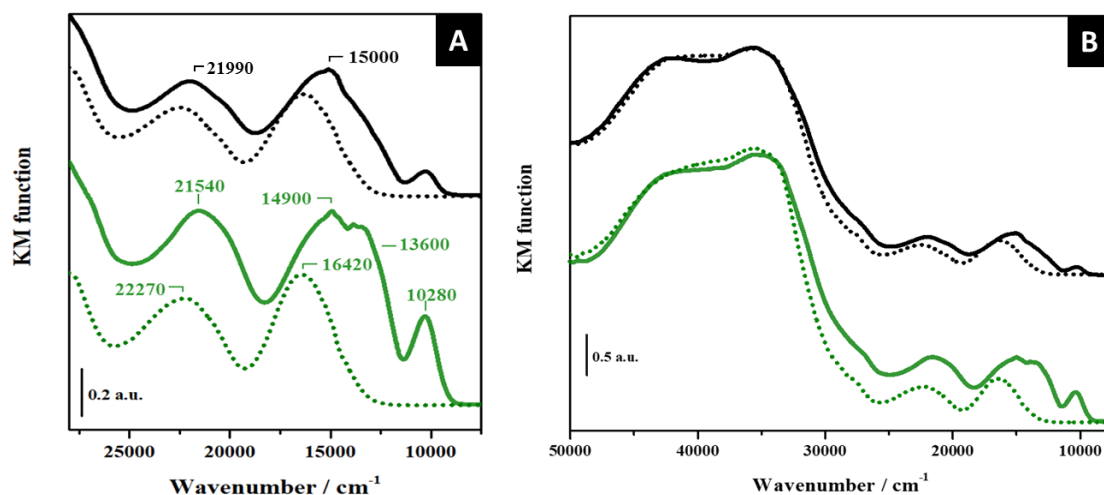


Figure 96: A) DR UV-Vis, visible range spectra of MIL-101(Cr) (green) and MIL-101-Me (black). B) DR UV-Vis spectra of MIL-101(Cr) (green) and MIL-101-Me (black). For both: in air (dotted curves) and after outgassing the samples at 150°C for 1h (solid lines).

The observations seen with the EPR are substantiated by UV-Vis and NIR. In the visible region in air for MIL-101(Cr), Figure 96A, two d-d transitions are observable at 22270 and 16420 cm^{-1} , corresponding to the ${}^4A_{2g} \rightarrow {}^4T_{2g}(F)$ and ${}^4A_{2g} \rightarrow {}^4T_{1g}(F)$ transitions respectively, which is typical of pseudo-octahedral Cr(III) sites within the framework^[223,335]. The MIL-101-Me spectra run in air (dotted lines) shows the d-d bands are blue-shifted with decreased intensities with respect to the MIL-101(Cr). The imidazole is a stronger ligand than water so this shift is expected as the crystal field splitting will have increased and so a larger amount of energy is required for electron promotion, leading to higher wavenumbers. For both, in the UV region, the charge transfer (CT) and ligand centred (LC) transitions are seen, Figure 96B.

To observe the CUS present the samples were evacuated at 150 °C so the coordinated water was removed. Removal was confirmed by the disappearance of the band at 5320 cm^{-1} in the NIR spectra, appendix Figure B2, following evacuation^[336]. The confirmation of water removal at this temperature verifies that during the synthesis procedure, the conditions used were sufficient to remove the water and expose the CUS so allowing grafting to occur. The intensity of the d-d

transitions increases and become broader with shoulders appearing at lower wavenumbers that were not evident in the spectra recorded in air, as seen in Figure 96. At 13600 cm^{-1} a shoulder peak is visible but also a new band at 10280 cm^{-1} appears which are assigned to the CUS Cr(III) sites now exposed following the heat and vacuum the samples were exposed to.^[223,337] For the MIL-101-Me analogue the d-d bands are blue-shifted compared to MIL-101(Cr) and occur with decreased intensities, indicating that a reduced number of CUS are seen versus the unmodified framework as would be envisaged with imidazole coordination to some of them. This, coupled with the shoulder peaks being less prominent due to the presence of the strong field ligand on Cr(III) sites such as an imidazole is, is highly indicative of the grafting of the imidazole to MIL-101(Cr)^[308].

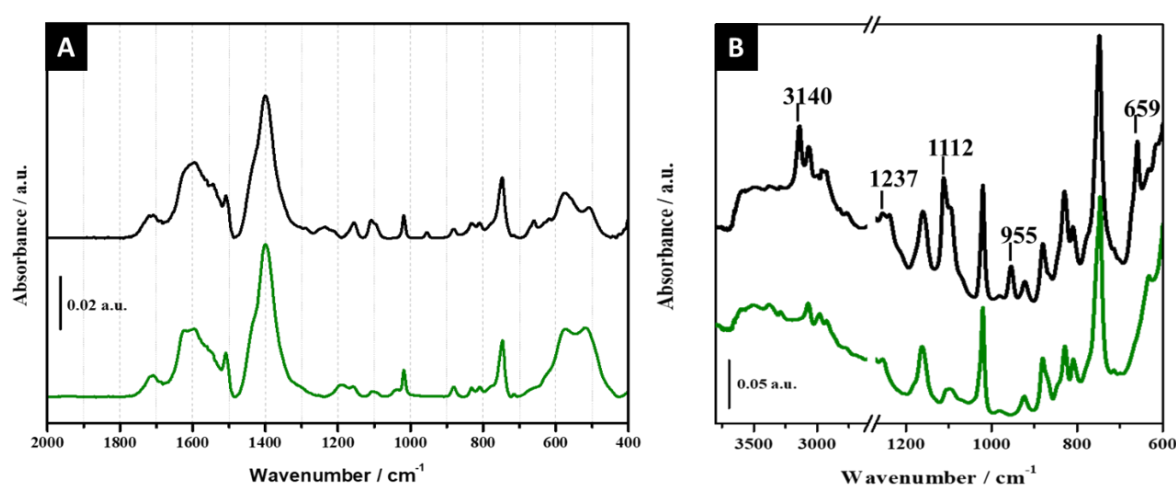


Figure 97: A) FT-IR spectra of MIL-101(Cr) and MIL-101-Me upon outgassing at 150°C for 1h. B) Full FT-IR spectra of MIL-101(Cr) and MIL-101-Me, recorded in KBr after outgassing the samples at room temperature for 2 hours. For both: MIL-101(Cr) (green) and MIL-101-Me (black).

The signals associated with the framework are observed in the Fourier Transform Infra-Red (FT-IR) spectra. Strong absorptions in the region of $1800 - 1300\text{ cm}^{-1}$, Figure 97A, are due to the dicarboxylate linker with the $\nu_{\text{as}}(\text{COO})$, $\nu_{\text{s}}(\text{COO})$ and $\nu(\text{C}-\text{C})$ stretches seen. Furthermore, at 1017 cm^{-1} the $\delta(\text{C}-\text{H})$ stretch and the out of plane band at 750 cm^{-1} , $\gamma(\text{C}-\text{H})$, due to the aromatic rings of the linker are also recorded^[338]. In MIL-101-Me, a new band at 3140 cm^{-1} is assigned to $\nu(\text{C}-\text{H})$ and which shifted compared to the unbound imidazole (3118 cm^{-1} , appendix Figure B3) this is also seen as the overtone band in the NIR region at 6180 cm^{-1} , appendix Figure B2. The presence of bound imidazole within the framework is therefore confirmed. Additional, imidazole indicative, features are visible at 1237 and 1112 cm^{-1} for $\delta(\text{C}-\text{H})$ in-plane and out-of-plane vibrations of the ring (Figure 97B).

Following the observation of the exposed CUS *via* UV-Vis, the Lewis acidity of MIL-101(Cr) and MIL-101-Me was investigated. Previous studies of CO₂ and epoxide reactions by MIL-101(Cr) and other materials indicate Lewis acidity is required for catalytic ability as the electron acceptor ability of the Lewis acid stabilises the alkoxide intermediate which is produced upon the ring opening of the epoxide. Deuterated acetonitrile, CD₃CN, was used as a molecular probe to study the C≡N stretching region (Figure 98). This was achieved by decreasing the CD₃CN pressure within the sampling pressure over time, to leave only those molecules with strong interaction with the framework – the CUS as acetonitrile is a weak Lewis base. A slight shoulder at *circa* 2275 cm⁻¹ appears as the probe molecule interacts with residual OH groups found within the framework^[51]. The band at 2318 cm⁻¹ relates to acetonitrile coordinated with the CUS Lewis acid sites of Cr(III)^[339]. Reduction of acetonitrile pressure causes an additional shoulder to appear at 2312 cm⁻¹. The detection of two components (2312 and 2318 cm⁻¹) indicates that two Cr(III) un-coordinated Lewis acid sites with different strength are present possibly owing to changes in the ligands within the local environment around the CUS. The adsorptions of CD₃CN on Cr(III) sites are less intense for the MIL-101-Me, as the grafted imidazole reduces the prevalence of Cr(III) CUS. In both of the materials a shift ($\Delta\nu_{\text{CN}}$) of 57 cm⁻¹ is seen (Figure 98, inset), which shows grafting the imidazole does not affect the Lewis acidity of the remaining Cr(III) CUS, otherwise the value of $\Delta\nu_{\text{CN}}$ would change.

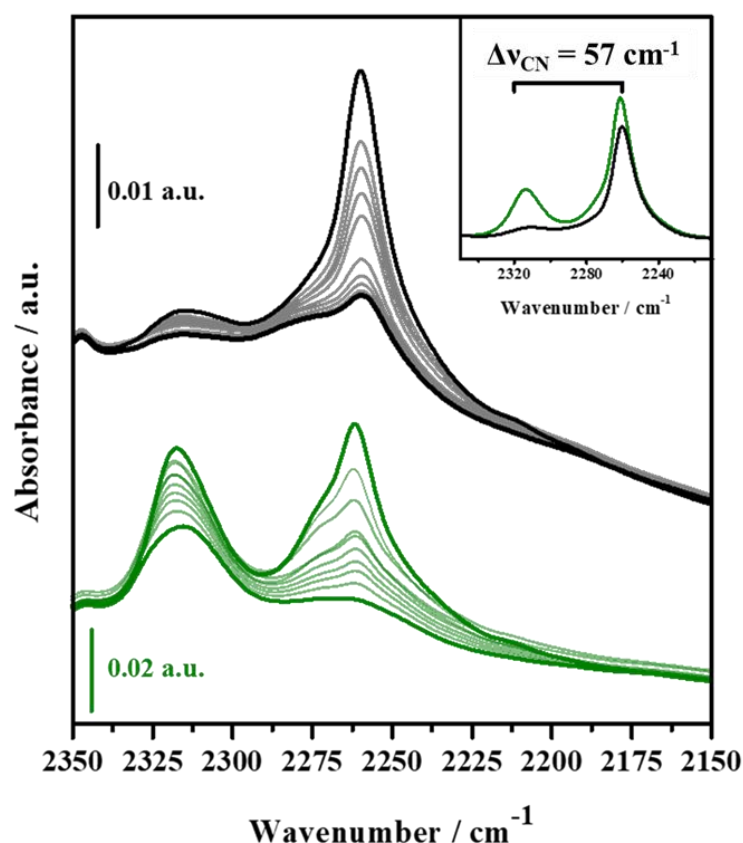


Figure 98: FT-IR difference spectra of decreasing CD_3CN coverages (from vapour pressure to vacuum) of MIL-101(Cr) (green curve) and MIL-101-Me (black curve). Samples were outgassed at $150\text{ }^\circ\text{C}$ prior to dosing. The band at 2261 cm^{-1} corresponds to physisorbed CD_3CN .

A further UV-Vis study was used to see the interaction of CO_2 with the framework. The samples were evacuated and subsequently dosed with CO_2 . The monitoring of the CO_2 adsorption on the unsaturated Cr(III) sites, at room temperature, was performed by DR UV-Vis spectroscopy (Figure 99). For MIL-101(Cr), the shoulder at 13600 cm^{-1} disappears and the band at 10280 cm^{-1} relating to the CUS sites is partially eroded. These observations imply that the introduction of CO_2 to the framework is altering the Cr(III) environment. The same behaviour is also observed for the MIL-101-Me material. It is shown then that the interaction between the CO_2 and the MIL-101(Cr) framework unsaturated sites is strong as CO_2 coordination on Cr(III) Lewis sites alters the CUS band intensity. This was confirmed as it was seen that the interaction between the CO_2 and the CUS is almost irreversible as degassing the samples at room temperature was shown to have minimal effect, Figure 99. The CO_2 can be removed from the system completely upon degassing the materials at $150\text{ }^\circ\text{C}$.

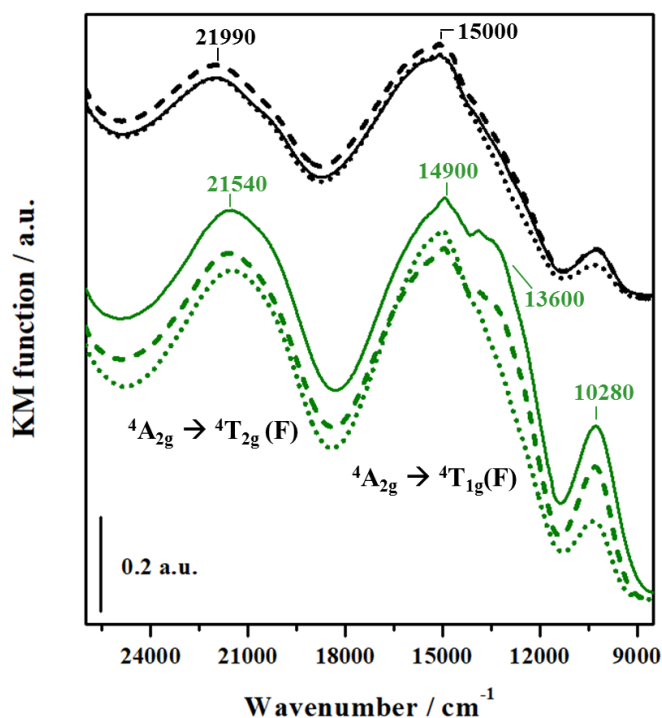


Figure 99: DR UV-Vis spectra of CO₂ adsorption (100 mbar, dotted lines) at room temperature on MIL-101(Cr) (green) and MIL-101-Me (black). Solid lines refer to non-dosed samples under vacuum, dashed lines to the samples upon outgassing CO₂ (at RT).

Computational and experimental data were collected and compared in order to validate the modelling which was being used. Density Functional Theory (DFT) was used to study the binding energy of the imidazole with chromium through electrostatic potential maps around the Cr₃O trimer cluster (Figure 100). Construction of a simplified MIL-101-Me model was built with one chromium atom in Cr₃O trimer with an incomplete coordination sphere therefore an unsaturated site, one chromium atom having the octahedral environment completed by a fluorine atom and the other chromium atom with the 1-methyl imidazole (resulting in a loading of 1.3 mmol g⁻¹). The Cr-imidazole binding energy was found to be 26 kcal mol⁻¹ with dispersion correction, indicating its strong interaction with exposed chromium site, confirming what was observed by TGA whereby degradation occurred concurrently with the framework breakdown. As would be expected, the fluorine atom was highly electronegative in both MIL-101(Cr) and MIL-101-Me. The significant differences between these two clusters is caused by the electric fields generated by the imidazole molecule within the MIL-101-Me structure. Alteration of the electron densities around the Cr₃O clusters owing to the grafted imidazole may produce a more favourable site for a catalytic reaction to proceed as the ability to interact with CO₂ or the epoxide and provide additional stabilization of transition states and species may have been introduced. The electronic field generated near the terminal imidazole may produce another favourable adsorption site for CO₂ to adsorb *via* the δ⁺ carbon atom in a side-on manner, when compared to the MIL-101(Cr).

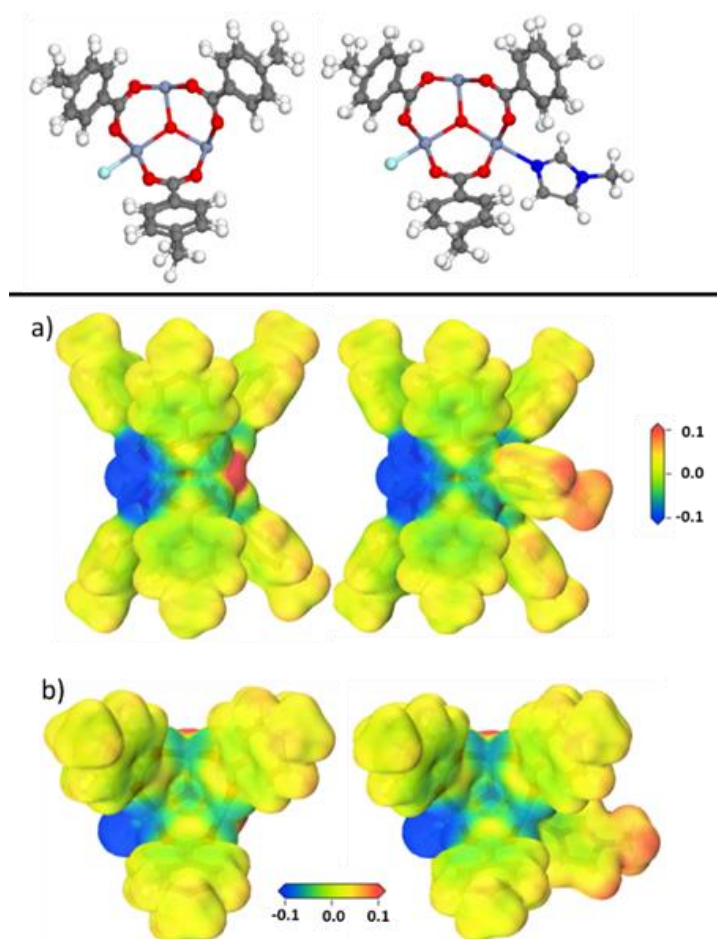


Figure 100: a) side on view of electrostatic potential maps around the Cr_3O trimer in MIL-101(Cr) (left) and MIL-101-Me (right) b) top-down electrostatic potential maps around the Cr_3O trimer in MIL-101(Cr) (left) and MIL-101-Me (right). Above: structure shown in a) without electrostatic potential maps, for reference.

The sorption of CO_2 was then investigated with Grand Canonical Monte Carlo (GCMC) simulations for MIL-101(Cr) and MIL-101-Me. For the GCMC simulations, the metal organic framework and the CO_2 adsorbate molecules were considered to be rigid. The partial charges used for this are shown in Chapter 2 in Table 9 and correspond to Figure 100. The interaction energies between adsorbate molecules and frameworks were studied with the Coulomb and Lennard-Jones potentials and parameters for frameworks were adopted from universal force field (UFF). All the parameters for CO_2 and N_2 are shown in Chapter 2 Table 10, which have been widely used for gas sorption in MOFs. To investigate the theorised additional binding site, adsorption isotherms of CO_2 at low pressure were generated for both MIL-101(Cr) and MIL-101-Me (Figure 101) and do show there is enhanced uptake in MIL-101-Me. The simulated values of the MIL-101(Cr) are in good agreement with the experimentally determined values, Figure 101. Uptake of 2.90 mmol g^{-1} at just over 1 bar was measured experimentally on the MIL-101(Cr) which compares favourably to literature values^[311,317]. For the MIL-101-Me a higher uptake of 3.01 mmol g^{-1} was determined at

the same pressure. The full isotherms for MIL-101(Cr) and MIL-101-Me collected experimentally, both adsorption and desorption, are shown in the Appendix, Figure B4. It is believed that the quadrupolar nature of the CO₂ molecule causes it to interact with the areas of electron density on the grafted imidazole therefore promoting additional CO₂ uptake of the modified material. Differences between the simulated and experimental values are not fully known, but likely due to the temperature for the experimental being lower than the set value (298 K) of the simulation and therefore would be expected to return a higher sorption value. Also the simulation does not account for any framework defects as they were not incorporated into the model. Consequently, those such as missing linkers that provide a greater number of CUS and elevate the capacity of the material could explain the higher MIL-101(Cr) experimental value versus the simulation. Repeat measurements undertaken experimentally, upon each of the various MIL-101-Me batches produced, returned a CO₂ capacity higher than that of the blank, MIL-101(Cr).

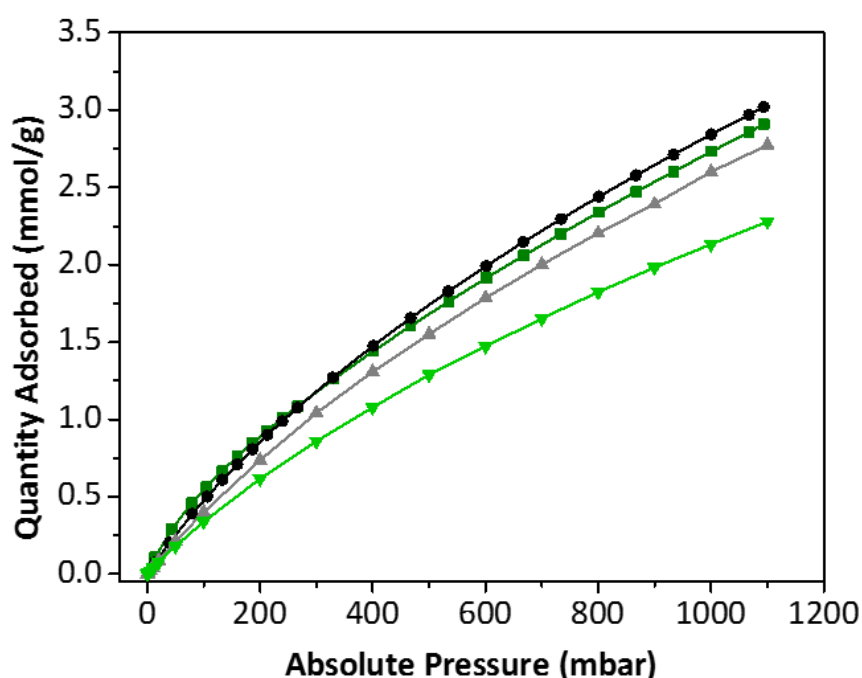


Figure 101: Adsorption isotherms of CO₂ in MIL-101(Cr) and MIL-101-Me at 298 K. MIL-101-Me experimental (black circle), MIL-101(Cr) experimental (dark green square), MIL-101-Me simulated (grey triangle) and MIL-101(Cr) simulated (light green triangle). Desorption not shown to aid clarity, see Appendix B4 for full isotherm.

A snapshot from the GCMC simulation, Figure 102, was taken. Only the pentagonal window of the structure is shown in order to discern the distinct sites where CO₂ sorption occurs on the clusters within the MIL-101(Cr) and MIL-101-Me structures and explain the adsorption results seen.

Identification of the precise site responsible for enhanced CO₂ binding in MIL-101-Me should then be possible. For MIL-101(Cr), two favourable binding sites were observed. Site (1) (see Figure 102 for numbering and location details) shows an interaction between the electron poor CUS of the Cr

atom and the oxygen of CO₂ in an end-on manner, with a corresponding Cr—OCO distance of 2.17 Å. The second site, (2), is where the electron rich fluorine is seen interacting with the carbon of CO₂, at an F—CO₂ distance of 2.43 Å, whereby the CO₂ is orthogonal to the Cr-F bond. Both of these sites, (1) and (2), are inherent to the framework and so therefore will be present also in MIL-101-Me as both the fluorine and the CUS sites still exist, but for the latter are in lower concentration depending on the extent of imidazole grafting undertaken. It was seen that the MIL-101-Me possesses an additional adsorption site, (3), which is produced by the grafted imidazole moiety and facilitates CO₂ sorption parallel to the 5-membered ring plane.

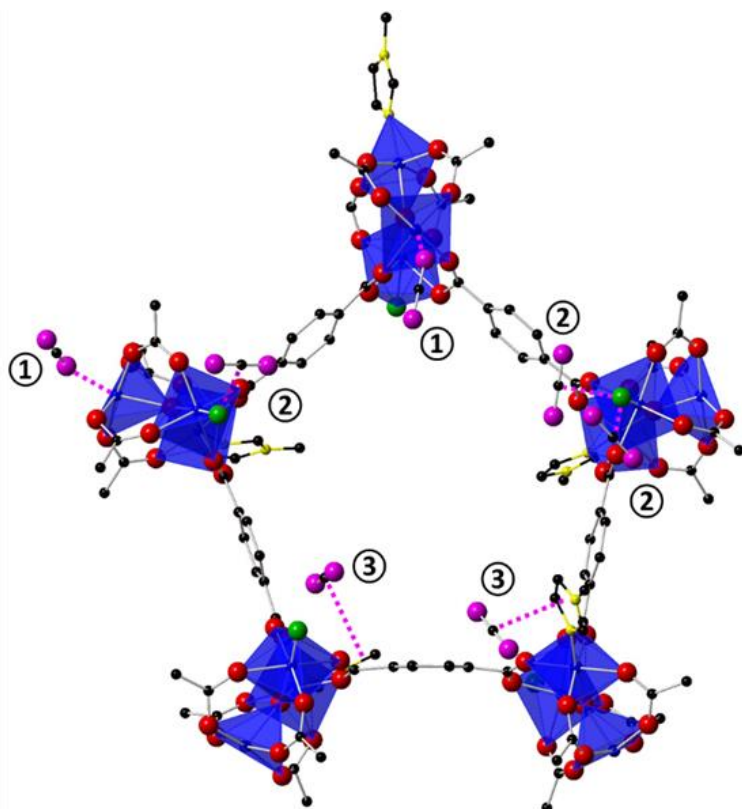


Figure 102: Simulated favorable CO₂ adsorption sites in one cross-sectional pentagonal cluster of MIL-101-Me. Chromium octahedra (blue), nitrogen (yellow), fluorine (green) and carbon (black), hydrogen atoms are hidden. For illustrative purposes - framework oxygen are red, carbon dioxide oxygen are pink. Numbers 1, 2 and 3 relate to distinct binding sites with distances of 2.17, 2.43 and 3.19 Å respectively.

The introduction of an additional site to the framework increases the CO₂ adsorption capacity of the MIL-101-Me material over that of the MIL-101(Cr) at low pressures. Radial distribution functions (RDFs) were calculated in order to quantify the interactions. As RDFs give the average distance the CO₂ is found from each of the binding sites they are useful to quantify interactions present. In RDF plots, the peak sharpness and intensity give an indication of the strength of the interaction between the studied components, in this case the framework and CO₂.

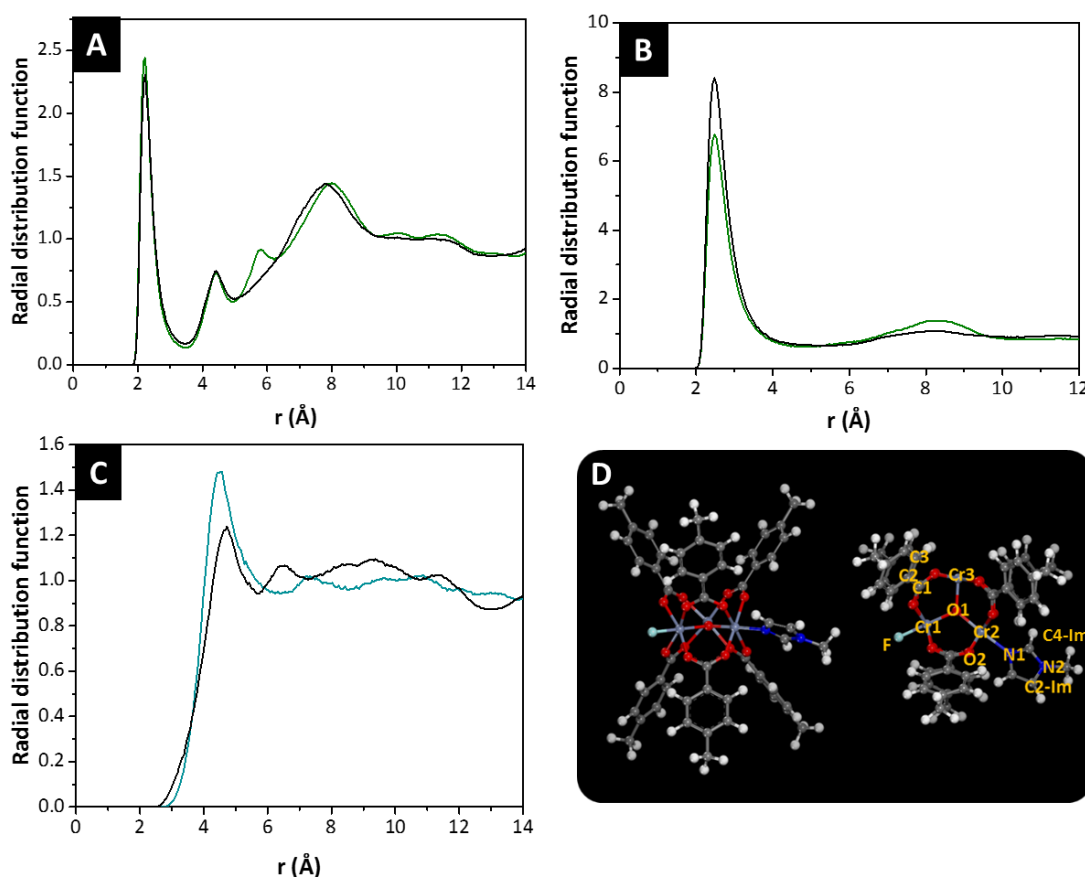


Figure 103: Radial distribution functions of A) CO₂ around the unsaturated Cr of MIL-101(Cr) (green) and MIL-101-Me (black), B) CO₂ around F atom of MIL-101(Cr) (green) and MIL-101-Me (black) and C) CO₂ around imidazole group in MIL-101-Me N2 (black) and C4-Im (blue). CO₂ pressure is 1000 mbar for all. D) Cr₃O cluster of MIL-101-Me depicting atom labelling – note: labelling is the same for MIL-101(Cr) minus those for the imidazole.

The RDF for the Cr-OCO interaction is similar for both as would be expected, given the results of the UV-vis which indicated equivalent properties of the CUS, Figure 103A. The strong F-CO₂ side-on interaction is seen as indicated by the sharpness of the peak in Figure 103B. The additional adsorption site provides peaks in the RDF for N2-Im and C4-Im (see Figure 103D for labelling specifics) from the imidazole interaction with CO₂, Figure 103C. It is thus theorised that this interaction is the reason for the higher sorption ability of MIL-101-Me for carbon dioxide. It was hoped then that the higher CO₂ sorption could bring out a greater catalytic ability for the framework through interaction with and retention of one of the proposed substrates leading to an increased likelihood of reaction occurring.

4.3.2 Catalytic testing

The MIL-101-based materials were tested for catalytic activity following the promising characterisation and simulation results.

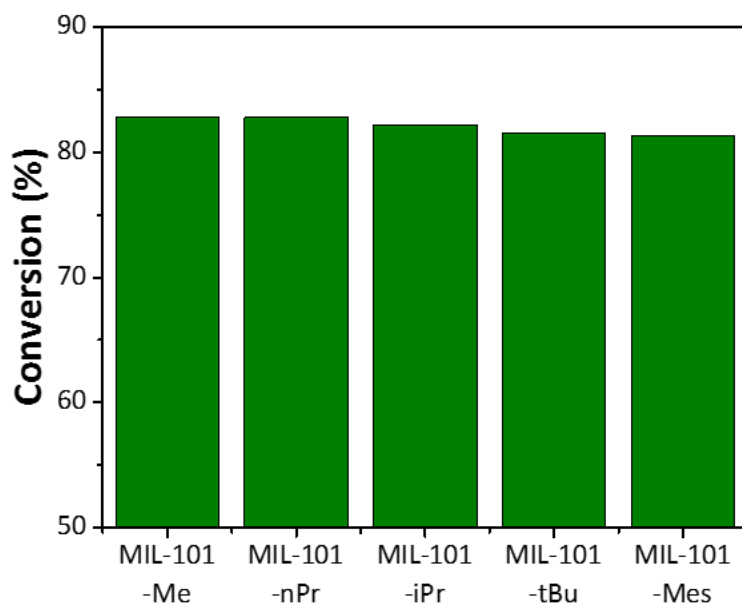


Figure 104: Conversion values for butylene oxide to butylene carbonate for MIL-101-R, whereby R relates to the functionality on the non-grafting nitrogen. Reaction conditions: butylene oxide (55 mmol), catalyst MIL-101-R (0.075 mol %), solvent free, 115 °C, 1.5 hours, 20 bar CO₂ (at RT). Analysed by ¹H NMR using mesitylene as an internal standard.

Formation of butylene carbonate from 1,2-butylene oxide and CO₂ was studied. Initially, differently functionalised imidazole moieties (whereby the different functionality relates to the structure on the non-grafting nitrogen, with structures shown in Chapter 3) were introduced to MIL-101(Cr). The subsequently formed materials were screened for the activity, Figure 104. In all cases the imidazole-grafted MIL-101(Cr) materials were active for the reaction. High conversion values, 83 – 81 mol % were observed for all of the different analogues, over only a short time period, 1.5 hours. There was little variation in catalytic activity with the different imidazole species, which implies the variation of the R group does not have any real effect on the rate of the reaction. What is shown by this however, is that from the consistency observed in the conversion values that the synthetic protocol is robust. This is evidenced by the fact that the grafting technique was able to be successfully reproduced across multiple, different batches and ultimately resulting in highly consistent results under catalytic testing. In all cases the above plot, Figure 104, the selectivity was found to be > 98 mol % towards the cyclic carbonate product

proving that the materials produced obtain a very high yield of the desired product and do so without promoting any pathways which lead to the formation of by-products.

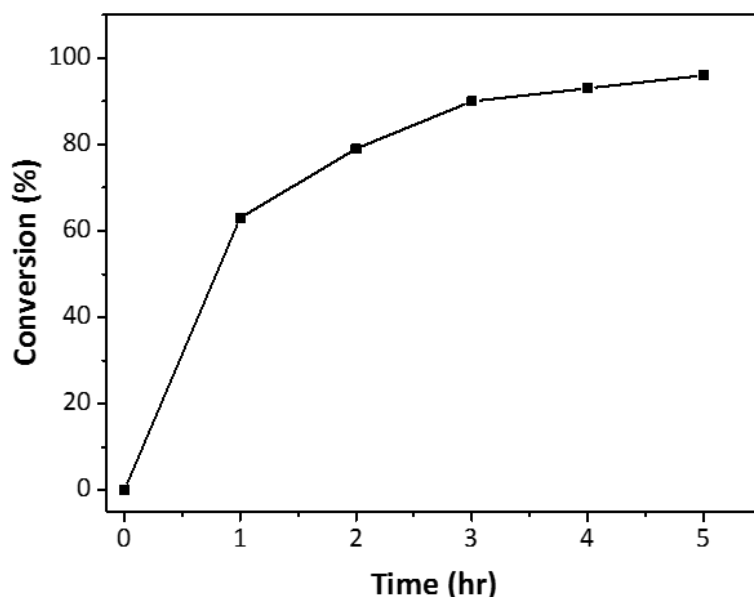


Figure 105: Conversion of butylene oxide to butylene carbonate over time. Reaction conditions: 5 g epoxide, 5 hours, 115 °C, time: see axis, 20 mg MIL-101-Me (1.88 mmol/g loading), 20 bar CO₂ (at RT). Analysed by ¹H NMR using mesitylene as an internal standard.

Note: each time point is a separate reaction.

Kinetic analysis showed that just after 5 hours the reaction went to completion, Figure 105, with a high selectivity for the cyclic carbonate observed in the functionalised MIL-101-Me again observed. The 1 hour time point can be used to evaluate the activity of the catalyst system, as the epoxide is not rate limiting initially so turnover frequency (TOF) can be used. A 63 mol % conversion was observed after an hour, giving an impressive TOF of 1144 hr⁻¹, the overall TON for the system at 5 hours (96 mol % conversion) is seen to be 1761. The lack of fresh substrate results in the slowing of the reaction rate rather than deactivation of the catalyst in the later time points. This will be addressed further with the undertaking of recycle tests, see later section.

As discussed above, the activity of the blank framework has previously been reported^[130,322]. The MIL-101(Cr) material produced for this work appears to have a higher activity (30 mol% conversion, Figure 106) than literature values, though different reaction conditions were applied which stops the systems being directly comparable. In all examples, Figure 104 and Figure 106, the activity of the grafted system is high, with the MIL-101-R species out-performing the bare MIL-101(Cr) system. These results are highly promising as the produced material are seen to be highly active for the CO₂ utilisation reaction and so validate the grafting of an imidazole to the framework to produce MIL-101-Me.

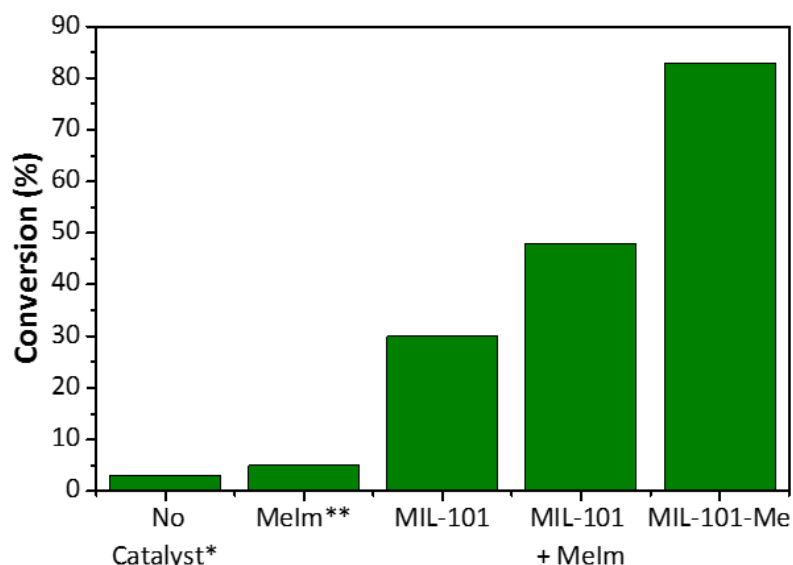


Figure 106: Conversion values of butylene oxide for the reaction with CO₂ to butylene carbonate (shown). Reaction conditions: butylene oxide (55 mmol), catalyst MIL-101-Me (0.96 mmol/g, 0.075 % mol), solvent free, 115 °C, 1.5 hours, 20 bar CO₂ (at RT). Analysed by ¹H NMR using mesitylene as an internal standard. Melm denotes 1-methylimidazole. *Blank (no catalyst) reaction time 24 hours. **Free imidazole reaction time 6 hours.

To probe further the synergistic effect of combining the imidazole species with the catalytically active chromium sites a physical mixture of 1-methyl imidazole and MIL-101(Cr) was created and the material was used within a catalytic trial. Care was taken to ensure the amounts of MIL-101(Cr) and imidazole matched that of the grafted MIL-101-Me system used (0.96 mmol g⁻¹ in this instance). The physical mixture showed significantly lower conversion (48 mol %) than the grafted MIL-101-Me system (83 mol %) whilst maintaining the high selectivity seen for MIL-101-Me. This result shows that the improved catalytic activity of the MIL-101-Me system does not derive from simply having the imidazole and MIL-101(Cr) species present within the reaction, but rather that the anchoring to the support is required. It is clear that the proximity between the imidazole that is achieved upon binding to the framework plays a key role. This can be explained by the simulation results whereby the Melm provided another adsorption site which may favourably place CO₂ and epoxide in close proximity. Similarly, this result also shows that the imidazole must be bound to the MIL-101(Cr) framework, otherwise it would be expected that the catalytic results would be near-identical for the grafted species and that of physically mixed version. The conversion value for the physical mixture is larger than the sum of the conversion values individually for Melm and MIL-101(Cr). This result would be expected if the synergy discussed is not present due to lack of binding. However, when the reaction temperature of 115 °C is considered then it is likely the higher than anticipated conversion which is observed in the case

occurs because the imidazole binds to the CUS of the framework *in-situ* during the reaction progression.

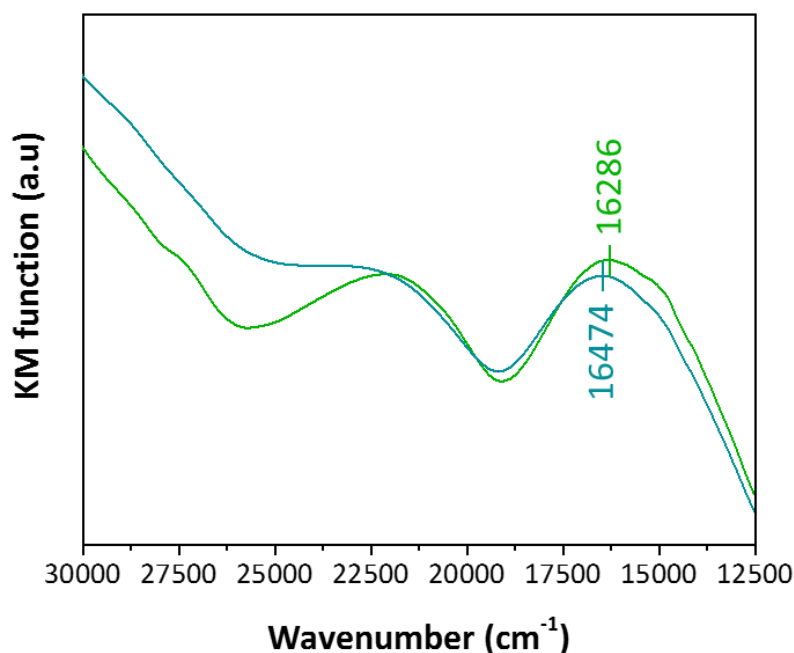


Figure 107: UV-Vis spectra of MIL-101(Cr) (green) and physical mixture of MIL-101(Cr) + Melm (blue). The physical mixture spectra is post-catalysis, the MIL-101(Cr) is as synthesised.

Evidence for this can be seen in the UV-Vis spectra of the solid which was collected, washed and dried post-catalysis for the physical mixture trial, see Figure 107. The two d-d transitions are again blue-shifted, with respect to the MIL-101(Cr), but not to the same degree as the specifically grafted version, MIL-101-Me. The lesser degree to which the shift occurs can be attributed to the lower timescale of the reaction versus synthesis period indicating that the grafting has not occurred to the same extent as in the MIL-101-Me. The loading of the imidazole in the physical mixture following reaction will thus likely be lower as some of the imidazole will not have been incorporated into the structure. The physical mixture displaying a higher conversion value than the sum of the two parts (imidazole result plus MIL-101(Cr) but not the same as the MIL-101-Me can be explained then as the *in-situ* grafting did not occur fully. Functionalisation of the chromium clusters with the imidazole species prior to reaction is shown to be crucial as it creates a heterogeneous catalyst which has significantly increased activity towards the butylene oxide, carbon dioxide coupling reaction studied than the un-functionalised MIL-101(Cr).

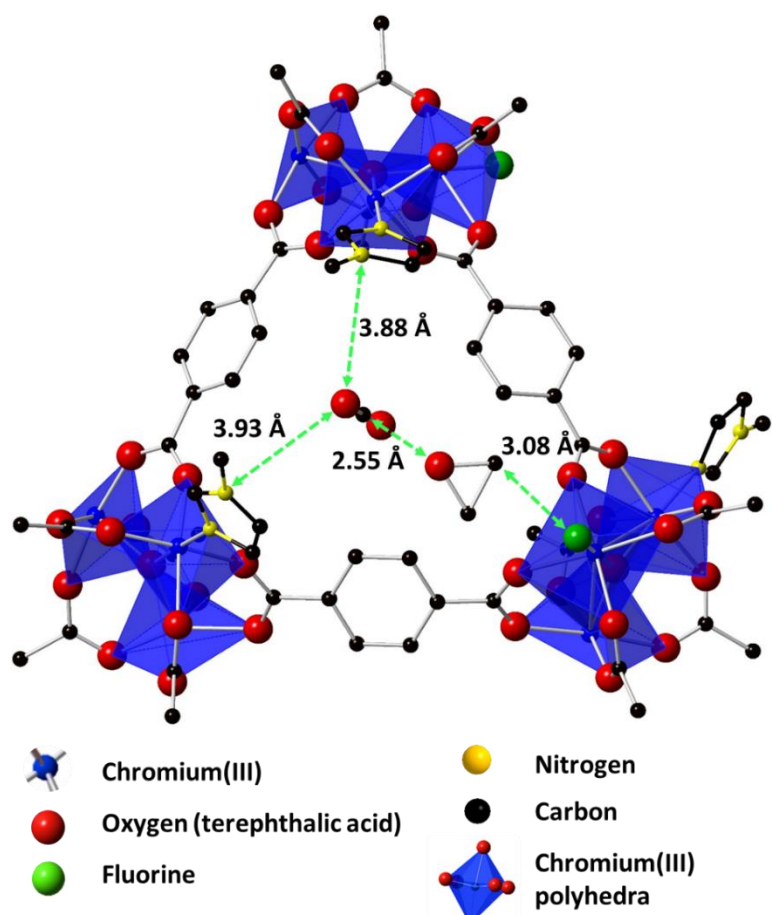


Figure 108: Favourable adsorption site for epoxide and CO₂ in a Cr₃O cluster trimer of MIL-101-Me; a “cave” formed by two grafted 1-methyl imidazole groups and F atom is shown. Note: butylene oxide side chain (-CH₂CH₃) was removed in order to ease the computational strain.

The interactions between MIL-101-Me and a mixture of CO₂ and epoxide was investigated computationally, with GCMC simulations, to account for the high catalytic ability that the material displayed upon testing. Figure 108, reveals that the CO₂ preferentially adsorbs between grafted imidazoles in site (3) as per Figure 102, whilst the epoxide interacts strongly with the electron rich F *via* the polarised carbon of the epoxide and in so doing occupies site (2) preferentially to CO₂. This was observed in the RDF of the F and the epoxide interaction, Figure 109A. As a consequence, the sorption site near the F atoms in MIL-101-Me is likely filled by the epoxide. The distance between the CO₂ and the epoxide is 2.55 Å, so the two substrates are held within close proximity of one another in the MIL-101-Me framework which will enhance the probability of the reaction occurring. The RDF of the epoxide-CO₂ distances further demonstrates the enhanced propensity to form epoxide-CO₂ clusters in MIL-101-Me compared to MIL-101(Cr), Figure 109B. The strong van der Waals interactions are not seen in the MIL-101(Cr), showing that the imidazole ring aids the sorption of CO₂ in MIL-101-Me and brings it to be held closely to the epoxide.

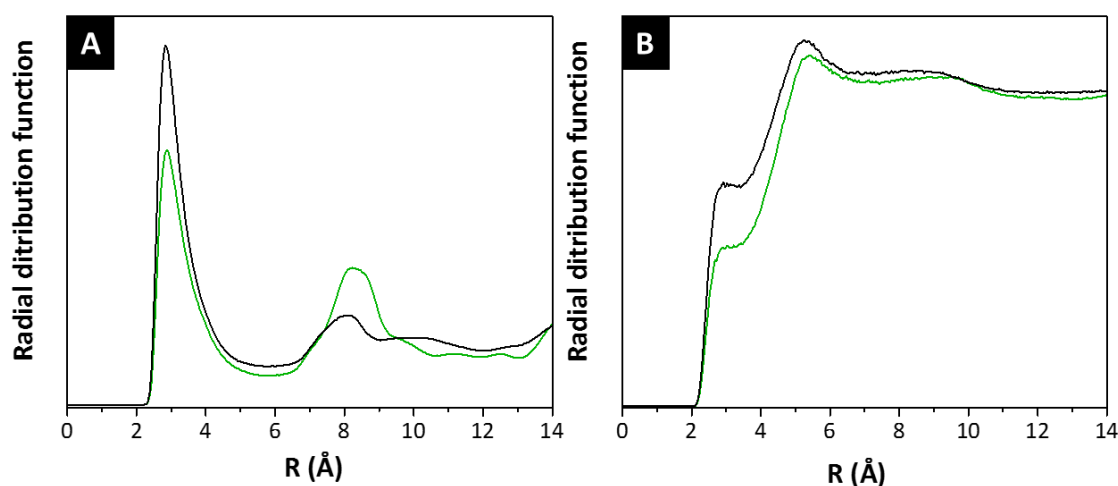


Figure 109: A) Radial distribution functions for epoxide and F atom in MIL-101(Cr) and MIL-101-Me and B) RDF for epoxide and CO₂ cluster formation in MIL-101(Cr) and MIL-101-Me. For both MIL-101(Cr) (green) and MIL-101-Me (black).

Further investigation of the formation of CO₂ and epoxide clusters was undertaken through DFT simulations. The cluster, above Figure 108, was again modelled to observe the interactions of the CO₂ and epoxide with the framework. These revealed that CO₂ preferentially adsorbs between grafted imidazoles in site (3), Figure 102. Again, the epoxide is held close to the fluorine, site (2), in good agreement with the GCMC simulations. The DFT calculated distance between the CO₂ and the epoxide is 2.75 Å, Figure 110A. The molecular orbitals, Figure 110B, detail how both of the grafted imidazole species help to stabilise CO₂ near the epoxide *via* π - π interactions. The overlap of the orbitals of the epoxide is clear and given their proximity will increase the likelihood of reaction between the two. For both the computational methods the same CO₂ and epoxide arrangement is observed with the additional site created by the imidazole key as the epoxide occupies the other sites where CO₂ would locate without the presence of the epoxide. The lower conversion values for MIL-101(Cr) then occurs as without the imidazole the CO₂ shall not be held in as close proximity to the epoxide causing the likelihood of the reaction occurring to lessen.

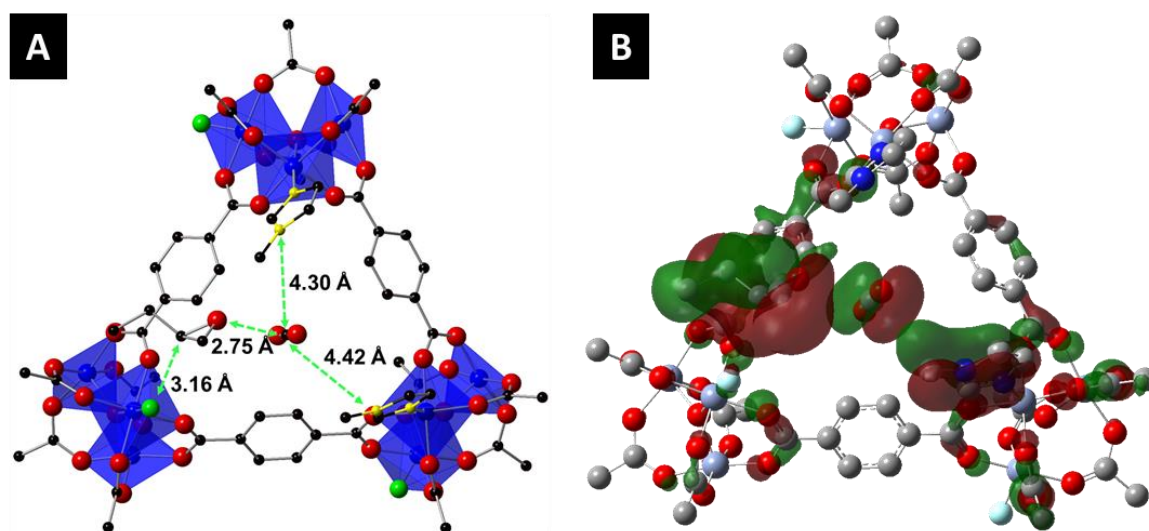


Figure 110: A) Favourable adsorption site for epoxide and CO₂ in a (Cr₃O)₃ cluster of MIL-101-Me, as determined by DFT modelling. B) Epoxide and CO₂ cluster with molecular orbitals shown.

A second example of the MIL-101-Me framework promoting the clustering of CO₂ and the epoxide, was calculated by DFT, bringing the two reagents within close proximity to one another in a different part of the framework. This second example occurs in a similar fashion to Figure 110, but in this instance within a different aperture; formed by three Cr₃O clusters containing: a grafted imidazole, an open metal site and the remaining and an F atom, Figure 111A. Here, the molecular orbitals clearly show a bridge between imidazole, CO₂ and epoxide again *via* π - π interaction, reinforcing further the requirement of the imidazole to help align the CO₂ and epoxide for reaction, but also evidence of another site for the reaction of the two reagents. The existence of another framework region which is responsible for promotion of the reaction between the reagents provides additional explanation for the enhanced activity of the MIL-101-Me material.

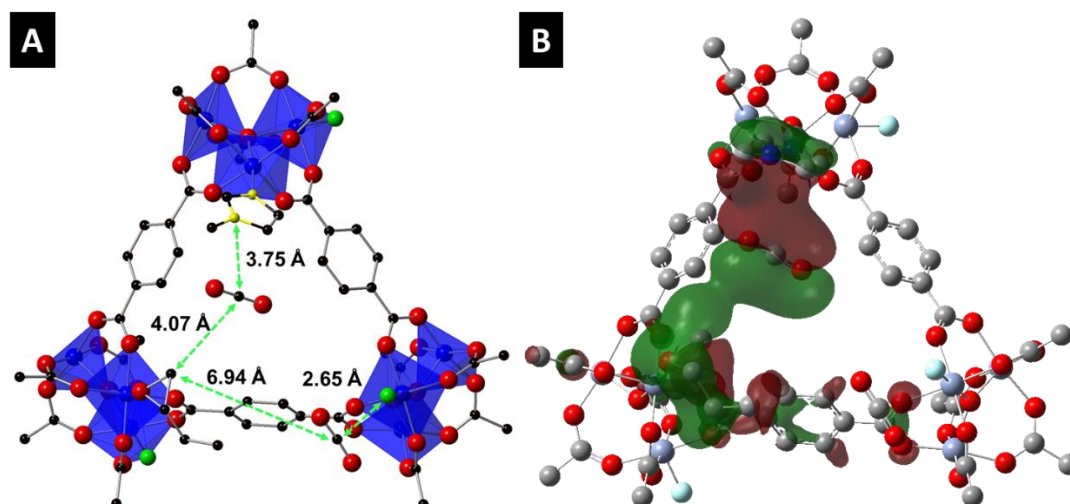


Figure 111: A) Distances between CO₂ and epoxide in the alternative cluster of CO₂ and epoxide in MIL-101-Me. B) Molecular orbital depiction showing π - π interaction.

In summary then, as the two reagents are brought closer together in MIL-101-Me it is more likely, *via* proximity effect, that they will react and the catalytic cycle ensue. The imidazole is seen to be of paramount importance to this occurring as it provides the additional sorption site for CO₂ without which, such as is the case in MIL-101(Cr), the epoxide is favoured to occupy the F and CUS sorption sites and there is then no further site available for CO₂ to occupy. The case in MIL-101(Cr) is then that the CO₂ and the epoxide are not likely to be found as close together on average within the framework and so the reaction rate will be lower, as has been observed.

4.3.2.1 Imidazole loading study

After the testing of the MIL-101-Me at 0.96 mmol/g loading a range of samples with higher 1-methyl imidazole loadings were synthesised. It was theorised that if the loading of the imidazole is increased then the CO₂ capacity will raise proportionally. If this occurs then the binding sites that have been seen, *via* computational studies, to be responsible for the raised activity of the MIL-101-Me material will be present greater concentrations and so the amount of CO₂ and epoxide clusters formed also higher. This should lead to higher activity towards the production of cyclic carbonates, due to improved conversion values.

Loading determination was again calculated from CHN values as seen in Table 35. All of the variants were synthesised from the same starting batch of MIL-101(Cr) in order to ensure that the starting, 'zero', value for the conversion should be the same, as the blank framework is known to be active for the reaction and in so doing negate any additional nitrogen content that would raise the calculated loading value, as per earlier discussion on the calculation of the loading, section 4.3.1.

| Entry | C / % | H / % | N / % | Loading / mmol g ⁻¹ |
|-------|-------|-------|-------|--------------------------------|
| 1 | 40.85 | 3.85 | 3.33 | 1.19 |
| 2 | 43.19 | 3.90 | 5.30 | 1.89 |
| 3 | 41.35 | 3.05 | 5.97 | 2.13 |

Table 35: Carbon, hydrogen and nitrogen percentage values for MIL-101-Me samples with different loading based off N %.

As the imidazole incorporation was shown to add an additional adsorption site boosting the capacity of the material, with respect to the MIL-101(Cr) framework, CO₂ adsorption studies of the differently loaded variants were obtained. In each case for the 1.19, 1.89 and 2.13 mmol/g MeIm MIL-101-Me materials, the adsorption amount was higher than that of the blank material, Figure 112. The 2.13 mmol/g is still below the maximum possible with the framework, up to approx. 3 mmol/g is possible although low CUS site concentrations were measured by FT-IR^[205]. The maximum uptake amount for each of the MIL-101-Me versions increased proportionally with the loading amount, indicating that it is the imidazole which was the modification responsible for the increase in the CO₂ capacity. Batch reactions were undertaken with the materials in order to establish whether the increased CO₂ uptake ability would translate to a heightened conversion value as would be expected.

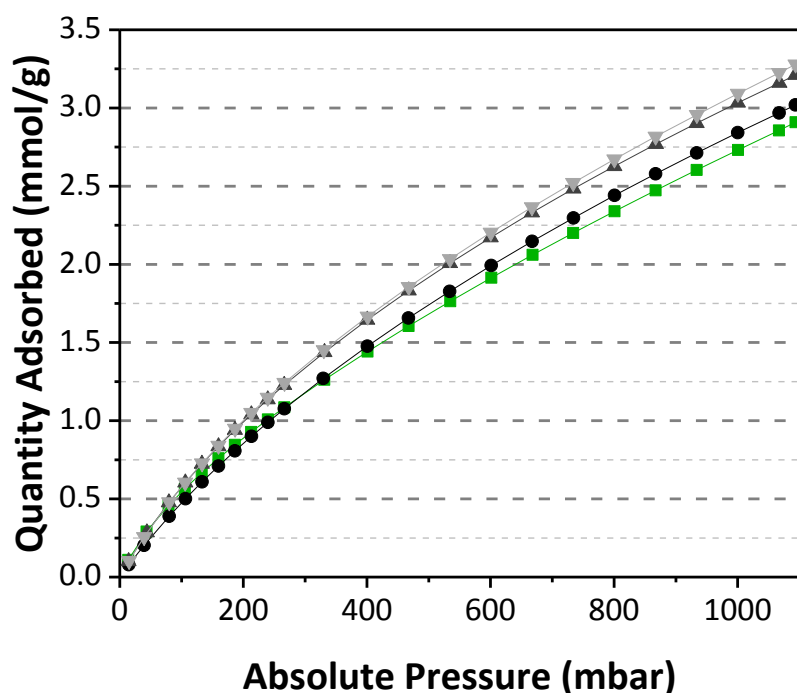


Figure 112: Adsorption isotherms of CO₂ by MIL-101(Cr) and varied MIL-101-Me analogues at 298 K. MIL-101(Cr) (green, square), MIL-101-Me with 1.19 mmol/g loading (black circle)

and MIL-101-Me with 1.89 mmol/g loading (dark grey triangle) and MIL-101-Me with 2.13 mmol/g loading (light grey triangle).

Each variant was tested under the same conditions, with the mass of catalyst added determined by the loading. Whilst the blank framework is active, it was assumed that the contribution the differences in masses therefore amount of un-functionalised framework within each sample contributing to conversion was negligible, in order to simplify the comparisons made. There is a clear increase of conversion with increase in loading of the imidazole within the framework. The conversion value of the 1.19 mmol/g version is lower than that of the 0.96 mmol/g in Figure 106 however, the reaction conditions used were not the same in terms of substrate amount and therefore differences are to be expected. The conversion value of the MIL-101(Cr) batch tested is comparable to that seen in Figure 106 indicating that the synthesis technique is highly reproducible in the formation of a consistent standard of MIL-101(Cr) from which the modified variants are produced. In each case the selectivity towards the blank was shown to be high, > 98 %, *via* NMR.

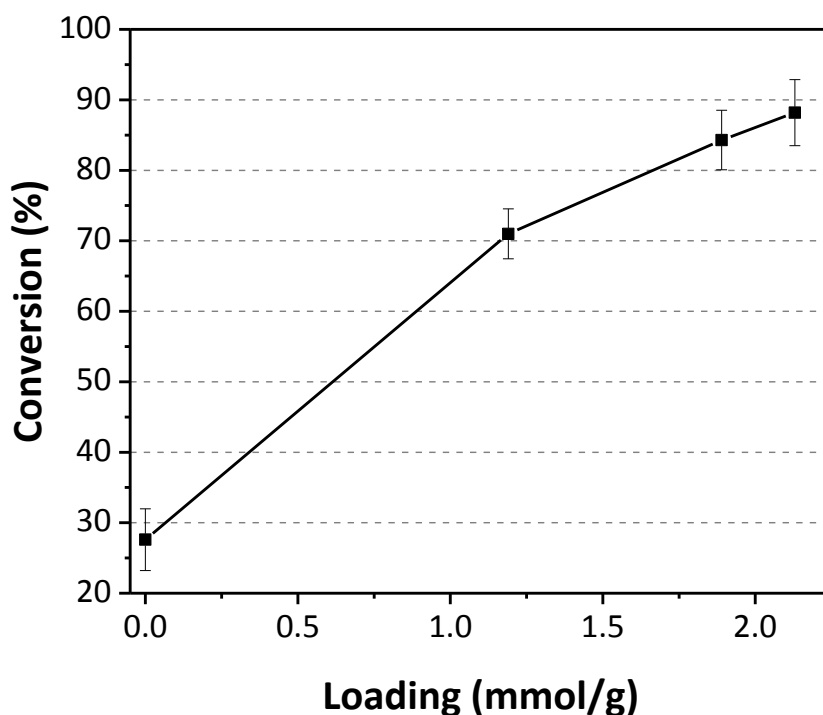


Figure 113: Average values for the conversion of butylene oxide to butylene carbonate with differing values of imidazole loading. Reaction conditions: butylene oxide (69 mmol), catalyst MIL-101-Me (0.06 % mol), solvent free, 115 °C, 1.5 hours, 20 bar CO₂ (at RT). Analysed by ¹H NMR using acetonitrile as an internal standard. Note: 'zero' loading denotes the blank framework MIL-101(Cr). Errors shown from two repeat measurements.

The results of the CO₂ adsorption and catalytic studies clearly indicate that a higher imidazole loading provides a higher CO₂ capacity which in-turn results in the greater catalytic ability of the MIL-101-Me material in the CO₂ and epoxide reaction. This confirms that the imidazole is responsible for the activity of the MIL-101-Me material.

4.3.2.2 Recycle tests

The heterogeneous nature of the imidazole-grafted MIL-101(Cr) catalyst was analysed through successive re-use and characterisation of the same MIL-101-Me sample. Results of the recycle test undertaken are shown in Table 36. It can be seen from this the MIL-101-Me can be recycled and does not suffer from a significant loss in activity. Selectivity towards the cyclic carbonate product was high across all three trials, with the desired product overwhelmingly formed. A marginal selectivity and appreciable conversion decrease were observed, but can be explained by the findings discussed below upon characterisation of the recovered material.

| Cycle | Conversion / % | Selectivity / % |
|-----------------|----------------|-----------------|
| 1 st | 97 | > 99 |
| 2 nd | 99 | 99 |
| 3 rd | 87 | 98 |

Table 36: Recycle tests on MIL-101-Me, conditions, 5 g of butylene oxide (69 mmol), 20 bar CO₂ at RT, 200 mg of MIL-101-Me (1.88 mmol g⁻¹ imidazole loading), 45 min.

The conditions of the reaction were modified to use a larger amount of catalyst to aid collection following reaction and allow for a larger mass to be available for use by various characterisation techniques. The high activity of the material can still be observed, given that the reaction time was shortened. A decrease in conversion is observed upon the second re-use implying that the MIL-101-Me may deactivate over time, if this was the case then the implementation of a regeneration cycle would need to be considered. From the UV-vis obtained post reaction the d-d transitions of the recovered material are comparable to that of the MIL-101-Me, following the grafting process, indicating that the imidazole grafting is maintained on the framework after use in a reaction, Figure 114.

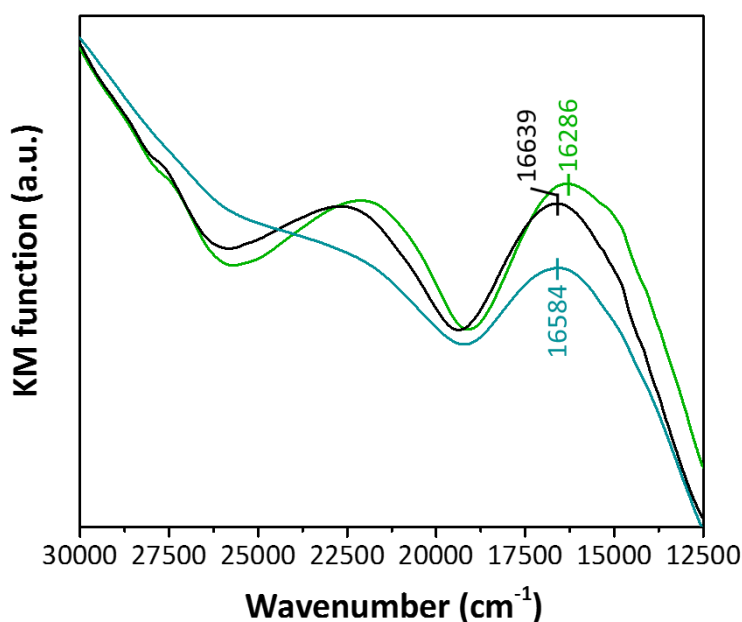


Figure 114: UV-Vis spectra of MIL-101(Cr) (green), MIL-101-Me pre-catalysis (black) and MIL-101-Me post-catalysis (blue), following the reactions undertaken in Table 36.

The transition occurring *circa* 22500 cm^{-1} appears as a shoulder to what is believed to be additional peaks due to organic species still remaining within the framework from the catalysis. This indicates that following use the catalyst may retain some of the products or reagents within the structure. Only moderate washing was employed after use and prior to reaction. Any retention of organic species within the pores would impact porosity. Such blocking of pores could be from larger by-products which form during catalysis which subsequently cannot leave the framework. To investigate this nitrogen adsorption studies were then undertaken to see how the material is affected by catalysis after a single cycle. It can be seen there is a clear decrease in the uptake amount following use of the material for a single iteration. The surface area of the MIL-101-Me for the sample in Figure 115 prior to use was $2602 \pm 44 \text{ m}^2/\text{g}$ and following collection dropped to $2057 \pm 40 \text{ m}^2/\text{g}$. Therefore some blocking of the material is seen after the first use and given this is likely to increase over sequential uses the drop in activity for the third cycle can be explained. An NMR study of the material after the last cycle using DCl or NaOD to degrade the MOF and release the organic moieties inside would allow for a greater understanding of the processes involved in the activity drop-off observed.

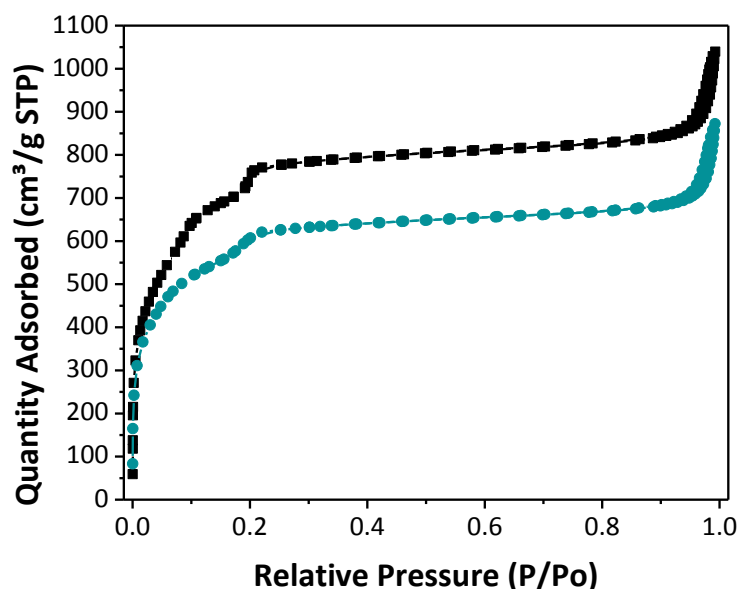


Figure 115: Nitrogen adsorption and desorption curves of MIL-101-Me (black) and MIL-101-Me after a single use in butylene oxide to butylene carbonate reaction (blue), reaction undertaken at 1 bar CO₂.

Activity loss could also stem from degradation of structural properties, it is essential that these are maintained following catalytic cycles. An SEM image after one catalytic cycle, see Figure 116, shows that there is little visible change in the particles once they have been used. All indicate that the size and shape is the same as following the PSM process. It can also be seen that the faces are still smooth, thus the particles have not degraded, and mechanical defects have not been introduced on the particle surface.

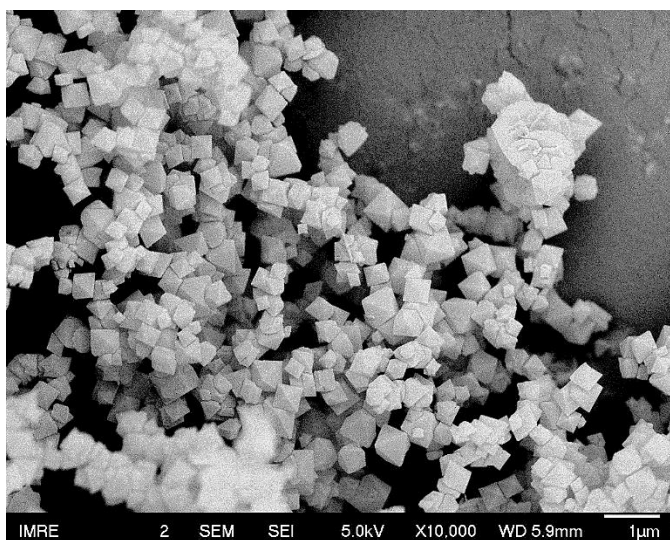


Figure 116: FESEM image of MIL-101-Me following a single reaction with butylene oxide and CO₂, Sample was gold sputtered for 20 seconds prior to imaging.

However, after 3 cycles of use – where, as per Table 36, there is the beginnings of activity drop-off – there was a notable difference in the XRD pattern of the material as shown in Figure 117. A loss of the Bragg peaks is observable for the catalyst which indicates that the crystal structure across the sample has been lost.

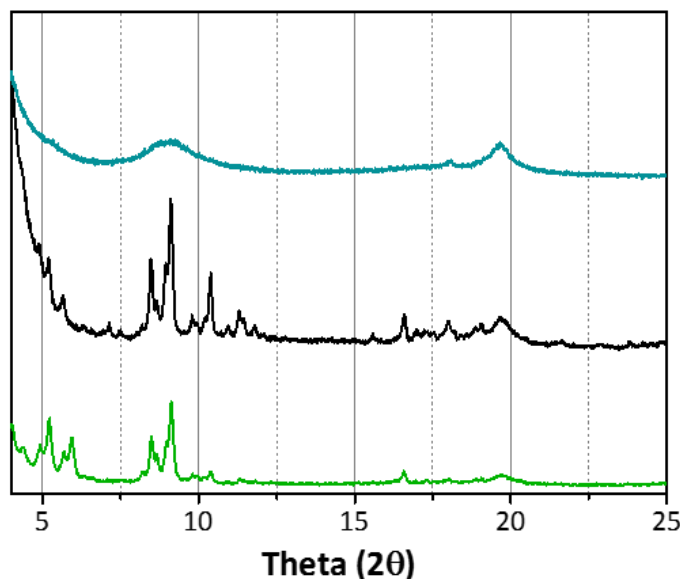


Figure 117: Powder XRD of MIL-101(Cr) (green), MIL-101-Me as synthesised (black) and MIL-101-Me for three cycles of use (blue).

The observations seen for the MIL-101-Me following catalysis, the reduction in porosity and surface area, incorporation of organic material into the framework and finally the loss of the crystallinity follows that reported by Zalomaeva *et al.*^[130] in their use of MIL-101(Cr) for CO₂ utilisation. No mechanism was put forward for the loss of framework stability and thus is something that requires further investigation in order to optimise the system fully and attain the benefits linked with a fully recyclable heterogeneous catalyst.

4.4 Conclusions and future work

4.4.1 Conclusions

The CUS sites present within MIL-101(Cr) were successfully used as handles for the incorporation of imidazole moieties into the framework. The anchoring of a range of imidazole species produced a hybrid MOF, MIL-101-Me ($\text{Cr}_3\text{F}(\text{H}_2\text{O})(\text{Melm})\text{O}(\text{BDC})_3 \cdot n\text{H}_2\text{O}$), with superior catalytic ability to not only the un-modified MIL-101(Cr) but also the majority of currently published literature where MOFs are employed as heterogeneous catalysts, with large, 1144 hr^{-1} TOF values seen after an hour of reaction (63 % yield).

Through extensive characterisation the synthesis method to produce the MIL-101-Me catalyst was evaluated and showed that the PSM technique employed did not have any significant detrimental effect on the properties of the framework. The CO_2 capacity of the MIL-101-Me was tested and found to be higher than that of the MIL-101(Cr) framework. Rationale for this was determined through a complementary modelling study. It was shown that the addition of the imidazole produces a favourable binding site for CO_2 and so at lower pressures the uptake of MIL-101(Cr) is greater when modified with an imidazole. The availability of coordinatively unsaturated sites provides unique handles for isolating the functionalised imidazole species within the framework, removing the need for a co-catalyst to be employed. Therefore, when run under reaction conditions the imidazole functionalised MIL-101(Cr) was shown to effectively catalyse the conversion of epoxides to cyclic carbonates under co-catalyst and solvent-free conditions. The imidazole-functionalised catalyst was found to have superior catalytic performance, when compared to the un-functionalised framework, as well as a physical mixture of imidazole and the MIL-101(Cr) framework, highlighting the importance of the CUS in the functionalised heterogeneous catalyst. The site-isolation of the imidazole led to high turnover frequencies and substantially reduced reaction times, making the methodology potentially industrially attractive. Reasoning for this was deduced from molecular simulations which showed that the specific binding of the imidazole to the coordinatively unsaturated chromium sites brings the epoxide into close proximity with the CO_2 improving the ensuing catalytic activity compared to MIL-101(Cr). It is then envisaged that the additional binding site for CO_2 with the imidazole ring is responsible for the close proximity between the CO_2 and epoxide during the reaction which, owing the proximity effects results in the substantially improved catalytic activity.

4.4.2 Future work

A number of ways to further optimise the MIL-101-R materials can be undertaken with the view to improving the activity and reusability. It was seen that the loading had a profound effect on the conversion obtained, therefore a study to optimise the loading amount would allow for either use of less catalytic material per reaction, shorter reaction times or a combination of these.

Furthermore, in addition to the modification of the amount of imidazole the R group of it has the potential to be modified also. When employing imidazole variants for CO₂ utilisation reactions the structure of the imidazole has been shown to have an effect^[119]. In the above study use of different, but solely C, H containing groups on the non-grafting nitrogen were employed but showed little variation, side-chains containing an OH group for example have been shown to be effective^[234]. Indeed, not only imidazole species need be used, other nitrogen containing structures may have efficacy following grafting to the CUS after PSM^[106,119,250].

Apart from the addition of nitric acid to the synthesis procedure, little optimisation of the framework synthesis was undertaken therefore scope for improvement is possible. For example, size modulation of the MIL-101(Cr) framework was not undertaken during the synthesis procedure and therefore resulted in relatively broad distribution of MIL-101(Cr) crystal sizes being produced. A number of studies have shown the use of modulators for control of particle size, but also for defect site creation and subsequent improvement in performance of the material^[340,341]. Application of these methods to the imidazole functionalised material could yield further improvement in catalytic ability. Reasons for this are two-fold. Firstly the lowering of the particle size may improve activity as it will provide a greater number of active sites on the outer most parts of the MOF material, but also reports have shown that the use of modulators improves CO₂ uptake which may improve catalytic ability^[342–344]. Secondly, use of a modulator, typically one that is a mono-carboxylic acid, produces defect sites within the framework. The defect sites produced would in theory increase the number of CUS present. For the MIL-101(Cr) system this would create more handles for the imidazole to be grafted onto giving a higher possible loading which, hopefully, would improve the effectiveness of the material in-line with the results that have been reported above.

The high activity of the PSM MIL-101(Cr) was observed to decrease over successive cycles. As such, for the material to be successfully re-used a means of regenerating it to regain the lost activity is required to be found. If as suspected the material is degrading through the loss of the framework structure then a solution to this could be found with MIL-100(Cr). This is a similar MOF to MIL-101(Cr) in that it is chromium based and therefore has unsaturated Lewis acid sites and so activity towards the cyclic carbonate production using CO₂ but, uses trimesic acid as the linker

instead of terephthalic acid and has been reported to be more amenable to recycling by Taherimehr *et al*.^[322]. Alternatively, the use of other MOF systems could be investigated for combination with the PSM to add the imidazole as literature examples of MOFs with high Lewis acidity and number of CUS have been reported^[345].

Appendix B

B.1 FESEM image of MIL-101(Cr) collapse

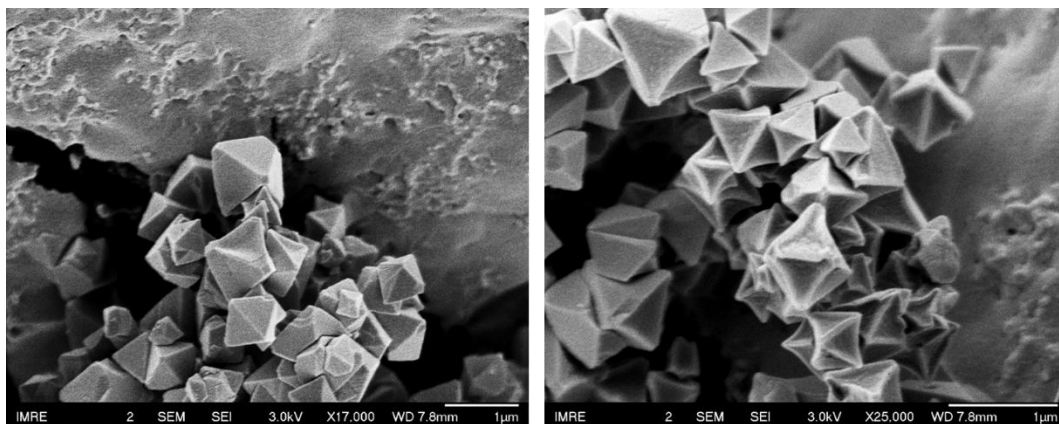


Figure B1: FESEM images of MIL-101(Cr) at beginning of measurement (left) and following exposure to electron beam for several minutes (right)

B.2 NIR of MIL-101(Cr) and MIL-101-Me

NIR confirmed the removal of water during the synthesis procedure as well as during the characterisation studies to observe the CUS.

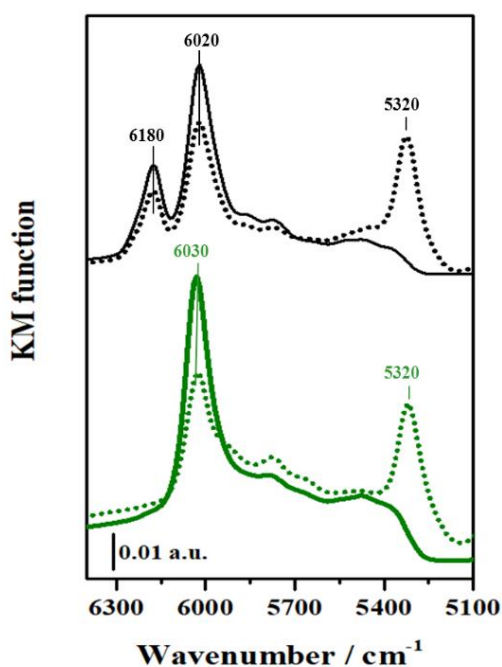


Figure B2: DR NIR spectra of MIL-101(Cr) (green) and MIL-101-Me (black) in air (dotted curves) and upon outgassing at 150°C for 1h (solid curves).

B.3 FT-IR of 1-methyl imidazole

To display the difference between the grafted and non-grafted methyl imidazole the FT-IR spectra of the free imidazole was obtained.

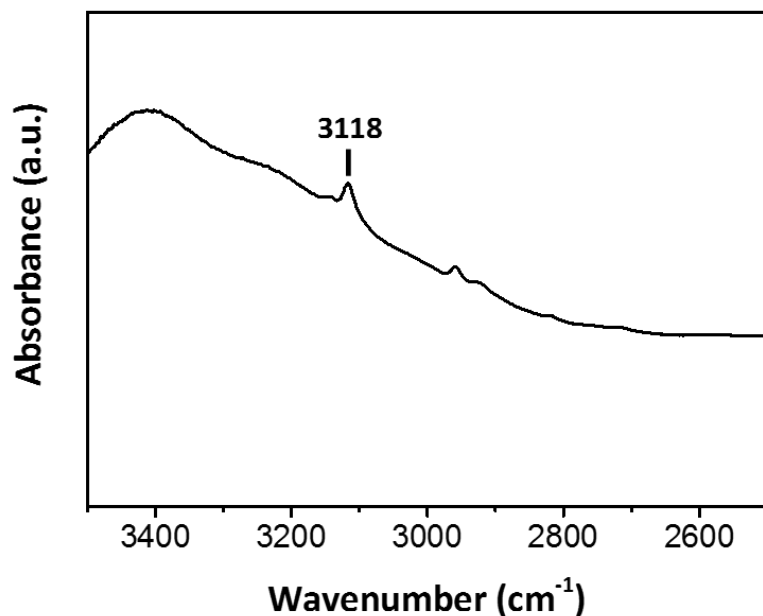


Figure B3: 2500 to 3500 cm^{-1} FT-IR of Melm prepared with KBr disc highlighting the ring C-H stretch.

B.4 Full CO_2 isotherms

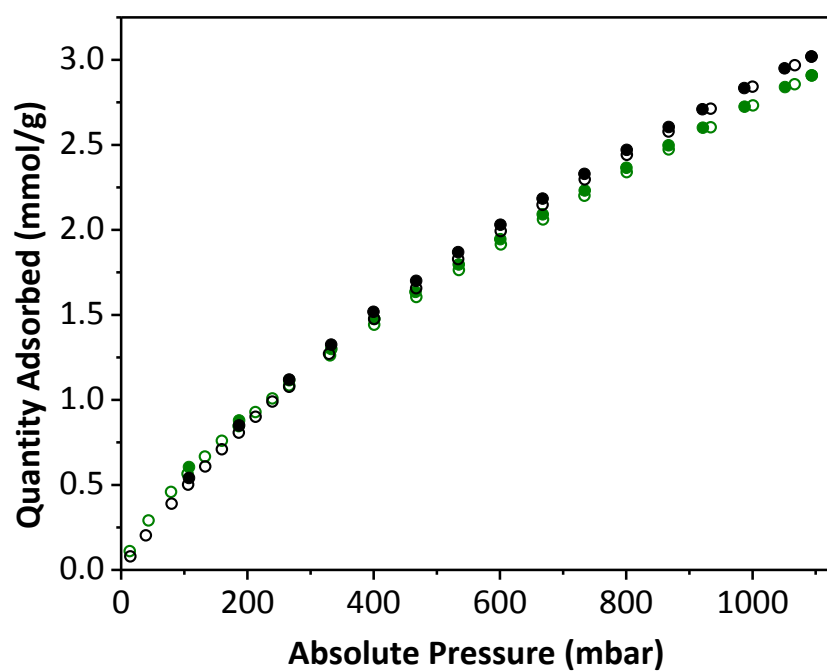


Figure B4: Experimental adsorption (open circles) and desorption (solid circles) isotherms of CO_2 in MIL-101(Cr) (green) and MIL-101-Me (black) at 298 K.

Chapter 5 Metal Organic Frameworks for use in tandem catalytic reactions

The initial stages of this work have been published as:

Hinde, C. S.; Webb, W. R.; Chew, B. K. J.; Tan, H. R.; Zhang, W.-H.; Hor, T. S. A.; Raja, R. *Chem. Commun.* **2016**, 52, 6557–6560.

Special Acknowledgements:

Dr Christopher Hinde: University of Southampton, UK (now Pall Corporation): For introduction to the tandem catalysis project and work which preceded my involvement, namely oxidation optimisation and synthesis parameters.

Hui Rui TAN and Kamal Patel: IMRE, Singapore: For aid with TEM imaging of the MNP/MOF samples.

Dr Debbie Seng: IMRE, Singapore: For help with XPS analysis of the MNP/MOF materials and discussion on the fitting of the data.

5.1 Metal Organic Frameworks for tandem reactions

5.1.1 Tandem reactions with MOFs

The use of a solid, heterogeneous catalyst for cascade processes is ideal as the benefits of them are amplified when the collection and re-use is considered *versus* homogeneous types^[150].

Metal Organic Frameworks (MOFs) are 'promising materials as heterogeneous catalysts because of their tuneable pores, their atomistically well-defined structures, their uniformly accessible catalytic centres, and site isolation' according to Climent *et al*^[150]. This ease of MOF modification, due to variance of both linker and metal, enables different chemical environments to be created – each of which can be considered as an active site for catalysis. Therefore, multiple catalytic sites on a MOF can be easily envisaged, through manipulation of the metal, linker and further functionality added post-synthetically, as discussed in Chapter 1^[60,61]. As an example case for a MOF, allow active site 1 to be a modified linker and active site 2 to be the metal site, see Figure 118, which therefore allows the MOF to catalyse the reaction of A to C in a cascade manner.

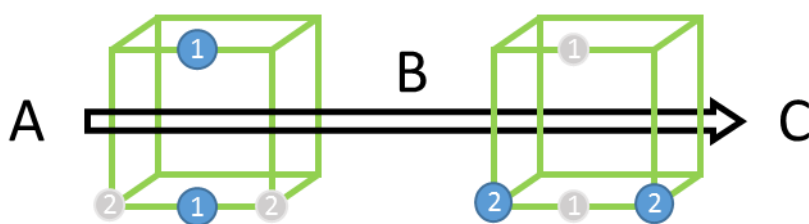


Figure 118: Example of tandem reaction on a MOF where A to B is catalysed by the linker, 1, and B to C is catalysed by the metal centre, 2.

Reviews by Dhakshinamoorthy *et al* and Huang *et al* highlighted the use of MOFs for cascade or multistep reactions and demonstrated how the large flexibility achievable through modification of the structure, both during and after synthesis afforded by MOFs makes them the perfect targets for development of these types of reactions^[60,61].

Additional to metal and linker alteration, the deposition of metal nanoparticles either onto or embedded within MOFs provides another means for insertion of an active site which have shown particular efficacy in oxidation reactions^[58,192,346]. Oxidation- Knoevenagel (KV) cascade reactions are of particular note as they combine two industrially important reactions together, as discussed in Chapter 1.3. Selective oxidation of an alcohol to an aldehyde is completed followed by a carbon-carbon bond formation in the subsequent Knoevenagel reaction of a methylene compound ($R-CH_2-R$) and the aldehyde formed in the oxidation stage, Figure 119. Oxidation is completed by one active site, such as nanoparticles and the KV reaction completed by a basic

functionality. In some examples the metal of the framework plays a key role in the reaction also, such as stabilisation or activation of the alkoxide intermediate^[347].

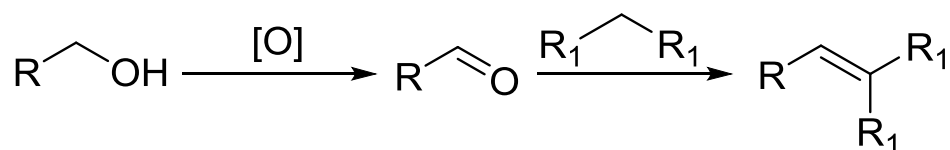


Figure 119: Tandem oxidation-Knoevenagel condensation reaction.

A number of different MOF materials have been reported to undertake the oxidation-Knoevenagel reaction and are summarised in Table 37.

| # | Material | Reaction conditions | Conv ^a (%) | Yield KV product (%) | Ref |
|---|------------------------------|--|-----------------------|----------------------|-------|
| 1 | UiO-66-NH ₂ | Benzyl alcohol, malononitrile, 48 hrs, 90 °C, O ₂ , p-xylene, white light irradiation. | 100 | 91 | [348] |
| 2 | Au@MIL-53(NH ₂) | Benzyl alcohol, malononitrile, 13 hrs, 100 °C, O ₂ , toluene. | 99 | 99 | [349] |
| 3 | MIL-101-NH ₂ (Fe) | Benzyl alcohol, malononitrile, 40 hrs, RT, O ₂ , trifluorotoluene/ acetonitrile, white light. | 88 | 72 | [350] |
| 4 | Au@Cu(II)-MOF | Oxidation: Benzyl alcohol, 23 hrs, 110 °C, air, toluene. KV: MeOH solution of malononitrile added, 7 hrs, RT. | 99 | 99 | [351] |
| 5 | Ru/UiO-66 | Oxidation: Benzyl alcohol, 1 hr, 100 °C, O ₂ , toluene. KV: Malononitrile, 5 hrs, 100 °C. | 100 | 89.3 | [352] |

Table 37: Summary of MOF based catalyst for tandem oxidation Knoevenagel condensation reactions. ^aConversion of benzyl alcohol.

Entries 1 and 3 used the photocatalytic ability of MOFs to complete the oxidation stage. In all cases above, the amine of the MOF linker catalysed the Knoevenagel condensation step, apart from entry 5 where interestingly UiO-66 is reported to be active for the condensation step. Often long reaction times were required, entries 1 and 3, or the reaction was split into two stages, entries 4 and 5. Entry 2 displays both excellent yield and uses O₂ as the oxidant source.

In order to undertake tandem reactions the MOF must be chemically stable and moreover, have the ability to withstand use for repeat cycles. To this end UiO-66 is an excellent framework, especially given the successful use for tandem reactions as above in Table 37 and high stability, as per Chapter 1.

5.1.2 UiO-66 family structure and properties

UiO-66 (University of Oslo-66) is a zirconium based terephthalate MOF. First produced by Cavka *et al* it comprises Zr_6 clusters interconnected by terephthalate linkers^[30]. Further derivatives forming isorecticular structures are also known such as UiO-67 with 4,4'-biphenyl-dicarboxylate (BPDC) linkers and UiO-68 which has terphenyl dicarboxylate (TPDC) as the linker. The framework symmetry for the latter two is the same but, with larger pore sizes, windows and surface areas due to longer linkers. The structure of UiO-66 is shown in Figure 121A and B. Each framework node (structural building unit, SBU) has the formula $Zr_6O_4(OH)_4(CO_2)_{12}$, whereby the CO_2 denotes the carboxylate of the terephthalate which links the SBUs, see Figure 120A. The zirconium(IV) square antiprismatic centres that occur as clusters of 6, as per the formula. Each Zr coordination sphere within the clusters is made up of entirely oxygen. For each zirconium, see Figure 120B for labelling, the coordination sphere is as follows: two of the oxygen are μ_3 bridging to other Zr in the cluster (1); four are from four different terephthalate linkers (2) and the final two of the coordination sphere are hydroxyl oxygens, which themselves are μ_3 bridging within the cluster (3). Throughout the framework each oxygen of a terephthalate is coordinated to a separate Zr. One end of the terephthalate is coordinated to two different Zr of the same cluster and the other end to two Zr of another cluster. This links the cluster and so propagates the framework. That each of the Zr_6 clusters share terephthalate linkers with 12 other clusters is one of the reasons for the high thermal, chemical and mechanical stability of the framework.

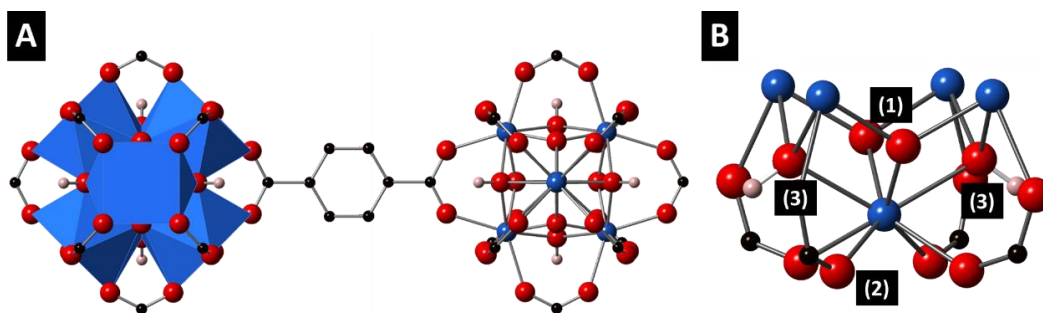


Figure 120: A) Two Secondary building units (SBUs) of UiO-66 detailing the Zr_6 cluster, linked *via* a terephthalate. B) Zr square antiprismatic coordination sphere: 1) μ_3 bridging oxygen, 2) bidentate terephthalate linkers and 3) μ_3 bridging hydroxyls. For all: Zr – blue (spheres and polyhedra); C – black spheres; O – red spheres and H – pink spheres.

Cavka *et al* reported UiO-66 thermally degrading at temperatures above 540 °C, claiming that the decomposition product seen at this point was benzene and as such UiO-66 possesses the theoretical maximum thermal stability possible for a hybrid framework formed from organic carboxylate linkers^[30] and was confirmed later by Valenzano *et al*^[353]. UiO-66 has a face-centred cubic (fcc) structure which causes two discrete pores to be present, one tetrahedral and one

octahedral of approximately 8 and 11 Å in diameter respectively^[354,355] as shown in Figure 121B, C and D. The pore windows within the UiO-66 structure are 6 Å and triangular in nature caused by the arrangement of the bridging linkers as depicted in Figure 121A, and large enough for a fully methylated benzene to enter^[30].

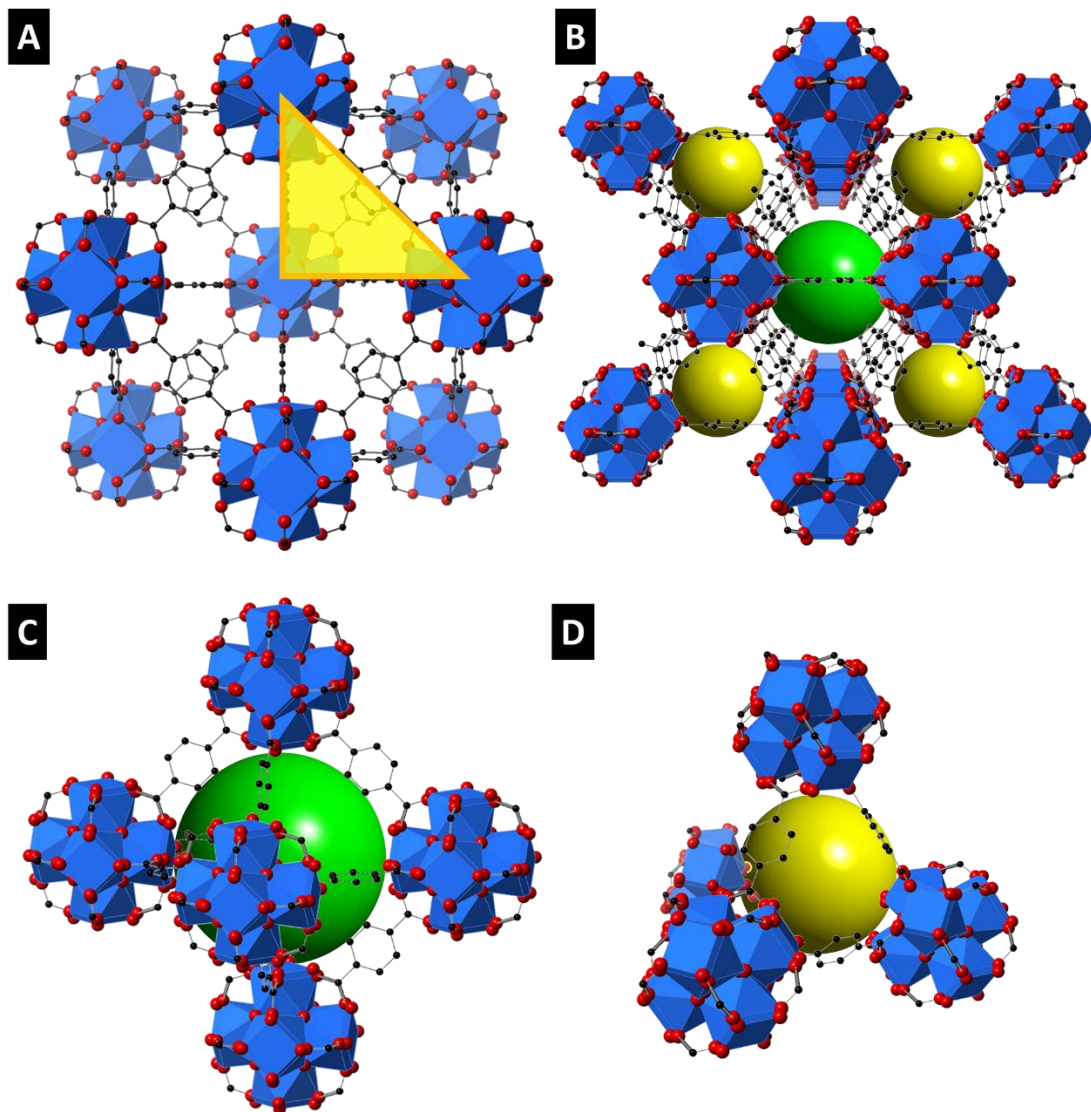


Figure 121: A and B) two representations of crystal structure of UiO-66 with pore window highlighted in yellow (A) and pores shown (B). C) Octahedral pore and D) Tetrahedral pore. For all: Zr – blue (polyhedra); C – black spheres; O – red spheres and H – have been hidden

The structure of UiO-66 can be modified in a multitude of ways during the synthesis stage to alter both the physical and chemical properties and in so doing allow for it to be carefully modified and tailored towards a desired catalytic application. A huge range of alterations, normally through different synthetic conditions, have been shown to be possible in the literature and are discussed in the following section to demonstrate further the rationale behind the selection of the UiO-66 framework.

Linker alteration *via* post synthetic exchange is challenging for UiO-66 as the high coordination of each terephthalate results in very high stability and so addition of functionality to the linker is generally completed during the synthesis stage. That is not to say it is not possible. Kim *et al* reported that through careful selection of the solvent, ligand exchange was possible within a pre-formed sample of UiO-66, giving access to mixed linker variants not able to be synthesised at high yields *via* solvothermal means^[356]. Furthermore, in another instance Kim *et al* showed that metal exchange is also possible on the framework with Zr/Ti and Zr/Hf UiO-66 synthesised by means of cation exchange^[86]. A number of other mixed linker versions of UiO-66 were produced by Chavan *et al* through use of differing ratios of terephthalic and 2-aminoterephthalic acid in the synthesis procedure to give a random dispersion of the amine throughout the framework structure^[224]. The introduction of an amine group in this way, occurs through use of 2-aminoterephthalic acid in place of terephthalic acid, Figure 122, in the synthesis stage. It is a popular choice for enabling further linker alteration and leads to the formation of UiO-66-NH₂^[84,357].

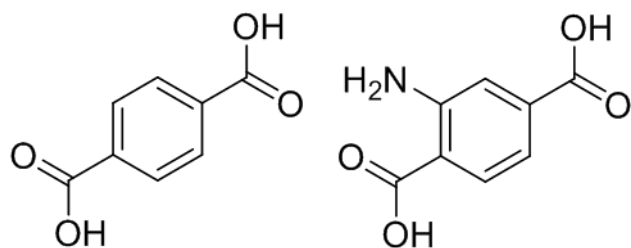


Figure 122: Structures of terephthalic acid (left) and 2-aminoterephthalic acid (right).

Amine addition to MOFs in this way has enabled catalytic reactions to be undertaken which exploited the basic nature of the group, such as the Knoevenagel reaction shown above^[358,359]. Also, once incorporated into the framework, post synthetic modification of the amine can be undertaken through analogous methods to those used by Jiang *et al*^[360] which produced azo, F and I substituted linkers on MIL-101(Cr). For UiO-66-NH₂ further modifications have also been demonstrated: Kandiah *et al* used anhydrides to create an amide group with the aim of improving CO₂ uptake^[229]; Liang *et al* used a linker with an imidazole to create an imidazolium for CO₂ and epoxide coupling^[148]. Often the manipulation of linker in these reactions occurs over multiple solvothermal synthesis steps and so can lead to low yields at the final stage. Kim *et al* reported that microwave synthesis can be used as a more direct approach to post synthetic modification and demonstrated the production of a cyano (CN) functionalised UiO-66 variant using a microwave procedure^[361].

Similarly, modification of the structural and physical properties of UiO-66 are possible during the synthesis stage. Hu *et al* have elegantly detailed the effect of linker and modulator on morphology, size, porosity and thermal stability of UiO-66^[362]. Modulators, as discussed in

Chapter 1, are key to many MOF synthesis procedures. For UiO-66 it has been shown that size, morphology and porosity can be altered by modulator choice. A large quantity of modulator promotes the creation of defect sites which can enhance catalytic ability or sorption capacity through creation of incomplete coordination spheres. Increased porosity by defect creation has an effect on the thermal stability of the MOF as a lower coordination number in a large number of zirconium atoms produces a framework structure which has lowered interconnectivity, as reported by Hu *et al* and Schaate *et al*^[82,362]. Therefore a trade-off between the stability of the MOF and the activity of it is likely to be required to optimise use.

Crystal size can be controlled in a number of ways. Firstly, quantities of a modulator, scaled to the linker and Zr precursor amounts can be used. The presence of a high amount of the modulator will generally decrease the particle size owing to increased chance of modulator Zr interaction leading to termination of the extending framework, as per Figure 11. Secondly, the pKa of the modulator is key, in a study of trifluoroacetic acid (TFA), formic acid (FA) and acetic acid (AA) – where acidity of TFA > FA > AA - by Hu *et al*^[362], particle size was seen to decrease with increase in acidity due to the lowered formation of terephthalate at lower pH. Different morphologies were noted also, with spherical particles seen for TFA and FA use and rhombohedral crystals observed for synthesis with AA. This is in-line with a recent study by Zhao *et al* who employed trimethylamine with AA to attain a higher level of control over crystal size producing highly monodisperse rhombohedral samples of tuneable size^[363]. Alternatively, through aging of the precursor Zr salt and modulator in DMF for several days prior to the addition of the linker, nano-sized crystals of UiO-66 as small as 10 nm have been reported, with good control over the size^[364]. Lastly, control of the size by addition of strong inorganic acids, such as hydrochloric acid (HCl) by Katz *et al*, showed that the acid aids in ‘*dissociating linkers and ultimately speeds up the connection of nodes to one another*’ therefore the presence of the strong acid increases the synthesis rate for UiO-66^[355]. The mechanisms of this were investigated by Zahn *et al* using fumarate, where an increase in the rate of formation was also reported, with evidence that the amounts of water in the synthesis is also key^[365]. In the report by Katz *et al* the increase in the surface area of their UiO-66 samples with high modulator amount was noted and explained through the creation of defect sites throughout the framework. This was confirmed by the increase in the measured size of the tetrahedral pore, see Figure 121D, from 8 to 11 Å because of the missing linkages^[355]. Control of the concentration of defects within a MOF has been shown to improve the catalytic ability^[366], with UiO-66(Zr) in particular being able to be tuned to effectively through modulation^[82,363,367,368].

The prevalence of defects within the UiO-66 framework can be manipulated^[368,369]. A high modulator amount can lead to incorporation of the modulator within the framework creating

additional Lewis acid sites through missing linkers. Vermoortele *et al* showed that use of a combination of HCl and TFA led to increased activity for the desired reaction of the study^[367]. An increased number of open sites within the framework alters the porosity of the material – with fewer linkers shown to increase the pore size significantly^[367]. With this knowledge synthesis conditions can be used to aid catalytic ability. For example, even if the reaction is being catalysed by the MOF linker, the increase in porosity from a large amount of modulator may improve performance, through greater access of the substrate to the extended UiO-66 framework. Alternatively, the defect sites created may increase catalytic ability through improving its ability to host catalytic species or the uncoordinated sites themselves are becoming available as reaction centres. In this way Gutov *et al* used different modulators to control the number of defect sites within UiO-66 which allowed the framework to be tailored towards catalytic applications, specifically new ligand addition to the CUS (similar to Chapter 4) and encapsulation of catalytic centres into the larger cavities^[370]. Ling *et al* reported that the defect sites are most often not Lewis sites but rather have charge balancing hydroxide anions due to replace the missing BDC²⁻ linkers, therefore Brønsted acid sites increase is observed allowing for UiO-66 to be envisaged as a solid acid catalyst in a similar manner to the AlPO materials previously discussed^[371].

Lastly, incorporation of nanoparticles to UiO-66 has been achieved in a number of ways, namely deposition^[372], impregnation^[198–200] and encapsulation^[201] with the resulting materials seen to be active for the oxidation of a range of alcohols, such as benzyl alcohol as shown in Chapter 1. The flexibility to be carefully tuned, chemical and thermal stability alongside the displayed amenity to being a host to nanoparticles, make UiO-66 an excellent candidate for use as a catalyst for a tandem process.

5.2 Aims and objectives

The aim of this Chapter is to produce MOF based catalysts capable of undertaking tandem reactions.

Firstly, This chapter will summarise the work undertaken in collaboration with and published by Hinde *et al*^[373] whereby the tandem reaction of alcohol oxidation followed by Knoevenagel condensation utilising Au NPs on amine UiO-66 (Au/UiO-66-NH₂). The published work was a proof of principle for the oxidation of cinnamyl alcohol to cinnamaldehyde followed by the sequential Knoevenagel condensation with malononitrile to yield cinnamylidene malononitrile as the final product, displayed generically by Figure 123^[373].

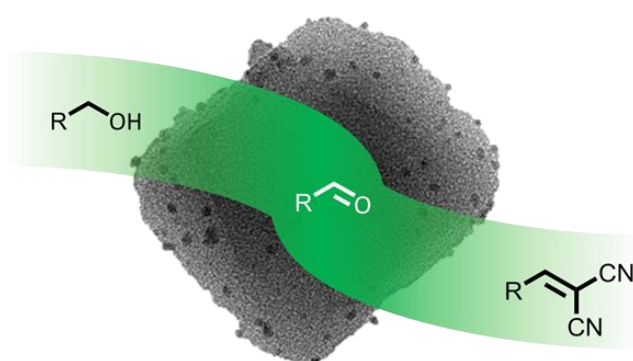


Figure 123: Diagrammatic representation of a tandem oxidation-Knoevenagel condensation reaction^[373].

Given the initial nature of the publication there was scope for the improvement of the catalyst. The abilities of the catalyst were investigated in more detail with extensive characterisation of the materials undertaken, such as UV-vis, FT-IR and XPS to better understand the nature of the catalyst. Expansion of the substrate scope of the existing material was undertaken whilst attempting to optimise the system for greater efficacy. The reaction that Hinde *et al* reported took 34 hours in total to complete and so through careful consideration of each step individually, reduction in reaction time was pursued. The main deficiency of the Au system highlighted by Hinde *et al* was the need for malononitrile addition following complete alcohol oxidation, therefore the reaction was one pot, but two steps. As such, the NP distribution across the MOF and type i.e. other noble metal nanoparticles which are known to be active for oxidation reactions, namely Pt and Pd – were investigated. Alteration of the MNP (metal nanoparticle) deposition stage and the metal type were investigated to overcome the inhibition of the oxidation observed.

Finally, preliminary attempts towards a second tandem reaction were explored using the MIL-101(Cr) investigated in Chapter 4 work to utilise CO₂ within a tandem reaction. This work has been included in this Chapter as it is a tandem reaction with a MOF and attempted to sequentially convert an olefin into an epoxide following which the insertion of CO₂ yields a cyclic carbonate, Figure 124, a reaction which has been suggested in the proceeding Chapters.

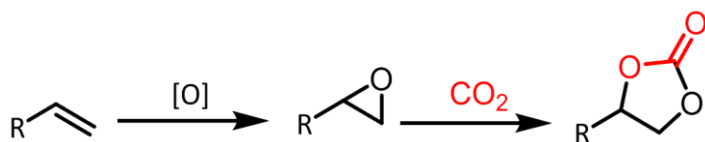


Figure 124: Proposed tandem reaction to convert an alkene to a cyclic carbonate with CO₂ utilisation *via* and epoxide.

The direct conversion of an alkene to a cyclic carbonate is attractive as it couples two currently separate methods into one and builds on the cyclic carbonate work which employs the MIL-101(Cr) framework.

5.3 Tandem oxidation-Knoevenagel condensation

The results and discussion section will include the work which was undertaken in collaboration with Christopher Hinde for the initial stages of the UiO-66 tandem project – where the tandem reaction was shown to be possible. Following this initial success, the catalyst material was investigated in more detail with the aim of fine tuning the tandem catalytic process through systematic optimisation of parameters. The structure and properties of the materials will first be discussed, with the catalytic results presented in the published work summarised prior to attempts to optimise the reaction being detailed.

5.3.1 Characterisation

Determination of structural properties and features of the as-synthesised catalyst is key to understanding behaviour. SEM images, Figure 125, show the morphology of the as-synthesised UiO-66 variants. The majority of the UiO-66 crystal have a rhombohedral shape to them. The UiO-66-NH₂ are on average smaller than UiO-66, despite both having a 10:1 ratio (mol) benzoic acid: linker/zirconium chloride, the reagent mixture is more dilute for the UiO-66-NH₂. Benzoic acid was used as a modulating agent for the synthesis as it enables good control over the size and distribution of crystals leading to high crystalline structures^[82]. The ratio above was selected due to the work of Schaate *et al* which reported the 10:1 ratio as producing the smallest size of MOF, and was thought would aid the Knoevenagel step of the reaction^[82]. Morphology of the UiO-66-NH₂ is hard to discern at SEM magnifications, given the small size observed, but appears to be a mixture of spherical and rhombohedral shaped material. The synthesis was seen to be highly reproducible over multiple iterations allowing a consistent support to be produced for the deposition of nanoparticles (NPs).

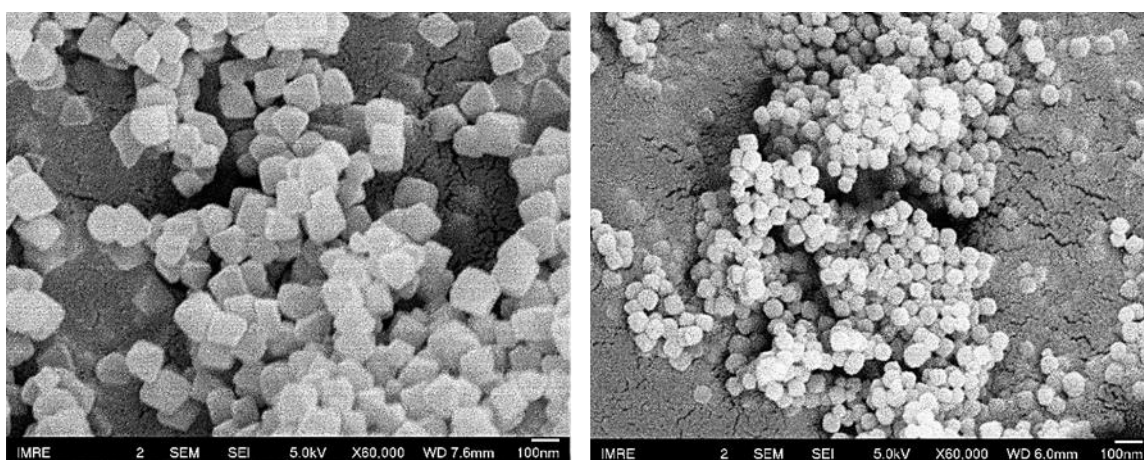


Figure 125: SEM images of UiO-66 (left) and UiO-66-NH₂ (right). Samples sputter coated with gold for 20s prior to imaging.

Structural characterisation of the UiO-66 variants was undertaken as follows and confirmed the crystallinity, porosity and thermal stability of the materials. To understand the effect the deposition stage had upon NPs or the UiO-66 and UiO-66-NH₂ supports, characterisation of both the NPs and the MOF was completed following deposition. Continuance of MOF porosity, crystallinity, physical and chemical properties is key following any post-synthetic modification stages, as seen previously in Chapter 4. Nitrogen adsorption studies investigated the impact of the deposition stage on the porosity of the two materials, UiO-66 and UiO-66-NH₂. UiO-66-NH₂ has a lower surface area and total capacity than UiO-66 owing to the amine groups which are present on each of the linkers.

For UiO-66 the blank framework is shown to be highly porous with high initial uptake, 0 – 0.05 P/P_0 , which occurs due the small size of the crystals as seen in the SEM imaging, and so causes a large external surface area to volume ratio. A slight hysteresis is observed at high pressure. The Au/UiO-66 displays a similar type II shaped isotherm, but with improved values to that of the unaltered framework. Both the adsorbed values and the surface area increased following the addition of the nanoparticles to the MOF, Table 38. This was unexpected but can be rationalised if the deposition stage is considered as a supplementary washing step. The formation and deposition of the NPs was undertaken in methanol – which was the solvent of choice during the purification stage of the synthesis. It likely then that further quantities of benzoic acid and/or terephthalate linker have been removed from the framework during the NP deposition process. This side-effect is beneficial as the higher porosity created in this way should aid catalysis.

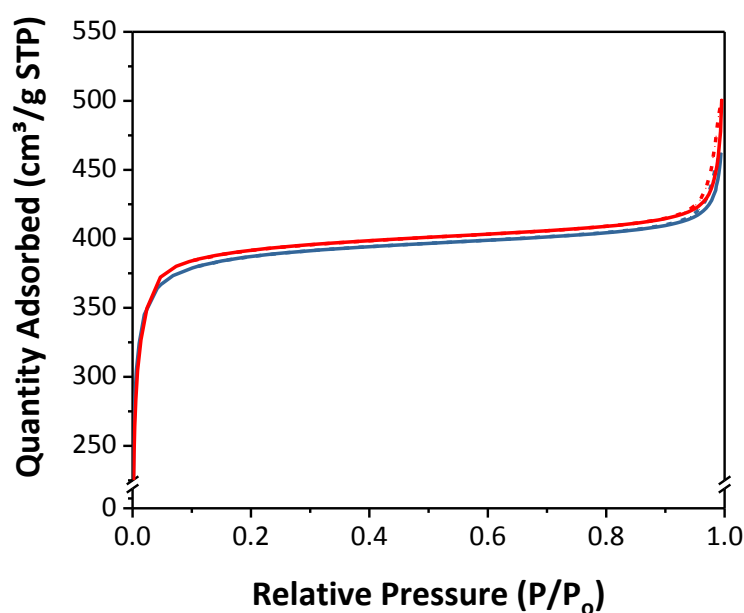


Figure 126: Nitrogen adsorption isotherms of UiO-66 (red) and Au/UiO-66 (blue). For both: adsorption curve (solid) and desorption curve (dotted).

The nitrogen adsorption isotherms of the UiO-66-NH₂ displayed similar patterns to that of the terephthalate linked version, whereby the adsorption capacity was improved upon the deposition stage. An increase in the surface area, Table 38, was also observed upon the deposition which again is attributed to the methanol further washing the material. Maintenance of the porosity is therefore seen and the methodology has not negatively impacted the porosity of the Au containing versions, but rather improved them.

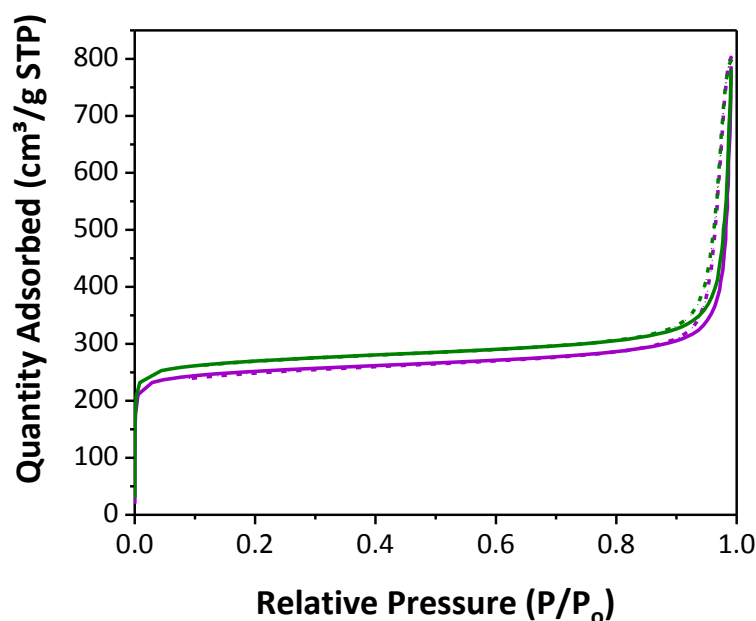


Figure 127: Nitrogen adsorption isotherms for UiO-66-NH₂ (purple) and Au/UiO-66-NH₂ (green).
For both: adsorption curve (solid) and desorption curve (dotted).

The surface area values for the UiO-66 materials, Table 38, are in excellent agreement with that reported of 1187 m²/g^[30] indicating that all stages of the synthetic procedure, especially the washing stages (seen to be highly important in the MIL-101(Cr) section of this work) were well optimised to produce the framework with the maximum surface area available for exploitation.

| Material | Surface area / m ² /g |
|---------------------------|----------------------------------|
| UiO-66 | 1158 ± 31 |
| Au/UiO-66 | 1169 ± 30 |
| UiO-66-NH ₂ | 779 ± 17 |
| Au/UiO-66-NH ₂ | 848 ± 19 |

Table 38: Surface area and pore volume values for the UiO-66 and UiO-66-NH₂ analogues

TGA curves were obtained of the materials to determine the thermal stability post deposition of the nanoparticles. Ensuring the stability is maintained is key to the framework being able to retain structure during catalysis at elevated temperatures. The blank framework mass loss curves were analysed and compared to literature and deposited versions.

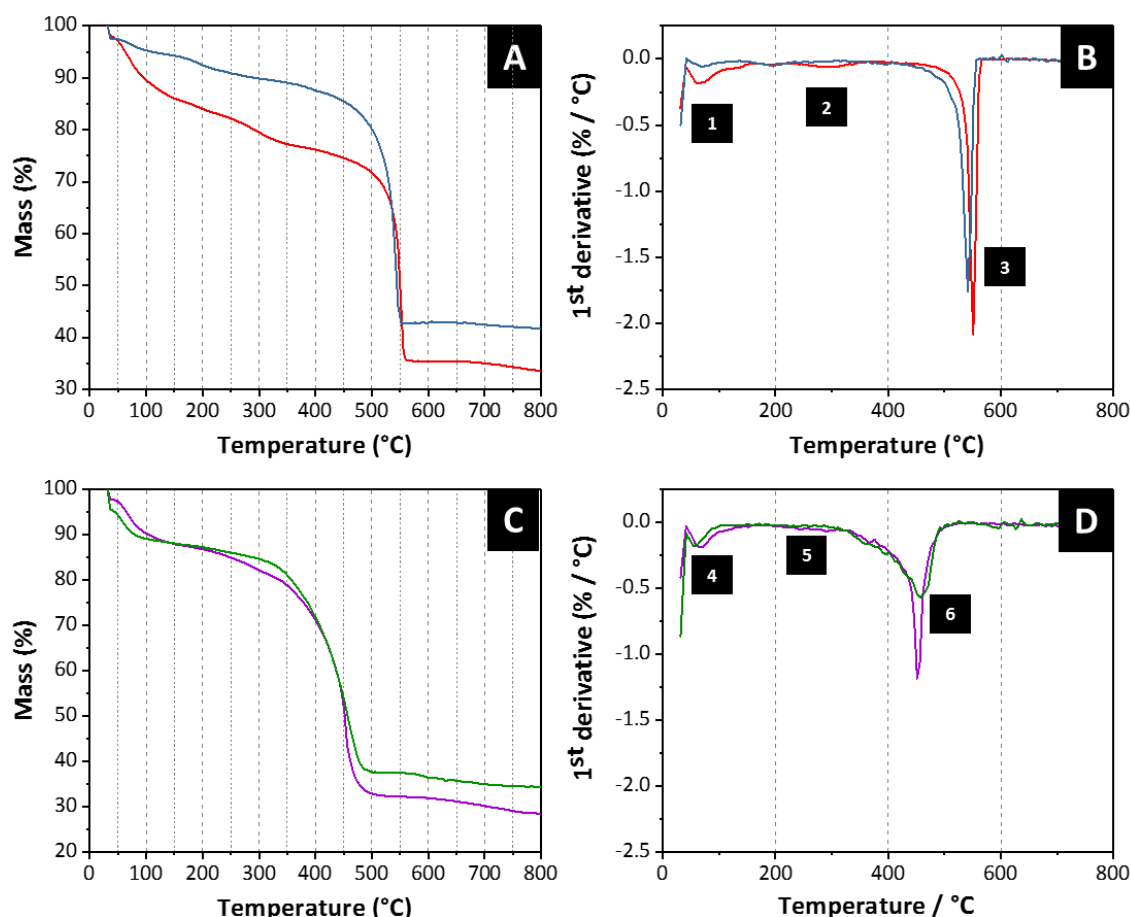


Figure 128: TGA curves of A) UiO-66 and Au/UiO-66, B) 1st derivative of UiO-66 and Au/UiO-66, C) UiO-66-NH₂ and Au/UiO-66-NH₂ and D) 1st derivative of UiO-66-NH₂ and Au/UiO-66-NH₂. In all cases UiO-66 (red), Au/UiO-66 (blue), UiO-66-NH₂ (purple) and Au/UiO-66-NH₂ (green). TGs taken in air at 10 °C/min ramp rate.

The TGA curves for the UiO-66 and Au/UiO-66 show that the highly thermal stability of the framework is maintained upon the deposition of the gold nanoparticles onto the framework. The decomposition temperature is very similar for both, measured from use of the first derivative, Figure 128B, in order to more easily determine the start of the loss processes occurring during thermal degradation. There are three key phases to the decomposition process. The initial stage is the solvent loss, labelled 1 which produced the first mass loss peak, the UiO-66 material shows a substantially higher initial loss – presumed to be significant solvent and unreacted organic material (linker or benzoic acid modulator) trapped within the framework. Accordingly, it shows a higher overall mass loss than the Au variant, greater than what would have been expected as the gold loading was low (approx. 1 % wt.). Another mass loss inflection is observed *circa* 250 °C which has been attributed to the dehydroxylation of the framework (see Figure 120 for hydroxyl location within the framework). This value is in excellent agreement with the dehydroxylation temperature range of 250-300 °C reported by Cavka *et al*^[30]. The unaltered UiO-66 framework displays marginally higher thermal stability to the Au/UiO-66 variant with the main decomposition

peaks occurring at, 486 and 436 °C respectively. The reason for the earlier breakdown in the Au/UiO-66 is unknown. The weight losses observed for UiO-66 and Au/UiO-66 are summarised in Table 39, and compared to the structural formulas reported within the literature^[30,353] and for the amine version^[84,357].

| Material | Weight loss / % |
|---|-----------------|
| UiO-66 (based on formula) | 53.7 |
| UiO-66 | 52.1 |
| Au/UiO-66 | 50.4 |
| UiO-66-NH ₂ (based on formula) | 56.1 |
| UiO-66-NH ₂ | 57.1 |
| Au/UiO-66-NH ₂ | 53.6 |

Table 39: Summary of weight loss percentages for the four synthesised materials with comparison to the theoretical amounts.

The weight loss percentages compare to that which would be expected for the blank materials. The weight loss for the amine is higher given that each linker possesses an amine functionality on it. The addition of nanoparticles causes a smaller weight loss for both frameworks because it adds to the inorganic component, making it a larger component which will remain.

The thermal stability of UiO-66-NH₂ is also unaltered upon the deposition of the nanoparticles. With reference to the labels in Figure 128D relating Figure 128C the loss stages can be described as follows. The initial loss, 4, is attributable to solvent trapped within the framework. Dehydroxylation is observed as the small inflection at 5, occurring at 200 °C. Overall the amine functionalised material is less thermally durable than the terephthalate linker analogue but nonetheless the degradation temperatures, labelled 6, of 331 °C for UiO-66-NH₂ and 296 °C for the Au/UiO-66-NH₂ far exceed those which will be employed for the tandem applications. For both materials a slight lowering of the thermal stability is noted upon addition of the nanoparticles, however is not considered large enough in either case to have a detrimental impact on any catalytic applications.

Powder x-ray diffraction (XRD) showed that the crystalline structure of the MOF was retained upon deposition of the NPs for both UiO-66 and UiO-66-NH₂, in agreement with previous characterisation results. There are no additional peaks or missing peaks observable in the as synthesised UiO-66 and UiO-66-NH₂ materials, when refinement was undertaken^[30]. This is also true when the Au NPs are deposited, which is expected given the high stability of the framework

and improbability of alteration of the structure upon stirring within a methanol solution. The loading of the nanoparticles is too low for any gold peaks to be observable.

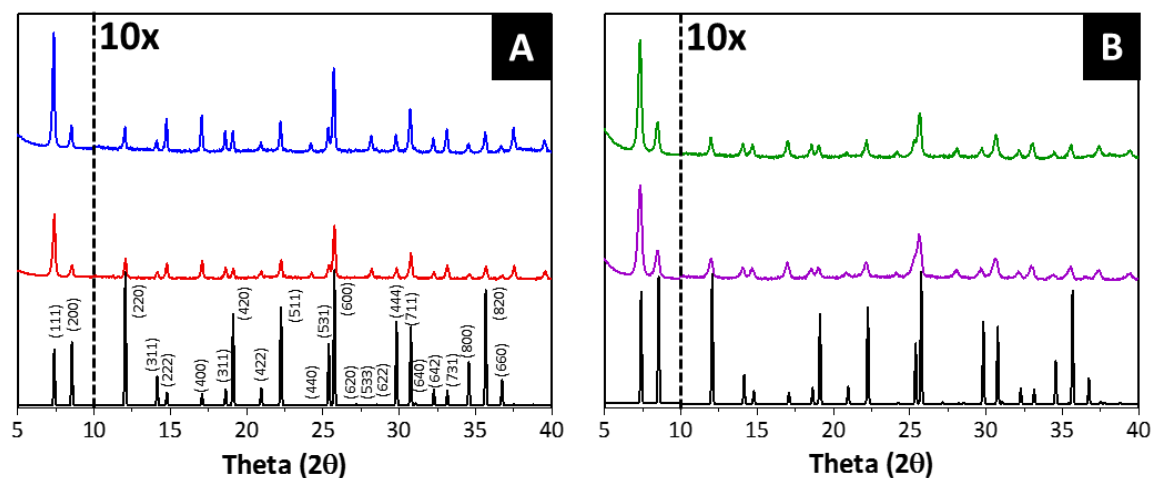


Figure 129: A) Powder X-ray diffraction of UiO-66 (red) and Au/UiO-66 (blue) and B) UiO-66-NH₂ (purple), Au/UiO-66-NH₂ (green). Values beyond that of 10 theta have been scaled 10 times as the two peaks below that have high intensity relatively, with UiO-66-simulated (black) for both.

In order for the UiO-66-NH₂ framework to undertake the proposed tandem reaction, the amine groups must have remained intact following the nanoparticle deposition procedure as they are required to undertake the deprotonation of the methylene compound in the KV condensation reaction. FT-IR was used to probe the material as the N-H peaks relating the 4-aminoterephthalic acid, will be easily discernible.

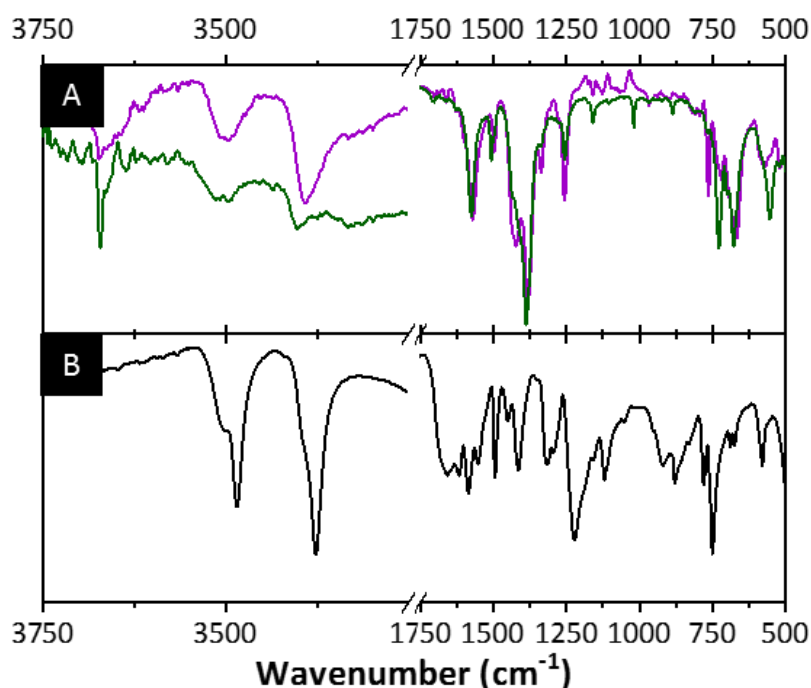


Figure 130: FT-IR of A) UiO-66-NH₂ (purple) and Au/UiO-66-NH₂ (green), B) 4-aminoterephthalic acid (black). The left region of both peaks has been expanded in order to highlight the N-H peaks.

The spectra for 4-aminoterephthalic acid is shown within Figure 130B, the two peaks at 3484 cm⁻¹ and 3376 cm⁻¹ are clearly observed, which are assigned to the symmetrical and asymmetrical stretching N-H vibrations of the amine group respectively, in excellent agreement with literature^[357]. At lower frequencies, the peak at 1583 cm⁻¹ corresponds to the N-H bending vibration, the C-N stretching vibrations (1340 cm⁻¹ and 1259 cm⁻¹) of aromatic amines are also seen. When incorporated into the MOF the primary N-H stretches are observed at 3505 and 3391 cm⁻¹ and the C-N stretch at 1256 cm⁻¹ as expected for both UiO-66-NH₂ and the Au variant, Figure 130A. In both cases these are comparable to the free ligand, 2-aminoterephthalic acid and so indicate that the linker has been unaltered in both the synthesis and post synthesis procedures and so will be available to undertake the KV reaction.

Analysis of the nanoparticles was undertaken to ensure that they had not been altered upon deposition onto the frameworks. The methanol solution of NPs prior to deposition has the characteristic cherry red colour of gold nanoparticles of very small, sub 10 nm, size. Given this, colouration of the nanoparticles UV-vis spectroscopy can be employed to monitor not only the existence of the nanoparticles but also is able to study the size of them^[225,374]. The surface plasmon resonance (SPR) peak is typically a broad peak in the visible region centred around 500 – 550 nm, dependent on the size, aggregation and chemical interactions when deposited on a surface^[374]. For both the Au/UiO-66 and Au/UiO-66-NH₂ it was apparent visually that an amount

of deposition has occurred due to the colour change of the samples, verification of this was obtained from the UV-vis, the x-axis was maintained as wavelength rather than wavenumber as per other sections of this thesis in order to allow for easier comparison to the literature used in supporting the analysis.

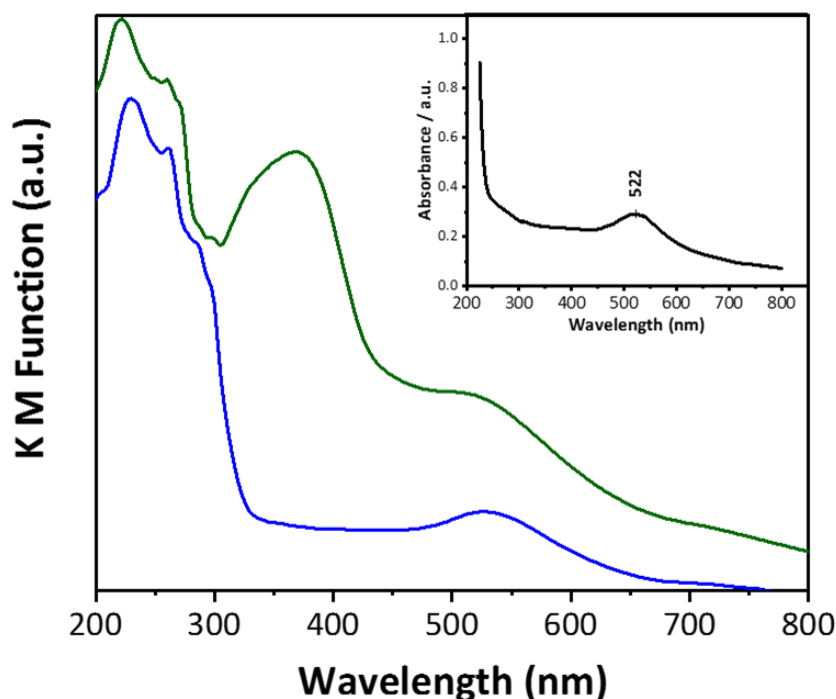


Figure 131: UV-vis of Au/Uio-66 (blue), Au/Uio-66-NH₂ (green) and Au NPs in methanol (inset, black, peak labelled for visualisation aid).

Figure 131 displays the two MOF frameworks after the deposition of the nanoparticles, the SPR peak is clearly seen at 527 nm for Au/Uio-66 and at 521 nm for the Au/Uio-66-NH₂ though peak position determination is made more difficult as it appears as a shoulder in the Uio-66-NH₂ spectra and maybe be aided by blank subtraction of Uio-66-NH₂ in the future. Both of these display good correlation to the peak position of the as synthesised NPs in methanol shown in the inset of Figure 131. Sizing of the nanoparticles using UV-vis is difficult by the monitoring of the peak position^[225,374], more so with the MOF based nanoparticles as the effect of the host MOF as well as the PVP stabilising agent on the peak position is currently not known. A study by Liu *et al* investigated the effect of the stabilising agent, but PVP was not included and the measurements were solution based^[375]. This is unfortunate, given the ease of undertaking UV-vis measurements which would allow for nanoparticle sizing of each batch synthesised to be completed – however it can still be employed to monitor for drastic differentiation from the expected. The additional peak in the Au/Uio-66-NH₂ is due to the amine group of the linker, which gives the framework the observed yellow colour, due to nonbonding to antibonding molecular orbital transitions (n to π^*) occurring in Uio-66-NH₂^[224,376].

Consequently, Transmission Electron Microscopy (TEM) was employed to study the size of Au nanoparticles prior to and following the deposition process. The nanoparticles within the methanol solution were concentrated and imaged as well as those which were successfully attached to the MOF. Size and shape of the Au NPs was discernible, seen to be very small (sub 10 nm) in size and spherical in nature. A statistical analysis was performed to analyse any change in size before and after deposition with as large a sample size as possible collected in order to gain the biggest oversight on the distributions present. A spherical approximation approach was undertaken for all statistical analysis of NP sizes, with the short axis of a nanoparticle measured, subsequent plots constructed show the raw counts of nanoparticles within each size division along the x-axis. This approach was employed for all measurements of NP size within this Chapter.

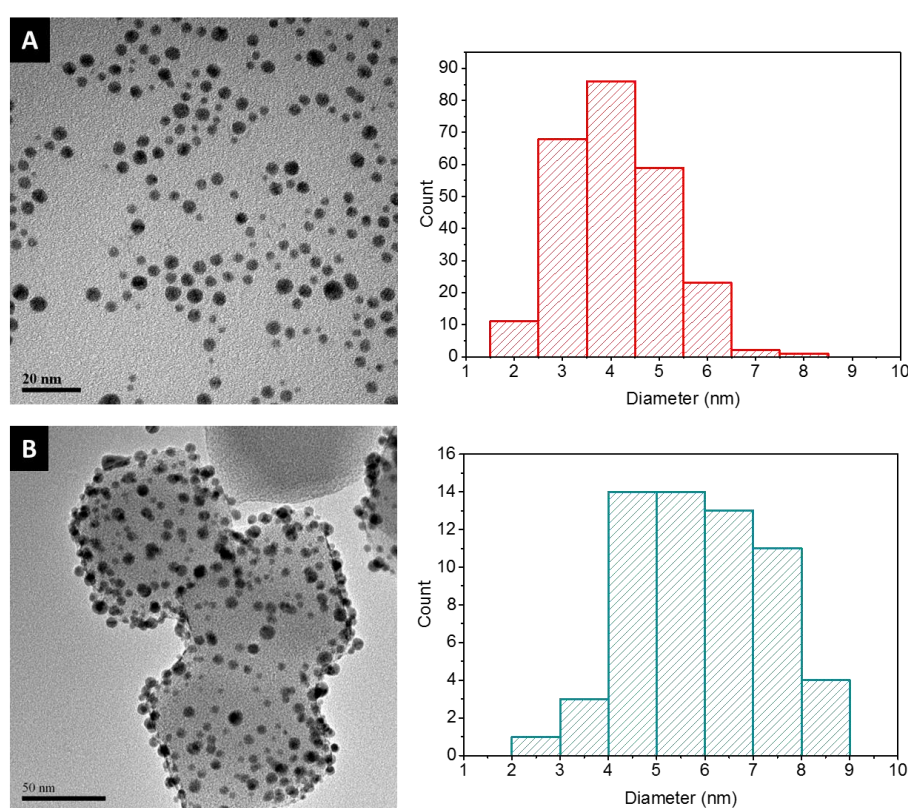


Figure 132: A) TEM of Au NPs (as synthesised in methanol) and B) Au/UiO-66. Each histogram plot based on statistical analysis of Au NPs (red) and Au/UiO-66 (blue) from 4 and 3 three images respectively.

Statistical analysis showed the average NP size is 5.8 ± 1.2 nm for the Au/UiO-66 sample, displayed in Figure 132. The PVP coated Au NPs remain intact following the deposition onto the surface of the MOF which is crucial in ensuring that the activity is maintained for the oxidation of substrates. The Au NPs in methanol have an average diameter of 4.1 ± 1.0 nm so the average of the NPs deposited are larger on average than those in solution before deposition. Whilst the averages are within error of one another, the maximum and minimum sizes of nanoparticles

measured, as shown by Table 40, are both larger for Au/UiO-66 indicating overall the distribution has increased marginally upon deposition. This was unexpected when considered that the nanoparticles are stabilised through the PVP – known to be effective at stabilising Au NPs and preventing aggregation^[196,377]. Nonetheless, the nanoparticles are still of sufficiently small diameter to be active for oxidation reactions.

| | Minimum (nm) | Maximum (nm) |
|----------------------|---------------------|---------------------|
| Au (NPs in methanol) | 2.0 | 7.9 |
| Au/UiO-66 | 2.7 | 8.5 |

Table 40: Maximum and minimum NP sizes measured for Au NPs and Au/UiO-66 from TEM.

From the above TEM, Figure 132B, the morphology of the MOF crystals remains unaltered by the deposition process. This was also seen for the UiO-66-NH₂ crystals where a rhombohedral morphology was observed before and after the nanoparticle deposition. In both, no visible defects are observable indicating, visually at least, that the deposition stage has not altered the framework, as confirmed by the XRD and TGA earlier. Notably, clustering of the nanoparticles appears to have occurred, where they are concentrated on specific crystals and no deposition has occurred on others, reasoning for this was not known but is investigated later in section 5.3.3.3. After confirmation of framework retention and the successful deposition of nanoparticles, X-ray Photoelectron Spectroscopy (XPS) was used for further analysis - more specifically to probe the oxidation state of the gold nanoparticles. In addition, the survey scan was analysed for extra peaks, such as those from starting material that remained unreacted and became incorporated within the framework during the synthesis process.

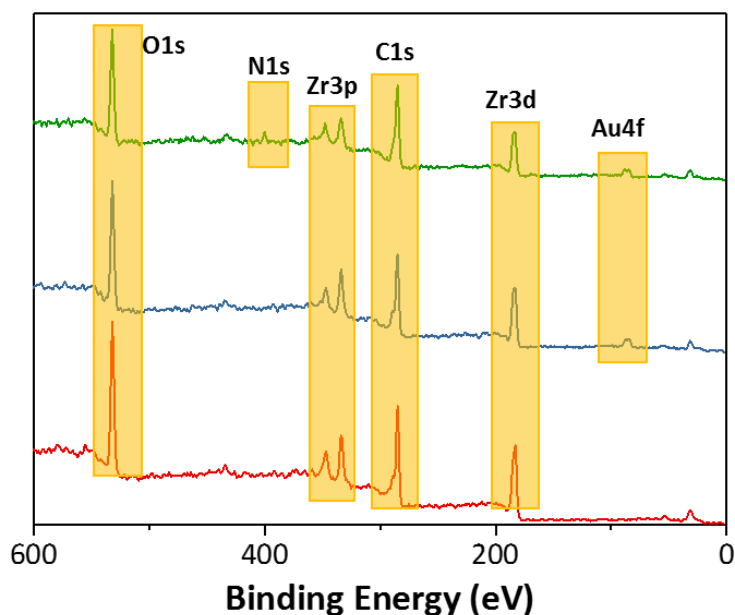


Figure 133: XPS survey scan for UiO-66 (red), Au/UiO-66 (blue) and Au/UiO-66-NH₂ (green) with regions of interest highlighted.

The survey scan, Figure 133, displays all the elements expected to be in each of the variants, with no other species observed, indicating sample purity. The framework provides Zr (3d and 3p) C and O peaks, with the addition of Au seen for the Au/UiO-66. The amine functionality of Au-UiO-66-NH₂, so crucial for the Knoevenagel condensation, is present with a peak in the N1s region as would be expected. Higher resolution scans of these regions allowed for further characterisation of the framework and identification of individual features within each of them.

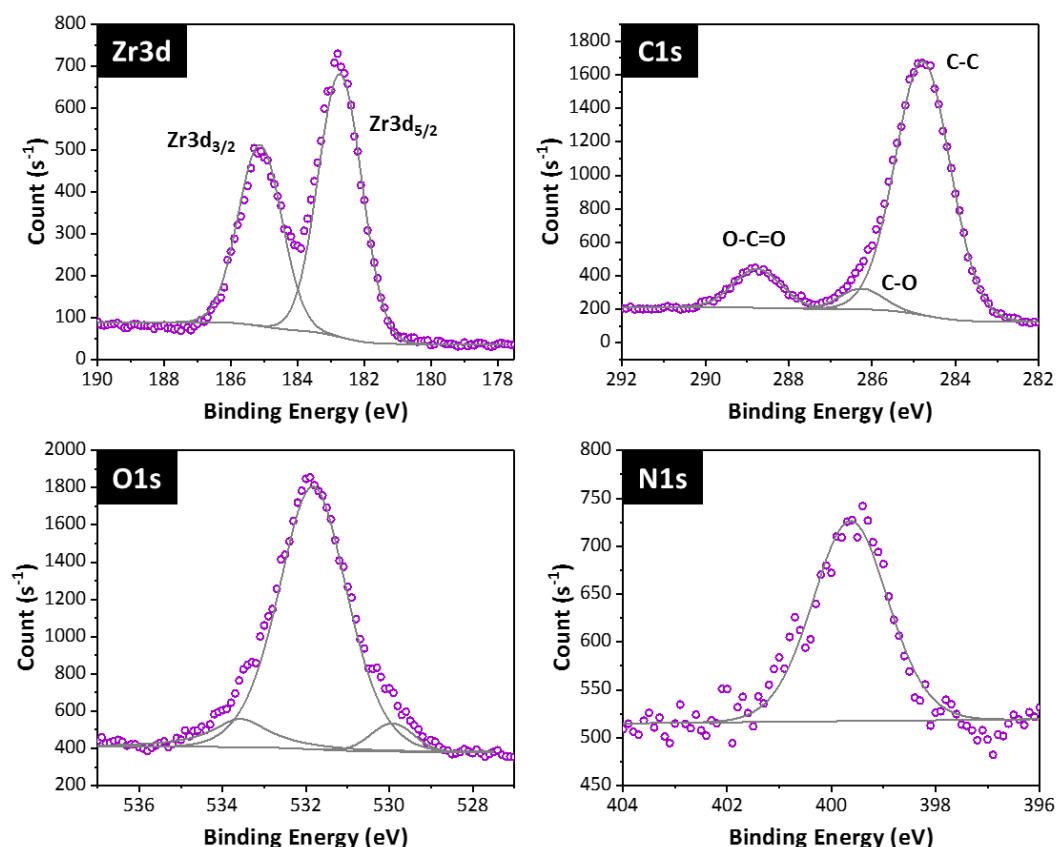


Figure 134: High resolution scans of the framework regions of UiO-66-NH₂

High resolution scans of the UiO-66-NH₂ are displayed in Figure 134. The Zr 3d region displays the typical doublet from the Zr₆ metal-oxo centres. The C1s region has three peaks: the C-C adventitious peak to which the linker will provide some intensity and also the C-O and O-C=O peaks from the linker – with the former a shoulder of the C-C peak. The O1s region displays smaller peaks as shoulders of the main peak and can be rationalised as there are oxygen atoms on the linker, as hydroxyl groups and as μ_3 bridging oxygen – providing at least three different oxygen species within the framework. The N1s from the amine functionality is shown as would be expected.

The Au present for Au/UiO-66 and Au/UiO-66-NH₂ should all be Au⁰ following the reduction by an excess of NaBH₄. To assist in visualising and confirming this, a measurement of sputtered gold was used as a reference material in the scan of the Au 4f region.

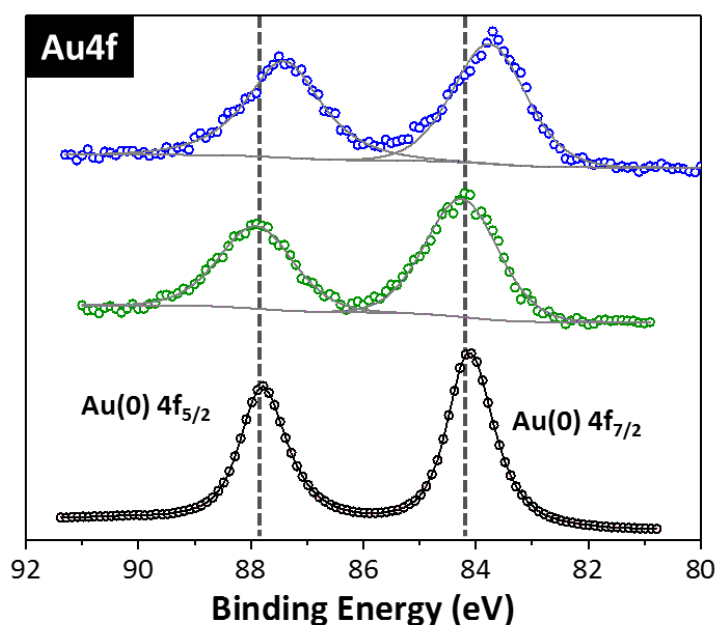


Figure 135: Au4f region showing sputtered gold (black), Au/Uio-66-NH₂ (green) and Au/Uio-66 (blue). Fitted curves in grey for samples.

The Au4f region displayed the characteristic doublet for gold, as was expected. When compared to the metallic gold reference it can be seen that there is little difference in peak positions of the Au/Uio-66 and Au/Uio-66-NH₂ indicating that the sample is all Au⁰. This is further confirmed as there is no indication of any gold precursor, through further doublets of differing positions and so oxidation state, which was not reduced during the synthesis process. Both of these observations validate the synthesis methodology, by showing the nanoparticles have been produced as they were intended and so will be able to then activate the alcohol substrate as required for oxidation occurrence.

ICP-OES measurements undertaken by Medac Ltd. were used to determine the loading of the gold present on the two framework types. A 1 wt. % loading was aimed for during the synthesis stage with a lower amount than theoretically possible seen to be deposited on each, see Table 41. The Au/Uio-66-NH₂ displayed a higher loading than the Uio-66, perhaps owing to a favourable interaction between either the PVP or gold NPs, with the surface amine functionalities from the linker.

| Material | Au / wt. % |
|---------------------------|------------|
| Au/Uio-66 | 0.63 |
| Au/Uio-66-NH ₂ | 0.87 |

Table 41: Weight % loadings of gold on the two Uio-66 variants.

Following the characterisation of the materials, showing that Au/UiO-66 and Au/UiO-66-NH₂ were produced catalytic testing was carried out on the two different variants for the tandem oxidation-KV reaction.

5.3.2 Tandem oxidation-KV reaction

Initial testing focussed on the optimisation of the oxidation reaction as detailed by Hinde *et al* where the variance of the amount of oxidant, catalyst and the ratio of the two was completed to produce a maxima for the yield of cinnamaldehyde^[373]. The majority of the oxidation optimisation work was undertaken using Au/UiO-66 without the amino group as there was no requirement for this to be present. The oxidation stage was undertaken employing *tert*-Butyl hydroperoxide (TBHP) as the oxidant. Whilst not as environmentally benign as using molecular oxygen, or hydrogen peroxide, in this specific case it is deemed acceptable as the decomposition product of TBHP is the same as the solvent employed for the reaction, *tert*-butanol (*t*-BuOH). Cinnamyl alcohol was used as the alcohol and malononitrile as the methylene compound which results in cinnamylidene malononitrile (CNMN) formation as the final product. Cinnamyl alcohol oxidation is industrially desirable as cinnamaldehyde is sought after as a flavour, antimicrobial agent and anticancer agent^[378] but also a precursor to pharmaceutically relevant materials such as the condensation product, cinnamylidene malononitrile^[379].

Under the optimised conditions, reactions using the Au/UiO-66-NH₂ variant were completed. A summary of the individual stages of each and the overall tandem are shown in Table 42, with Figure 136 depicting entry 7, where both stages were completed.

| # | Catalyst | Time (hrs) | Oxidation | | Knoevenagel | | Yield CNMN (%) |
|---|--|------------|-----------|----------|-------------|----------|-------------------|
| | | | Conv. (%) | Sel. (%) | Conv. (%) | Sel. (%) | |
| 1 | Blank(Ox) | 10 | 8 | 88 | - | - | - |
| 2 | Au/UiO-66-NH ₂ | 10 | 98 | 99 | - | - | - |
| 3 | Blank(KV) | 24 | - | - | 40 | 93 | 37 |
| 4 | UiO-66-NH ₂ ^a | 24 | - | - | 83 | 98 | 81 |
| 5 | Blank(Ox-KV) ^b | 34 | 11 | 98 | 99 | 83 | 9 |
| 6 | Au/UiO-66-NH ₂ | 24 | 1 | 99 | 99 | 98 | 1 |
| 7 | Au/UiO-66-NH ₂ ^b | 34 | 79 | 98 | 99 | 98 | 78 |

Table 42: Summary of oxidation and Knoevenagel investigations and overall tandem reactions.

Reaction conditions: Cinnamyl alcohol (0.1 g), Au/UiO-66-NH₂ (40 mg; 0.87 wt. %)

TBHP (1.2 eq), *t*-BuOH (7 mL), 10 hours, 70 °C. ^a40 mg of UiO-66-NH₂ used.

^bMalononitrile added at 10 hours (0.1 g). Monitored by GC with chlorobenzene as ITSD (0.2 g).

Similar activity was seen for the oxidation stage as for the optimised values of the Au/UiO-66. The Knoevenagel reaction saw very rapid initial conversion which declined over time and continued to increase steadily. Attempts to undertake the reaction as a one-pot, two stage process were ultimately unsuccessful as the addition on malononitrile was seen to lead to inhibition of the oxidation process which was ascribed to unfavourable interaction with the nanoparticles, Table 42, entry 6. Entry 7 is depicted below in Figure 136, where owing to the result of entry 6 a significant proportion of cinnamyl alcohol oxidation was allowed to occur before the introduction of the malononitrile (at 10 hours reaction time).

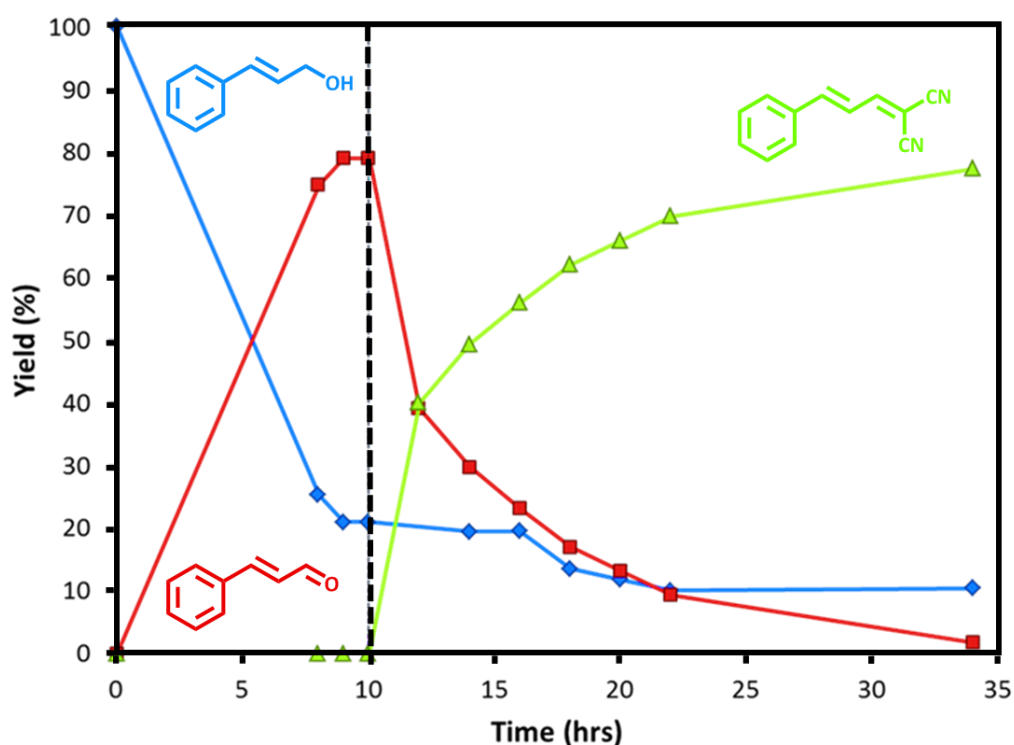


Figure 136: Tandem reaction of cinnamyl alcohol to cinnamylidene malononitrile *via* cinnamaldehyde using Au/UiO-66-NH₂. Reaction conditions: 40 mg Au/UiO-66-NH₂, 70 °C, TBHP, 0.75 mmol cinnamyl alcohol, 1.2 equiv. TBHP(aq), 7 mL *t*-BuOH, 0.75 mmol malononitrile. Dotted line at 10 hours indicates the addition of the malononitrile^[373].

It can be seen that the addition of the malononitrile at 10 hours reaction time triggers the disappearance of the aldehyde from the reaction mixture as the amine functionalities on the linker will begin to catalyse the Knoevenagel condensation reaction. As discussed, the condensation reaction occurs quickly at first and then slows to a steady rate over time until near

complete conversion of the aldehyde to cinnamylidene malononitrile occurs. This could be due to concentration of the aldehyde becoming limiting or some form of deactivation of the amine functionalities. Deactivation was considered as post-reaction it was noted that the collected catalyst retains, even after sonication a difference in colour to the un-used, as-synthesised material. Analysis by FT-IR following the tandem reaction using benzyl alcohol was undertaken and compared to the un-used Au/Uio-66-NH₂.

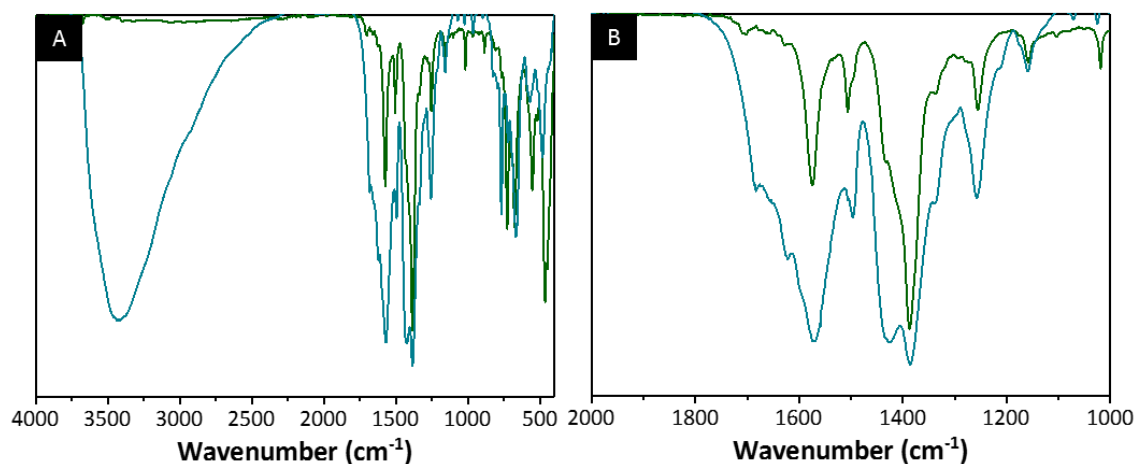


Figure 137: FT-IR of A) Au/Uio-66-NH₂ before catalysis (green) and after catalysis (blue). B) 2000-1000 cm⁻¹ region.

The indication from this result is that the formation of an imine occurs, seen as a shoulder peak at *circa* 1640 cm⁻¹ Figure 137B. The formation of an imine, *via* reaction of the aldehyde from the oxidation and the amine of the MOF, may lead to the partial deactivation of the amine functionalities and explain the decline of the KV rate as seen. The large OH peak observed in the used catalyst is assumed to be from the retention of an alcohol or water within the catalyst such as methanol, *t*-BuOH or benzyl alcohol. Imine formation may explain the cause of the monitored drop-off in activity *via* the mechanism shown proposed by Panchenko *et al*^[347] and Wirz *et al* shown in Figure 138^[380].

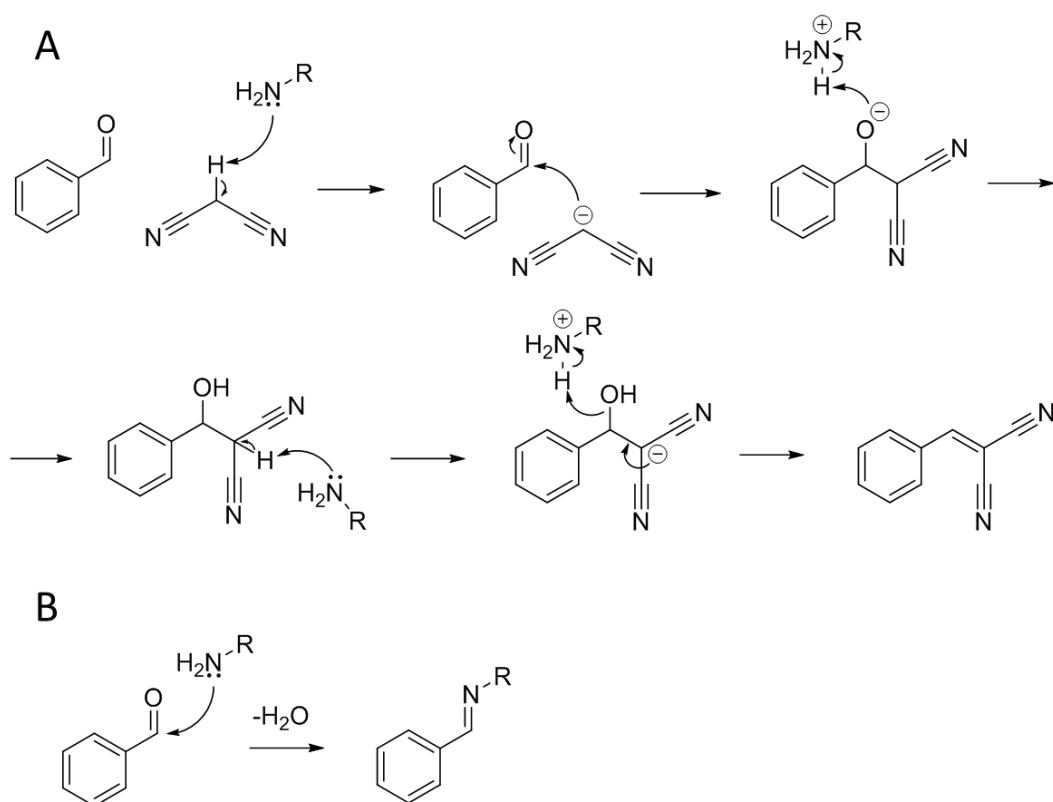


Figure 138: A) Knoevenagel condensation reaction between benzaldehyde and malononitrile and B) Imine formation by reaction of benzaldehyde with the amine functionalities of the MOF. R = UiO-66-NH₂ extended framework.

The imine formation shown in Figure 138B then conceivably prevents the KV reaction, Figure 138A, from occurring through essentially capping the amine functionality and stopping the condensation from occurring. However, this is not necessarily the case and further understanding is needed. Moreover, a DFT study of the reaction on IRMOF-3 showed that the imine formation may in fact be key to the reaction by acting as the base for the methylene compound deprotonation^[381]. If so then after higher initial conversion catalysed by the imine, the remaining conversion rate may be lowered not by the capping of the amine as previously suggested but by the need for imine reversal. A detailed analysis of the benzaldehyde concentrations and mass balance of the reaction may provide more evidence to substantiate one of the pathways. Optimisation attempts for the KV half of the reaction are then dependent on greater understanding of these processes as the FT-IR obtained is not conclusive in proving that imine formation or explaining the active site. Techniques such as TGA and NMR following digestion of the MOF would enable further understanding and so optimisation.

5.3.3 Oxidation optimisation

Investigation into the oxidation reaction was used to expand the substrate scope of the starting alcohol. Additionally, with focus on the use of different synthetic approaches, the Au/UiO-66-NH₂ material was manipulated with the view to undertaking the tandem reaction without the need for completion of the oxidation prior to addition of the methylene compound.

5.3.3.1 Pt and Pd/UiO-66

Despite the encouraging results from the tandem reaction, the deactivation of the oxidation reaction with the addition of the malononitrile at the start is disappointing as it complicates the reaction. For example, in the substrate study, section 5.3.3.2 – because it was known that the oxidation would be deactivated, it was required that the monitoring of the rate of each alcohol oxidation was undertaken, a time intensive process. Optimisation to allow for initial methylene compound addition is required. Hinde *et al* suggested that ‘the malononitrile was inhibiting the oxidation step on the Au NPs, possibly due to unfavourable interactions between the malononitrile and the Au NPs’^[373]. Therefore other NP species which are active for the oxidation reaction, Pt and Pd nanoparticles were produced. They have been shown to be similarly effective for benzyl alcohol oxidation as gold nanoparticles when either deposited on or encapsulated within MOFs^[192,382]. Deposition onto UiO-66 occurred *via* an analogous method to the Au NPs synthesis, resulting in Pd/UiO-66 and Pt/UiO-66, see section 2.1.3.3. After characterisation these were tested for activity in the conversion of benzyl alcohol to benzaldehyde, and their activity compared to the Au analogue, to confirm that the activity was comparable and that they would be viable alternatives to gold nanoparticles.

Prior to catalysis, XRD, N₂ adsorption, TEM and XPS were used to determine any detrimental effect on the MOF the nanoparticle deposition had caused, with the latter two techniques used to evaluate the NPs also. The loading of the MNPs on the UiO-66 was determined through ICP-OES to allow comparison with the Au variant through TON calculation. XRD analysis showed that the framework structure was unaltered upon deposition of both Pd and Pt nanoparticles. The sampling size was small in both cases and so the intensity of the peaks are lower with respect to the blank framework, but also causing the signal to noise ratio to be lower. The samples retain both crystallinity and phase purity after the deposition of the nanoparticles as was seen for the Au/UiO-66 hybrid material discussed earlier, and shows that the facile colloidal deposition method leaves the framework structure unaltered.

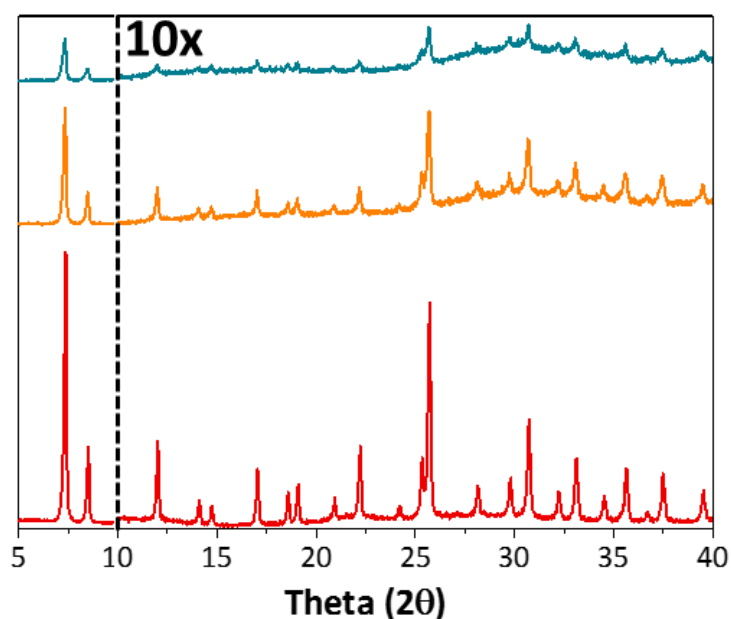


Figure 139: XRD patterns of UiO-66 (red), Pd/UiO-66 (orange) and Pt/UiO-66 (turquoise). Values beyond that of 10 theta have been scaled 10 times as the two peaks below that have high intensity relatively.

Nitrogen adsorption studies displayed good agreement with UiO-66 for Pd/UiO-66 with little variance in either the BET surface area or the isotherm shape and uptake quantities observed. The Pt/UiO-66 shows an appreciable decrease in both the quantities adsorbed and BET surface area, Figure 140. This indicates that some of the internal area of the MOF has been filled during the deposition process, the reason for which is not known but could be from excess PVP within the synthesis or alternatively, may allude to NP impregnation. The latter seems unlikely when the TEM statistical analysis is considered, Figure 142, as the average size of the Pt NPs is in excess of the pore diameters expected of UiO-66 and discussed in section 5.1.2. Interestingly for both, the increased uptake capacity seen for Au NPs was not observed in either case. Given that the batch of UiO-66 used was different and variances between batches occur, it may be that for this batch that no additional porosity increase could be obtained. Nevertheless, and despite the reduction seen in the Pt/UiO-66, the overall porosity of the materials was retained, indicating that the methodology is transferrable to these different metal nanoparticles.

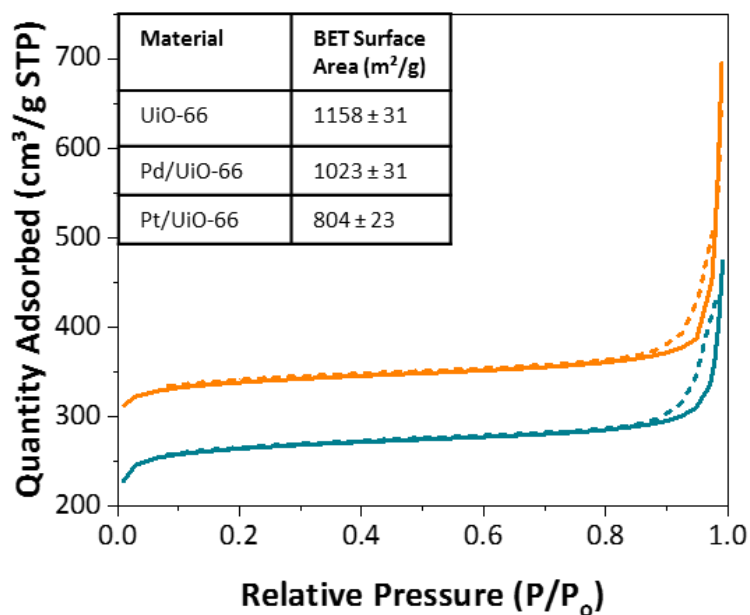


Figure 140: Nitrogen isotherms of Pd/UiO-66 (orange) and Pt/UiO-66 (turquoise), with BET surface area values, inset. For both: adsorption curve (solid) and desorption curve (dotted).

XPS of the Pt and Pd region were analysed to determine if the successful reduction of the nanoparticles in each case had been accomplished. Complications arose for the Pd region as it overlaps with the Zr3p peaks which are significantly higher in intensity given that it is the framework metal. Nonetheless the Pd 3d_{3/2} and 3d_{5/2} peaks are seen, Figure 141A, with the latter seen as a shoulder of the Zr3p_{3/2} peak. Neither metallic Pt nor Pd was available at the time of measurement for comparison, and so literature values were used for the evaluation of the oxidation state. For the Pd/UiO-66 to literature values for Pd@UiO-66 and Pd/UiO-66 indicate that Pd(0) is present based upon the peak positions of 340.87 and 335.87 eV^[383–385]. Furthermore, any higher oxidation state Pd in the sample would be visible through appearance of another doublet of peaks positioned at higher binding energy with respect to the Pd(0). Therefore because of observation of no further Pd peaks it is confirmed that only Pd(0) is present.

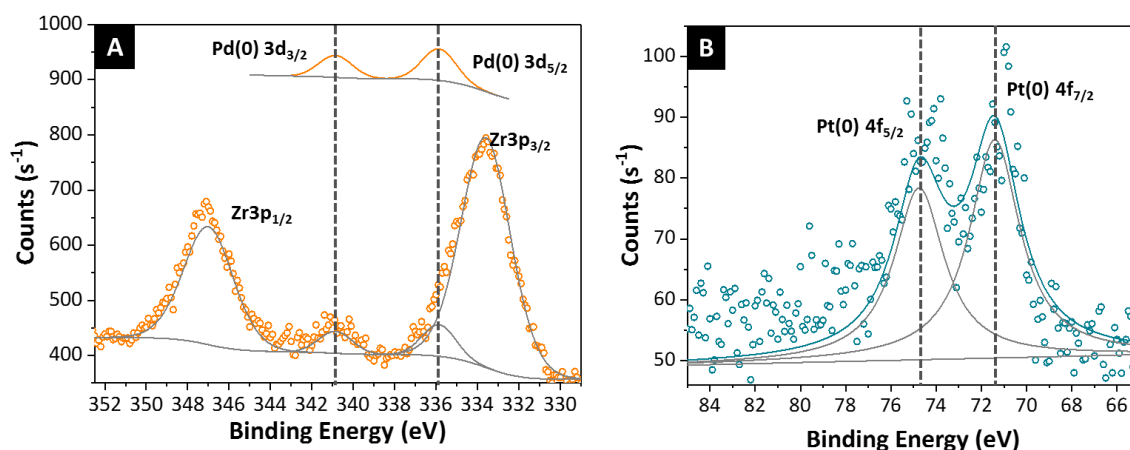


Figure 141: XPS regions for A) Pd on Pd/UiO-66, with Pd peaks offset, above, for visualisation, and B) Pt on Pt/UiO-66.

Analysis of Pt in Pt/UiO-66, Figure 141B, returned low counts despite increasing the number of scans used in the measurement. Nevertheless, the peaks observed were sufficient to see that the Pt was all in the reduced form with closely related peak values to a metallic Pt reference and Pt@MIL-101(Cr) (74.4 and 71.1 eV) reported by Zhao *et al.*^[386] but also those values reported for the synthesis of Pt@UiO-66^[387].

For both, the low XPS peak intensities indicate that whilst the deposition has clearly been successful, the weight % loadings are expected to be low. This is seen in the TEM where small clusters of NPs are observed, but that Pt and Pd nanoparticles have been deposited successfully onto UiO-66. In both cases, the nanoparticles appear spherical in nature and the MOF has not been altered by deposition as by visual inspection of the MOF there appears to be no change to the surface, nor the overall morphology.

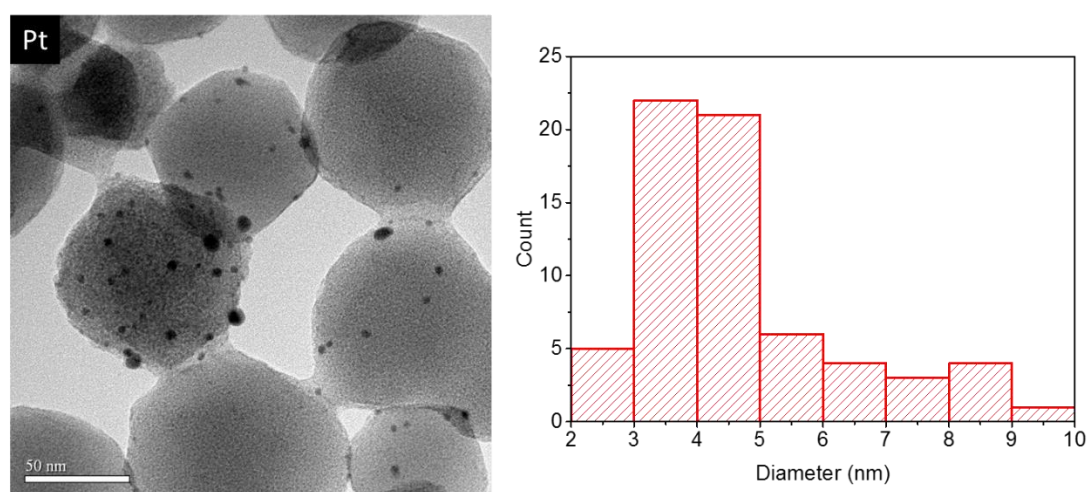


Figure 142: TEM image of Pt/UiO-66 with histogram detailing Pt NP size distribution.

Measurements undertaken on three images of Pt/UiO-66.

For the Pt NPs a wider range of diameters were observed, as seen in the histogram in Figure 142 and summarised in Table 43, with an average diameter of 4.7 nm measured. The distribution of the NPs around the MOF appears to be more uniform than was observed for the Au NP systems, yet there were still some MOF crystals with densely packed amounts of NPs on the surface, and some with no deposition having occurred at all.

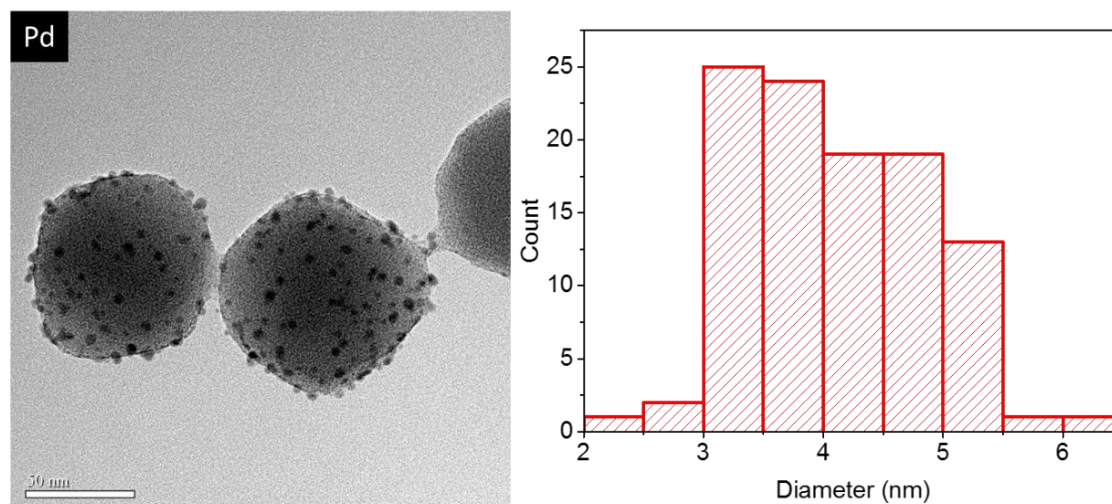


Figure 143: TEM image of Pd/Uio-66 with histogram detailing Pd NP size distribution.

Measurements undertaken on three images of Pd/Uio-66.

The Pd analogue displayed the same dense clustering of NPs that was observed with the Au NPs and to a lesser extent with the Pt versions. The size distribution was narrow, with only 3.8 nm between the smallest and the largest nanoparticles measured, summarised in Table 43.

Production of NPs for both metals has then been achieved with small diameters and monodisperse sizes observed indicating that good control is offered by the synthesis technique. Whilst it is known that Pt and Pd are less influenced by the average NP size^[58], production of small nanoparticles is still advantageous in order to maximise the number of surface sites available for reaction.

| | Pd/Uio-66 | Pt/Uio-66 |
|--------------|-----------|-----------|
| Average (nm) | 4.1 ± 0.7 | 4.7 ± 1.7 |
| Maximum (nm) | 6.2 | 9.2 |
| Minimum (nm) | 2.4 | 2.3 |

Table 43: Summary of maximum, minimum and average diameter of Pd and Pt NPs measured on Pd/Uio-66 and Pt/Uio-66 respectively.

The loading of the Pt and Pd was determined for use in turnover number calculations to allow for the comparison of the different nanoparticles in the oxidation step. As was expected for the Pt

and Pd, given the previous characterisation results, the loading of the NPs on UiO-66 was low, with the loading of the Pd lower than the Pt, see Table 44. This aids in explaining the low counts from the XPS as the spot size was 400 μm therefore as the clustering was greater on the Pd than Pt, if a region with large Pd clusters is analysed for Pd/UiO-66 the intensity shall be higher. Conversely, the chance of there being very little Pt in the analysis region is higher for Pt/UiO-66.

| Material | Loading / wt. % |
|-----------|-----------------|
| Pt/UiO-66 | 0.55 |
| Pd/UiO-66 | 0.48 |

Table 44: Loading values of Pt and Pd on the UiO-66 framework.

The characterisation demonstrates that the two alternative metal NPs can be applied for use in a test oxidation reaction but also it shows the versatility of the nanoparticle synthesis methodologies and the robustness of the UiO-66 MOF, validating its selection as the support. Au, Pt and Pd/UiO-66 were tested for their benzyl alcohol oxidation ability over a 24 hour period. The catalyst amount was lowered to 20 mg from 40 mg, in order to have better chance to elucidate the differences between the different NPs. Monitoring of the reaction progression was undertaken *via* ^1H NMR rather than GC-MS in this case. If comparably active for the oxidation then the use of Pd and Pt could provide alternative to the use of Au NPs and may solve the need for delayed malononitrile addition.

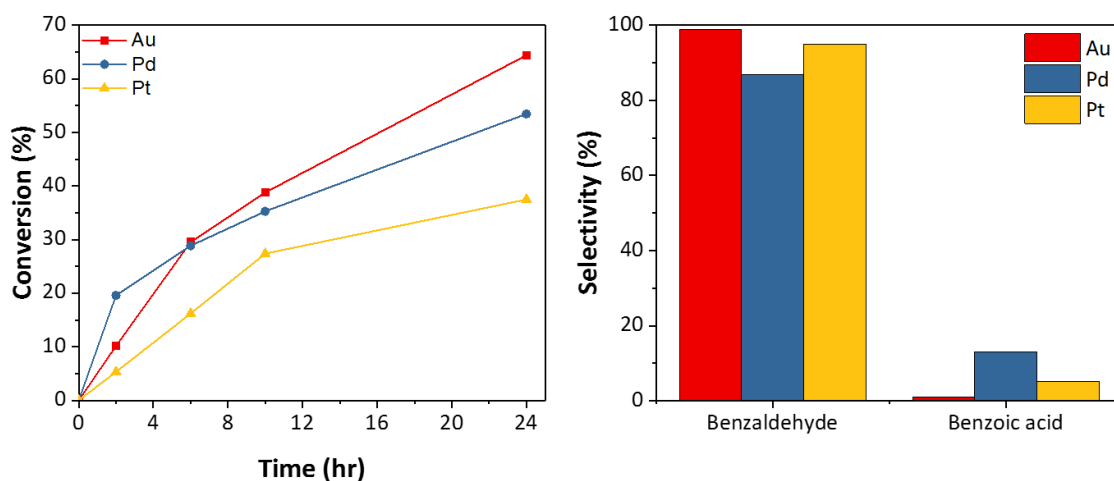


Figure 144: Benzyl alcohol oxidation conversion (left) and selectivity towards benzaldehyde and benzoic acid (right). Reaction conditions: 20 mg MNPs/UiO-66, 80 $^{\circ}\text{C}$, 0.75 mmol benzyl alcohol, 1.2 eq TBHP (aq), 7 mL *t*-BuOH, 24 hours.

All three NPs show the ability to undertake the oxidation of benzyl alcohol with TBHP as the oxidant, alongside crucially, good selectivity. Benzyl alcohol was used rather than cinnamyl

alcohol to allow for easier comparison with literature values across the three MNP systems^[382]. Benzoic acid was observed as a component of the reaction mixture for each of the three, with Au NPs displaying the best aldehyde selectivity, 98 %. Au and Pd variants showed the best activity towards benzyl alcohol conversion, but the Pd did suffer from lowered selectivity. Given the different loadings it is better to compare turnover values in order to account for the differences in amounts of MNPs present for each. TONs calculated for the three (based upon wt. % and not adjusted for average NP size) were calculated to be 751, 499 and 443 for Au, Pt and Pd respectively, indicating the Au variant is best suited for oxidation. For both Pd^[383,388] and Pt^[387,389] NPs on UiO-66-NH₂ and other MOFs benzyl alcohol oxidation has been achieved but comparison is difficult as reaction conditions vary. Nevertheless, the activity of the materials is clearly observed with reasonable TON values achieved by all three tested. Additionally, the use of Pd and Pt opens up the materials for use in other reactions such as hydrogenations^[346,386] therefore vastly increasing the versatility of these systems once the synthesis procedure has been fully refined. Different tandem reactions can then be envisaged, with some examples detailed previously in the discussion of tandem reactions within Chapter 1 and Pd@IRMOF-3 by Zhao *et al* and example of a Knoevenagel-hydrogenation tandem reaction^[156].

5.3.3.1.1 Post oxidation analysis

To be able to be re-used the NPs must retain: fixation to the surface, size and oxidation state. Therefore, following testing in the oxidation of benzyl alcohol the three MNP/UiO-66 materials were characterised using TEM to evaluate the NPs for the first two categories.

For Au/UiO-66 statistical analysis of NP size was undertaken on TEM images obtained of the collected catalysts, shown in Figure 145 and summarised in Table 45 and compared against the pre-catalysis sizes previously calculated.

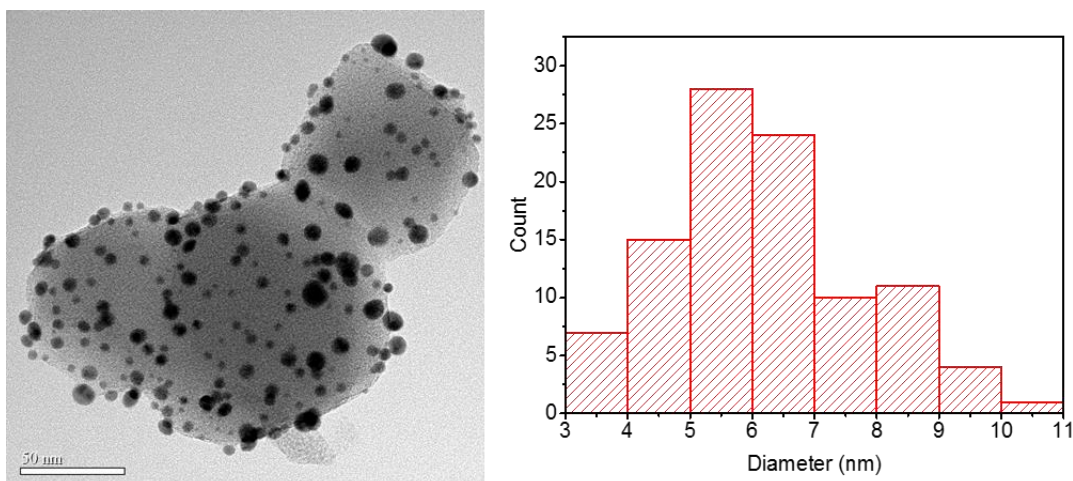


Figure 145: TEM image (left) of Au/UiO-66 following use for the oxidation of benzyl alcohol, histogram (right) of Au NP size. Measurement undertaken on two images of Au/UiO-66 (used).

Au NP sizes are larger in all three diameter categories: minimum, maximum and average size after use. As size is known to affect the catalytic activity of Au NPs it is essential that the correct size is maintained following use in order to allow for the Au/UiO-66 material to be reused.

| | Au/UiO-66 | Au/UiO-66 (single cycle) |
|--------------|---------------|--------------------------|
| Average (nm) | 5.8 ± 1.2 | 6.2 ± 1.6 |
| Maximum (nm) | 8.5 | 10.7 |
| Minimum (nm) | 2.7 | 3.3 |

Table 45: Summary of maximum, minimum and average diameter of Au NPs measured for Au/UiO-66 and Au/UiO-66 (following one use for benzyl alcohol oxidation).

Whilst slight increase in the NP size is measured for all, the average diameters for the pre and post catalyst are within error of one another. The increase in maximum size observed is notable and has shifted from 8.50 nm in the pre-catalysis Au/UiO-66 to 10.7 nm after reaction, a diameter at which a large drop-off in activity was reported by Abad *et al* for Au/TiO₂ use in alcohol oxidation^[173].

TEM measurements were repeated also for the Pt and Pd varieties following benzyl alcohol oxidation and summarised in Table 46. The Pt variant shows little to no change upon use, with the mean average and maximum sizes being nominally lower in those measured after the catalysis, (prior to catalysis values were 4.7 nm and 9.2 nm for Pt average and maximum size, respectively), indicating that they are robust under the reaction conditions which is promising for re-use. The Pd

variants displayed an overall increase across the three variables measured, though again the increase was not drastic and within the errors calculated.

| | Pt (nm) | Pd (nm) |
|---------|---------------|---------------|
| Mean | 4.5 ± 0.9 | 5.0 ± 1.6 |
| Minimum | 3.0 | 2.9 |
| Maximum | 8.0 | 8.8 |

Table 46: Summary of maximum, minimum and average diameter of Pt and Pd NPs measured by TEM following a single use for benzyl alcohol oxidation.

Visual inspection of the MOF crystal surfaces appears to show that no obvious defects have been introduced during the catalysis, Figure 146, and the NPs themselves were observed to maintain the spherical nature seen beforehand. This is however only a qualitative assessment and XRD and XPS would impart greater confidence to these claims.

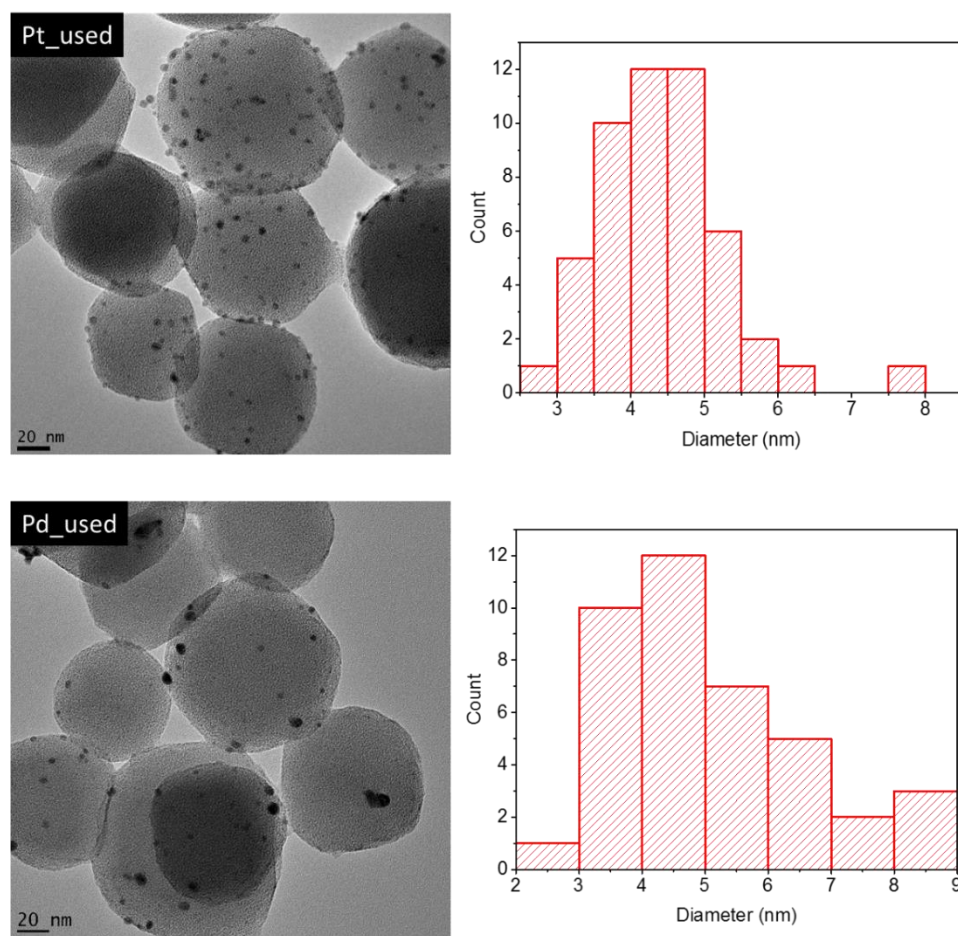


Figure 146: TEM images of Pd and Pt NPs on UiO-66 after use in the oxidation of benzyl alcohol with size distribution histogram shown (right). Measurements undertaken on two images for both Pd and Pt/UiO-66 (used).

ICP-OES was collected to see if significant leaching of the NPs from the UiO-66 material. Whilst a significant amount of NPs are still obviously present on the support (TEM) it is important to maintain adherence with the support as any leached materials shall not be recoverable for re-use.

| Material | Loading / wt. % | Loading after 1 st cycle/ wt. % |
|--|-----------------|--|
| Pt/UiO-66 | 0.55 | 0.64 |
| Pd/UiO-66 | 0.48 | 0.45 |
| Au/UiO-66 | 0.63 | - |
| Au/UiO-66-NH ₂ ^a | 0.87 | 0.84 |

Table 47: Comparison between MNP loading before and after catalysis. ^aResult from catalyst collected during the studies of benzyl alcohol oxidation, Table 48.

From Table 47 it is seen that the loading decreased by 3.44 % for the Au/UiO-66-NH₂ and by 6.25 % for the Pd/UiO-66 material both of which indicate a small proportion of the NPs were lost from the material surface during reaction, with the difference marginally larger than the experimental error. The result for the Pt material has been disregarded as increase in the loading is not possible, the ratio of the Zr wt. % to the Pt wt. % in the used Pt sample was significantly different to the pre-catalysis measurement indicating this result is unreliable. Use of the framework metal quantities in this way as a reference for all ICP-OES allowed them to be checked for consistency. The quantity collected from the Au/UiO-66 was attempted to be re-used in a recycle study and as a result, a sample of Au/UiO-66-NH₂ used for the oxidation studies (see later section) was analysed to evaluate Au NPs again with good indication that the NPs were not leaching in significant amounts.

For the Au, Pd and Pt materials the maintenance of the NPs size and loading has been achieved with only small changes after catalysis seen. The shifts observed in the sizes of the nanoparticles for Au and Pd are relatively small when considered against the average size for each, but given the smallest sizes measured within the distributions for the as-synthesised versions of each, a degree of nanoparticle aggregation cannot be discounted entirely. If occurring significantly, and nanoparticles are aggregating, then a larger shift might have been expected. Nonetheless, the changes in the values are appreciable to have been detected and therefore requires further understanding. The effect on the ability of the catalyst of these subtleties is needed to be found and should be done so through recycle tests.

5.3.3.2 Alcohol substrate scope

After undertaking the oxidation-KV tandem reaction, further investigation on the Au/UiO-66-NH₂ was used to evaluate the scope of reactions possible with these materials and highlight and extend their versatility.

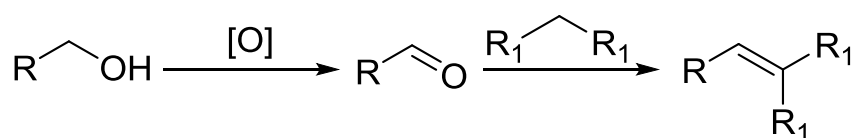


Figure 147: Tandem cascade of alcohol to aldehyde followed by Knoevenagel condensation.

Expansion of the substrate scope was undertaken to ascertain the flexibility of the catalyst towards a range of alcohols, therefore focussing on the first part of Figure 147 and varying the structure of R. A wide range of final compounds are conceivable to be formed by altering the alcohol. Activity towards industrially attractive transformations was attempted and so vanillyl, furfuryl and benzyl alcohols as well as linear 1-hexanol were tested to gauge the flexibility of the NPs on Au/UiO-66-NH₂. The final products were identified using the MS functionality of the GC-MS for vanillyl alcohol and furfuryl alcohol as these were not commercially available and in this case quantification was obtained through observation of the loss of the aldehyde peak, see appendix Figure C1 for MS results. The results of the oxidation study are summarised in Table 48.

| Alcohol | Conversion / % | Aldehyde selectivity / % | time (oxidation) / hrs | time (KV) / hrs | KV product yield / % |
|------------------|----------------|--------------------------|------------------------|------------------|----------------------|
| Cinnamyl alcohol | 79 | > 99 | 10 | 24 | 78 ^a |
| Benzyl alcohol | 99 | 95 | 14 | 14 | 94.1 |
| Vanillyl alcohol | 99 | 90 | 10 | 14 | 89.1 |
| Furfuryl alcohol | 99 | > 97 | 72 | 48 | 96.0 |
| 1-hexanol | 11 | 0 | 8 | ^b n/a | 0 |

Table 48: Conversion, selectivity and yield values for the oxidation of a range of alcohol to their respective aldehydes followed by Knoevenagel condensation with malononitrile.

Reaction conditions: 40 mg Au/UiO-66-NH₂, 80 °C, 0.75 mmol alcohol, 1.2 eq TBHP (aq), 7 mL *t*-BuOH, 0.75 mmol malononitrile, see table for reaction times. ^aPublished values. ^bReaction was stopped as hexanoic acid only was produced.

It is seen that the Au/UiO-66-NH₂ is able to undertake the oxidation-KV reaction beginning with a range of alcohol compounds and malononitrile as the methylene compound. A range of varying

rates and selectivities were seen. In each case the reaction was monitored until the oxidation was seen to go to near completion, at which point the malononitrile was added.

Benzyl alcohol oxidation occurred at a similar rate to that of cinnamyl alcohol, given the higher conversion calculated, yet was not as selective towards the aldehyde with benzoic acid seen as the main side-product. However, the longer timescale of oxidation made sampling difficult and therefore the reaction could have been completed prior to 14 hours at which point over oxidation would have been encouraged adding error to comparisons made. Whilst benzoic acid is an important industrial product, methodologies for its production are well known and so this is not a reasonable target molecule for this oxidation process^[390]. The KV component of the benzyl alcohol tandem reaction was seen to occur over a shortened timescale to cinnamaldehyde conversion and maintained the high selectivity throughout. Oxidation of vanillyl alcohol occurred over a similar timescale to benzyl alcohol and saw conversion of the vanillin intermediate to the KV product in 10 hours. Vanillyl alcohol oxidation is industrially important as the intermediate formed, synthetic vanillin, is used extensively as a flavouring and in perfumes, as the natural product is difficult to produce and so expensive^[391,392]. Furfuryl alcohol required a much longer timescale to be converted to furfural, however did so at high selectivity (over 97 %) which led to a high yield of the final condensation product. Lengthy reaction times have been reported for furfuryl alcohol oxidation with respect to other catalysts^[173,387]. Yet, despite the length of the reaction, the selectivity shown is promising and results in a high yield of the final product, 96 %. Monitoring of the oxidation of hexanol did observe the formation of hexanal, however the level of the aldehyde remained consistent over time and ultimately the production of hexanoic acid was observed through over oxidation. This reaction then would be more feasible once the methylene compound addition at the beginning can occur as the methylene compounds would feasibly react with the aldehyde before further oxidation had the chance to occur. Nonetheless, the Au/UiO-66-NH₂ hybrid materials is able to undertake the oxidation of a selection of alcohols to their respective aldehydes and then onto the condensation product upon the addition of malononitrile at high yields (> 78 %) demonstrating the versatility of this catalyst towards the oxidation-Knoevenagel reaction.

5.3.3.3 Investigation of Au NP distribution

From the TEM images obtained during the characterisation stage, it was noted that the deposition of the nanoparticles did not occur on all of the UiO-66 crystals equally, with the same observed also for the UiO-66-NH₂ MOF, Figure 148.

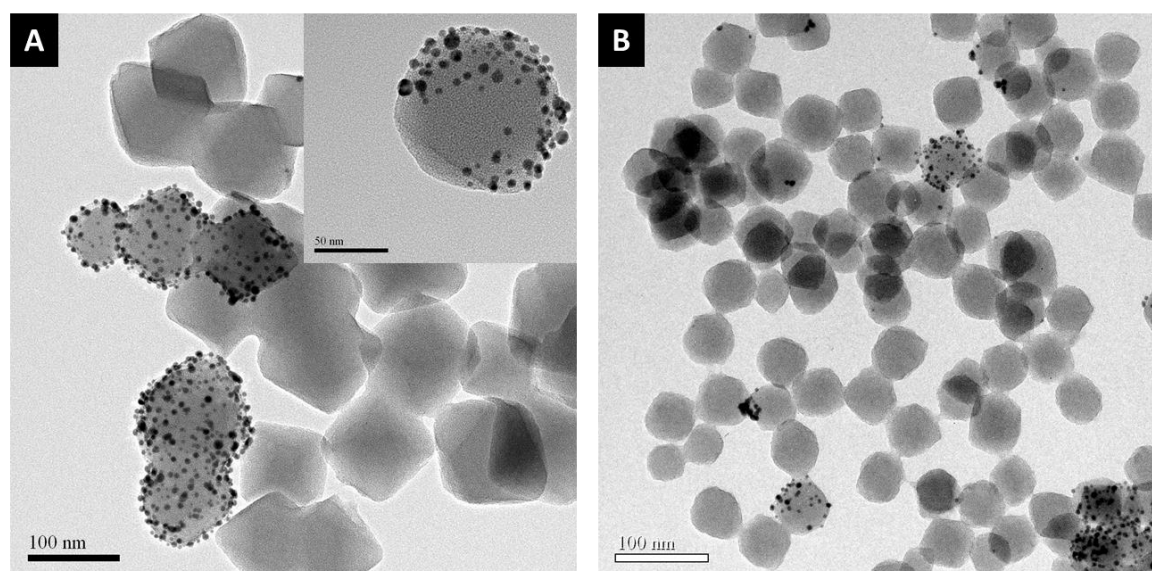


Figure 148: A) Au/UiO-66 and crystal with partial coverage (inset) and B) Au/UiO-66-NH₂ detailing non-uniform deposition across crystals within the same sample.

Given that the MOF sample used for deposition of NPs each time originated from the same synthesis batch it was expected that the coverage would occur evenly across the surfaces of the MOF. For both UiO-66 structures this was not observed and rather complete coverage of select crystals is apparent, rather than each crystal having a degree of surface occupation by the NPs. It is thought that the interaction which occurs between the MOF upon deposition of an initial NP encourages further deposition to occur upon that same MOF particle, as evidenced by the inset of Figure 148A, whereby coverage would appear to occur *via* deposition of NPs next to NPs already deposited on that crystal.

The occurrence of such uneven deposition may affect catalytic potential with the close proximity of the NPs to one another preventing them from working effectively as single sites for the oxidation. To determine this, and improve the performance if found to be true, several steps were taken to promote the uniform deposition of the nanoparticles onto the MOF with the hope that improved catalytic performance would be achieved:

1. The MOF sample was thoroughly ground, prior to addition to the NP solution in order to lessen the chances of large aggregations which would prevent deposition to those MOF particles within the centres of such clusters.
2. The stirring rate of the solution was increased following the MOF addition to break-up any remaining aggregations but also prevent any of the sample sticking to the reaction vessel.
3. The synthesis of the UiO-66-NH₂ was manipulated in order to obtain greater control of the morphology.

4. Lastly, impregnation of the Au NPs was attempted to ensure the Au NPs were placed in discrete locations in relation to one another.

Steps 1 and 2 were implemented for all nanoparticle syntheses following initial TEM imaging and observation of the clustering. Step 3 of the above was undertaken as the UiO-66-NH₂ particles seen in Figure 148B, are a mixture of morphologies and sizes. Production of more monodisperse MOF particles with regards to size and shape may promote more uniform NP deposition. The work of Zhao *et al* was used to synthesise well-defined and monodisperse UiO-66-NH₂^[363]. A modified procedure used acetic acid as the modulator with trimethylamine (TEA) to aid terephthalic acid deprotonation and allowed for the close control of the MOF size and shape, Figure 149. The subsequent deposition of Au NPs resulted in NPs well-dispersed upon individual crystals yet still MOF crystals remain unaltered and therefore uniform distribution was not obtained by closer control of the MOF size and shape.

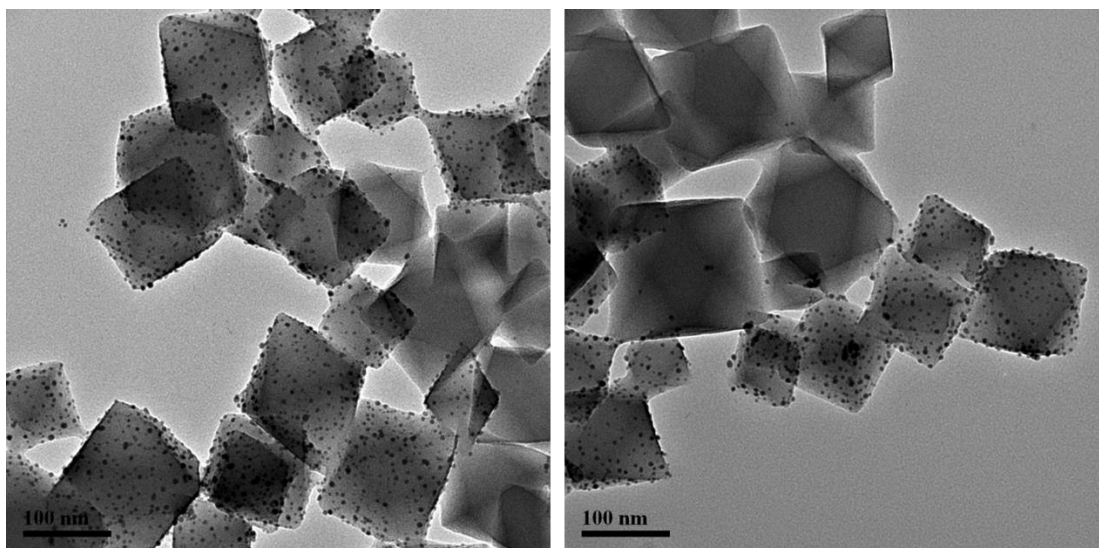


Figure 149: TEM images of Au/UiO-66-NH₂ using acetic acid as the modulator.

Step 4 was investigated through consideration and modification of the work by Gu *et al* whereby Au@UiO-66-NH₂ was produced^[201]. This method required the PVP coated NPs to be added to the MOF synthesis solution, with the Au NPs acting as nucleation point for MOF growth which itself is promoted by acetic acid addition to encourage Zr-oxo cluster formation (the SBU shown in Figure 120A) and so MOF formation^[201]. Encapsulation was attempted in order to force the separation of the nanoparticles as the MOF would grow around each and so force uniform distribution of the Au NPs across the sample.

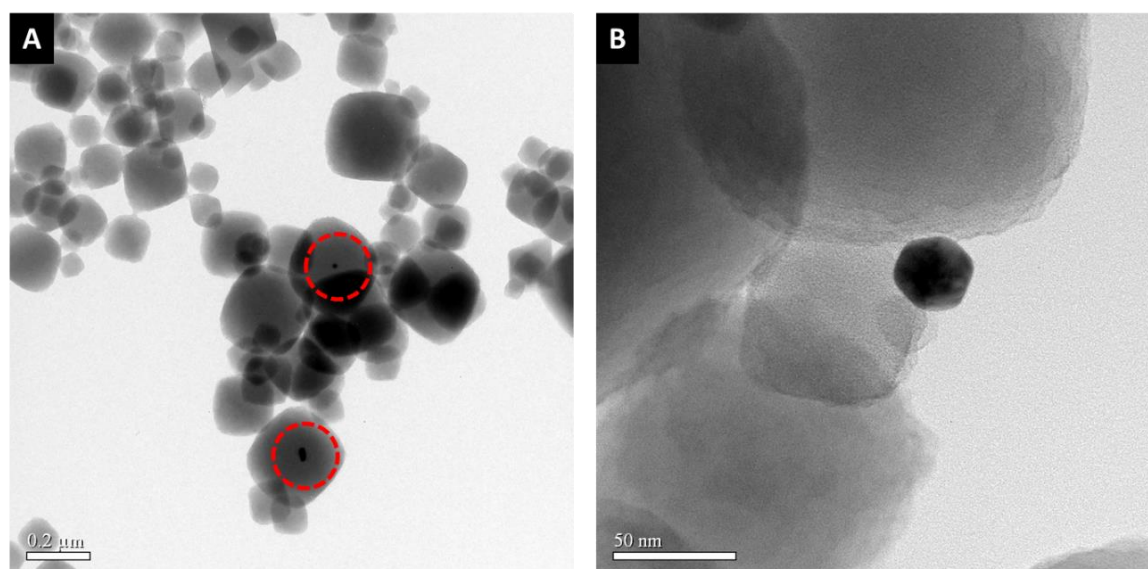


Figure 150: TEM images of samples prepared through attempted encapsulation of Au NPs with A) NPs highlighted appearing centred to the MOF particle and B) Au NP not encapsulated.

From the TEM images, above, it was clear that neither the size of the nanoparticle or the control over the MOF size was maintained. Over several attempts, difficulty was met in reproduction of the literature results and was attributed to the use of smaller nanoparticles than employed by the report by Gu *et al.*^[201]. Whilst there was evidence of some possible encapsulation, Figure 150A, there was also a significant number of nanoparticles both not encapsulated and also of greatly increased size, Figure 150B. These results can also be observed in the TEM images by Gu *et al.*, where loss of control over consistent nanoparticle and MOF size is seen, however not to the same extent as in Figure 150, above. The breakdown of the nanoparticles when included in the synthesis mixture for UiO-66 has been reported, with the formation of HCl being attributed for the dissolution of nanoparticles^[393,394]. In this way the reliable formation of nanoparticles of closely controlled size may not be possible when attempted using this encapsulation technique. Encapsulation was therefore not pursued further as the synthesis control was lost for MOF and NP. Furthermore, when considered for catalytic purposes the Au/MOF ratio would be very low as there is only one NP per MOF and as a consequence greater amounts of catalysts may be required for oxidation or reaction times lengthened, as evidenced by the 24 hours reaction time and only 30 % conversion reported for their application in benzyl alcohol oxidation by Gu *et al.*^[201]. Finally, the necessity of reagents to diffuse through the MOF was reported to prevent oxidation of bulky alcohols^[201] which adds a limitation to the system that is not present for Au/UiO-66-NH₂ as the surface nature of the reaction overcomes this.

A ‘middle ground’ between deposition and encapsulation then may yield a promising material by means of impregnation methods, as defined in Chapter 1. A variation of the methodologies documented by Aijaz *et al.*^[395] (double solvent approach) and Pan *et al.*^[396] (single solvent approach to produce Pt and Pd respectively) within the MIL-101(Cr) architecture was attempted for UiO-66-NH₂. For the single solvent approach, the procedure by Luan *et al.* and Leus *et al.* for impregnation of Au NPs within UiO-66 analogues was employed^[199,200]. Through introduction of the salt to a stirred suspension of the MOF it was hoped that the impregnation of the gold would occur, along with size control of the resulting nanoparticles formed as pore sizes within the MOF architecture would dictate size but also ensure well-dispersed Au NP formation. The gold salt is initially external to the MOF architecture, therefore subsequent nanoparticles are likely to form on the surface or partially within the framework and thus be more accessible to reagents than those fully encapsulated. Additionally, MOF shape and size control is still possible as the synthesis stage of the MOF and NP are maintained as individual stages. The MOF, UiO-66-NH₂, was subsequently suspended in hexane (in an adaption of the double solvent approach) and methanol prior to an aliquot of HAuCl₄ solution being added to produce a 1 wt. % loading of Au.

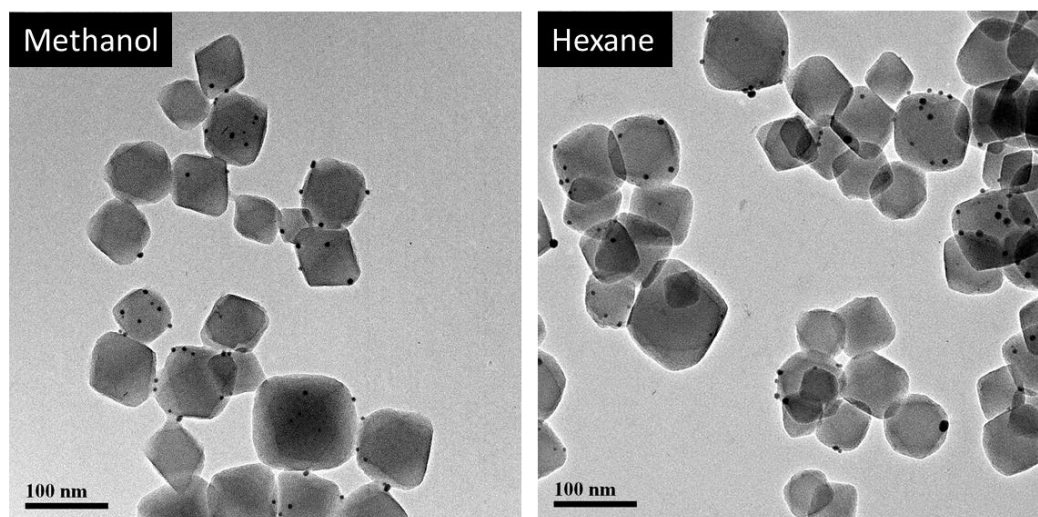


Figure 151: TEM images of Au NPs on UiO-66-NH₂ synthesised in methanol and hexane.

The results for both solvents are shown in Figure 151 where it can be seen that the formation of Au NPs of monodispersed size have been formed, see Table 49 and appendix Figure C2 (greater magnification images). The statistical analysis shows the NPs to be less varied than the PVP versions, despite the lack of use of a stabilising agent. The sizes are in good agreement to a similar methanol based preparation on UiO-66^[199] but higher than the average sizes in the literature where complete impregnation within the pores was claimed^[200,397]. Whether the coverage is more uniform or rather the loading is lower requires the collection of ICP-OES to determine the weight percentage of these materials; however, even if lower in loading weight % the isolated nature of the NPs may be beneficial if each site is individually seen to be more active.

| Size / nm | Methanol | Hexane |
|--------------------|----------|--------|
| Average | 5.3 | 5.7 |
| Standard deviation | 0.8 | 1.4 |
| Maximum | 6.9 | 8.3 |
| Minimum | 3.3 | 2.7 |

Table 49: Size distribution summary for Au NPs on UiO-66-NH₂. Sample size were 44 and 43 for hexane and methanol respectively.

Whether the nanoparticles are on the surface of the MOF or have been impregnated within the pores is hard to determine. The size distributions of the nanoparticles which were measured are on average higher than would be expected for those when complete impregnation was attained, indicating that the Au species are likely on the surface of the MOF. Even the smallest of the range measured are unlikely to be within the framework pores, given that the larger octahedral pore is 1.1 nm (11 Å) in diameter^[397]. Modulator was used in the synthesis of the MOF which is known to create larger pores and cavities in UiO-66 through missing linker defects^[368]. In this case then the MOF may be able to host some of the smallest NPs measured, Table 49, as has been observed with other NP@MOFs^[194,398]. This method of NP deposition/impregnation is facile to undertake and therefore, given the results displayed is promising towards efforts to obtain full control of the location of the nanoparticles both on the MOF and with respect to one another. Determination of the exact location of the nanoparticles is challenging and would require greater characterisation in order draw meaningful conclusions, as noted by Dhakshinamoorthy *et al* who reported the requirement for several characterisation techniques in combination with TEM to unequivocally determine NP location with the MOF^[58].

These Au/UiO-66-NH₂ systems, Figure 151, produced from deposition/impregnation in methanol and hexane are obtained without PVP therefore need to be investigated further as they may provide a method for either improvement of the oxidation reaction rates through greater access to the gold nanoparticle surface of the substrate. In an ideal case, the modifications above will allow for the tandem reaction to be undertaken where all of the reagents, including malononitrile, are added at the start, and so performed as a one pot, single step reaction.

5.4 Tandem epoxidation-CO₂ utilisation

5.4.1 MIL-101(Cr)

A number of studies have detailed the use of MIL-101(Cr) hybrid materials for epoxidation (oxidation) reactions. Maksimchuk *et al* used polyoxotungstates deposited within MIL-101(Cr) to produce the epoxide from an alkene^[338,399]. Sun *et al* used single and mixed metal MIL-101(Cr/Fe) to convert styrene to styrene oxide^[85] and Saikia *et al* used Au NPs on an amino variant, Au/MIL-101-NH₂(Cr), to undertake the same reaction^[400]. The ability then of modified MIL-101(Cr) to complete an epoxidation reaction allows for a tandem reaction to be envisaged where an alkene, such as styrene, is converted to its respective carbonate, *via* the epoxide, as displayed in Figure 152.

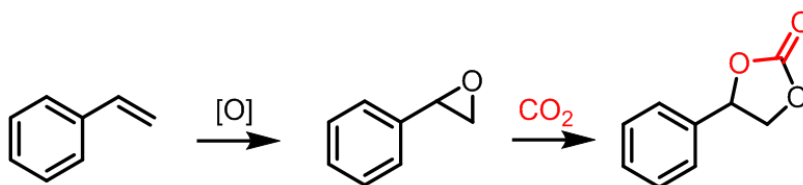


Figure 152: Proposed tandem reaction to convert styrene to styrene carbonate *via* the epoxide using an oxidant and CO₂.

Relatively few literature examples are present for the reaction of alkenes directly to cyclic carbonates. Sathe *et al* considered the two reactions separately under flow conditions to produce a range of cyclic carbonates using a methyltrioxorhenium catalyst for the epoxidation and an Al-complex with TBAI co-catalyst for the cyclic carbonate synthesis^[300]. Han *et al* used polyoxometalates in a zinc MOF to undertake the conversion of a range of alkenes under batch conditions resulting in high yield and control of the stereochemistry, however, long reaction times > 48 hours and in some cases up to 120 hours were reported^[299]. In the cases where the tandem reaction has been undertaken a co-catalyst was often employed for the cyclic carbonate step, the downsides of which have been detailed and addressed in Chapters 3 and 4 of this work. Given that the second, CO₂ utilisation step, has been optimised in Chapter 4 of this work, then only the epoxidation reaction is required to be investigated for viability with MIL-101(Cr). As such, the epoxidation step will be explored, initially with unmodified MIL-101(Cr), with the view to ultimately employing a modified version of MIL-101-Me(Cr) as a catalyst for both stages of the epoxidation-CO₂ utilisation reaction.

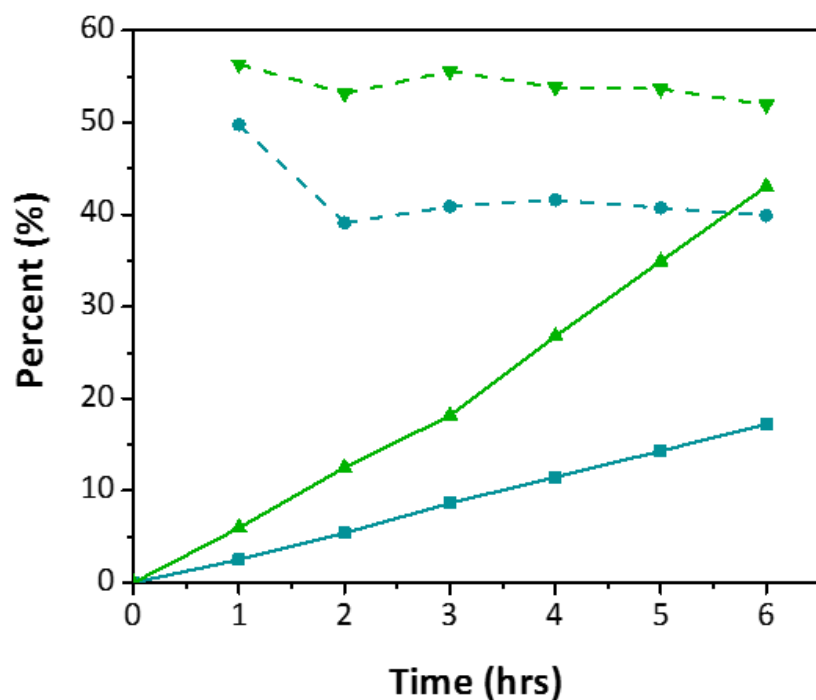


Figure 153: Conversion of styrene and selectivity towards styrene oxide by MIL-101(Cr) (green) and no catalyst (blue). For both: conversion (solid) and selectivity (dashes). Reaction conditions: Acetonitrile (5 mL), 70 °C, 4.8 mmol styrene, 1.2 eq TBHP (5.5 M/decane) and 20 mg MIL-101(Cr) (green only). Analysed by GC, chlorobenzene (0.1 g) as ITSD.

Using unmodified MIL-101(Cr) as a starting point catalytic trials were undertaken to attempt to convert styrene to styrene oxide. As an oxidant, TBHP but this time in decane was used, as a trial with the aqueous version saw the epoxide converted to the diol *via* addition of water. When compared against the blank reaction, MIL-101(Cr) improved both the conversion and the selectivity of the reaction over a 6 hour reaction period at 70 °C, Figure 153. Selection of 70 °C as the reaction temperature rather than the 115 °C employed for the CO₂ utilisation studies in Chapter 4 was to prevent the degradation of the TBHP during the reaction. Selectivity for the epoxide was consistent for the MIL-101(Cr) reaction and was observed to decrease as a function of time for the blank (no catalyst) reaction. In both (MIL-101(Cr) and the blank) the side products of the reaction were identified to be phenylacetaldehyde (due to rearrangement of the epoxide) and benzaldehyde.

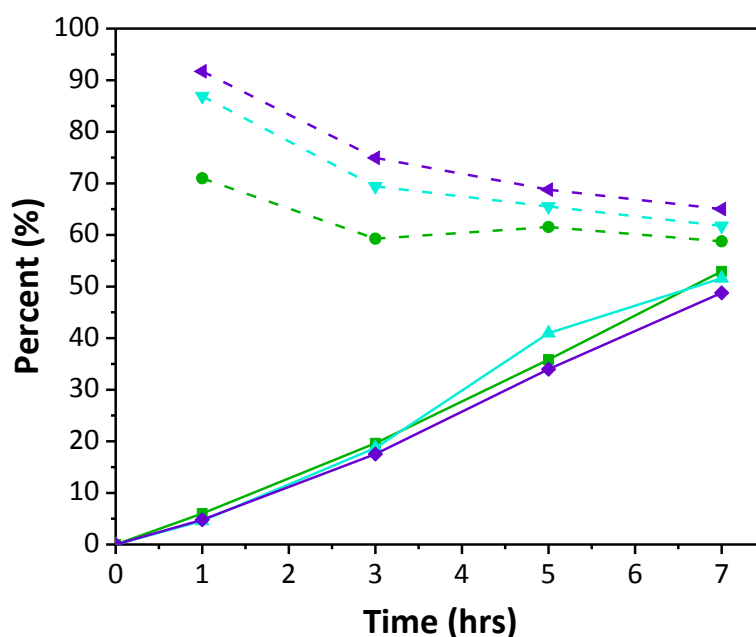


Figure 154: Conversion of styrene and selectivity towards styrene oxide by MIL-101(Cr) (green), MIL-101(Cr) synthesised with 50 mol % benzoic acid (light blue) and MIL-101(Cr) synthesised with 100 mol % benzoic acid (purple). For all: conversion (solid) and selectivity (dashes). Reaction conditions: Acetonitrile (5 mL), 70 °C, 4.8 mmol styrene, 1.2 eq. TBHP (5.5 M/decane) and 20 mg catalyst (as above). Analysed by GC, chlorobenzene (0.1 g) as ITSD. Benzoic acid mol % are with respect to the linker.

Introduction of additives and modulators (nitric and benzoic acid) to the synthesis preparation of MIL-101(Cr) was screened in an attempt to improve the conversion values through smaller MOF particle size leading to a more favourable surface area ratio and it was also hoped that this would produce an increased number of defect sites within the MOF that could facilitate the reaction^[319,367]. The conversion values returned by the MIL-101(Cr) synthesised in the presence of differing amounts of benzoic acid modulator were consistent across the samples tested, see Figure 154. However, what was apparent was the increased selectivity towards styrene oxide in the initial stages of the reaction (0 – 5 hours) for the modulated examples and therefore whilst the conversion is similar the yield of styrene oxide is higher. The initial stage is most important as it would be hoped that the epoxide would quickly react onwards to the cyclic carbonate upon application for the whole of the tandem reaction as the cyclic carbonate formation of MIL-101-Me occurs quickly, as per Chapter 4. In the above the lack of an onwards reaction increases the probability that the epoxide shall be converted into a by-product and so accounts for the decrease in the selectivity values measured over time. Comprehensive characterisation of the MIL-101(Cr) produced using modulators above, is then needed to determine the reason for the selectivity improvement seen. Nitrogen adsorption studies coupled with FT-IR with acetonitrile as a probe

molecule would allow for investigation of whether the number of CUS sites has increased, and SEM imaging would allow for size determination.

The deposition of Au nanoparticles (NPs) onto the MIL-101(Cr) was attempted as another means to improve the conversion values, using a similar method to Saikia *et al.*^[400]. A double solvent approach similar to that described by Aijaz *et al.*^[395] yielding promising results.

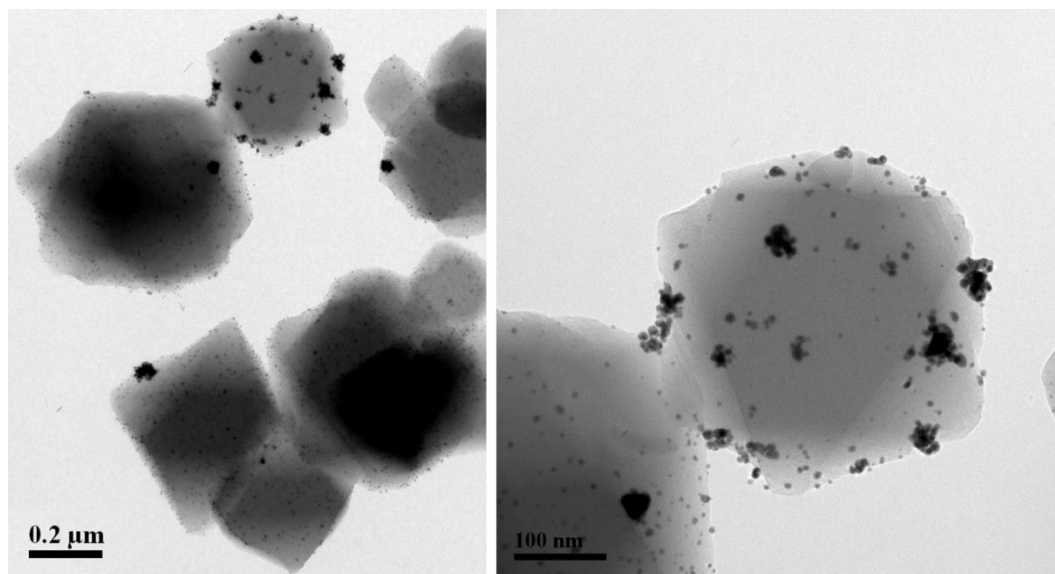


Figure 155: TEM images of Au@MIL-101(Cr) formed from a double solvent approach of water/hexane followed by reduction with NaBH₄.

As can be seen in Figure 155, for the double solvent approach in an attempted to produce encapsulated NPs, that the majority of the MOF crystals have nanoparticles present on them which appear to be similar in size and well-dispersed. However, there are large aggregated Au species present where the double solvent approach has not been successful in forcing all the aqueous HAuCl₄ into the framework and so pore directed NP formation was not uniformly achieved, similar to that reported by Hwang *et al.*^[205]. Clearly, optimisation of this technique for Au NPs is still required, yet for the non-aggregated NPs, Figure 155, a size distribution study revealed an average size of 4.57 ± 0.83 nm with maximum and minimum sizes of 6.84 and 3.41 nm respectively and so close control of the size has been achieved. The lower sizes are within the range expected for NPs impregnated within MIL-101(Cr) given the pores of the structure are 29 and 34 Å in diameter.

Au@MIL-101(Cr), was investigated using XPS to determine the efficacy of the synthesis method to produce the required Au(0) species on the MIL-101(Cr). Survey scans showed peaks within the regions expected to be present within the MOF, Figure 156B, namely those relating to chromium, carbon, oxygen and gold from the NPs. Further higher resolution scans of the specific regions are displayed in Figure 156, referenced to the adventitious carbon peak which was set at 284.4 eV.

Within the C 1s region, see Figure 156A, a small shoulder of the C-C peak was observed relating to C-O environments and another peak at 288.8 eV for O=C-O, both of which are ascribed to the linker of the MOF. Accordingly, the Cr2p doublet is observed, fitting of the $2p_{3/2}$ is shown only, Figure 156C^[333]. As expected after TEM imaging the Au4f peaks are observed, with low intensities (as low Au amounts were used experimentally). Comparison of Au4f_{7/2} and Au4f_{5/2} positions to other support based NPs^[401], Au NPs on MIL-101(Cr)-NH₂^[400] and the reference peaks of sputtered gold was undertaken. Saikia *et al* reported the peaks of the Au4f doublet in Au/MIL-101-NH₂ at 83.8 and 87.4 eV^[400], which compare to the 83.69 and 87.39 eV found experimentally and so the peaks shown can be attributed to the Au(0) state indicative of complete reduction of the precursor salt with NaBH₄.

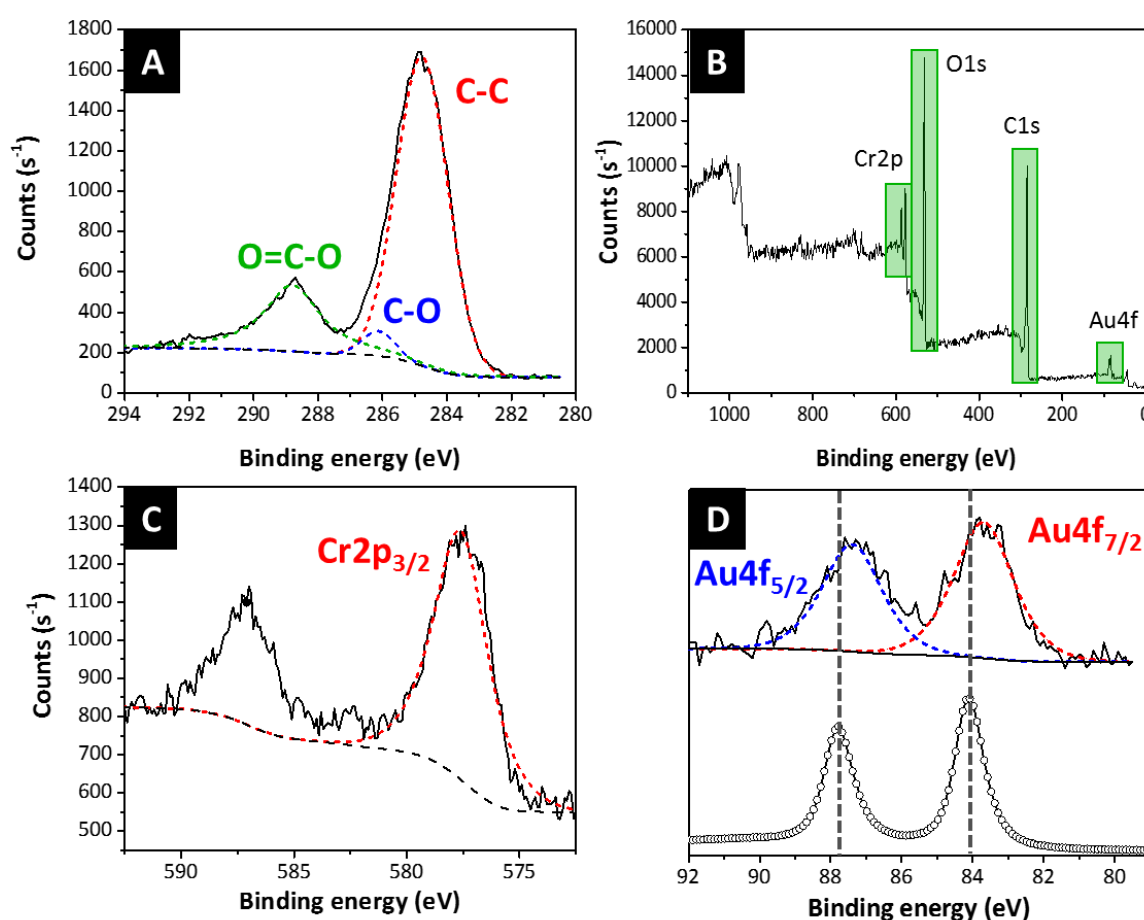


Figure 156: XPS spectra for Au@MIL-101(Cr) of A) C1s region, B) survey scan of Au@MIL-101(Cr) with Cr 2p, O 1s, C 1s and Au 4f regions highlighted, C) Cr2p region and D) Au4f region, with sputtered Au reference added. Note: black (dotted) is baseline for all.

Au@MIL-101(Cr) was tested for activity in the conversion of styrene to styrene oxide under similar conditions to those used in the previous trials. After a 6 hour time period, the Au@MIL-101(Cr) sample displayed a lower conversion (25 mol %, Table 50) than the modulated examples above, indicating that addition of NPs may not provide significant improvement to warrant use.

Selectivity at the 6 hour point, (70 %), towards the epoxide is improved on the MIL-101(Cr) results detailed previously, with phenylacetaldehyde and benzaldehyde again identified as the by-products, but is only slightly improved to those in Figure 154, again not sufficiently to warrant use of Au NPs. The Au@MIL-101(Cr) activity appears similar to that by Saikia *et al*^[400] with comparable selectivity and conversion towards the epoxide, Table 50.

| Catalyst | T / °C | Catalyst / mol % | t / hrs | Conversion / % | Selectivity / % | Ref |
|----------------------------|-----------------|------------------|---------|----------------|-----------------|-----------|
| Au@MIL-101(Cr) | 70 | 0.021 | 6 | 25 | 70 | This work |
| Au/MIL-101-NH ₂ | 82 ^a | 0.025 | 8 | 29.4 | 78.5 | [400] |

Table 50: Reaction conditions, conversion and selectivity values for styrene epoxidation in acetonitrile by Au NPS on MIL-101(Cr) variants, first entry analysed by ¹H NMR.

^aReflux conditions were stated.

Saikia *et al* reported that the best conversion and selectivity results were observed for the reaction undertaken in toluene. When this was attempted, the oxidation of toluene as well as decane (from TBHP) and mesitylene (the ITSD) were observed in the reaction mixture making the analysis of the reaction challenging and preventing reaction completion as the oxidant was consumed in formation of the by-products. It would appear then that the ability of the MIL-101(Cr) framework is sufficiently high without the need for Au NP addition. Given the initial selectivity is high, it is hoped that the decrease in selectivity over time stems from the conversion of the epoxide to the side products following formation, rather than production of the by-products in the first instance. Thus, when undertaken as a tandem reaction it is hoped that the styrene oxide would react onwards to the carbonate before any side reactions can occur. Future testing of the MIL-101(Cr) systems with an imidazole functionalised, as per Chapter 4, is required and it is anticipated that the tandem reaction of epoxidation followed by sequential CO₂ utilisation would be able to be achieved. It must be noted that the competition between the possible CUS as the site for oxidation but also the site of imidazole binding will need to be considered. However, given the proposed formula of Cr₃F(H₂O)(Melm)O(BDC)₃·nH₂O for MIL-101-Me if a loading of 1 mmol/g is maintained then an equivalent amount of CUS will be maintained.

5.5 Conclusions and Future Work

5.5.1 Oxidation-Knoevenagel

Combination of PVP coated Au NPs and subsequent deposition on UiO-66-NH₂ lead to the formation of Au/UiO-66-NH₂. This hybrid material has been shown to be able to undertake a tandem alcohol oxidation-Knoevenagel condensation reaction. More specifically cinnamyl, benzyl, vanillyl and furfuryl alcohols were able to undergo oxidation selectively to their respective aldehydes followed by Knoevenagel condensation with malononitrile to produce the final products in a single pot, two step manner with high yields (> 78 %) observed for the four products produced. Unfortunately, completion of the reaction in a single step was not shown to be possible with Au/UiO-66-NH₂, as it was seen that the addition of malononitrile (the methylene compound for the condensation step) at the start of the reaction caused the deactivation of the oxidation stage. A number of methods were employed to address this deficiency of the system.

Firstly, distribution of the nanoparticles across the MOF was observed to be non-uniform in nature. Investigation of deposition strategies to improve the dispersion and so site isolation of the nanoparticles led to greater control in the morphology of the MOF and of the dispersion of the nanoparticles across the MOF surface. Au NPs without PVP were demonstrated to produce the most evenly distributed nanoparticles on UiO-66-NH₂ MOF surface and therefore are required to be tested to determine the effect of the increased dispersion and the lack of PVP use on the catalytic activity. Impregnation of the nanoparticles was the rationale behind not employing PVP as the capping agent, further attempts to encourage formation of nanoparticles within the framework should be undertaken as these NPs would be well defined in their size and so should display excellent activity towards the oxidation reaction. In this respect the use of isorecticular UiO-67 may aid impregnation as the larger, 8 Å pore windows may aid entrance of the gold precursor, furthermore UiO-67 maintains the thermal stability seen in UiO-66 but with larger surface area which may aid reactions^[30].

Secondly, other metal nanoparticles, Pt and Pd, were deposited onto the UiO-66 MOF using the same PVP method as for Au NPs. Close control on the size of the nanoparticles was observed with their activity towards the selective oxidation of benzyl alcohol to benzaldehyde shown. It was hoped that these materials, once tested, may facilitate the reaction in a one pot, one step manner, if they do not suffer from the same deactivation, during the oxidation. Additionally, the use of Pd and Pt opens up the materials for use in other reactions such as hydrogenations^[346,386] and so, as shown in Chapter 1, other tandem reactions can be employed using these such as the tandem Knoevenagel-hydrogenation reaction previously discussed.

Therefore, future work should be devoted to fully testing and characterising the un-stabilised Au on the UiO-66-NH₂ MOF in order ensure the continuation of the nanoparticles and MOF properties following use. For this as well as Pt and Pd analogues (when prepared on the amine analogue), malononitrile addition at $t = 0$ should be attempted and therefore allow for lowered reaction times to be achieved. The use of molecular oxygen would be employed for the oxidation stage, given the positive results of other MOF-based reactions for benzyl alcohol oxidation as shown in Chapter 1.

For the second half of the reaction, the Knoevenagel condensation stage has as yet not been optimised. The reason for the fast initial rate of reaction is not fully understood, but given the results shown in this Chapter and with consideration of the literature for this reaction, was believed to involve the formation of an imine upon reaction of the aldehyde with the pendant amine functionalities of the MOF. The KV condensation reaction relies on the amines of the framework for deprotonation of the methylene compound, therefore, given the large numbers that should be present the reaction rate was slower than expected, explainable by the imine formation.

Despite this improved performance for the KV should still be accessible *via* a number of approaches:

1. MOF particle size control;
2. Increase in porosity.

Alteration of the size of the MOF particle changes the surface area to volume ratio. Reaction of the intermediate aldehyde with a methylene compound requires the amine of the linker, which will occur fastest if the aldehyde and methylene have easy access to it. Thus, a situation whereby the reaction is occurring on the surface of the MOF rather than requiring the diffusion of reagents into the pores is desirable. Ideally then, a smaller particle is more desirable as the surface area per unit mass is greatest. Given the MOF particles used in the tandem reactions are already small in size, around 100 nm for the UiO-66-NH₂, it was considered that the size of the particles would be unlikely to be able to be reduced further with increased modulator use as increased MOF sizes were reported by Schaate *et al* with greater amount of benzoic acid use^[82].

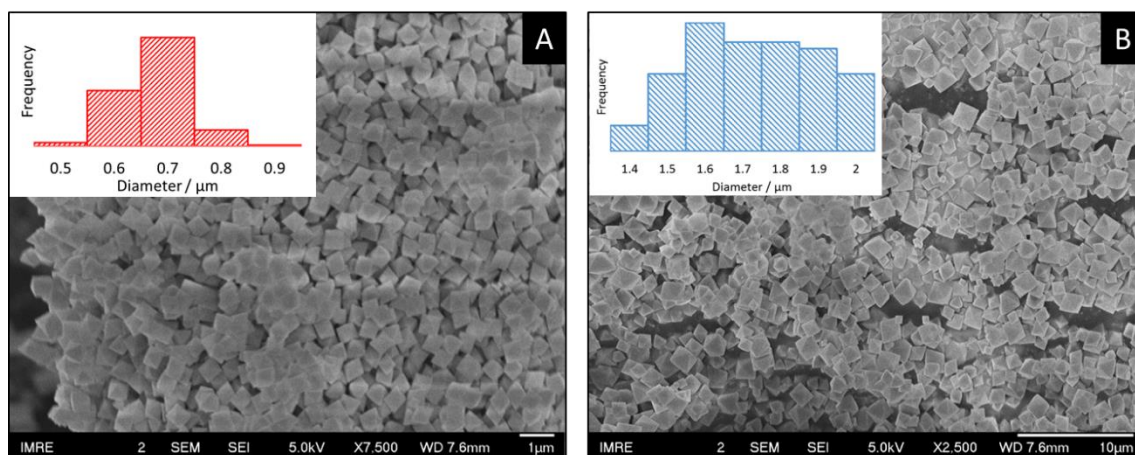


Figure 157: SEM images of UiO-66-NH₂ synthesised with acetic acid (600:1, linker) with A) Triethylamine (TEA) addition (8 mM) and B) no TEA. Measurements of size undertaken on the images shown.

Nevertheless, larger particles were synthesised to determine any correlation. Size modulation was achieved through the use of acetic acid in combination with trimethylamine^[363] and the resulting crystals were produced with well-defined rhombohedral crystals, Figure 157. The sizes produced are distinctly different to one another and the existing size MOF particles, in order to exaggerate any effects on catalysis. It was interesting to note that with such large modulator use the nitrogen adsorption amount was increased, along with surface area, with 862.58 m²/g compared to the values of 779.09 m²/g and 847.84 m²/g for the benzoic acid synthesis for UiO-66-NH₂ and Au/UiO-66-NH₂ (where it was speculated the deposition stage acted as a wash). Therefore use of large amounts of acetic acid modulator in combination with TEA can produce a MOF where access to the framework interior is more achievable by substrates, providing a route to the second point in the above list.

A substrate scope study, with respect to the methylene compound, would be interesting to undertake. It should allow for greater understanding of the influence of the acidity of the methylene protons to be investigated and the reaction mechanism understood in greater detail. Acidity of the protons is related to the side groups of the methylene, CN for malononitrile. It is likely that the greater the acidity of the methylene protons the faster the reaction will occur. This could allow for further investigation of the reaction and lead to determination of why the reaction slows and how the catalyst can be regenerated following use.

5.5.2 Alkene epoxidation-CO₂ utilisation

A second tandem reaction was attempted, namely the conversion of alkenes to cyclic carbonates *via* the epoxide intermediate. MIL-101(Cr) was studied for the epoxidation of styrene and shown

to be able to produce styrene oxide with modulation of the synthesis methodology used shown to be able to improve selectivity towards the epoxide, with 70 % selectivity observed. Given the results of Chapter 4, it is envisaged that a MIL-101(Cr) based material shall be able to be active for both stages of the reaction, now that both halves have been shown to be possible separately.

Future work would aim to combine the two halves and produce cyclic carbonates from CO₂ and alkenes with the use of an oxidant. Furthermore, the Au/UiO-66-NH₂ analogue can also be investigated as this has been extensively characterised and synthesised for the work in the earlier stages of this Chapter. The rationale for this selection comes from the UiO-66-NH₂ framework itself has been shown to be able to undertake the conversion of CO₂ and epoxides by Kim *et al.*^[127] therefore, with the Au NP system already synthesised and characterised it was proposed the tandem reaction displayed in Figure 152 may be possible with this material.

Appendix C

C.1 GC-MS identification of condensation products

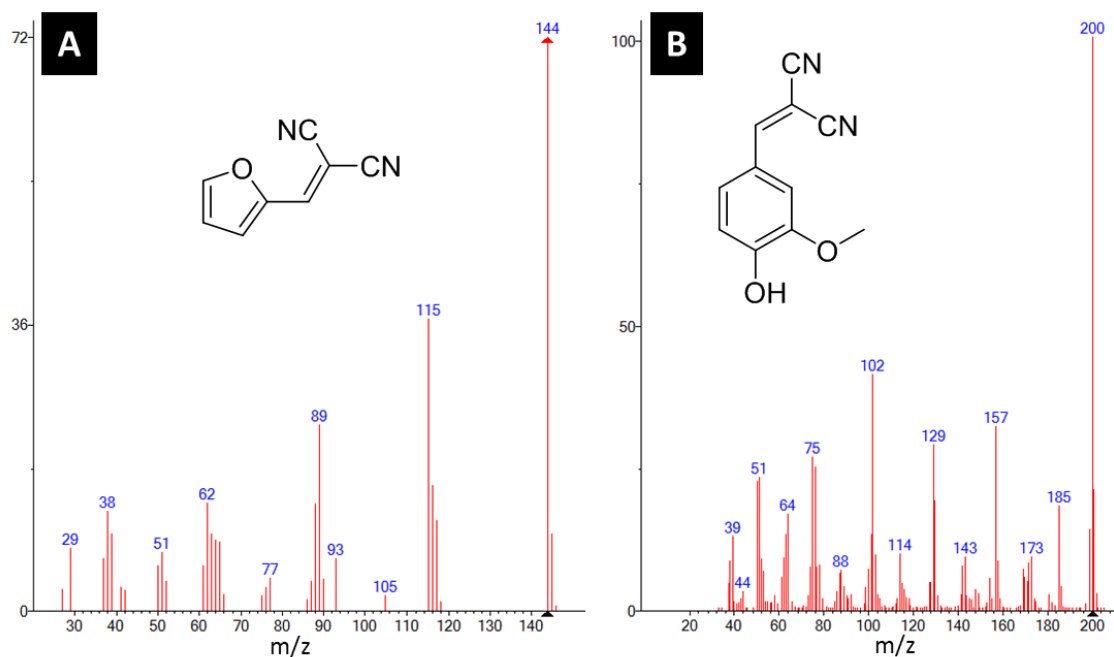


Figure C1: MS of A) condensation product of furfural and B) vanillin.

C.2 Au NPs size distribution images

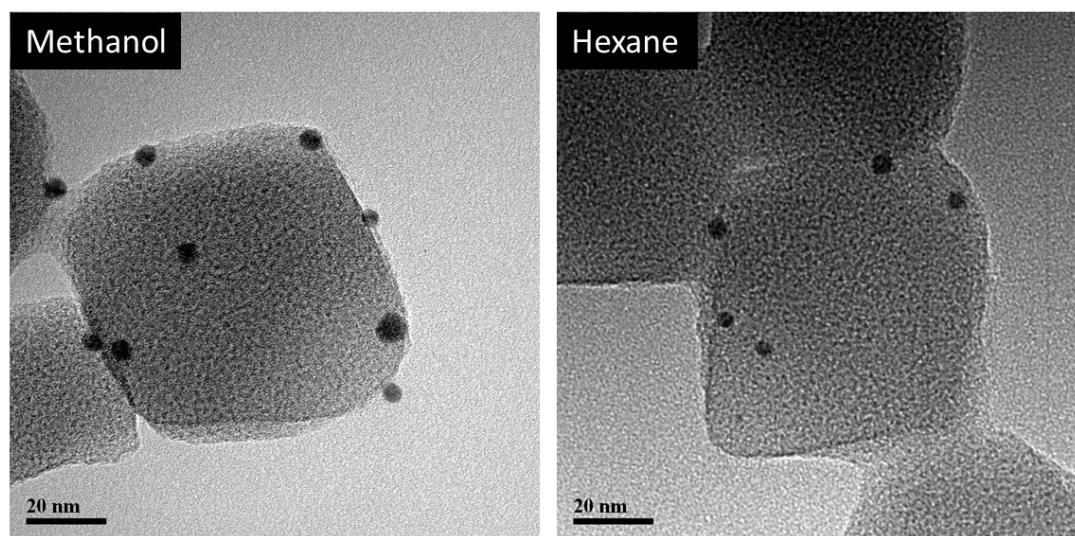


Figure C2: TEM images of Au NPs on UiO-66-NH₂ produced in methanol and hexane at greater resolution to aid NP size determination.

Chapter 6 Summary

The summary serves to evaluate the outcomes of this body of work and detail where further efforts should be addressed. Within each of the results and discussion Chapters (3-5) a conclusions and future work section has been included where the results achieved and the direction in which further work should progress are highlighted in more explicit detail, with reference to literature where applicable. What will follow here is this more generalised summary linking all the work together.

6.1 Harnessing silanols for heterogeneous, organocatalytic CO₂ utilisation

Silanols were shown to be able to be functionalised with a range imidazolium species through a facile covalent anchoring strategy. The created heterogeneous silica-based organocatalysts could catalyse the reaction of epoxides and CO₂ to produce the cyclic carbonate product at high yields with large turnover numbers observed. Extensive characterisation of the materials validated the synthesis approach and detailed the structure of the organic component was retained both upon synthesis and after re-use in a catalytic cycle.

Analogous anchoring of the imidazolium onto HP SAPO-5 showed that the acidity of the framework resulted in the lowering of the previously high selectivity of the silica versions by promotion of the rearrangement of the epoxide to the aldehyde product. Nevertheless, catalytic production of the cyclic carbonate on this more complex support was achieved. Optimisation of the support was undertaken by alteration of the dopant within the framework, *via* type II substitution, and it was shown that the lowering of the framework acidity improved the yield of the cyclic carbonate accordingly, through an increase in the selectivity.

The catalytic activity of the silica-based imidazolium materials was observed to be affected by the loading, imidazole structure, pore diameter and most crucially the halide (anion). The latter was determined to be the active catalytic species in the initiation of the reaction *via* ring-opening of the epoxide and so allowed for the mechanism of action to be stated. Recycle tests displayed significant loss of activity upon re-use of the material but retention of the loading of the organic component was confirmed by post-catalysis characterisation. This led to the development of a method which allowed the silica based imidazolium to rely solely on the organic moiety for catalysis through synthesis of an N-heterocyclic carbene from the anchored imidazolium. Introduction of carbon dioxide formed a stable carboxylate intermediate that was isolated,

characterised and tested for efficacy in the production of cyclic carbonate from CO₂.

Characterisation enabled the presence of the carboxylate to be unequivocally proven, with reversible removal of the CO₂ from the carbene being displayed. Catalytic testing of a range of NHC systems showed high yields of the cyclic carbonate are achievable. Therefore the NHC catalyst enables the undertaking of the CO₂ and epoxide reaction *via* an alternative reaction mechanism to the imidazolium version, whereby carbon dioxide and not the epoxide is activated first and so may provide access to different reactions with carbon dioxide.

6.1.1 Ongoing and Future Work

Future work on the imidazolium species on HP supports should attempt to continue to improve the problems faced with the lowered selectivity observed towards the cyclic carbonate when using this support. After which, the focus should shift towards realising the potential of using this more complex support as it allows multiple functionalities to be introduced. The tandem reaction, suggested in Chapter 3 and Chapter 5, of sequential epoxidation-CO₂ utilisation should be explored and used to highlight the possibility for tandem reactions within these hierarchically porous structures.

The development of the silica based NHC catalysts is still in its infancy with the synthesis, characterisation and catalytic testing requiring greater development. The extent to which the imidazolium is converted to the carboxylate was not quantified during the characterisation, therefore it is not known if the complete deprotonation of the precursor imidazolium was achieved. Furthermore, the retention of the potassium within the silica following the production of the carboxylate was seen and linked to potassium iodide being formed. As a consequence of these two observations, the true catalytic ability of the NHC-CO₂ materials was not able to be conclusively stated as both the unconverted imidazolium and the potassium iodide have the potential to undertake the coupling of CO₂ and epoxides themselves.

Future work should then focus on the refinement of the synthesis method in order to ensure that the complete conversion of the anchored imidazolium species to the NHC-CO₂ is achieved and that the deprotonation step does not produce potassium iodide. Routes to achieving this have been detailed in the above and should be facile to undertake.

6.2 Imidazole functionalised MIL-101(Cr) for enhanced CO₂ utilisation

The work within Chapter 3 demonstrated the effectiveness of imidazole containing materials to act as catalysts for the utilisation of CO₂ in cyclic carbonate synthesis. The introduction of functionalised imidazole species onto a range of different solid supports, beginning with hierarchically porous materials, as discussed above, was continued and led to the use of the coordinatively unsaturated sites within MIL-101(Cr) as handles for imidazole grafting. The resulting MIL-101-Me materials was shown to be a highly active catalyst for the reaction between CO₂ and epoxides, with TOF values of up to 1144 hr⁻¹ calculated. The combination of the imidazole and MIL-101(Cr) resulted in the creation of well-isolated catalytic sites throughout the MOF which were responsible for the significantly improved rate of cyclic carbonate formation, under co-catalyst and solvent-free conditions. Molecular modelling simulations (GCMC and DFT) were complemented with an array of spectroscopic investigations to reveal an improved understanding of the nature of the active sites and the associated catalytic mechanism. The specific binding of the imidazole to the coordinatively unsaturated chromium species was proven and was shown to result in the clustering of the epoxide and CO₂ during catalysis. Therefore, the combination of the imidazole with the CUS of the framework led to the enhancement of the pre-existing CO₂ capture and conversion ability of MIL-101(Cr). It is envisaged that the additional binding site introduced with the functionalised imidazole, allied with the Lewis acid sites, as evidenced from the FT-IR spectroscopic studies, facilitated epoxide activation and by stabilisation of reaction intermediates, leads to the enhanced CO₂ utilisation observed.

6.2.1 Ongoing and Future Work

Recycle studies of the MIL-101(Cr) indicated the loss of activity and framework structure after a number of cycles. Therefore future work should fully characterise the MIL-101-Me material after catalysis to better understand why the framework loses structure after use. If these shortcomings cannot be overcome in MIL-101(Cr) then different MOF structures with CUS as handles for imidazole incorporation can be investigated for efficacy in the reaction. Furthermore, other variants of the MIL series, such as the trimesic acid based MIL-100(Cr), which would be expected to offer similar chemical environment but improved chemical stability during reaction should be attempted to achieve a MOF catalyst capable of re-use over a greater number of successive cycles.

The synthetic approach used in the functionalisation of MIL-101(Cr) therefore offers a large scope for extending the design of MOFs for the chemical fixation of CO₂. For example, the

copolymerisation with epoxides, to afford polycarbonates, has been recently undertaken by Stewart *et al* by building on this work in the use of another MOF within the MIL series^[402].

6.3 Metal Organic Frameworks for use in tandem catalytic reactions

To demonstrate further the ability of MOFs to be carefully designed towards specific catalytic processes, as shown in Chapter 4, their use for two different tandem reactions was demonstrated. For each reaction pairing, the ease of manipulation during and post-synthesis of the MOFs allowed for the multiple functionalities required for the tandem reaction to occur, to be introduced.

In the first cascade reaction studied, the colloidal deposition of gold nanoparticles onto UiO-66-NH₂ was undertaken and the resulting hybrid MOF was able to undertake the conversion of a range of alcohols to their respective aldehyde (using the Au NPs) followed by Knoevenagel condensation with malononitrile (using the amine functionality on the linker). High selectivity towards the aldehyde was displayed by the gold nanoparticles and the amine linker was shown to be effective in the conversion of the aldehyde to the condensation product by acting as a basic functionality for deprotonation of the methylene compound.

Attempts to undertake the reaction *via* one pot, one step route resulted in the deactivation of the oxidation pathway and led to the malononitrile to be required to be added after the oxidation had been completed. A number of methods to overcome this were attempted through alteration of synthesis with respect to the oxidation half of the tandem reaction. The clustering of gold nanoparticles within close proximity of one another was observed to occur during the deposition process. Encapsulation, impregnation and deposition without PVP capping of the nanoparticles was attempted to promote a more uniform distribution of the nanoparticles on the surface of, or throughout the MOF. Additionally, Pt and Pd nanoparticles on UiO-66 were created and employed for the selective oxidation of benzyl alcohol, it was hoped the deactivation observed for gold nanoparticles may be overcome through different MNP use.

The second cascade reaction built on the work of Chapter 4. An epoxidation-CO₂ utilisation reaction was envisaged, based upon the MIL-101-Me material which has been shown to be highly active for the second stage. MIL-101(Cr) was shown to be able to undertake the epoxidation of styrene using TBHP as an oxidant, and improved selectivities were shown when the use of a modulator was employed in the synthesis stage. The possibility of a MIL-101(Cr) based catalyst to undertake the successive epoxidation-CO₂ utilisation tandem reaction has been shown, albeit only in the separate parts at this stage. Nevertheless, it has been demonstrated that another tandem reaction will be able to be undertaken after the careful manipulation of a MOF to tailor the functionality of it.

6.3.1 Ongoing and Future Work

Future work on both of the tandem reactions detailed should concentrate on the completion of both in a single pot, single step manner; where all of the reagents are added at $t = 0$ and the two reactions occur successively without the need for any further addition of reagents or monitoring of the reaction. Once both are able to be undertaken in such a way then optimisation of the processes should be completed. For the oxidation-Knoevenagel, the issues surrounding the suggested formation of an imine between the amine functionalities of the MOF and the aldehyde have not been properly addressed in this work and so need to be studied in greater detail. Once they are fully understood then the optimisation of the Knoevenagel side of the reaction also will result in improvement in the reaction times required.

The scope for tandem reactions catalysed by MOFs is vast and so a wide-array of reactions can be envisaged. Development of MOF based catalysts to complete multiple tandem reactions should be sought owing to the greater efficiency and so more sustainable nature of these system. In some cases the existing materials are present which can continue this work; for example, the Pt/UiO-66 and Pd/UiO-66 analogues can be applied to the isorecticular UiO-66-NH₂ and used in a Knoevenagel-hydrogenation reaction.

References

- [1] J. M. Thomas, W. J. Thomas, *Principles of Heterogeneous Catalysis*, Wiley-VCH Verlag GmbH & Co. KGaA, **2015**.
- [2] A. P. W, D. F. Shriver, *Inorganic Chemistry*, Oxford University Press, **1999**.
- [3] P. Atkins, J. de Paula, *Elements of Physical Chemistry*, Oxford University Press, **2009**.
- [4] R. Masel, *Chemical Kinetics and Catalysis*, A John Wiley & Sons Inc., **2001**.
- [5] E. S. Kolboe, *Focus Catal.* **2002**, 2002, 8.
- [6] G. A. Somorjai, Y. Li, *Introduction to Surface Chemistry and Catalysis*, John Wiley & Sons. Inc., **2010**.
- [7] B. Cornils, W. A. Herrmann, *J. Catal.* **2003**, 216, 23–31.
- [8] J. M. Thomas, R. Raja, D. W. Lewis, *Angew. Chemie - Int. Ed.* **2005**, 44, 6456–6482.
- [9] R. Raja, M. E. Potter, S. H. Newland, *Chem. Commun.* **2014**, 5940–5957.
- [10] G. Rothenberg, in *Kirk-Othmer Encycl. Chem. Technol.*, John Wiley & Sons, Inc., Hoboken, NJ, USA, **2010**, pp. 1–43.
- [11] B. List, R. A. Lerner, C. F. Barbas, *J. Am. Chem. Soc.* **2000**, 122, 2395–2396.
- [12] K. A. Ahrendt, C. J. Borths, D. W. C. MacMillan, *J. Am. Chem. Soc.* **2000**, 122, 4243–4244.
- [13] D. W. C. MacMillan, *Nature* **2008**, 455, 304–308.
- [14] B. List, J. W. Yang, *Science (80-.)*. **2006**, 313, 1584–1586.
- [15] H. Pellissier, *Tetrahedron* **2007**, 63, 9267–9331.
- [16] A. Berkessel, H. Groger, in *Asymmetric Organocatalysis*, Wiley-VCH Verlag GmbH & Co. KGaA, Weinheim, FRG, **2005**, pp. 409–435.
- [17] F. Cozzi, *Adv. Synth. Catal.* **2006**, 348, 1367–1390.
- [18] C. T. Kresge, M. E. Leonowicz, W. J. Roth, J. C. Vartuli, J. S. Beck, *Nature* **1992**, 359, 710–712.
- [19] X. S. Zhao, X. Y. Bao, W. Guo, F. Y. Lee, *Mater. Today* **2006**, 9, 32–39.

- [20] A. P. Wight, M. E. Davis, *Chem. Rev.* **2002**, *102*, 3589–3614.
- [21] D. J. Xuereb, R. Raja, *Catal. Sci. Technol.* **2011**, 517–534.
- [22] D. J. Xuereb, J. Dzierzak, R. Raja, *Catal. Today* **2012**, *198*, 19–34.
- [23] H. Yang, G. Zhang, X. Hong, Y. Zhu, *Microporous Mesoporous Mater.* **2004**, *68*, 119–125.
- [24] M. D. Jones, R. Raja, J. M. Thomas, B. F. G. Johnson, D. W. Lewis, J. Rouzaud, K. D. M. Harris, *Angew. Chemie - Int. Ed.* **2003**, *42*, 4326–4331.
- [25] T. Maschmeyer, F. Rey, G. Sankar, J. M. Thomas, *Nature* **1995**, *378*, 159–162.
- [26] D. Dhar, I. Beadham, S. Chandrasekaran, *Proc. Indian Acad. Sci. (Chem. Sci.)* **2003**, *115*, 365–372.
- [27] F. Calderón, R. Fernández, F. Sánchez, A. Fernández-Mayoralas, *Adv. Synth. Catal.* **2005**, *347*, 1395–1403.
- [28] S. L. James, *Chem. Soc. Rev.* **2003**, *32*, 276.
- [29] O. M. Yaghi, M. O’Keeffe, N. W. Ockwig, H. K. Chae, M. Eddaoudi, J. Kim, *Nature* **2003**, *423*, 705–714.
- [30] J. H. Cavka, U. Olsbye, N. Guillou, S. Bordiga, K. P. Lillerud, S. Jakobsen, U. Olsbye, N. Guillou, C. Lamberti, S. Bordiga, et al., *J. Am. Chem. Soc.* **2008**, *130*, 1–19.
- [31] G. Férey, C. Mellot-Draznieks, C. Serre, F. Millange, J. Dutour, S. Surblé, I. Margiolaki, *Science* **2005**, *309*, 2040–2042.
- [32] P. Z. Moghadam, A. Li, S. B. Wiggin, A. Tao, A. G. P. Maloney, P. A. Wood, S. C. Ward, D. Fairen-Jimenez, *Chem. Mater.* **2017**, *29*, 2618–2625.
- [33] J. L. C. Rowsell, O. M. Yaghi, *Microporous Mesoporous Mater.* **2004**, *73*, 3–14.
- [34] H. Furukawa, K. E. Cordova, M. O’Keeffe, O. M. Yaghi, *Science* **2013**, *341*, 1230444–1230444.
- [35] S. T. Meek, J. A. Greathouse, M. D. Allendorf, *Adv. Mater.* **2011**, *23*, 249–267.
- [36] B. Li, H.-M. Wen, W. Zhou, B. Chen, *J. Phys. Chem. Lett.* **2014**, *5*, 3468–3479.
- [37] J. R. Li, R. J. Kuppler, H. C. Zhou, *Chem. Soc. Rev.* **2009**, *38*, 1477–1504.
- [38] L. J. Murray, D. Mircea, J. R. Long, *Chem Soc Rev* **2009**, *38*, 22.

- [39] K. Sumida, D. L. Rogow, J. A. Mason, T. M. McDonald, E. D. Bloch, Z. R. Herm, T. H. Bae, J. R. Long, *Chem. Rev.* **2012**, *112*, 724–781.
- [40] J. A. Mason, M. Veenstra, J. R. Long, *Chem. Sci.* **2014**, *5*, 32–51.
- [41] D. J. Wales, J. Grand, V. P. Ting, R. D. Burke, K. J. Edler, C. R. Bowen, S. Mintova, A. D. Burrows, *Chem. Soc. Rev.* **2015**, *44*, 4290–4321.
- [42] L. E. Kreno, K. Leong, O. K. Farha, M. Allendorf, R. P. Van Duyne, J. T. Hupp, *Chem. Rev.* **2012**, *112*, 1105–1125.
- [43] D. Bradshaw, A. Garai, J. Huo, *Chem. Soc. Rev.* **2012**, *41*, 2344–2381.
- [44] M. A. Chowdhury, *J. Biomed. Mater. Res. - Part A* **2017**, *105*, 1184–1194.
- [45] P. Horcajada, R. Gref, T. Baati, P. K. Allan, G. Maurin, P. Couvreur, G. Férey, R. E. Morris, C. Serre, *Chem. Rev.* **2012**, *112*, 1232–1268.
- [46] J. Gascon, A. Corma, F. Kapteijn, F. X. Llabre i Xamena, *ACS Catal.* **2014**, *4*, 361–78.
- [47] J. Lee, O. K. Farha, J. Roberts, K. A. Scheidt, S. T. Nguyen, J. T. Hupp, *Chem. Soc. Rev.* **2009**, *38*, 1450–1459.
- [48] A. Corma, H. Garcia, F. X. Llabres i Xamena, *Chem. Rev.* **2010**, *110*, 4606–4655.
- [49] M. Ranocchiari, J. A. van Bokhoven, *Phys. Chem. Chem. Phys.* **2011**, *13*, 6388.
- [50] D. Farrusseng, S. Aguado, C. Pinel, *Angew. Chemie - Int. Ed.* **2009**, *48*, 7502–7513.
- [51] S. M. J. Rogge, A. Bavykina, J. Hajek, H. Garcia, A. I. Olivos-Suarez, A. Sepúlveda-Escribano, A. Vimont, G. Clet, P. Bazin, F. Kapteijn, et al., *Chem. Soc. Rev.* **2017**, *46*, 3134–3184.
- [52] N. V. Maksimchuk, O. V. Zalomaeva, I. Y. Skobelev, K. A. Kovalenko, V. P. Fedin, O. A. Kholdeeva, *Proc. R. Soc. A Math. Phys. Eng. Sci.* **2012**, *468*, 2017–2034.
- [53] J. Liu, L. Chen, H. Cui, J. Zhang, L. Zhang, C.-Y. Su, *Chem. Soc. Rev.* **2014**, *43*, 6011–6061.
- [54] J. Maina, C. Pozo-Gonzalo, L. Kong, J. Schutz, M. R. Hill, L. Dumeé, *Mater. Horiz.* **2017**, *4*, 345–361.
- [55] M. H. Beyzavi, C. J. Stephenson, Y. Liu, O. Karagiari, J. T. Hupp, O. K. Farha, *Front. Energy Res.* **2015**, *2*, 1–10.
- [56] D. Ma, B. Li, K. Liu, X. Zhang, W. Zou, Y. Yang, G. Li, Z. Shi, S. Feng, *J. Mater. Chem. A* **2015**,

3, 23136–23142.

- [57] A. Dhakshinamoorthy, A. M. Asiri, H. Garcia, *Chem. - A Eur. J.* **2016**, *22*, 8012–8024.
- [58] A. Dhakshinamoorthy, A. M. Asiri, H. Garcia, *ACS Catal.* **2017**, *7*, 2896–2919.
- [59] L. Ma, C. Abney, W. Lin, *Chem. Soc. Rev.* **2009**, *38*, 1248.
- [60] Y.-B. Huang, J. Liang, X.-S. Wang, R. Cao, *Chem. Soc. Rev.* **2017**, *46*, 126–157.
- [61] A. Dhakshinamoorthy, H. Garcia, *ChemSusChem* **2014**, 2392–2410.
- [62] N. Kornienko, Y. Zhao, C. S. Kley, C. Zhu, D. Kim, S. Lin, C. J. Chang, O. M. Yaghi, P. Yang, *J. Am. Chem. Soc.* **2015**, *137*, 14129–14135.
- [63] C. A. Downes, S. C. Marinescu, *ChemSusChem* **2017**, *10*, 4374–4392.
- [64] H. Bin Wu, X. W. (David) Lou, *Sci. Adv.* **2017**, *3*, eaap9252.
- [65] H. Zhang, X. Liu, Y. Wu, C. Guan, A. K. Cheetham, J. Wang, *Chem. Commun.* **2018**, *54*, 5268–5288.
- [66] L. Zeng, X. Guo, C. He, C. Duan, *ACS Catal.* **2016**, *6*, 7935–7947.
- [67] Y. Li, H. Xu, S. Ouyang, J. Ye, *Phys. Chem. Chem. Phys.* **2016**, *18*, 7563–7572.
- [68] S. Wang, X. Wang, *Small* **2015**, *11*, 3097–3112.
- [69] X. Yu, L. Wang, S. M. Cohen, A. A. Tahir, Y. Z. Khimyak, P. V. Wiper, J. R. Darwent, M. J. Rosseinsky, M. Bosch, L. Zou, *CrystEngComm* **2017**, *124*, 7558–7562.
- [70] A. Dhakshinamoorthy, A. M. Asiri, H. Garcia, *Catal. Sci. Technol.* **2016**, *6*, 5238–5261.
- [71] P. Valvekens, F. Vermoortele, D. De Vos, *Catal. Sci. Technol.* **2013**, *3*, 1435.
- [72] K. K. Tanabe, S. M. Cohen, *Angew. Chemie - Int. Ed.* **2009**, *48*, 7424–7427.
- [73] M. Fujita, S. Washizu, K. Ogura, Y. J. Kwon, *J. Am. Chem. Soc.* **1994**, *116*, 1151–1152.
- [74] L. Alaerts, E. Séguin, H. Poelman, F. Thibault-Starzyk, P. A. Jacobs, D. E. De Vos, *Chem. - A Eur. J.* **2006**, *12*, 7353–7363.
- [75] D. Y. Hong, Y. K. Hwang, C. Serre, G. Férey, J. S. Chang, *Adv. Funct. Mater.* **2009**, *19*, 1537–1552.
- [76] S. Bhattacharjee, C. Chen, W.-S. Ahn, *RSC Adv.* **2014**, *4*, 52500–52525.

- [77] U. Mueller, M. Schubert, F. Teich, H. Puetter, K. Schierle-Arndt, J. Pastré, *J. Mater. Chem.* **2006**, *16*, 626–636.
- [78] A. U. Czaja, N. Trukhan, U. Müller, *Chem. Soc. Rev.* **2009**, *38*, 1284.
- [79] S. Yuan, L. Feng, K. Wang, J. Pang, M. Bosch, C. Lollar, Y. Sun, J. Qin, X. Yang, P. Zhang, et al., *Adv. Mater.* **2018**, *1704303*, 1–35.
- [80] K. S. Park, Z. Ni, A. P. Côté, J. Y. Choi, R. Huang, F. J. Uribe-Romo, H. K. Chae, M. O’Keeffe, O. M. Yaghi, *Proc. Natl. Acad. Sci. U. S. A.* **2006**, *103*, 10186–91.
- [81] A. U. Czaja, N. Trukhan, U. Müller, *Chem. Soc. Rev.* **2009**, *38*, 1284–1293.
- [82] A. Schaate, P. Roy, A. Godt, J. Lippke, F. Waltz, M. Wiebcke, P. Behrens, *Chem. - A Eur. J.* **2011**, *17*, 6643–6651.
- [83] S. M. Cohen, *Chem. Rev.* **2012**, *112*, 970–1000.
- [84] S. J. Garibay, S. M. Cohen, *Chem. Commun.* **2010**, *46*, 7700–7702.
- [85] J. Sun, G. Yu, Q. Huo, Q. Kan, J. Guan, *RSC Adv.* **2014**, *4*, 38048.
- [86] M. Kim, J. F. Cahill, H. Fei, K. A. Prather, S. M. Cohen, *J. Am. Chem. Soc.* **2012**, *134*, 18082–18088.
- [87] C. M. Friend, B. Xu, *Acc. Chem. Res.* **2017**, *50*, 517–521.
- [88] M. Lancaster, *Green Chemistry: An Introductory Text*, Royal Society Of Chemistry, Cambridge, **2002**.
- [89] J. Warner, P. Anastas, *Green Chemistry: Theory and Practice*, **1998**.
- [90] S. L. Y. Tang, R. L. Smith, M. Poliakoff, *Green Chem.* **2005**, *7*, 761.
- [91] R. A. Sheldon, *Comptes Rendus l’Académie des Sci. - Ser. IIC - Chem.* **2000**, *3*, 541–551.
- [92] A. Corma, H. Garcia, *Top. Catal.* **2008**, *48*, 8–31.
- [93] D. J. Cole-Hamilton, *Science* **2003**, *299*, 1702–1706.
- [94] G. Ertl, H. Knozinger, J. Weitkamp, *Preparation of Solid Catalysts*, Wiley-VCH Verlag GmbH & Co. KGaA, **1999**.
- [95] M. Besson, *Fine Chemicals through Heterogeneous Catalysis*, Wiley-VCH Verlag GmbH & Co. KGaA, **2001**.

- [96] M. Bowker, *The Basis and Applications of Heterogeneous Catalysis*, **1998**.
- [97] M. Mikkelsen, M. Jørgensen, F. C. Krebs, *Energy Environ. Sci.* **2010**, *3*, 43–81.
- [98] N. Homs, J. Toyir, P. Ramirez De La Piscina, in *New Future Developments in Catalytic Activation of Carbon Dioxide* (Ed.: S.L. Suib), Elsevier, **2013**, pp. 1–23.
- [99] Y. Toda, H. Hirayama, N. Kuganathan, A. Torrisi, P. V. Sushko, H. Hosono, *Nat. Commun.* **2013**, *4*, 1–8.
- [100] H.-J. Freund, M. W. Roberts, *Surf. Sci. Rep.* **1996**, *25*, 225–273.
- [101] S. Foltran, R. Mereau, T. Tassaing, *Catal. Sci. Technol.* **2014**, *4*, 1585.
- [102] C. J. Whiteoak, A. Nova, F. Maseras, A. W. Kleij, *ChemSusChem* **2012**, *5*, 2032–2038.
- [103] J.-Q. Wang, K. Dong, W.-G. Cheng, J. Sun, S.-J. Zhang, *Catal. Sci. Technol.* **2012**, *2*, 1480.
- [104] C.-H. Guo, H.-S. Wu, X.-M. Zhang, J.-Y. Song, X. Zhang, *J. Phys. Chem. A* **2009**, *113*, 6710–6723.
- [105] M. North, R. Pasquale, C. Young, *Green Chem.* **2010**, *12*, 1514.
- [106] M. Alves, B. Grignard, R. Mereau, C. Jerome, T. Tassaing, C. Detrembleur, *Catal. Sci. Technol.* **2017**, *7*, 2651–2684.
- [107] T. Sakakura, J. C. Choi, H. Yasuda, *Chem. Rev.* **2007**, *107*, 2365–2387.
- [108] B. Schöffner, F. Schöffner, S. P. Verevkin, A. Börner, *Chem. Rev.* **2010**, *110*, 4554–4581.
- [109] R. Zevenhoven, S. Eloneva, S. Teir, *Catal. Today* **2006**, *115*, 73–79.
- [110] A.-A. G. Shaikh, S. Sivaram, *Chem. Rev.* **1996**, *96*, 951–976.
- [111] P. G. Bruce, S. A. Freunberger, L. J. Hardwick, J.-M. Tarascon, *Nat. Mater.* **2011**, *11*, 172–172.
- [112] J. H. Clements, *Ind. Eng. Chem. Res.* **2003**, *42*, 663–674.
- [113] C. H. Van Vegeten, K. A. J. B. Ten, G. M. T. De Less, *Process for the Preparation of Cyclic Organic Carbonates*, **2013**, WO2013189861 A1.
- [114] Y. Wang, D. J. Darensbourg, *Coord. Chem. Rev.* **2018**, *372*, 85–100.
- [115] G. Trott, P. K. Saini, C. K. Williams, *Phil. Trans. R. Soc. A* **2016**, *374*.

- [116] D. J. Darensbourg, *Chem. Rev.* **2007**, *107*, 2388–2410.
- [117] D. J. Darensbourg, R. M. Mackiewicz, A. L. Phelps, D. R. Billodeaux, *Acc. Chem. Res.* **2004**, *37*, 836–844.
- [118] D. J. Darensbourg, M. W. Holtcamp, *Coord. Chem. Rev.* **1996**, *153*, 155–174.
- [119] C. Martín, G. Fiorani, A. W. Kleij, *ACS Catal.* **2015**, *5*, 1353–1370.
- [120] P. K. Saini, C. Romain, C. K. Williams, *Chem. Commun.* **2014**, *50*, 4164–7.
- [121] F. Jutz, A. Buchard, M. R. Kember, S. B. Fredriksen, C. K. Williams, *J. Am. Chem. Soc.* **2011**, *133*, 17395–17405.
- [122] G. Fiorani, W. Guo, A. W. Kleij, *Green Chem.* **2015**, *17*, 1375–1389.
- [123] M. North, R. Pasquale, *Angew. Chemie - Int. Ed.* **2009**, *48*, 2946–2948.
- [124] C. Martín, G. Fiorani, A. W. Kleij, *ACS Catal.* **2015**, *5*, 1353–1370.
- [125] H. Büttner, L. Longwitz, J. Steinbauer, C. Wulf, T. Werner, *Top. Curr. Chem.* **2017**, *375*.
- [126] J. Song, Z. Zhang, S. Hu, T. Wu, T. Jiang, B. Han, *Green Chem.* **2009**, *11*, 1031.
- [127] J. Kim, S. N. Kim, H. G. Jang, G. Seo, W. S. Ahn, *Appl. Catal. A Gen.* **2013**, *453*, 175–180.
- [128] W. Y. Gao, Y. Chen, Y. Niu, K. Williams, L. Cash, P. J. Perez, L. Wojtas, J. Cai, Y. S. Chen, S. Ma, *Angew. Chemie Int. Ed.* **2014**, *53*, 2615–2619.
- [129] L. Liu, S. M. Wang, Z. B. Han, M. Ding, D. Q. Yuan, H. L. Jiang, *Inorg. Chem.* **2016**, *55*, 3558–3565.
- [130] O. V. Zalomaeva, A. M. Chibiryaev, K. A. Kovalenko, O. A. Kholdeeva, B. S. Balzhinimaev, V. P. Fedin, *J. Catal.* **2013**, *298*, 179–185.
- [131] P. Z. Li, X. J. Wang, J. Liu, J. S. Lim, R. Zou, Y. Zhao, *J. Am. Chem. Soc.* **2016**, *138*, 2142–2145.
- [132] G.-Y. Hwang, R. Roshan, H.-S. Ryu, H.-M. Jeong, S. Ravi, M.-I. Kim, D.-W. Park, *J. CO2 Util.* **2016**, *15*, 123–130.
- [133] H.-H. Wang, L. Hou, Y.-Z. Li, C.-Y. Jiang, Y.-Y. Wang, Z. Zhu, *ACS Appl. Mater. Interfaces* **2017**, *9*, 17969–17976.
- [134] Y. H. Han, Z. Y. Zhou, C. Bin Tian, S. W. Du, *Green Chem.* **2016**, *18*, 4086–4091.
- [135] D. A. Yang, H. Y. Cho, J. Kim, S. T. Yang, W. S. Ahn, *Energy Environ. Sci.* **2012**, *5*, 6465–6473.

- [136] H. Y. Cho, D. A. Yang, J. Kim, S. Y. Jeong, W. S. Ahn, *Catal. Today* **2012**, *185*, 35–40.
- [137] M. H. Beyzavi, R. C. Klet, S. Tussupbayev, J. Borycz, N. A. Vermeulen, C. J. Cramer, J. F. Stoddart, J. T. Hupp, O. K. Farha, *J. Am. Chem. Soc.* **2014**, *136*, 15861–15864.
- [138] Z. Zhou, C. He, J. Xiu, L. Yang, C. Duan, *J. Am. Chem. Soc.* **2015**, *137*, 15066–15069.
- [139] M. Zhu, D. Srinivas, S. Bhogeswararao, P. Ratnasamy, M. A. Carreon, *Catal. Commun.* **2013**, *32*, 36–40.
- [140] L. Yang, L. Yu, G. Diao, M. Sun, G. Cheng, S. Chen, *J. Mol. Catal. A Chem.* **2014**, *392*, 278–283.
- [141] X. H. Ji, N. N. Zhu, J. G. Ma, P. Cheng, *Dalt. Trans.* **2018**, *47*, 1768–1771.
- [142] J. Liang, Y.-Q. Xie, X.-S. Wang, Q. Wang, T.-T. Liu, Y.-B. Huang, R. Cao, *Chem. Commun.* **2018**, *54*, 342–345.
- [143] S. Senthilkumar, M. S. Maru, R. S. Somani, H. C. Bajaj, S. Neogi, *Dalt. Trans.* **2018**, *47*, 418–428.
- [144] M. Nourian, F. Zadehahmadi, R. Kardanpour, S. Tangestaninejad, M. Moghadam, V. Mirkhani, I. Mohammadpoor-Baltork, M. Bahadori, *Catal. Commun.* **2017**, *94*, 42–46.
- [145] L. Tang, S. Zhang, Q. Wu, X. Wang, H. Wu, Z. Jiang, *J. Mater. Chem. A* **2018**, *00*, 1–10.
- [146] Z. Xue, J. Jiang, M.-G. Ma, M.-F. Li, T. Mu, *ACS Sustain. Chem. Eng.* **2017**, *5*, 2623–2631.
- [147] L. G. Ding, B. J. Yao, W. L. Jiang, J. T. Li, Q. J. Fu, Y. A. Li, Z. H. Liu, J. P. Ma, Y. Bin Dong, *Inorg. Chem.* **2017**, *54*.
- [148] J. Liang, R.-P. Chen, X.-Y. Wang, T.-T. Liu, X.-S. Wang, Y.-B. Huang, R. Cao, *Chem. Sci.* **2017**, *8*, 1570–1575.
- [149] F.-X. Felpin, E. Fouquet, *ChemSusChem* **2008**, *1*, 718–724.
- [150] M. J. Climent, A. Corma, S. Iborra, M. J. Sabater, *ACS Catal.* **2014**, *4*, 870–891.
- [151] T. Ishida, M. Nagaoka, T. Akita, M. Haruta, *Chem. - A Eur. J.* **2008**, *14*, 8456–8460.
- [152] T. Toyao, M. Saito, Y. Horiuchi, M. Matsuoka, *Catal. Sci. Technol.* **2014**, *4*, 625.
- [153] H. Liu, Y. Li, H. Jiang, C. Vargas, R. Luque, *Chem. Commun.* **2012**, *48*, 8431.
- [154] J. Perles, N. Snejko, M. Iglesias, M. Á. Monge, *J. Mater. Chem.* **2009**, *19*, 6504.

- [155] T. Toyao, M. Fujiwaki, Y. Horiuchi, M. Matsuoka, *RSC Adv.* **2013**, 3, 21582.
- [156] M. Zhao, K. Deng, L. He, Y. Liu, G. Li, H. Zhao, Z. Tang, *J. Am. Chem. Soc.* **2014**, 136, 1738–1741.
- [157] A. M. Rasero-Almansa, A. Corma, M. Iglesias, F. Sánchez, *ChemCatChem* **2013**, 5, 3092–3100.
- [158] T. T. Dang, Y. Zhu, S. C. Ghosh, A. Chen, C. L. L. Chai, A. M. Seayad, *Chem. Commun.* **2012**, 48, 1805.
- [159] F. G. Cirujano, F. X. Llabrés i Xamena, A. Corma, *Dalt. Trans.* **2012**, 41, 4249.
- [160] C. Rösler, R. A. Fischer, *CrystEngComm* **2015**, 17, 199–217.
- [161] M. Haruta, M. Daté, *Appl. Catal. A Gen.* **2001**, 222, 427–437.
- [162] S. K. Hashmi, G. J. Hutchings, *Angew. Chemie - Int. Ed.* **2006**, 45, 7896–936.
- [163] C. Della Pina, E. Falletta, L. Prati, M. Rossi, *Chem. Soc. Rev.* **2008**, 37, 2077–2095.
- [164] M. Haruta, *Nature* **2005**, 437, 1098–1099.
- [165] G. J. Hutchings, *ACS Cent. Sci.* **2018**, acscentsci.8b00306.
- [166] R. J. White, R. Luque, V. L. Budarin, J. H. Clark, D. J. Macquarrie, *Chem. Soc. Rev.* **2009**, 38, 481–494.
- [167] J. M. Campelo, D. Luna, R. Luque, J. M. Marinas, A. a. Romero, *ChemSusChem* **2009**, 2, 18–45.
- [168] G. Bond, D. Thompson, *Gold Bull.* **2000**, 33, 41–50.
- [169] G. C. Bond, C. Lious, D. T. Thompson, *Catalysis by Gold*, Imperial College Press, **2007**.
- [170] W. Choi, H. Song, in *Gold Nanoparticles Physics, Chem. Biol.*, World Scientific (Europe), **2017**, pp. 165–200.
- [171] G. C. Bond, in *Gold Nanoparticles Physics, Chem. Biol.*, IMPERIAL COLLEGE PRESS, **2012**, pp. 171–197.
- [172] M. Haruta, *Faraday Discuss.* **2011**, 152, 11–32.
- [173] A. Abad, A. Corma, H. García, *Chem. A Eur. J.* **2008**, 14, 212–222.
- [174] C. S. Hinde, S. Van Aswegen, G. Collins, J. D. Holmes, T. S. A. Hor, R. Raja, *Dalton Trans.*

2013, 42, 12600–5.

- [175] C. S. Hinde, D. Ansovini, P. P. Wells, G. Collins, S. Van Aswegen, J. D. Holmes, T. S. A. Hor, R. Raja, *ACS Catal.* **2015**, 5, 3807–3816.
- [176] T. Mallat, A. Baiker, *Chem. Rev.* **2004**, 104, 3037–3058.
- [177] A. Abad, P. Concepción, A. Corma, H. García, *Angew. Chemie - Int. Ed.* **2005**, 44, 4066–4069.
- [178] A. Corma, H. Garcia, *Chem. Soc. Rev.* **2008**, 37, 2096.
- [179] A. Barau, V. Budarin, A. Caragheorgheopol, R. Luque, D. J. Macquarrie, A. Prella, V. S. Teodorescu, M. Zaharescu, *Catal. Letters* **2008**, 124, 204–214.
- [180] N. R. Jana, L. Gearheart, C. J. Murphy, *Langmuir* **2001**, 17, 6782–6786.
- [181] M. Brust, J. Fink, D. Bethell, D. J. Schiffrin, C. Kiely, *J. Chem. Soc. Chem. Commun.* **1995**, 1655.
- [182] X. Fang, H. Ma, S. Xiao, M. Shen, R. Guo, X. Cao, X. Shi, *J. Mater. Chem.* **2011**, 21, 4493.
- [183] N. G. Bastús, J. Comenge, V. Puntès, *Langmuir* **2011**, 27, 11098–11105.
- [184] J. Kimling, M. Maier, B. Okenve, V. Kotaidis, H. Ballot, A. Plech, *J. Phys. Chem. B* **2006**, 110, 15700–15707.
- [185] J. Turkevich, P. C. Stevenson, J. Hillier, *Discuss. Faraday Soc.* **1951**, 11, 55.
- [186] S. D. Perrault, W. C. W. Chan, *J. Am. Chem. Soc.* **2009**, 131, 17042–17043.
- [187] H. Song, R. Rioux, J. Hoefelmeyer, R. Komor, K. Niesz, *J. Am. Chem. Soc.* **2006**, 126, 3027–3037.
- [188] W. Hou, N. A. Dehm, R. W. J. Scott, *J. Catal.* **2008**, 253, 22–27.
- [189] D. Seo, J. C. Park, H. Song, *J. Am. Chem. Soc.* **2006**, 128, 14863–14870.
- [190] D. Seo, C. Il Yoo, I. S. Chung, S. M. Park, S. Ryu, H. Song, *J. Phys. Chem. C* **2008**, 112, 2469–2475.
- [191] A. S. Sharma, H. Kaur, D. Shah, *RSC Adv.* **2016**, 6, 28688–28727.
- [192] Q. Yang, Q. Xu, H.-L. Jiang, *Chem. Soc. Rev.* **2017**, 46, 4774–4808.
- [193] M. Meilikhov, K. Yusenko, D. Esken, S. Turner, G. Van Tendeloo, R. A. Fischer, *Eur. J. Inorg.*

- Chem.* **2010**, 3701–3714.
- [194] D. Esken, S. Turner, O. I. Lebedev, G. Van Tendeloo, R. A. Fischer, *Chem. Mater.* **2010**, *22*, 6393–6401.
- [195] M. Müller, S. Turner, O. I. Lebedev, Y. Wang, G. Van Tendeloo, R. A. Fischer, *Eur. J. Inorg. Chem.* **2011**, *5*, 1876–1887.
- [196] H. Liu, Y. Liu, Y. Li, Z. Tang, H. Jiang, *J. Phys. Chem. C* **2010**, *114*, 13362–13369.
- [197] J. Juan-Alcañiz, J. Ferrando-Soria, I. Luz, P. Serra-Crespo, E. Skupien, V. P. Santos, E. Pardo, F. X. Llabrés I Xamena, F. Kapteijn, J. Gascon, *J. Catal.* **2013**, *307*, 295–304.
- [198] J. Zhu, P. C. Wang, M. Lu, *Appl. Catal. A Gen.* **2014**, *477*, 125–131.
- [199] K. Leus, P. Concepcion, M. Vandichel, M. Meledina, A. Grirrane, D. Esquivel, S. Turner, D. Poelman, M. Waroquier, V. Van Speybroeck, et al., *RSC Adv.* **2015**, *5*, 22334–22342.
- [200] Y. Luan, Y. Qi, H. Gao, N. Zheng, G. Wang, *J. Mater. Chem. A* **2014**, *2*, 20588–20596.
- [201] Z. Gu, L. Chen, B. Duan, Q. Luo, J. Liu, C. Duan, *Chem. Commun.* **2016**, *52*, 116–119.
- [202] F. Medina, C. Michon, F. Agbossou-Niedercorn, *European J. Org. Chem.* **2012**, *2012*, 6218–6227.
- [203] J. Liu, J. Chen, J. Zhao, Y. Zhao, L. Li, H. Zhang, *Synthesis (Stuttg.)* **2003**, 2661–2666.
- [204] D. Jiang, A. D. Burrows, K. J. Edler, *CrystEngComm* **2011**, *13*, 6916.
- [205] Y. K. Hwang, D.-Y. Hong, J.-S. Chang, S. H. Jhung, Y.-K. Seo, J. Kim, A. Vimont, M. Daturi, C. Serre, G. Férey, *Angew. Chemie - Int. Ed.* **2008**, *47*, 4144–4148.
- [206] S. B. Dassault, **n.d.**
- [207] S. Grimme, *J. Comput. Chem.* **2006**, *27*, 1787–1799.
- [208] M. B. H. Ketko, J. Rafferty, J. I. Siepmann, J. J. Potoff, *Fluid Phase Equilib.* **2008**, *274*, 44–49.
- [209] Y. F. Chen, R. Babarao, S. I. Sandler, J. W. Jiang, *Langmuir* **2010**, *26*, 8743–8750.
- [210] C. Hammond, *The Basics of Crystallography and Diffraction*, Oxford University Press, **2015**.
- [211] K. S. W. Sing, *Pure Appl. Chem.* **1985**, *57*, 603–619.
- [212] M. Thommes, K. Kaneko, A. V. Neimark, J. P. Olivier, F. Rodriguez-Reinoso, J. Rouquerol, K. S. W. Sing, *Pure Appl. Chem.* **2015**, *87*.

- [213] M. Thommes, K. A. Cychoz, *Adsorption* **2014**, *20*, 233–250.
- [214] S. Brunauer, P. H. Emmett, E. Teller, *J. Am. Chem. Soc.* **1938**, *60*, 309–319.
- [215] G. Attard, C. Barnes, *Surfaces*, Oxford University Press, **1998**.
- [216] S. Lowell, J. E. Shields, M. A. Thomas, M. Thommes, **2004**, pp. 58–81.
- [217] J. Rouquerol, P. Llewellyn, F. Rouquerol, *Stud. Surf. Sci. Catal.* **2007**, *160*, 49–56.
- [218] M. Weller, T. Overton, J. Rourke, F. Armstrong, *Inorganic Chemistry*, Oxford University Press, **2014**.
- [219] A. J. Foster, R. F. Lobo, *Chem. Soc. Rev* **2010**, *39*, 4783–4793.
- [220] M. Hunger, J. Weitkamp, *Angew. Chemie Int. Ed.* **2001**.
- [221] N. Baccile, F. Babonneau, *Microporous Mesoporous Mater.* **2008**, *110*, 534–542.
- [222] M. T. Weller, N. A. Young, *Characterisation Methods in Inorganic Chemistry*, Oxford University Press, **2017**.
- [223] D. Scarano, G. Spoto, S. Bordiga, L. Carnelli, G. Ricchiardi, A. Zecchina, *Langmuir* **1994**, *10*, 3094–3104.
- [224] S. M. Chavan, G. C. Shearer, S. Svelle, U. Olsbye, F. Bonino, J. Ethiraj, K. P. Lillerud, S. Bordiga, *Inorg. Chem.* **2014**, *53*, 9509–9515.
- [225] W. Haiss, N. T. K. Thanh, J. Aveyard, D. G. Fernig, *Anal. Chem.* **2007**, *79*, 4215–4221.
- [226] A. G. Pelmenschikov, R. A. van Santen, J. Janchen, E. Meijer, *J. Phys. Chem.* **1993**, *97*, 11071–11074.
- [227] O. Fesenko, L. Yatsenko, M. Brodin, Eds. , *Nanomaterials Imaging Techniques, Surface Studies, and Applications*, Springer New York, New York, NY, **2013**.
- [228] H. Zhou, Y.-M. Wang, W.-Z. Zhang, J.-P. Qu, X.-B. Lu, *Green Chem.* **2011**, *13*, 644.
- [229] M. Kandiah, S. Usseglio, S. Svelle, U. Olsbye, K. P. Lillerud, M. Tilset, *J. Mater. Chem.* **2010**, *20*, 9848–9851.
- [230] O. D. Sparkman, Z. Penton, F. G. Kitson, *Gas Chromatography and Mass Spectrometry*, Elsevier, **2011**.
- [231] E. de Hoffmann, in *Kirk-Othmer Encycl. Chem. Technol.*, John Wiley & Sons, Inc., Hoboken,

- NJ, USA, **2005**.
- [232] A. Lund, M. Shiotani, S. Shimada, *Principles and Applications of ESR Spectroscopy*, Springer Netherlands, Dordrecht, **2011**.
- [233] D. Goldfarb, S. Stoll, Eds. , *EPR Spectroscopy: Fundamentals and Methods*, John Wiley & Sons Ltd., **2018**.
- [234] M. Cokoja, M. E. Wilhelm, M. H. Anthofer, W. A. Herrmann, F. E. Kühn, *ChemSusChem* **2015**, *8*, 2436–2454.
- [235] Y. Xiong, F. Bai, Z. Cui, N. Guo, R. Wang, *J. Chem.* **2013**, *2013*.
- [236] Q. W. Song, L. N. He, J. Q. Wang, H. Yasuda, T. Sakakura, *Green Chem.* **2013**, *15*, 110–115.
- [237] T. Sakai, Y. Tsutsumi, T. Ema, *Green Chem.* **2008**, *10*, 337–34.
- [238] T. Takahashi, T. Watahiki, S. Kitazume, H. Yasuda, T. Sakakura, *Chem. Commun.* **2006**, 1664–1666.
- [239] Y. Xiong, Y. Wang, H. Wang, R. Wang, *Polym. Chem.* **2011**, *2*, 2306.
- [240] Y. Xiong, H. Wang, R. Wang, Y. Yan, B. Zheng, Y. Wang, *Chem. Commun.* **2010**, *46*, 3399.
- [241] Y. P. Patil, P. J. Tambade, S. R. Jagtap, B. M. Bhanage, *J. Mol. Catal. A Chem.* **2008**, *289*, 14–21.
- [242] Y. Du, F. Cai, D. L. Kong, L. N. He, *Green Chem.* **2005**, *7*, 518–523.
- [243] Y. Zhao, J. S. Tian, X. H. Qi, Z. N. Han, Y. Y. Zhuang, L. N. He, *J. Mol. Catal. A Chem.* **2007**, *271*, 284–289.
- [244] S. Udayakumar, S. W. Park, D. W. Park, B. S. Choi, *Catal. Commun.* **2008**, *9*, 1563–1570.
- [245] X. Chen, J. Sun, J. Wang, W. Cheng, *Tetrahedron Lett.* **2012**, *53*, 2684–2688.
- [246] J. Q. Wang, D. L. Kong, J. Y. Chen, F. Cai, L. N. He, *J. Mol. Catal. A Chem.* **2006**, *249*, 143–148.
- [247] J. Tharun, D. W. Kim, R. Roshan, Y. Hwang, D. W. Park, *Catal. Commun.* **2013**, *31*, 62–65.
- [248] V. Besse, N. Illy, G. David, S. Caillol, B. Boutevin, *ChemSusChem* **2016**, *9*, 2167–2173.
- [249] A. Corma, V. Fornes, M. T. Navarro, J. Perezpariente, *J. Catal.* **1994**, *148*, 569–574.
- [250] Q. W. Song, Z. H. Zhou, L. N. He, *Green Chem.* **2017**, *19*, 3707–3728.

- [251] F. Jutz, J. M. Andanson, A. Baiker, *Chem. Rev.* **2011**, *111*, 322–353.
- [252] J. Peng, Y. Deng, *New J. Chem.* **2001**, *25*, 639–641.
- [253] K. R. Roshan, G. Mathai, J. Kim, J. Tharun, G. A. Park, D. W. Park, *Green Chem.* **2012**, *14*, 2933–2940.
- [254] H. J. Choi, M. Selvaraj, D. W. Park, *Chem. Eng. Sci.* **2013**, *100*, 242–248.
- [255] J. Sun, J. Wang, W. Cheng, J. Zhang, X. Li, S. Zhang, Y. She, *Green Chem.* **2012**, *14*, 654–660.
- [256] Y. Xie, Z. Zhang, T. Jiang, J. He, B. Han, T. Wu, K. Ding, *Angew. Chemie Int. Ed.* **2007**, *46*, 7255–7258.
- [257] R. A. Watile, K. M. Deshmukh, K. P. Dhake, B. M. Bhanage, *Catal. Sci. Technol.* **2012**, *2*, 1051.
- [258] X. Zhang, D. Su, L. Xiao, W. Wu, *J. CO₂ Util.* **2017**, *17*, 37–42.
- [259] W. Zhang, Q. Wang, H. Wu, P. Wu, M. He, *Green Chem.* **2014**, *16*, 4767–4774.
- [260] S. H. Newland, D. J. Xuereb, E. Gianotti, L. Marchese, R. Rios, R. Raja, *Catal. Sci. Technol.* **2015**, *5*, 660–665.
- [261] C. Aprile, F. Giacalone, P. Agrigento, L. F. Liotta, J. A. Martens, P. P. Pescarmona, M. Gruttadauria, *ChemSusChem* **2011**, *4*, 1830–1837.
- [262] S. Udayakumar, V. Raman, H. L. Shim, D. W. Park, *Appl. Catal. A Gen.* **2009**, *368*, 97–104.
- [263] J. N. Appaturi, F. Adam, *Appl. Catal. B Environ.* **2013**, *136-137*, 150–159.
- [264] S. Udayakumar, M.-K. Lee, H.-L. Shim, D.-W. Park, *Appl. Catal. A Gen.* **2009**, *365*, 88–95.
- [265] J. Wang, J. Leong, Y. Zhang, *Green Chem.* **2014**, *16*, 4515–4519.
- [266] J. Q. Wang, X. D. Yue, F. Cai, L. N. He, *Catal. Commun.* **2007**, *8*, 167–172.
- [267] O. Martínez-Ferraté, G. Chacón, F. Bernardi, T. Grehl, P. Brünner, J. Dupont, *Catal. Sci. Technol.* **2018**, *8*, 3081–3089.
- [268] A. S. Aquino, F. L. Bernard, J. V. Borges, L. Mafra, F. D. Vecchia, M. O. Vieira, R. Ligabue, M. Seferin, V. V. Chaban, E. J. Cabrita, et al., *RSC Adv.* **2015**, *5*, 64220–64227.
- [269] Q. Su, Y. Qi, X. Yao, W. Cheng, L. Dong, S. Chen, S. Zhang, *Green Chem.* **2018**, *20*, 3232–3241.

- [270] M. Sankar, T. G. Ajithkumar, G. Sankar, P. Manikandan, *Catal. Commun.* **2015**, *59*, 201–205.
- [271] M. H. Anthofer, M. E. Wilhelm, M. Cokoja, M. Drees, W. A. Herrmann, F. E. Kühn, *ChemCatChem* **2015**, *7*, 94–98.
- [272] M. E. Wilhelm, M. H. Anthofer, M. Cokoja, I. I. E. Markovits, W. A. Herrmann, F. E. Kühn, *ChemSusChem* **2014**, *7*, 1357–1360.
- [273] A. M. Hardman-Baldwin, A. E. Mattson, *ChemSusChem* **2014**, *7*, 3275–3278.
- [274] L. F. Xiao, F. W. Li, J. J. Peng, C. G. Xia, *J. Mol. Catal. A Chem.* **2006**, *253*, 265–269.
- [275] A. Sainz Martinez, C. Hauzenberger, A. R. Sahoo, Z. Csendes, H. Hoffmann, K. Bica, *ACS Sustain. Chem. Eng.* **2018**, acssuschemeng.8b02627.
- [276] A. J. Arduengo, R. L. Harlow, M. Kline, *J. Am. Chem. Soc.* **1991**, *113*, 361–363.
- [277] H. A. Duong, T. N. Tekavec, A. M. Arif, J. Louie, *Chem. Commun.* **2004**, *2*, 112–113.
- [278] H. Zhou, W. Zhang, C. Liu, J. Qu, X. Lu, *J. Org. Chem.* **2008**, *73*, 8039–8044.
- [279] Y. Kayaki, M. Yamamoto, T. Ikariya, *Angew. Chemie - Int. Ed.* **2009**, *48*, 4194–4197.
- [280] H. Zhou, W. Z. Zhang, Y. M. Wang, J. P. Qu, X. B. Lu, *Macromolecules* **2009**, *42*, 5419–5421.
- [281] S. N. Talapaneni, O. Buyukcakir, S. H. Je, S. Srinivasan, Y. Seo, K. Polychronopoulou, A. Coskun, *Chem. Mater.* **2015**, *27*, 6818–6826.
- [282] L. Yang, H. Wang, *ChemSusChem* **2014**, *7*, 962–998.
- [283] P. P. Pescarmona, M. Taherimehr, *Catal. Sci. Technol.* **2012**, *2*, 2169.
- [284] F. Castro-Gómez, G. Salassa, A. W. Kleij, C. Bo, *Chem. - A Eur. J.* **2013**, *19*, 6289–6298.
- [285] N. Kihara, N. Hara, T. Endo, *J. Org. Chem.* **1993**, *58*, 6198–6202.
- [286] J. A. Castro-Osma, J. Martínez, F. De La Cruz-Martínez, M. P. Caballero, J. Fernández-Baeza, J. Rodríguez-López, A. Otero, A. Lara-Sánchez, J. Tejeda, *Catal. Sci. Technol.* **2018**, *8*, 1981–1987.
- [287] F. D. Bobbink, D. Vasilyev, M. Hulla, S. Chamam, F. Menoud, G. Laurenczy, S. Katsyuba, P. J. Dyson, *ACS Catal.* **2018**, *8*, 2589–2594.
- [288] L. Han, H. J. Choi, S. J. Choi, B. Liu, D. W. Park, *Green Chem.* **2011**, *13*, 1023–1028.
- [289] S. Ghazali-Esfahani, H. Song, E. Păunescu, F. D. Bobbink, H. Liu, Z. Fei, G. Laurenczy, M.

- Bagherzadeh, N. Yan, P. J. Dyson, *Green Chem.* **2013**, *15*, 1584–1589.
- [290] A. H. Jadhav, G. M. Thorat, K. Lee, A. C. Lim, H. Kang, J. G. Seo, *Catal. Today* **2016**, *265*, 56–67.
- [291] S. H. Newland, W. Sinkler, T. Mezza, S. R. Bare, M. Carravetta, I. M. Haies, A. Levy, S. Keenan, R. Raja, *ACS Catal.* **2015**, *5*, 6587–6593.
- [292] R. Kore, M. Tumma, R. Srivastava, *Catal. Today* **2012**, *198*, 189–196.
- [293] D. H. Lee, M. Choi, B. W. Yu, R. Ryoo, *Chem. Commun.* **2009**, 74–76.
- [294] H. Tian, Z. Zhang, H. Chang, X. Ma, *J. Energy Chem.* **2017**, *26*, 574–583.
- [295] H. Jin, M. B. Ansari, S.-E. Park, *Catal. Today* **2015**, *245*, 116–121.
- [296] D. Liu, G. Li, J. Liu, Y. Wei, H. Guo, *ACS Appl. Mater. Interfaces* **2018**, *10*, 22119–22129.
- [297] J. Paterson, M. Potter, E. Gianotti, R. Raja, *Chem. Commun.* **2011**, *47*, 517–519.
- [298] R. M. Leithall, V. N. Shetti, S. Maurelli, M. Chiesa, E. Gianotti, R. Raja, *J. Am. Chem. Soc.* **2013**, *135*, 2915–2918.
- [299] Q. Han, B. Qi, W. Ren, C. He, J. Niu, C. Duan, *Nat. Commun.* **2015**, *6*, 10007.
- [300] A. A. Sathe, A. M. Nambiar, N. Sturgis, M. Rioux, *Catal. Sci. Technol.* **2017**, *7*, 2–3.
- [301] Z. Tasci, A. Kunduracioglu, I. Kani, B. Cetinkaya, *ChemCatChem* **2012**, *4*, 831–835.
- [302] Y. Yuan, Y. Xie, D. Song, C. Zeng, S. Chaemchuen, C. Chen, F. Verpoort, *Appl. Organomet. Chem.* **2017**, *31*, 1–6.
- [303] C. Baerlocher, L. B. McCusker, D. H. Olson, *Atlas of Zeolite Framework Types*, **2007**.
- [304] Z. Y. Gu, X. P. Yan, *Angew. Chemie - Int. Ed.* **2010**, *49*, 1477–1480.
- [305] C.-X. Yang, X.-P. Yan, *Anal. Chem.* **2011**, *83*, 7144–7150.
- [306] Q. Yan, Y. Lin, C. Kong, L. Chen, *Chem. Commun.* **2013**, *49*, 6873–6875.
- [307] J. Yu, L.-H. Xie, J.-R. Li, Y. Ma, J. M. Seminario, P. B. Balbuena, *Chem. Rev.* **2017**.
- [308] X. Wang, H. Li, X.-J. Hou, *J. Phys. Chem. C* **2012**, *116*, 19814–19821.
- [309] X. J. Hou, H. Li, P. He, *Comput. Theor. Chem.* **2015**, *1055*, 8–14.
- [310] A. Khutia, C. Janiak, *Dalt. Trans.* **2014**, *43*, 1338–1347.

- [311] P. L. Llewellyn, S. Bourrelly, C. Serre, A. Vimont, M. Daturi, L. Hamon, G. De Weireld, J. Chang, D. Hong, Y. K. Hwang, et al., *Langmuir* **2008**, 7245–7250.
- [312] A. Henschel, K. Gedrich, R. Kraehnert, S. Kaskel, *Chem. Commun.* **2008**, 4192.
- [313] L. Bromberg, Y. Diao, H. Wu, S. A. Speakman, T. A. Hatton, *Chem. Mater.* **2012**, 24, 1664–1675.
- [314] M. A. Nasalevich, M. van der Veen, F. Kapteijn, J. Gascon, *CrystEngComm* **2014**, 16, 4919.
- [315] M. Wen, K. Mori, T. Kamegawa, H. Yamashita, *Chem. Commun.* **2014**, 50, 11645–11648.
- [316] Q. X. Luo, M. Ji, M. H. Lu, C. Hao, J. S. Qiu, Y. Q. Li, *J. Mater. Chem. A* **2013**, 1, 6530–6534.
- [317] P. Chowdhury, C. Bikkina, S. Gumma, *J. Phys. Chem. C* **2009**, 113, 6616–6621.
- [318] Z. Zhang, S. Huang, S. Xian, H. Xi, Z. Li, *Energy and Fuels* **2011**, 25, 835–842.
- [319] D. M. Jiang, A. D. Burrows, K. J. Edler, *CrystEngComm* **2011**, 13, 6916–6919.
- [320] Y. Hu, W. M. Verdegaal, S.-H. Yu, H.-L. Jiang, *ChemSusChem* **2014**, 7, 734–737.
- [321] Y. Lin, H. Lin, H. Wang, Y. Suo, B. Li, C. Kong, L. Chen, *J. Mater. Chem. A* **2014**, 2, 14658–14665.
- [322] M. Taherimehr, B. Van de Voorde, L. H. Wee, J. A. Martens, D. E. De Vos, P. P. Pescarmona, *ChemSusChem* **2017**, 10, 1283–1291.
- [323] M. Ding, H. L. Jiang, *ACS Catal.* **2018**, 8, 3194–3201.
- [324] D. Liu, G. Li, H. Liu, *Appl. Surf. Sci.* **2018**, 428, 218–225.
- [325] T. Loiseau, G. Férey, *J. Fluor. Chem.* **2007**, 128, 413–422.
- [326] T. Zhao, F. Jeremias, I. Boldog, B. Nguyen, S. K. Henninger, C. Janiak, *Dalt. Trans.* **2015**, 44, 16791–16801.
- [327] O. I. Lebedev, F. Millange, C. Serre, G. Van Tendeloo, G. Férey, *Chem. Mater.* **2005**, 17, 6525–6527.
- [328] T. A. Vu, G. H. Le, C. D. Dao, L. Q. Dang, K. T. Nguyen, P. T. Dang, H. T. K. Tran, Q. T. Duong, T. V. Nguyen, G. D. Lee, *RSC Adv.* **2014**, 4, 41185–41194.
- [329] J.-Y. Zhang, N. Zhang, L. Zhang, Y. Fang, W. Deng, M. Yu, Z. Wang, L. Li, X. Liu, J. Li, *Sci. Rep.* **2015**, 5, 13514.

- [330] Z. Zhang, S. Zhang, Q. Yao, G. Feng, M. Zhu, Z.-H. Lu, *Inorg. Chem. Front.* **2018**, *5*, 370–377.
- [331] X. Sun, Q. Xia, Z. Zhao, Y. Li, Z. Li, *Chem. Eng. J.* **2014**, *239*, 226–232.
- [332] X. Wang, H. Li, X.-J. Hou, *J. Phys. Chem. C* **2012**, *116*, 19814–19821.
- [333] M. C. Biesinger, B. P. Payne, A. P. Grosvenor, L. W. M. Lau, A. R. Gerson, R. S. C. Smart, *Appl. Surf. Sci.* **2011**, *257*, 2717–2730.
- [334] M. C. Biesinger, C. Brown, J. R. Mycroft, R. D. Davidson, N. S. McIntyre, *Surf. Interface Anal.* **2004**, *36*, 1550–1563.
- [335] B. M. Weckhuysen, R. A. Schoonheydt, *Chem. Rev.* **1996**, *96*, 3327–3349.
- [336] A. Vimont, J. M. Goupil, J. C. Lavalley, M. Daturi, S. Surblé, C. Serre, F. Millange, G. Férey, N. Audebrand, *J. Am. Chem. Soc.* **2006**, *128*, 3218–3227.
- [337] R. L. Puurunen, B. M. Weckhuysen, *J. Catal.* **2002**, *210*, 418–430.
- [338] N. V. Maksimchuk, M. N. Timofeeva, M. S. Melgunov, A. N. Shmakov, Y. A. Chesalov, D. N. Dybtsev, V. P. Fedin, O. A. Kholdeeva, *J. Catal.* **2008**, *257*, 315–323.
- [339] M. Boronat, P. Concepción, A. Corma, M. Renz, S. Valencia, *J. Catal.* **2005**, *234*, 111–118.
- [340] Z. Fang, B. Bueken, D. E. De Vos, R. A. Fischer, *Angew. Chemie Int. Ed.* **2015**, *54*, 7234–7254.
- [341] B. Liu, K. Vellingiri, S.-H. Jo, P. Kumar, Y. S. Ok, K.-H. Kim, *Nano Res.* **2018**.
- [342] S. Chong, G. Thiele, J. Kim, *Nat. Commun.* **2017**, *8*.
- [343] S. Chaemchuen, Z. Luo, K. Zhou, B. Mousavi, S. Phatanasri, M. Jaroniec, F. Verpoort, *J. Catal.* **2017**, *354*, 84–91.
- [344] T. Zhao, S.-H. Li, L. Shen, Y. Wang, X.-Y. Yang, *Inorg. Chem. Commun.* **2018**, *96*, 47–51.
- [345] C. Palomino Cabello, G. Gómez-Pozuelo, M. Opanasenko, P. Nachtigall, J. Čejka, *Chempluschem* **2016**, *81*, 828–835.
- [346] A. Dhakshinamoorthy, H. Garcia, *Chem. Soc. Rev.* **2012**, *41*, 5262–5284.
- [347] V. N. Panchenko, M. M. Matrosova, J. Jeon, J. W. Jun, M. N. Timofeeva, S. H. Jung, *J. Catal.* **2014**, *316*, 251–259.
- [348] T. Toyao, M. Saito, Y. Horiuchi, M. Matsuoka, *Catal. Sci. Technol.* **2014**, *4*, 625–628.

- [349] Y. Qi, Y. Luan, X. Peng, M. Yang, J. Hou, G. Wang, *Eur. J. Inorg. Chem.* **2015**, 2015, 5099–5105.
- [350] D. Wang, Z. Li, *Catal. Sci. Technol.* **2015**, 5, 1623–1628.
- [351] J. S. Wang, F. Z. Jin, H. C. Ma, X. B. Li, M. Y. Liu, J. L. Kan, G. J. Chen, Y. Bin Dong, *Inorg. Chem.* **2016**, 55, 6685–6691.
- [352] Q. Yang, H.-Y. Zhang, L. Wang, Y. Zhang, J. Zhao, *ACS Omega* **2018**, 3, 4199–4212.
- [353] L. Valenzano, B. Civalleri, S. Chavan, S. Bordiga, M. H. Nilsen, S. Jakobsen, K. P. Lillerud, C. Lamberti, *Chem. Mater.* **2011**, 23, 1700–1718.
- [354] S. Biswas, J. Zhang, Z. Li, Y. Y. Liu, M. Grzywa, L. Sun, D. Volkmer, P. Van Der Voort, *Dalt. Trans.* **2013**, 42, 4730–4737.
- [355] M. J. Katz, Z. J. Brown, Y. J. Colón, P. W. Siu, K. A. Scheidt, R. Q. Snurr, J. T. Hupp, O. K. Farha, *Chem. Commun.* **2013**, 49, 9449.
- [356] M. Kim, J. F. Cahill, Y. Su, K. A. Prather, S. M. Cohen, *Chem. Sci.* **2012**, 3, 126–130.
- [357] M. Kandiah, M. H. Nilsen, S. Usseglio, S. Jakobsen, U. Olsbye, M. Tilset, C. Larabi, E. A. Quadrelli, F. Bonino, K. P. Lillerud, *Chem. Mater.* **2010**, 22, 6632–6640.
- [358] A. Dhakshinamoorthy, M. Opanasenko, J. Čejka, H. Garcia, *Adv. Synth. Catal.* **2013**, n/a–n/a.
- [359] J. Gascon, U. Aktay, M. Hernandez Alonso, G. Vanklink, F. Kapteijn, *J. Catal.* **2009**, 261, 75–87.
- [360] D. Jiang, L. L. Keenan, A. D. Burrows, K. J. Edler, *Chem. Commun.* **2012**, 48, 99–102.
- [361] M. Kim, J. Sergio, Garibay, S. M. Cohen, *Inorg. Chem.* **2011**, 50, 729–731.
- [362] Z. Hu, I. Castano, S. Wang, Y. Wang, Y. Peng, Y. Qian, C. Chi, X. Wang, D. Zhao, *Cryst. Growth Des.* **2016**, 16, 2295–2301.
- [363] Y. Zhao, Q. Zhang, Y. Li, R. Zhang, G. Lu, *ACS Appl. Mater. Interfaces* **2017**, 9, 15079–15085.
- [364] M. Taddei, K. C. Dömbgen, J. A. Van Bokhoven, M. Ranocchiari, *Chem. Commun.* **2016**, 52, 6411–6414.
- [365] G. Zahn, P. Zerner, J. Lippke, F. L. Kempf, S. Lilienthal, C. A. Schröder, A. M. Schneider, P. Behrens, *CrystEngComm* **2014**, 16, 9198–9207.

- [366] Z. Fang, J. P. Dürholt, M. Kauer, W. Zhang, C. Lochenie, B. Jee, B. Albada, N. Metzler-Nolte, A. Pöpl, B. Weber, et al., *J. Am. Chem. Soc.* **2014**, *136*, 9627–9636.
- [367] F. Vermoortele, B. Bueken, G. Le Bars, B. Van De Voorde, M. Vandichel, K. Houthoofd, A. Vimont, M. Daturi, M. Waroquier, V. Van Speybroeck, et al., *J. Am. Chem. Soc.* **2013**, *135*, 11465–11468.
- [368] H. Wu, Y. S. Chua, V. Krungleviciute, M. Tyagi, P. Chen, T. Yildirim, W. Zhou, *J. Am. Chem. Soc.* **2013**, *135*, 10525–10532.
- [369] T. D. Bennett, A. K. Cheetham, A. H. Fuchs, F. X. Coudert, *Nat. Chem.* **2016**, *9*, 11–16.
- [370] O. V. Gutov, M. G. Hevia, E. C. Escudero-Adán, A. Shafir, *Inorg. Chem.* **2015**, *54*, 8396–8400.
- [371] S. Ling, B. Slater, *Chem. Sci.* **2016**, *7*, 4706–4712.
- [372] L. Ning, S. Liao, X. Liu, P. Guo, Z. Zhang, H. Zhang, X. Tong, *J. Catal.* **2018**, *364*, 1–13.
- [373] C. S. Hinde, W. R. Webb, B. K. J. Chew, H. R. Tan, W.-H. Zhang, T. S. A. Hor, R. Raja, *Chem. Commun.* **2016**, *52*, 6557–6560.
- [374] V. Amendola, M. Meneghetti, *J. Phys. Chem. C* **2009**, *113*, 4277–4285.
- [375] X. Liu, M. Atwater, J. Wang, Q. Huo, *Colloids Surfaces B Biointerfaces* **2007**, *58*, 3–7.
- [376] S. Chavan, J. G. Vitillo, D. Gianolio, O. Zavorotynska, B. Civalleri, S. Jakobsen, M. H. Nilsen, L. Valenzano, C. Lamberti, K. P. Lillerud, et al., *Phys. Chem. Chem. Phys.* **2012**, *14*, 1614–1626.
- [377] A. Mirescu, U. Prüße, *Catal. Commun.* **2006**, *7*, 11–17.
- [378] R. G. Eilerman, U. by Staff, *Kirk-Othmer Encycl. Chem. Technol.* **2014**, 1–11.
- [379] A. Levitzki, A. Gazit, M. Chorev, C. Gilon, *Benzylidene- and Cinnamylidene-Malononitrile Derivatives for the Inhibition of Proliferative Processes in Mammalian Cells.*, **1995**, EP0614661A3.
- [380] R. Wirz, D. Ferri, A. Baiker, *Langmuir* **2006**, *22*, 3698–3706.
- [381] R. Cortese, D. Duca, *Phys. Chem. Chem. Phys.* **2011**, *13*, 15995–16004.
- [382] D. Amarajothi, A. M. Asiri, H. Garcia, *Chem. Commun.* **2017**.
- [383] X. Li, Z. Guo, C. Xiao, T. W. Goh, D. Tesfagaber, W. Huang, *ACS Catal.* **2014**, *4*, 3490–3497.

- [384] G. Huang, Q. Yang, Q. Xu, S. H. Yu, H. L. Jiang, *Angew. Chemie - Int. Ed.* **2016**, *55*, 7379–7383.
- [385] L. Shen, W. Wu, R. Liang, R. Lin, L. Wu, *Nanoscale* **2013**, *5*, 9374–9382.
- [386] M. Zhao, K. Yuan, Y. Wang, G. Li, J. Guo, L. Gu, W. Hu, H. Zhao, Z. Tang, *Nature* **2016**, *539*, 76–80.
- [387] H. Liu, L. Chang, L. Chen, Y. Li, *J. Mater. Chem. A* **2015**, *3*, 8028–8033.
- [388] G. J. Chen, J. S. Wang, F. Z. Jin, M. Y. Liu, C. W. Zhao, Y. A. Li, Y. Bin Dong, *Inorg. Chem.* **2016**, *55*, 3058–3064.
- [389] S. Proch, J. Herrmannsdörfer, R. Kempe, C. Kern, A. Jess, L. Seyfarth, J. Senker, *Chem. - A Eur. J.* **2008**, *14*, 8204–8212.
- [390] J. L. Opgrande, E. E. Brown, M. Hesser, J. Andrews, in *Kirk-Othmer Encycl. Chem. Technol.*, John Wiley & Sons, Inc., Hoboken, NJ, USA, **2003**.
- [391] J. Panten, H. Surburg, in *Ullmann's Encycl. Ind. Chem.*, Wiley-VCH Verlag GmbH & Co. KGaA, Weinheim, Germany, **2016**, pp. 1–45.
- [392] J.-P. Vidal, in *Kirk-Othmer Encycl. Chem. Technol.*, John Wiley & Sons, Inc., Hoboken, NJ, USA, **2006**.
- [393] K. Tulig, K. S. Walton, *RSC Adv.* **2014**, *4*, 51080–51083.
- [394] M. C. M. Daniel, D. Astruc, *Chem. Rev.* **2004**, *104*, 293–346.
- [395] A. Aijaz, A. Karkamkar, Y. J. Choi, N. Tsumori, E. Rönnebro, T. Autrey, H. Shioyama, Q. Xu, *J. Am. Chem. Soc.* **2012**, *134*, 13926–13929.
- [396] Y. Pan, B. Yuan, Y. Li, D. He, *Chem. Commun.* **2010**, *46*, 2280–2282.
- [397] R. Wu, X. Qian, K. Zhou, H. Liu, B. Yadian, J. Wei, H. Zhu, Y. Huang, *J. Mater. Chem. A* **2013**, *1*, 14294–14299.
- [398] S. Diring, S. Furukawa, Y. Takashima, T. Tsuruoka, S. Kitagawa, *Chem. Mater.* **2010**, *22*, 4531–4538.
- [399] N. V. Maksimchuk, K. A. Kovalenko, S. S. Arzumanov, Y. A. Chesalov, M. S. Melgunov, A. G. Stepanov, V. P. Fedin, O. A. Kholdeeva, *Inorg. Chem.* **2010**, *49*, 2920–2930.
- [400] M. Saikia, V. Kaichev, L. Saikia, *RSC Adv.* **2016**, *6*, 106856–106865.

- [401] M. P. Casaletto, A. Longo, A. Martorana, A. Prestianni, A. M. Venezia, *Surf. Interface Anal.* **2006**, *38*, 215–218.
- [402] D. J. Stewart, M. E. Potter, R. Raja, *Patent Pending*, **2018**.